Deep Ultraviolet Light-Emitting Diodes for High-Speed Optical Communications

PhD Thesis

By Daniel M. Maclure

Institute of Photonics, Department of Physics
University of Strathclyde, Glasgow

Supervisors Professor Martin D. Dawson
and Dr Johannes Herrnsdorf

Declaration of Authorship

This thesis is the result of the author's original research. It has been composed by the author and has not been previously submitted for examination, which has led to the award of a degree.

Signed:……………

Date:……………….

Contents

List of figures

List of tables

Abstract

Micro-light-emitting diodes (μLEDs), defined as LEDs with dimensions below 100 μm, are at the forefront of innovation, including for deep ultraviolet (DUV) emission. The rapid advances in μLED technology have unlocked new potentials for applications in high-resolution displays and, notably, optical wireless communications. This thesis presents a thorough characterisation of DUV μLEDs and explores their implementation in wireless communication systems.

Through a series of in-depth experiments, this research noted pronounced size-dependent behaviours in μLEDs, including variations in turn-on voltage, optical output power, quantum efficiency, and modulation bandwidth. Smaller devices were found to require higher turn-on voltages and lower efficiencies but higher bandwidths. These observations demonstrated the necessity for continued research into contact technologies and the fundamentals of device operation for DUV μLEDs.

Pushing the boundaries of optical wireless communication, this work demonstrates key advances in wavelength-division multiplexing (WDM) for the ultraviolet spectrum. Notably, the first three-wavelength UV communication system is showcased, achieving a combined data throughput of nearly 10 Gbps, one of the highest reported in the UV regime. While the performance of UVB-emitting devices used here lagged behind that of the other wavelengths, this provides a clear trajectory for future refinement.

Furthermore, this thesis reports on the development of medium-range, line-of-sight DUV μLED communication links, achieving data rates up to 1 Gbps over unprecedented distances of 100 metres. This stands as the highest data rate attained over such a range using a single μLED pixel at any wavelength at the time of writing. The capabilities of μLEDs were further explored through a two-mirror system, enabling multi-reflection transmission and achieving significant data rates over short distances (less than 10 metres).

The research also investigates non-line-of-sight (NLOS) communication using commercially available DUV LEDs. These experiments demonstrate a robust kilobits-per-second link, benefiting from the milliwatt-level optical power of current DUV commercial devices. The integration of novel, single-photon-sensitive DUV detectors facilitated NLOS links, including around-corner communication, opening promising new directions for ultraviolet optical wireless technology.

In summary, this thesis delivers insights into the size-dependent phenomena of DUV μLEDs, establishes their promise for high-speed optical wireless communication, and showcases both line-of-sight and non-line-of-sight data transmission. Collectively, these findings advance the field of ultraviolet optoelectronics and lay the groundwork for future innovation in μLED-based communication technologies.

Abbreviations

AC - alternating current

AlGaN - aluminium gallium nitride

APD - avalanche photodiode

BER - bit error rate

DC - direct current

DUV - deep ultraviolet

EQE - external quantum efficiency

FEC - forward error correction

FOV - field of view

FPGA - field programmable gate array

FS - free space

FSOC - free space optical communications

GaN - gallium nitride

LEDs - light-emitting diodes

LOS - line of sight

MQW - multiple quantum well

µLEDs - micro-LEDs

NLOS - non-line of sight

OFDM - orthogonal frequency division multiplexing

OOK - on-off keying

OWC - optical wireless communications

PMT - photomultiplier tube

PV - photovoltaics

QAM - quadrature amplitude modulation

SNR - signal to noise ratio

SPAD- single photon avalanche diode

UV-Ultraviolet

VLC-visible light communications

WDM- Wavelength-division multiplexing

Acknowledgements and preface

Firstly, I would like to thank Dr Jonathan McKendry for all the support throughout this PhD project, for helping me with the projects, and for answering my questions, regardless of how daft they were. I would also like to thank my supervisors, Prof Martin Dawson and Dr Johannes Herrnsdorf, for all the support and guidance during my PhD. I would like to thank Jordan Hill and Dr Enyuan Xie for supplying the devices used in this work and helping me understand the fabrication steps of the devices. I would also like to thank Dr Matthew Warden from Fraunhofer UK for the kind support and guidance during my PhD. I would also like to thank Hichem Zimi for working with me at the end of my PhD and for asking questions which forced me to research a topic and understand some of the processes. I would like to thank Dr Mohamed Islim, Dr Cheng Chen and Professor Harald Haas from the LiFi Research and Development Centre, University of Cambridge (formerly the Universities of Edinburgh and Strathclyde) for all the help and support with the optical communications protocol. Without their expertise, this project would not have been possible. I would like to thank Mr Ronnie Roger for keeping the clean room up and running, which allowed a steady stream of high-quality devices to flow.

I would like to thank my family, especially my mum, Karen, and my dad, Mark, for their love and support throughout this process. I would like to thank my sister Mia for her support throughout my undergraduate and postgraduate studies. I would also like to thank my grandparents, Margret and John, for all the years of support throughout this journey. Finally, I would like to thank Eleni Margariti for all the support and help throughout this PhD journey.

I would like to thank Mrs Jaffery, my high school physics teacher, who inspired me to pursue a physics degree.

In memory of Mary Maclure (1946-2023)

Chapter 1 Introduction

1. 1 Outline of the thesis

This thesis examines multiple aspects of deep ultraviolet (DUV) communications, with a primary focus on optimising data rates and extending transmission distances. This thesis will aim to use DUV microLEDs in conjunction with state-of-the-art encoding methods in order to demonstrate the ability of these devices to create high-speed indoor communications links.

Chapter 1 presents the foundational physics of semiconductors and the operational principles of Light Emitting Diodes (LEDs), along with introductory information on optical communications and encoding methods used in this work.

Chapter 2 analyses the characteristics of DUV micro light-emitting diode (μLED) devices, considering size-dependent parameters such as LIV turn-on voltage, external quantum efficiency, and bandwidth. The impact of device dimensions on system performance is evaluated, and a comparative analysis is conducted across different device arrays.

Chapter 3 follows on from this, focusing on wavelength-division multiplexing (WDM) by incorporating multiple UV devices (UV-A, UV-B, and UV-C) and exploring their integration into a single system. The goal is to aggregate high-data-rate channels to maximise the combined throughput on a single channel.

Chapter 4 examines DUV communication at longer ranges (5-116m). This section evaluates the effects of different bias conditions on data transmission rates. It describes two experimental setups using one- and two-mirror arrangements to increase optical path lengths and examine the impact of distance on a line-of-sight (LOS) link.

Chapter 5 considers non-line-of-sight (NLOS) communication using commercial DUV LEDs, evaluating device performance in terms of signal strength and achievable data rates in short-range NLOS contexts.

Finally, Chapter 6 summarises the findings and outlines potential directions for future research.

1. 2 Introduction to LEDs

The investigation of semiconductor materials began in the early twentieth century. Henry Joseph Round first reported light emission from carborundum in 1907 [1,2]. Early research focused on characterising semiconductor material properties but work from Bell Laboratories in the late 1950s contributed to developments such as the transistor and practical solar cells [3]. These advances led to the emergence of companies such as Texas Instruments and Hewlett-Packard, which facilitated the mass production of semiconductor- based light-emitting diodes (LEDs). During the next decade, red LEDs were developed, albeit with low efficiency initially, and the available range of wavelengths expanded over the coming years [4].

Over the past twenty years, the LED industry has grown substantially [5], influenced by technological advances such as the creation of gallium nitride (GaN)-based white and blue LEDs in the 1990s by Nakamura, Amano, and Akasaki, whose achievements were recognised with the Nobel Prize in 2014 [6]. By 2020, LED lighting technology had become common in residential settings, mainly due to its improved energy efficiency (as shown in Figure 1-1(a), longer operational lifespan (about 20,000 hours), lower costs, and reduced environmental impact compared to traditional lighting.

Blue and violet GaN-based LEDs were initially used in consumer products, displays, and general lighting. Still, their applications have since expanded to underwater communications, reflecting changes in consumer demand and technology. However, in recent years, due to research on disinfection, DUV devices have seen increased interest and have been improving rapidly in quality [7–11]. Figure 1-1(b) summarises the applications of UV LED technology across multiple areas, highlighting the rich opportunities for these sources. One key application is NLOS and LOS communications; other applications in research include lithography and material curing, which can be used in semiconductor device production (e.g., masked photoetching). DUV devices are also used in medical applications such as sterilisation and the treatment of skin conditions such as psoriasis, which involves exposing damaged skin to UV light in order to help alleviate symptoms.

(a)

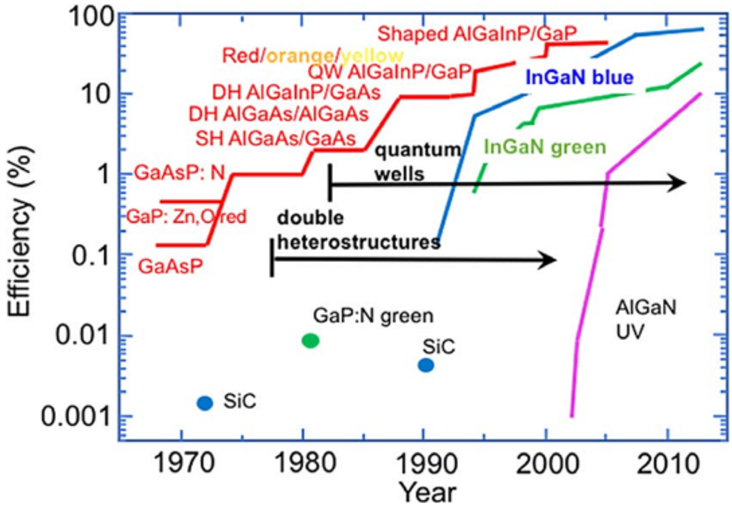

(b)

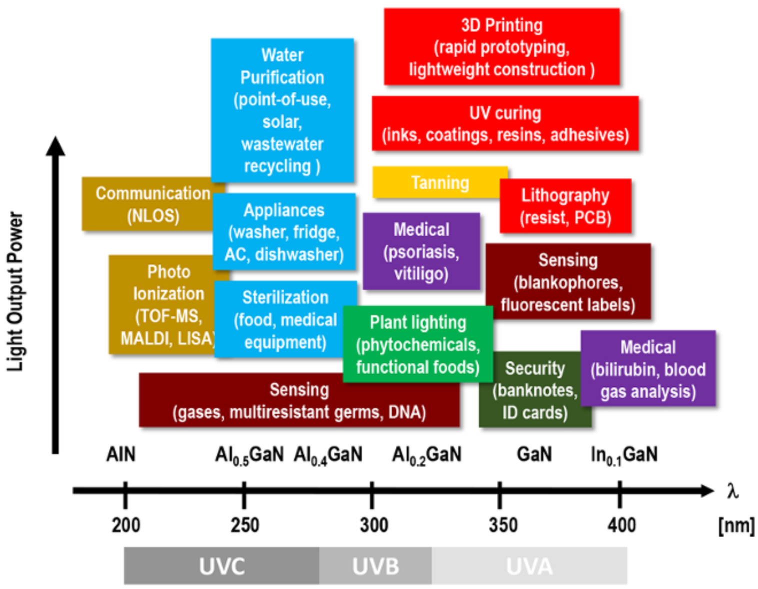

Figure 1-1. a) Improvement over time in the external efficiency of LEDs [12] b) Examples of DUV LED applications as a function of wavelength [13].

1.2.1. Material science of semiconductors

This section will primarily focus on what makes semiconductors important for producing LEDs, as LEDs are semiconductor-based devices that produce light.

Materials can broadly be divided into three groups according to their electrical conductivity: conductors, semiconductors and insulators. In conductive materials, such as metals (e.g. copper and gold), the valence and conduction bands overlap, as shown in Figure 1-2, allowing charge carriers to move freely and enabling efficient electrical conduction. In contrast, insulators, such as rubber and wood, exhibit substantial energy gaps between these bands, which severely restrict the movement of carriers and confine charge. However, when subjected to sufficiently high voltages, even insulators may briefly conduct electricity.

Semiconductors occupy an intermediate position. Their band structure resembles that of insulators but with a much narrower energy gap. This smaller bandgap (typically 1-3 eV) allows electrons to be excited into the conduction band with relatively little energy, enabling electrical conduction under suitable conditions [14]. Because of this, semiconductors can support carrier movement however their electrical conductivity increases with temperature, a property opposite to that of metals, which become more resistive as they heat up. Elements like silicon (Si) and germanium (Ge) are classic examples of intrinsic (pure) semiconductors. However, it should be noted that this work uses wideband gap semiconductors such as GaN and AlN, which have band gaps >3eV, which is larger than the typical range of semiconductors. This has both benefits, such as the ability to operate at higher temperatures and higher voltages, which have been a major driver of development in GAN-based electronics, and disadvantages, such as poor hole injection and high p-layer resistivity, something which will be discussed later in this chapter. The electrical properties of a semiconductor can be engineered by intentionally doping it with selected impurities, as will be discussed in Section 1.2.2. Some semiconductors are made from alloys, such as AlGaN, which allow their bandgap energy to be tuned, as will be discussed in Section 1.2.3.

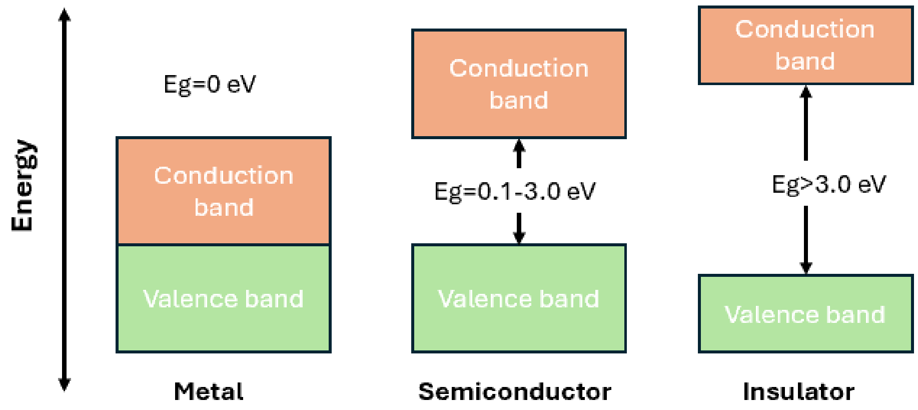

Figure 1-2. Schematic band structure of metals, semiconductors and insulators demonstrating the typical bandgap energies

1.2.2. Doping

To create functional semiconductor devices, doping is commonly used to engineer the electrical properties of the semiconductor layers. When a material is intentionally infused with impurities to alter its electrical properties, it is known as an extrinsic semiconductor. In contrast, materials without doping are referred to as intrinsic semiconductors [15]. An illustration of the principle of doping is shown in Figure 1-3, which uses silicon doping as an example. For n-type doping, a group 5 element (such as phosphorus) is introduced into silicon (a group 4 element), adding extra electrons and creating an energy level just below the conduction band. An example of such doping is shown in Figure 1-3a. This makes it easier for electrons to move and conduct electricity. In p-type doping, a group 3 element (such as Boron) is added, resulting in "holes" (missing electrons) in the valence band, as shown in Figure 1-3 b. These holes created by the excitation of electrons into states above the Valence band edge, which have been introduced by the dopant, allow for positive charge transport, turning the material into a p-type semiconductor. When n-type and p-type semiconductors are joined, their surplus electrons and holes combine and can emit light, a phenomenon that will be discussed in more detail in the next section.

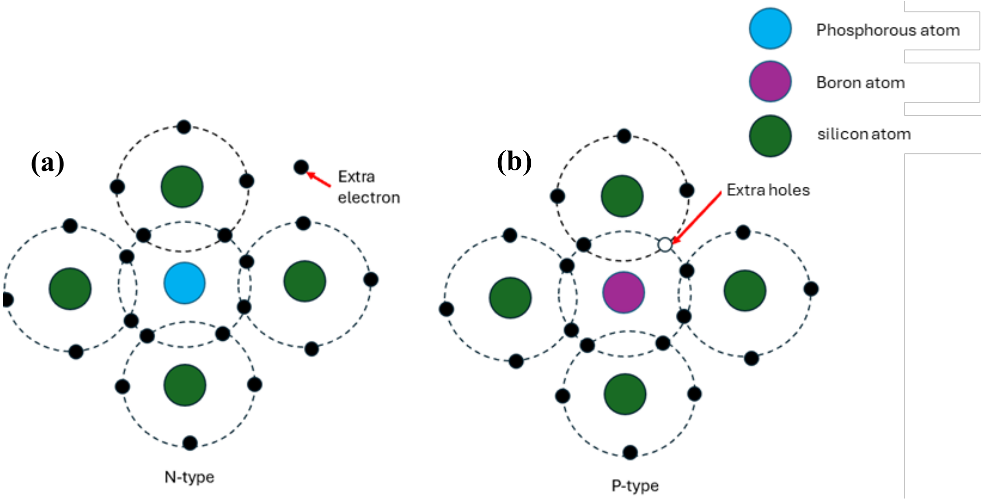

Figure 1-3 Example of doping a) n-doping and b) p-doping, taking silicon as a reference.

When manufacturing UV LEDS using Aluminium Indium Gallium Nitride (AlInGaN), doping with Si and Mg is commonly used to create n-type and p-type material [16,17]. In the next section, the material properties of AlInGaN will be discussed in more detail.

1.2.3. Aluminium Indium Gallium Nitride (AlInGaN)

The LEDs and μLEDs to be shown later in this thesis are all based on the AlGaInN quaternary semiconductor alloy system.

In contrast to silicon, the AlGaInN semiconductor alloy is classified as a direct bandgap material, which facilitates efficient electron-hole recombination processes without reliance on phonon assistance. As illustrated in Figure 1-4, InGaN alloys are capable of visible light emission, whereas AlGaN alloys extend the spectral range into the ultraviolet, reaching up to the >6 eV bandgap characteristic of AlN. Through precise compositional engineering, AlGaN can be tailored to emit electroluminescence across the entire UV spectrum, including the UV-C region from 280 nm down to approximately 225 nm. Typically, these heterostructures are fabricated as multilayer thin films grown on sapphire substrates [18,19], with increasing aluminium concentrations used to create shorter-wavelength devices.

However, UV LEDs present severe design challenges, including difficulties with the contacts (cathode and anode), poor current spreading [20–22], and high turn-on voltages, which will be examined in Chapter 2 [16]. With this material, it is possible to engineer UV-emitting devices, which will be discussed in the following section.

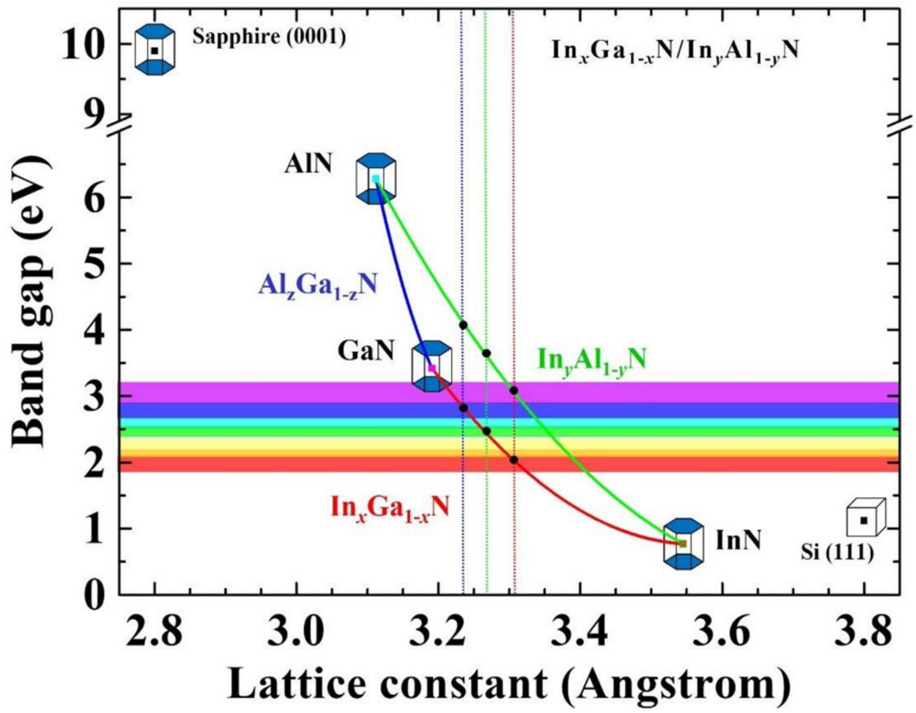

Figure 1-4. Band gap energy vs lattice constant for a range of binary, ternary and quaternary compound semiconductors. The AlInGaN alloy shows band gaps from 0.7eV (InN) to 6eV (AlN) and is the basis of nitride visible and UV LED technology[23].

1. 3 Diodes

Building on the fundamentals of semiconductor materials, the following section will examine the basic principles of light-emitting diodes (LEDs), beginning with an exploration of junction diodes, which are the foundation of many optoelectronic devices.

1.3.1. Junction diodes

A p-n junction diode consists of three distinct regions: an n-type region, a p-type region, and the intervening depletion region, as shown in Figure 1-5. This structure is the basis of several important semiconductor devices, including LEDs and solar cells. The depletion region, sandwiched between the p- and n-type regions, is typically much narrower (on the order of nm) than the heavily doped areas on either side. Here, electrons from the n-type side diffuse across the junction into the p-type region, leading to an accumulation of negative charge at the p-type boundary and a corresponding build-up of positive static charge at the n-type interface. This arrangement creates an internal electric field that forms the basis for diode operation.

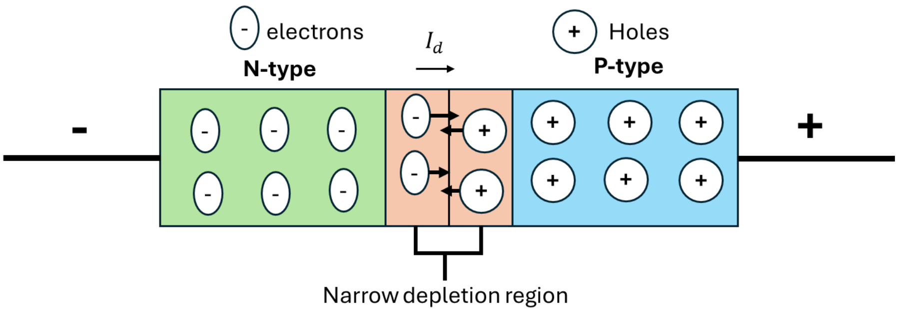

Figure 1-5 A P-N diode junction in a forward bias configuration.

The formation of a potential barrier at the p-n junction effectively restricts the flow of charge carriers. When a diode is forward-biased, the barrier height is reduced, allowing charge carriers to cross the junction and generate current. This mechanism is key to understanding the operation of LEDs. In contrast, applying a reverse bias increases the barrier, further impeding charge carrier movement and blocking current flow. Only a minimal diffusion current may persist if a sufficiently large reverse voltage is applied. As a result, diodes serve as one-way valves for current in electronic circuits.

Key parameters such as the diffusion voltage and the depletion region's width are critical to diode performance. The diffusion voltage can be calculated using the following equation:

$$V_D = \frac{kT}{e} \ln \frac{N_A N_D}{{n_i}^2} \tag{1.1}$$

where N_A acceptor concentration and N_D donor concentrations and n_i is the intrinsic carrier concentration of the semiconductor. The depletion layer width is given by:

$$W_D = \sqrt{\frac{2\varepsilon}{e}(V_D - V)(\frac{1}{N_A} + \frac{1}{N_D})} \tag{1.2}$$

Junction diodes are commonly found in two forms, with homojunctions (diodes made from a single material) proving less effective at confining electrons. As a result, most commercial devices favour heterojunction structures, which combine different materials to enhance electron trapping and overall performance.

1.3.2. Light-emitting Diodes (LEDs)

LEDs are a form of junction diode that converts electrical energy into light, and as covered in section 1.1.1, are a class of solid-state devices widely used in lighting and industrial applications. What distinguishes light-emitting diodes from conventional diodes is that when electrons and holes recombine in an LED, their energy is (ideally) released as photons. In recent decades, advancements in semiconductor materials have enabled LEDs to emit photons across wavelengths from ultraviolet to infrared, dramatically broadening their utility.

As discussed in section 1.2.3 the bandgap energy in an LED can be tuned by altering the semiconductor alloy composition, and the relation of emission wavelength and bandgap energy is given in the equation below:

$$E_e - E_h \approx E_g = hf \qquad (1.3)$$

Here, E_g is the bandgap energy, E_e is the electron energy, E_h the energy of the hole, h is the Planck constant, and f is the frequency of the photons [24].

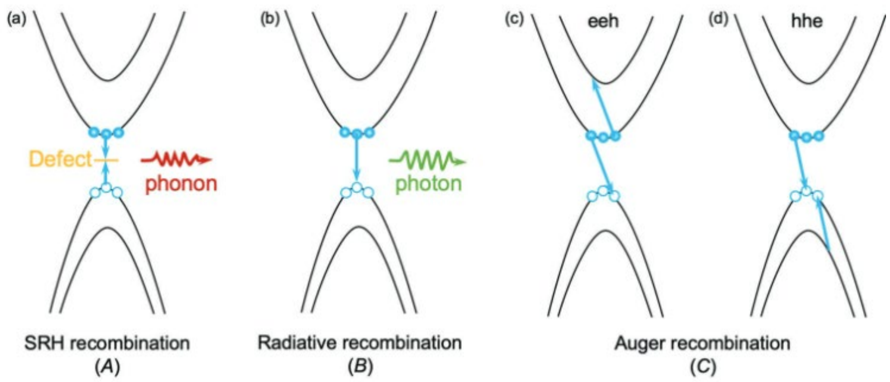

***Figure 1-6 Example of recombination for a) Shockley Reid Hall b) radiative recombination, and c) Auger recombination** [25]*

Multiple recombination processes govern the behaviour of semiconductor devices. Within the device, carrier recombination may proceed via radiative processes, which generate photon emission, or through non-radiative mechanisms, resulting in energy loss without light production [26]. These different types of recombination are presented in Figure 1-6. Radiative recombination produces photon emission, while non-radiative mechanisms such as Shockley-Read-Hall (SRH) recombination, caused by electron interactions with crystal defects and Auger recombination [27] where energy is transferred to another charge carrier instead of creating light, primarily generates heat. At high current densities, as seen in μLEDs, which will be discussed in Chapter 2, non-radiative losses like SRH and Auger recombination become increasingly impactful, resulting in greater thermal output and accelerated device deterioration.

It is important to note the distinction between LED and laser emission. LEDs emit incoherent light through spontaneous emission that is typically unpolarised, while lasers produce coherent light through stimulated emission which is typically polarised, making polarization-based operation more challenging with LEDs.

1.3.3. Quantum well structures

Modern light-emitting semiconductor structures typically feature active regions constructed from quantum wells. These quantum wells possess nanometre thicknesses, comparable to the electron de Broglie wavelength, which results in quantum confinement perpendicular to the well plane [28–31]. The wells are delineated by higher bandgap barriers on each side, effectively localising charge carriers. This localisation, coupled with the spatial overlap of electron and hole wave functions, enables efficient recombination [17,32] (see Figure 1-7). This basic phenomenon can be described using the Schrodinger equation and a particle in a box model using the following equation:

$$-\frac{\hbar^2}{2m^*}\frac{d^2\varphi(x)}{dx^2} + v(x) = E\varphi(x) \tag{1.4}$$

Here, m^* is the effective mass of the electron (hole) in the semiconductor, *v(x)*, the potential energy profile determined by the band offsets between well and barrier materials. *E* are the allowed energy levels inside the well and *φ(x)* is the wavefunction describing the probability amplitude of carriers. Mathematically, the model can be described as a finite well potential, and the well region has lower potential energy for electrons and holes, while the barrier regions have higher potential energy. As a result for electrons, the equation can be simplified to:

$$E_n \approx \frac{n^2\pi^2\hbar^2}{2m^*L^2} \tag{1.5}$$

Where E_n is the quantised energy level, and L defines the well width, where a thinner well can result in higher energy and, as a result, shorter wavelength emissions. The effective mass of the electrons is given by m^* and is material dependent.

(a)

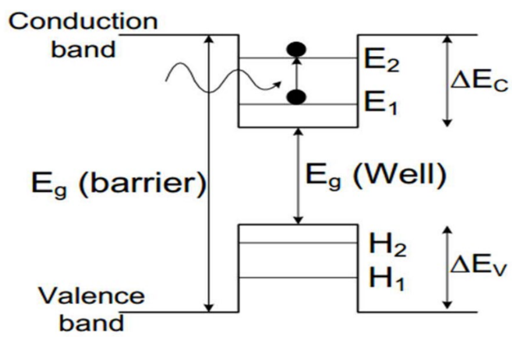

(b)

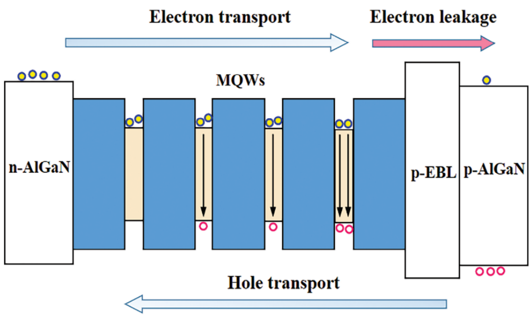

***Figure 1-7 a) Quantum well particle in a box where E_g(well) and E_g(barrier) are the energy gap for the well and the barrier. Furthermore, E and H represent the energy levels the electrons and holes can occupy, respectively** [33] **and b) Quantum well structure for AlGaN device** [34].*

A practical LED structure generally consists of multiple quantum wells sandwiched between carrier injection layers [32]. In nitride-based LED architectures, a wider bandgap electron blocking layer (EBL) is frequently incorporated to minimise electron leakage and overflow [35]. Quantum well compositions are commonly chosen to remain under coherent strain with the growth substrate, compressive strain which yields TE-polarised emission being often selected to optimise light extraction efficiency [36]. For instance, a typical AlGaN based UVC LED may incorporate a number of quantum wells [37,38], with individual well and barrier thicknesses of approximately 1.5 nm and 5 nm, respectively. These advances in nanoscale engineering and material selection serve as a foundation for the development of micro-LEDs [39], which will be explored in greater detail in the subsequent sections.

1.3.4. MicroLEDs (μLEDs)

Micro-LEDs (μLEDs), first developed in the late 1990s and early 2000s, are LEDs distinguished by their exceptionally small dimensions typically < 100 μm while those up to ~300 μm are classified as mini-LEDs, as illustrated in Figure 1-8. Unlike conventional LEDs, which are manufactured on larger chips, μLEDs offer remarkable advantages in terms of efficiency, compactness, and versatility.

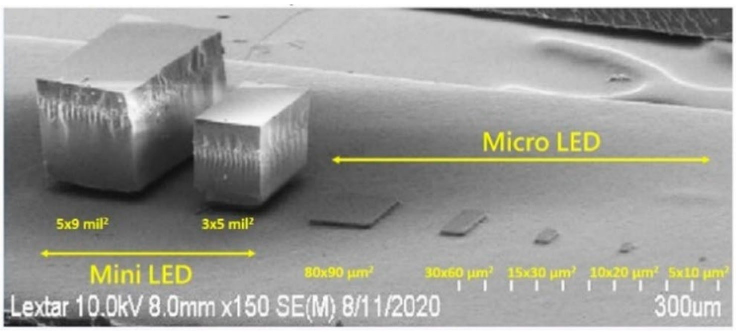

Figure 1-8. Examples of μLEDs and mini-LEDs *[40].*

Recent years have witnessed a surge of interest in μLED technology, especially for advanced display systems (see Figure 1-9 (a)). This μLED technology facilitates the development of large-scale arrays and offers remarkable improvements in image resolution, though the high costs of manufacturing remain a barrier to broader commercial adoption.

A particular focus is the integration of inorganic μLEDs into backlighting architectures, where they compete with Organic Light Emitting Diodes (OLEDs) by delivering superior energy efficiency, lifetime and enhanced colour contrast [41]. Current research momentum is driven by the promise of μLED screens to revolutionise visual fidelity and lower power consumption. Today, μLEDs are making significant inroads into applications such as augmented reality (AR) and virtual reality (VR), with advancements spanning consumer electronics, commercial displays [15,42,43], and defence technologies [26,44]. It is important to note that the μLED devices discussed here for displays predominantly emit within the visible spectrum. Progress in CMOS driver integration has enabled the fabrication of ever smaller µLED arrays, paving the way for innovations like the "Mega Projector" [45] a device capable of producing optical QR codes and compact image projections combining both displays and communication systems (see Figure 1-9 (b)).

(a)

(b)

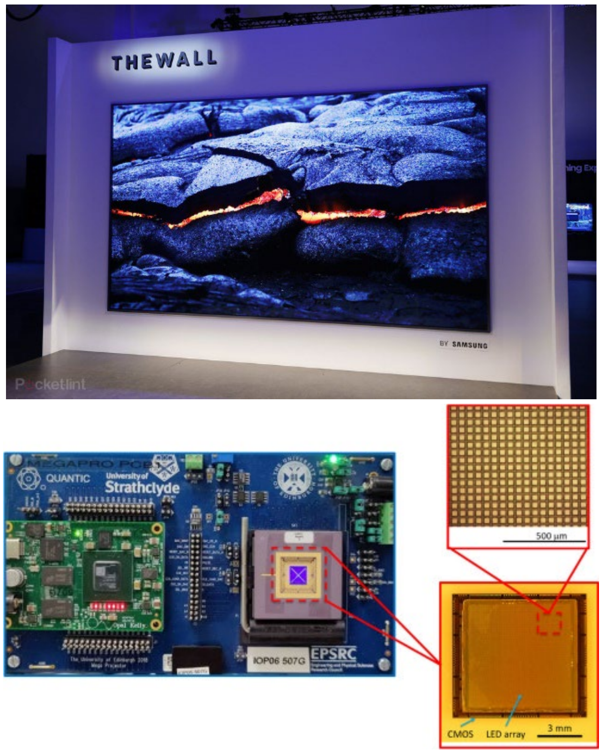

Figure 1-9. a) TV screen using µLEDs** [46] **and b) a photograph of a 128x128 LED array and its driver board** [45] **.

µLEDs have also emerged as compelling candidates for optical transmitters in optical communication systems, primarily due to their exceptionally high modulation bandwidths (which can reach 100s of MHz), a result of their small size. This is a large increase compared to standard broad-area LEDs with modulation bandwidths on the order of 10s of MHz, which will be examined in Chapter 2 [47–51]. This characteristic enables µLEDs to support significantly higher data rates than many traditional light sources, opening the door to high-speed free-space optical communication links [52–55]. This behaviour is demonstrated in the following equation:

$$f_c = \frac{1}{2\pi\tau} = \frac{1}{2\pi RC}$$

Where f_c is the cut off frequency in this case the -3dB bandwidth frequency and R is the resistance and C is capacitance However, it is important to note that while the fabrication of μLED arrays is progressing rapidly for visible wavelengths, technological limitations remain in the deep ultraviolet (DUV) spectral region [56–59].

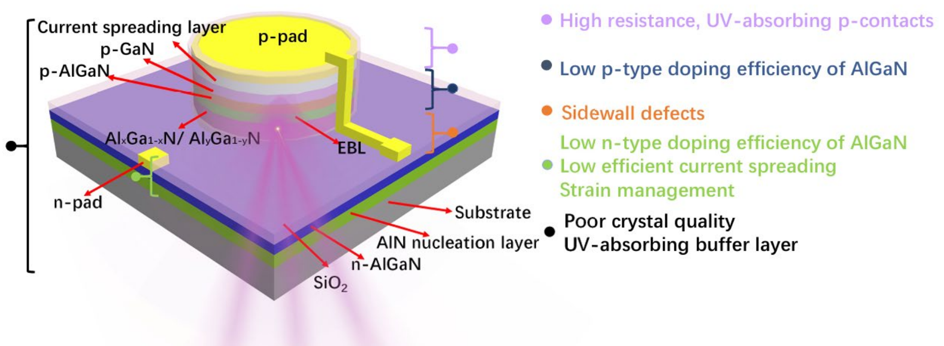

Figure 1-10 Schematic of a DUV AlGaN LED [60].

At present, the construction of DUV μLED arrays with a similar level of integration and performance as their visible-spectrum counterparts is not yet feasible [61,62]. As a result, the research in this thesis focuses on single-pixel DUV μLED devices. By leveraging the intrinsically high bandwidth of these DUV emitters, this work aims to systematically examine the maximum achievable data rates (an example of one of these devices is shown in Figure 1-10). Through experimental investigation, this work seeks to establish the fundamental limits and potential of DUV μLEDs for high-speed optical communication, thereby laying the groundwork for future advances, such as those enabled by large arrays.

1. 4 Wireless Communications

As discussed to this point, UV LEDs and UV μLEDs are useful emitters for high-data optical wireless communications. In addition to these transmitters, there have to be supporting modulation schemes and high-bandwidth detectors. This section will discuss the key fundamental concepts of communications that underpin the experimental work presented in subsequent chapters, including the various forms of optical communications and modulation, which will be used in chapters 3-5.

1.4.1. Optical Communications

Since the Industrial Revolution, communication technologies have evolved rapidly from the telegraph and telephone to radio transmission, mobile phones and culminating in the widespread use of smart Internet of Things (IoT) devices [63,64]. Each innovation increased connectivity and required higher data rates, and as a result, this progress has led to the current "bandwidth crunch", where growing demand is outpacing the capabilities of available radio and microwave frequencies, as shown in Figure 1-11 [65–67] .

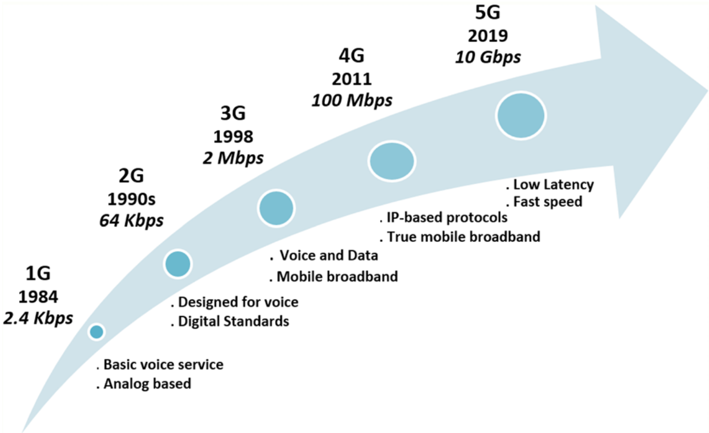

Figure 1-11 The growth in mobile data rate demands over time*[68]*

To overcome these constraints, operators are turning to new areas of the electromagnetic spectrum, such as infrared, visible, and ultraviolet light [69]. These spectral regions offer much broader bandwidth, potentially more than 2,600 times greater than that of radio frequencies [44,66]. Free-Space Optical Wireless Communication (FSOC) has emerged as a promising technology, capable of delivering ultra-fast data links for scenarios where traditional approaches like satellite radio or underwater acoustic communications fall short (see Figure 1-12) shows such a network, for both fixed and mobile infrastructure at ground level in the atmosphere and in space.

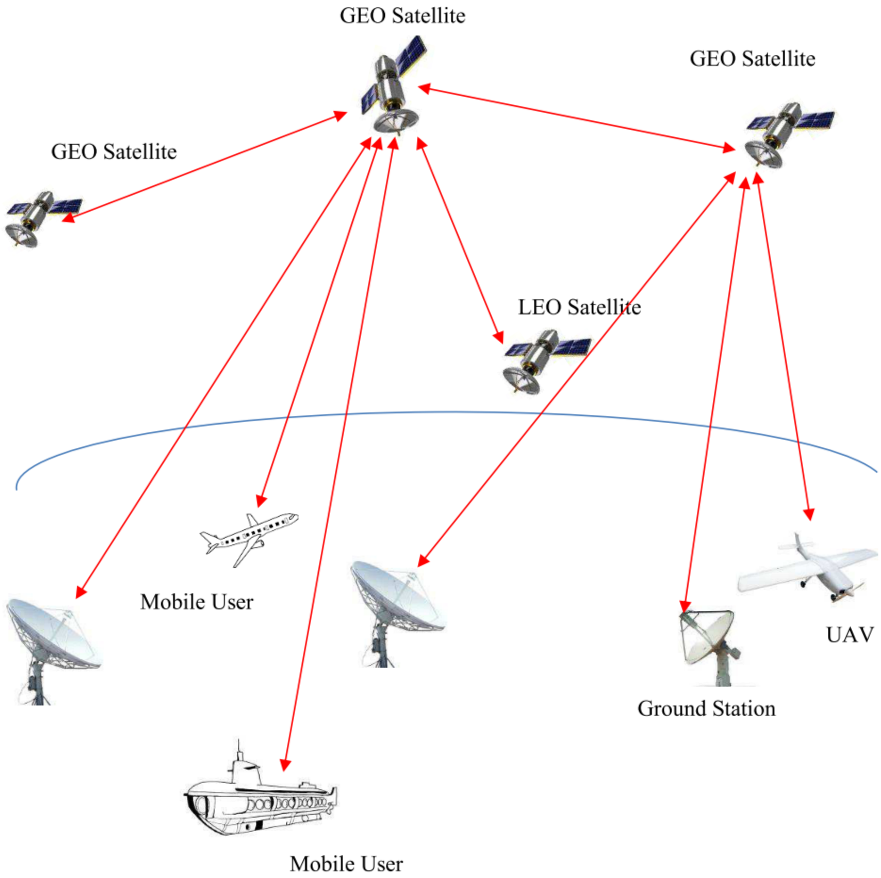

***Figure 1-12 An example of a free-space optical communications network over a range of Km using infrared laser sources** [70].*

Optical communications have a long history, from ancient beacon fires used for long-distance signalling to naval visual communication using searchlights during the world wars [70]. Today, the field of FSOWC is experiencing renewed attention, thanks to advancements in fibre optics, laser technology, and sophisticated modulation techniques.

The development of modern Optical Wireless Communication (OWC) systems began in the 1970s. OWC offers significant advantages, including potentially seamless integration with existing infrastructure, such as indoor lighting, for data transmission. Compared to lasers (e.g. laser diodes and LDs), LEDs reduce eye and skin safety risks and, due to their Lambertian emission pattern, can be deployed more flexibly. LEDs now the standard for residential lighting [71,72] can transmit data at high speeds without visible flicker. Technologies like Li-Fi, which build on this approach, enable secure communication within a room [55,73], since light cannot pass through walls, providing a valuable complement to Wi-Fi. Examples of indoor FSOWC setups are shown in Figure 1-13. In these systems, LEDs are typically used for wide-area coverage, while lasers are preferred for long-distance, highly directional links. The following sections explore the key categories of free-space optical communication: line-of-sight (LOS) and non-line-of-sight (NLOS) systems.

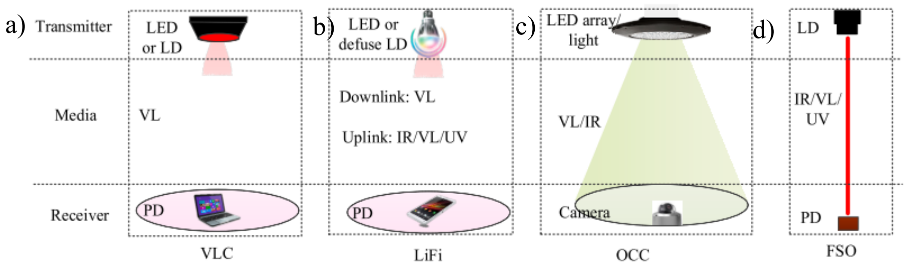

Figure 1-13 Examples of optical communication techniques: a) demonstration of a single source to connect to a single item using an LED, b)LiFi using existing room lighting for optical communication, c) optical camera communications using a camera as a receiver, d) laser optical communication commonly used for long-range communications here VLC means visible light communication, OCC is optical camera communication and FSO is free space optical communication. *[63].*

1.4.2. Line of Sight (LOS)

Optical wireless communication systems are generally divided into LOS and non-line-of-sight (NLOS) categories. In practice, free space infrared communication and most Light Fidelity (LiFi) setups which use existing room lighting rely heavily on LOS configurations, as they offer straightforward alignment and superior signal quality through direct, unobstructed light paths [66]. For these systems to function at their best, both the transmitter and receiver must remain within each other's view commonly, for instance, with the transmitter installed on the ceiling and the receiver placed on a desk (see Figure 1-14).

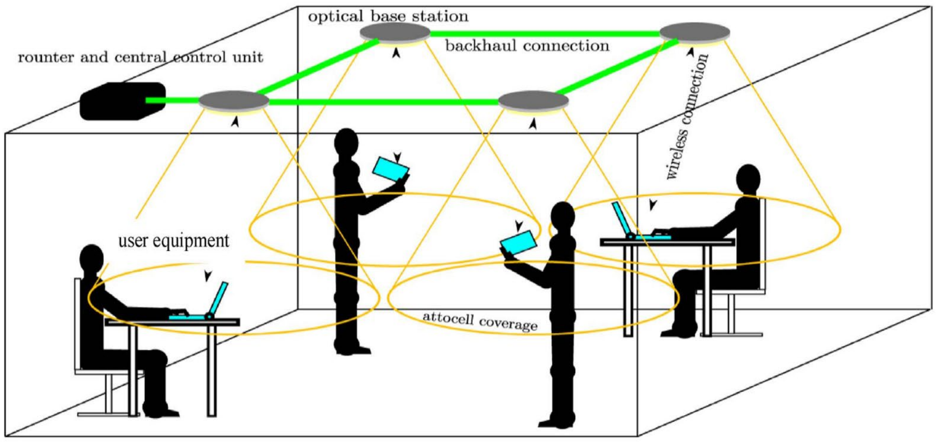

Figure 1-14 A LiFi setup harnessing lighting in an office space to supply internet to multiple users [74].

Recent developments in LiFi technology have showcased 100Mbps to Gbps data transmission [75], enabling seamless high-speed communication in office settings [76]. The built-in security of these systems, thanks to their confinement within enclosed spaces, has sparked growing interest in defence and enterprise sectors. Moreover, LOS optical wireless communication boasts immense bandwidth for applications such as inter-satellite and satellite-to-ground links.

However, LOS optical channels in urban/crowded environments face several challenges: multipath interference from surface reflections, obstructions such as walls, and occasional connection losses due to receiver blockage. Achieving reliable performance in low-light, photon-limited scenarios remains an active area of research. Outdoor deployments are further complicated by weather conditions rain, fog, and haze can all diminish signal strength, making adaptive beam steering essential for maintaining robust performance [63]. While this approach can add complexity and cost, it still delivers far higher data rates than traditional radiofrequency (RF) systems.

The most stable LOS operation occurs when both transmitter and receiver are stationary, especially in well-controlled indoor environments. Due to the challenges stated above, researchers are also focusing on developing advanced non-line-of-sight (NLOS) communication strategies, which will be explored in the next section.

1.4.3. Non-Line of Sight (NLOS)

Non-Line-of-Sight (NLOS) propagation is a vital aspect of modern wireless communication, particularly in urban environments where buildings and other obstructions frequently block direct transmission paths. In such environments, electromagnetic signals do not travel straight from transmitter to receiver, instead they interact with their surroundings, such as gas molecules in the air, leading to significant scattering [77]. However, this scattering occurs over a range of kilometres, and as a result, NLOS systems using scattering are often longer-range communications systems. However, in the UV, there is a higher absorption coefficient, which can limit range, and at the moment, most long-range work relies on LOS and diffuse LOS.

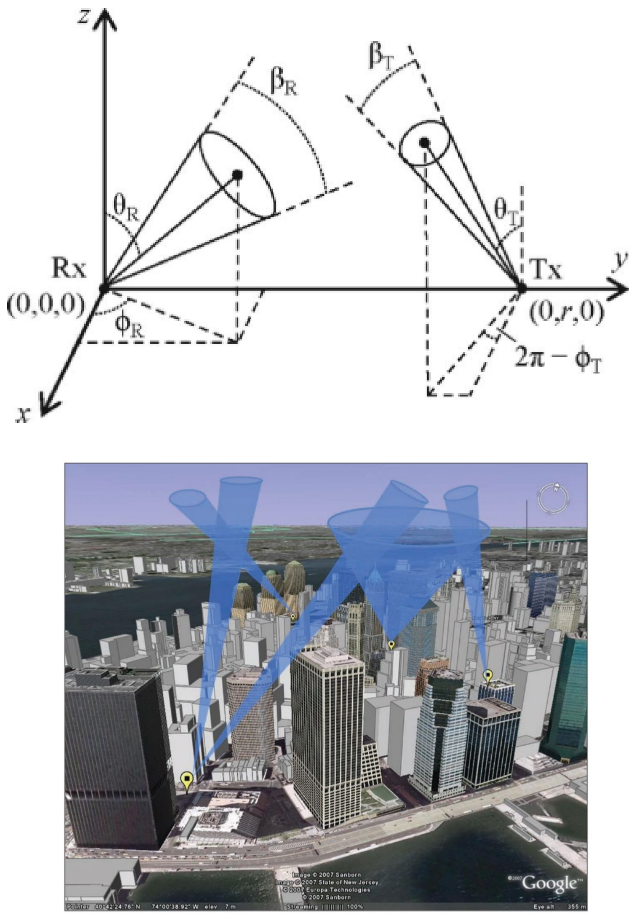

Figure 1-15 ***A theoretical set-up for NLOS UV communication with multiple scattering events. The transmitter (Tx) and detector (Rx),*** $\boldsymbol{\beta_r}$ ***is the field of view of the receiver,*** $\boldsymbol{\beta_t}$ ***beam angle of the transmitter, the zenith and azimuth angles of the transmitter are given as*** $(\boldsymbol{\theta_T}, \boldsymbol{\emptyset_T})$ ***and the receiver as*** $(\boldsymbol{\theta_R}, \boldsymbol{\emptyset_R})$ *[78].* ***b) Example of NLOS DUV applications*** *[79].*

The advancement of NLOS communication techniques (see the schematic in Figure 1-15) has become crucial for expanding the practical use of OWC systems [80], which often struggle with the limitations imposed by LOS requirements, especially in dense urban areas [81–83]. Recently, deep ultraviolet (DUV) communication has emerged as a leading NLOS technology, attracting growing academic interest [84–87], especially for distances up to a few kilometres, which is theoretically possible, but practical demonstrations have been limited. Compared with line-of-sight communications, data rates are often lower due to lower SNRs. NLOS systems also rely on sensitive detectors like PMTs and SPADs, which are typically bandwidth-limited compared to the faster APDs used in LOS systems, resulting in lower data rates.

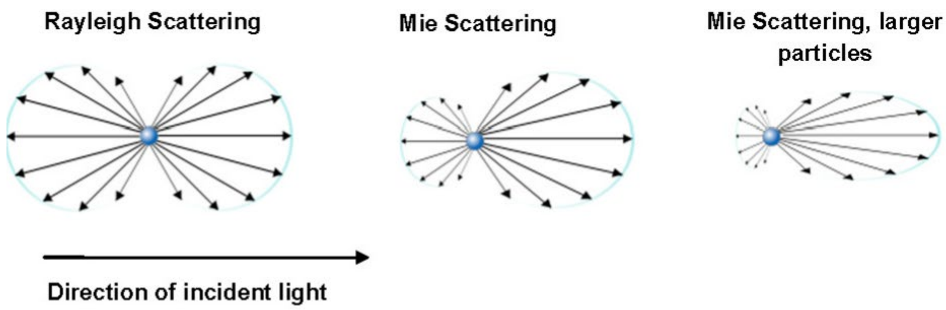

Figure 1-16 Diagram showing Rayleigh scattering and Mie scattering, with the third image demonstrating that larger particles have an impact on Mie scattering.*[88]*

In deep ultraviolet (DUV) communications, the nature of scattering is governed by two principal mechanisms: Rayleigh [89] and Mie scattering [90,91]. Mie scattering becomes especially relevant in conditions where atmospheric particles, such as those found in fog or pollution [63], are similar in size to the wavelength of DUV light. In contrast, Rayleigh scattering dominates when the particles primarily molecules like oxygen and nitrogen are much smaller than the wavelength of the radiation. Notably, Rayleigh scattering intensifies as the wavelength decreases (equation 1.4) [89,92,93], meaning that ultraviolet signals are far more prone to this effect than their visible or infrared counterparts. As a result, DUV transmissions must contend with greater attenuation but also benefit from unique propagation characteristics, making them a compelling choice for specialised NLOS applications.

$$Rayleigh\ scattering\ \propto \frac{1}{\lambda^4} \tag{1.4}$$

As particle size increases, Mie scattering becomes more directional, as shown in Figure 1-16. Both Mie and Rayleigh scattering are forms of elastic scattering, meaning that the photons' energy remains unchanged during the interaction. Over longer distances, atmospheric turbulence caused by aerosols adds further complexity [94–98]. Models of haze and fog conditions indicate that both the size and concentration of Mie scatterers affect optical path loss, and that total path loss increases with distance [88,99,100]. The following section explores DUV communications in detail and discusses the integration of innovative DUV µLEDs within these systems.

1.3.4 UV/DUV communications and DUV µLED communications

Ultraviolet (UV) light occupies a unique segment of the electromagnetic spectrum, defined by its short wavelengths and high photon energies. UV radiation is typically divided into three bands: UVA (400–300 nm), which largely reaches the Earth's surface, UVB (around 300 nm) and UVC (100-280 nm), which is almost entirely absorbed by the upper atmosphere, rarely making it to the ground. This strong atmospheric absorption of UVC makes deep ultraviolet (DUV) communications appealing, as such wavelengths are naturally virtually absent at ground level on Earth (see Figure 1-17) and therefore the UVC region presents a low-noise window for OWC.

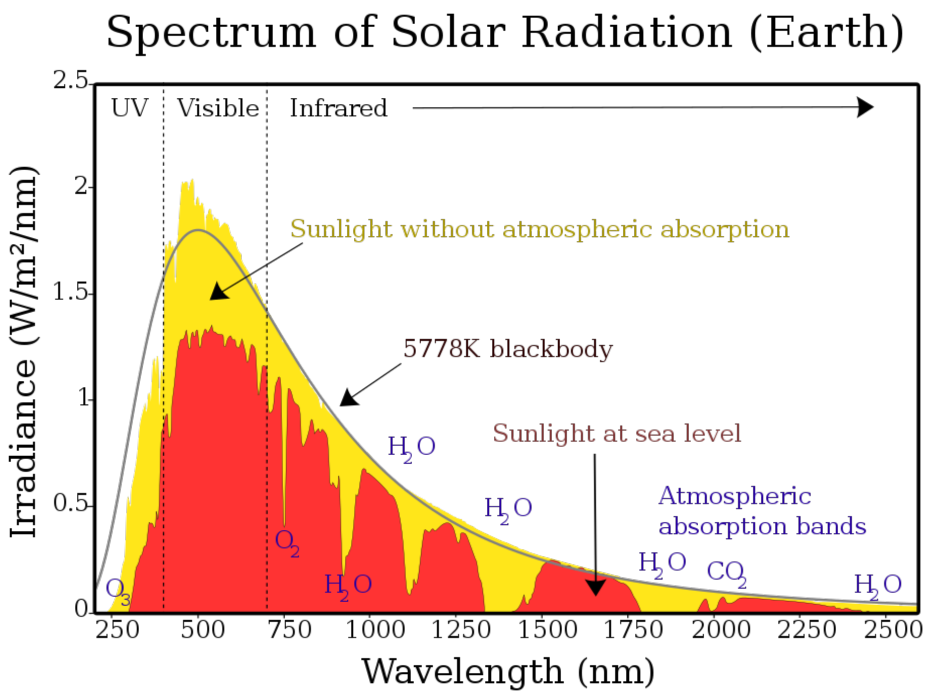

Figure 1-17 The solar irradiance distribution emitted by the sun and the absorption curves of the atmosphere** [101]**.

Originally, mercury lamps were the primary source of UV light for these purposes, but technological advances have shifted the focus to DUV LEDs. DUV LEDs, built from materials like aluminium gallium nitride (AlGaN), offer far greater bandwidths (the range of frequencies a device can transmit data over) from tens to several hundreds of megahertz (MHz) compared to mercury flash lamps, which are typically limited to the kilohertz range [102,103]. These DUV LEDs also avoid the environmental and safety hazards associated with mercury, making them not only more practical but also safer in operation.

For communications, DUV light's low background noise and significant scattering properties make it especially promising for NLOS and diffuse line-of-sight applications [104–107]. Unlike visible or infrared light, DUV signals require far less precise alignment, simplifying their use in situations where pointing and tracking are challenging [108]. Despite their advantages, DUV systems require careful attention to safety. Human tissue is not adapted for prolonged or intense exposure to these wavelengths, which can be ionising at high doses. However, many applications are designed for environments with little or no human presence, such as aerial platforms [109,110] and intersatellite links [111], where atmospheric absorption further limits ground-level exposure and ensures the signal is obscured from a ground observer.

A promising new direction for future UV communications lies in the development of high bandwidth μLED arrays. At present, DUV μLEDs require high turn-on voltages, limiting their integration with standard electronics and making large arrays difficult to scale, thus limiting their usage in communications applications. Recent improvements in fabrication are beginning to address these issues [20,112,113]. Our work focuses on communications using deep ultraviolet μLEDs, which are valued for their high bandwidth and suitability for short-range optical links. While DUV μLEDs are less efficient and emit lower optical powers than those in the visible spectrum, our work seeks to analyse their performance in a series of characterisation and communications experiments (see chapters 2-4). Given the current scarcity of studies on DUV μLED systems, these results represent a meaningful contribution to the field.

The following section provides an overview of the modulation schemes used in the optical transmission experiments described in this work.

1.4.4. Modulation and Multiplexing

Modulation lies at the heart of data transmission, enabling information to be efficiently encoded onto a carrier wave for communication across various distances. In early commercial radio broadcasting, the most widely used techniques were amplitude modulation (AM) and frequency modulation (FM) which are analogue encoding methods. AM encodes data by varying the carrier wave's amplitude in step with the input signal. In contrast, FM does so by adjusting the carrier's frequency higher amplitude signals result in greater frequency deviation. FM is a popular choice for commercial radio due to its superior resistance to static and interference.

In contrast, optical communication systems rely on advanced modulation formats such as pulse amplitude modulation (PAM) and Quadrature amplitude modulation (QAM), paired with orthogonal frequency-division multiplexing (OFDM), which are also commonly used in both fibre-optic and copper-based telecommunications. Both these modulation schemes rely on intensity modulation, which works by varying the intensity of the chosen light source in order to encode data. Direct detection is used to detect the signal intensity modulation and allows for the recording of the received data, which can then allow for decoding processes to begin. This subsection will examine some of the modulation schemes used in this work, starting with the simplest form, on-off keying (OOK), a form of amplitude modulation also used in the NLOS work presented in Chapter 5. Following that, we will discuss Quadrature amplitude modulation QAM and OFDM, which are more complex methods of encoding and multiplexing, which are used throughout the work demonstrated in Chapters 3 and 4.

1.4.5. On-Off Keying (OOK)

On-off keying (OOK) is a straightforward yet powerful modulation technique, widely used for transmitting binary information[114]. In this method, a logical '1' is represented by the presence of a signal during a bit interval, while a logical '0' is indicated by its absence. An example is shown in Figure 1-19. OOK can also be used with highly sensitive photodetectors like photomultiplier tubes (PMTs) or single-photon avalanche diodes (SPADs) as will be shown in Chapter 5 [115].

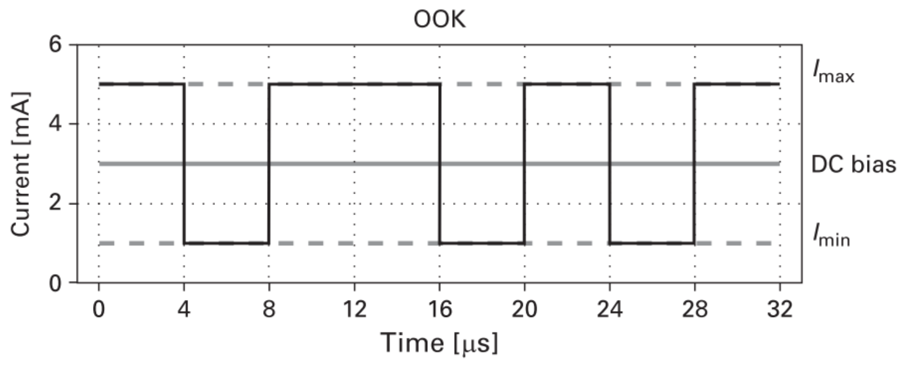

***Figure 1-18 An example of an OOK modulation scheme with an intensity being varied with time** [116].*

The simplicity and energy efficiency of OOK make it highly attractive for resource-limited systems. However, this basic modulation scheme is more susceptible to noise (as the scheme is based on modulated intensity stray light in an optical communications system or from an unknown source, which can change the modulation intensity and can result in errors) and environmental interference than more advanced modulation schemes like orthogonal frequency-division multiplexing (OFDM), which offer superior spectral efficiency and improved noise resilience. Consequently, OOK is best suited for applications requiring low complexity and cost, but its heightened sensitivity to noise and spectral inefficiency remain notable drawbacks compared to the robustness and spectral efficiency achievable with OFDM-based systems.

1.4.6. Quadrature Amplitude Modulation (QAM)

Quadrature Amplitude Modulation (QAM) is an advanced modulation technique employed in contemporary communication systems to enhance data transmission efficiency [117–119]. This method integrates two amplitude-modulated signals of the same frequency, one in the phase component I and the other in the quadrature Q, within a single channel, thereby significantly increasing bandwidth utilisation (an example of 16-QAM is shown in Figure 1-20).

By modulating both the amplitude and phase of the carrier wave, QAM allows for the representation of multiple bits per symbol, for example, for 16 QAM, which uses 16 different constellation points where every symbol can have 4 binary bits, as this relation is described as 2^n where *n* represents the number of bits per symbol, facilitating high-speed data transfer. QAM is extensively utilised in a variety of applications, including digital television, broadband internet, and cellular networks [125,126], where it contributes to higher data rates and improved signal quality. Its ability to transmit higher volumes of data within a fixed bandwidth underscores its vital role in the evolving field of digital communications.

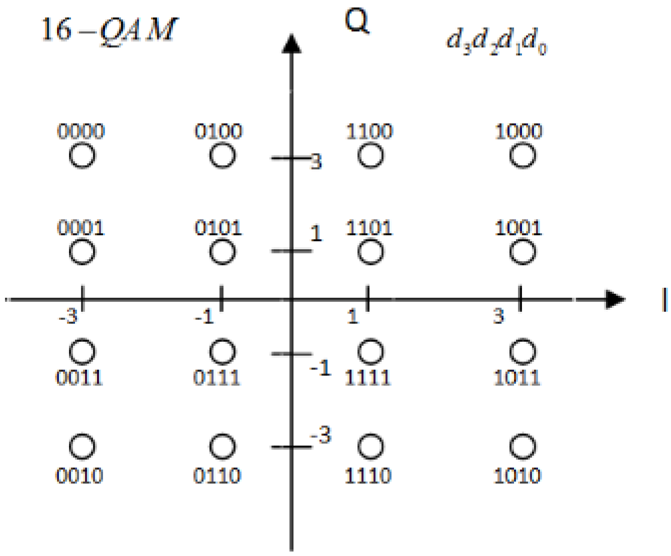

Figure 1-19 An example constellation diagram of QAM (I- in-phase and Q-quadrature) *[120].*

1.4.7. Orthogonal frequency division multiplexing (OFDM)

Orthogonal Frequency Division Multiplexing (OFDM) is a cornerstone of modern wireless communication, underpinning both 4G and 5G systems [114,116,119,121]. By dividing the available spectrum into multiple orthogonal subchannels, OFDM enables multiple channels to transmit data simultaneously, thus maximising spectral efficiency without the need for traditional guard bands (see Figure 1-21). The orthogonality of these subcarriers ensures that each one reaches its peak amplitude precisely when the others are at zero, significantly reducing inter-symbol interference and allowing for higher overall data throughput [122,123].

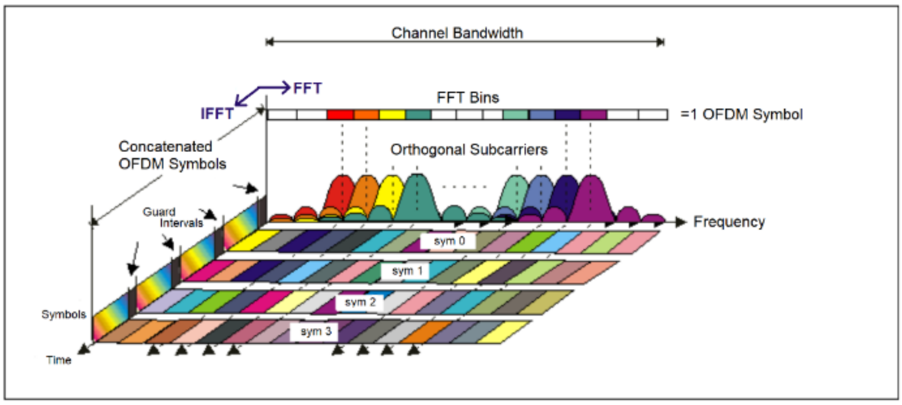

Frequency-Time Representative of an OFDM signal

Figure 1-20 Diagram of the theory of OFDM encoding *[124].*

The implementation of OFDM involves transforming the data into discrete frequency packets using an Inverse Fast Fourier Transform (IFFT), which shifts the signals into the time domain for transmission [125]. At the receiver end, a Fast Fourier Transform (FFT) converts the incoming signals back into the frequency domain, faithfully reconstructing the original data [126]. This approach not only optimises bandwidth usage and minimises signal distortion but also supports high-speed data transfer. However, these benefits come with added complexity, as OFDM systems require advanced signal processing, such as matched filters (which is a linear method of filtering which relies on knowing the signal being transmitted) [117,127–129]. Pulse shaping is also used to minimise inter-symbol interference by shaping the waveform of the transmitted signal to fit within in the bandwidth range of the transmitter thus keeping data rates low, the details of these components and their roles will be explored in detail in Chapter 3.

OFDM is both complex and bipolar. OFDM in optical communications uses intensity modulation and direct detection (IM/DD). As a result, the signal must be real and unipolar. As a result, Hermitian symmetry is used to get a real signal, and the subcarriers are equally spaced across frequencies between $(-\frac{1}{2}T_s,\frac{1}{2}T_s)$ of the sampling period of the time domain. However, if a DC bias is applied to the system, it uses DCO-OFDM, which requires the signal to be real and unipolar. As a result, Hermitian symmetry is used to get a real signal, and the subcarriers are equally spaced across frequencies between (minus 1 half cap T sub s,1 half cap T sub s close paren of the sampling for a positive and real signal. As the source often has a limited dynamic range, clipping levels need to be implemented to minimise clipping. Single-tap equalisation can be used in OFDM. This allows the lower-frequency signal with the higher SNR to sacrifice some of its SNR to boost the SNR of the higher-frequency signals, thereby enabling a higher data rate and lower BER [130].

1.4.8. Bit Error Rate & Signal to Noise ratio

The bit error rate (BER) measures wireless communication reliability by comparing the ratio of incorrect bits received to the total number of transmitted bits. BER is determined by comparing each sent bit with its received counterpart. Errors arise from issues like signal degradation, poor synchronisation, and noise. A BER of 0.5 is a “worst case scenario”, indicating that the receiver was unable to reliably decode any of the transmitted bits – the BER saturates at 0.5 as even in this scenario the receiver would correctly “guess” that a received bit was either a logic 0 or a logic 1 50% of the time, on average.

Key factors affecting BER include low signal strength and a poor signal-to-noise ratio (SNR). Lower SNR increases BER due to greater noise influence. Eye diagrams visually assess digital signal integrity in PAM (see Figure 1-22) an open, wide eye diagrams indicate a high SNR and reliable data transmission. In contrast, a closed eye reflects a lower SNR and higher BER [131].

When signal strength nears the noise floor, distinguishing between ones and zeros becomes increasingly complex, especially with synchronisation errors raising the likelihood that noise corrupts the data, leading to incorrect bit decoding.

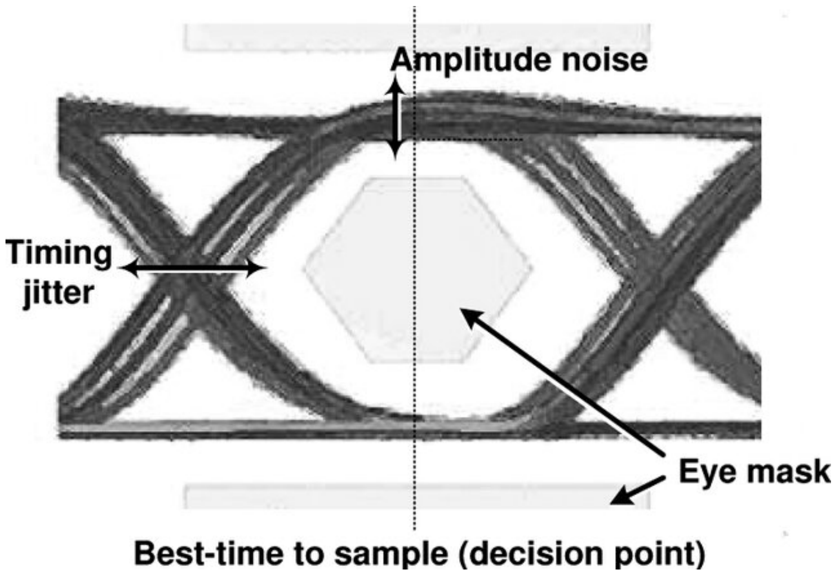

Figure 1-21 An example of an Eye diagram *[131].*

1.4.9. Forward error correction

To overcome errors in communication links, error correction can be applied to enable reliable communication systems. Forward error correction (FEC) is an important method used in this work (see chapters 3 and 4) to reduce the bit error rate (BER) by embedding redundant bits within transmitted data [79,114,117,132]. This redundancy allows communication systems to detect and correct errors without retransmitting the data, significantly boosting link reliability as long as the BER remains below a certain threshold. For example, it is common to allocate about 7% of the total data stream to FEC overhead. This is illustrated in Figure 1-23, which compares transmitted and received signals.

$$2^r \geq m + r + 1 \quad (1.6)$$

Among the various FEC techniques, Hamming codes are often utilised for their practical balance between complexity and performance (see equation 1.6). Redundant bits are inserted into the data stream at positions corresponding to powers of two, with m being the total number of information bits and r the redundant bits calculated using a standard equation. In this thesis, a threshold BER of 3.8×10^{-3} is adopted, necessitating a 7% FEC overhead figures that align with common practice in optical wireless communications literature. This allows the final data rate to be determined and ensures a reliable optical link.

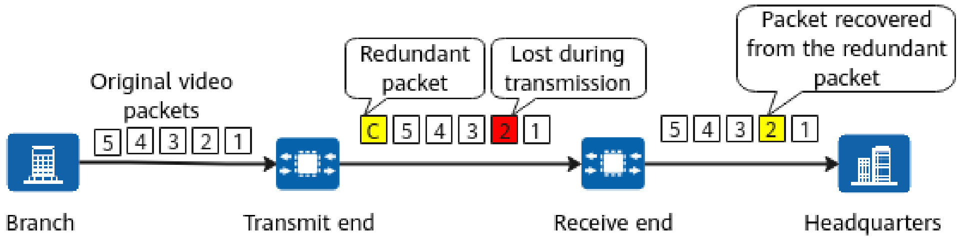

Figure 1-22 An example of FEC in a communications system demonstrating the use of redundant bits to correct for errors [133].

1. 5 Detectors

Photodetectors are fundamental components in optical communication systems, as they convert incoming light signals into corresponding electrical signals, enabling decoding. In this work, particular attention is paid to detectors, especially those tailored for deep ultraviolet (DUV) applications, which, despite ongoing advancements, still lag behind their visible-spectrum counterparts in terms of performance.

Three main types of detectors avalanche photodiodes (APDs), single-photon avalanche diodes (SPADs), and photomultiplier tubes (PMTs) are employed in the experimental work to be discussed later in chapters 2 to 5.

1.5.1. Avalanche Photodiodes (APDs)

Avalanche photodiodes (APDs) played a central role in this research, serving as the primary detectors for bandwidth measurements in Chapter 2 and communications analysis in Chapters 3 and 4. APDs operate by applying a reverse bias, which, upon reaching a critical voltage, triggers avalanche multiplication: a single absorbed photon releases multiple charge carriers, resulting in a marked amplification of the photocurrent, as shown in Figure 1-24 (a) and (b). For this investigation, a custom-built, ultraviolet-sensitive APD with a 1 GHz bandwidth (Hamamatsu C5668 8867) was employed. While this detector offers considerable advantages for deep ultraviolet (DUV) applications, its bandwidth is still somewhat limited when compared to APDs designed for the visible spectrum.

(a)

(b)

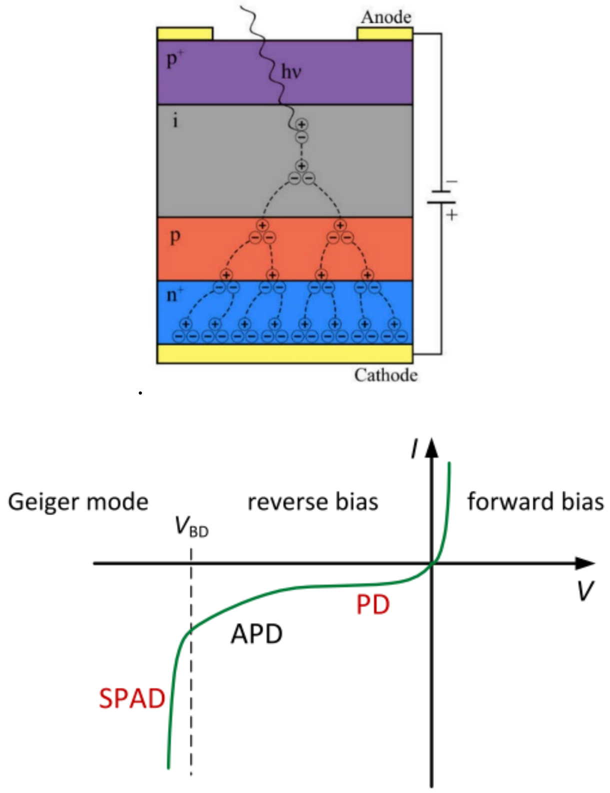

Figure 1-23 a) A diagram of a photodiode (including an illustration of gain via avalanche breakdown)[134] and b) shows the IV characteristics involved in an avalanche breakdown where the reverse voltage is increased. *[135].*

Its small active area (about 300 µm^2) helped achieve high bandwidth by reducing capacitance but also demanded precise optical alignment and introduced challenges in pointing and tracking. To suppress unwanted DC signals and mitigate background noise, AC coupling was implemented, allowing the detector to work seamlessly with orthogonal frequency-division multiplexing (OFDM) and advanced encoding techniques. This capability distinguishes APDs used in the communications work in chapters 3 and 4 from single-photon avalanche diodes (SPADs) and photomultiplier tubes (PMTs), which were used in chapters 2 and 5, which do not differentiate between DC and AC components and are thus more vulnerable to interference from ambient light.

However, the need for precise alignment achieved here using XYZ micrometre stages can limit the practical deployment of high-bandwidth, small-area APDs, especially in NLOS scenarios where their sensitivity is a limiting factor. As a result, more sensitive detectors, such as SPADs and PMTs, are also worth considering, as will be shown in Chapter 5. Nevertheless, the primary focus of this work remained on evaluating data transmission rates using DUV μLEDs with APDs as the primary detection platform.

1.5.2. SPADs

Single-photon avalanche diodes (SPADs) are exceptionally sensitive photodetectors that play a vital role in advanced optical systems and will be used in Chapter 2 to study the external quantum efficiency of the LEDs. SPADs typically operate in what's known as Geiger mode, where they are reverse-biased significantly above their breakdown voltage (see Figure 1-24 (b) and Figure 1-25) [135]. This configuration, together with specialised quenching circuits, enables the detection of single photons, which cannot be achieved by an APD, as a larger number of photons are needed to generate a photocurrent; as a result, APDs are far less sensitive than SPADs. The SPAD outputs these photon counts as discrete electrical pulses while also ensuring that the avalanche process is promptly halted after each event; thus, it is possible to detect photons with precise timing. However, this detection method introduces a brief period of "dead time" following each photon detection [136], which limits the detector's maximum bandwidth to a few 10s of megahertz; even with these lower-bandwidth SPADs, they have proven useful in applications such as LiDAR [104,134] where the high bandwidths could allow for faster pulses which could allow for greater range resolution however the low optical powers could be problematic. Initial silicon-based SPADs had limited quantum efficiency in the DUV spectrum, restricting their use in DUV applications due to inadequate detector sensitivity. Modern research aims to enhance the DUV sensitivity of silicon-based SPADs and improve the bandwidth. Despite these strides, DUV solar-blind SPADs still face challenges from crystalline defects, which can increase dark count rates and reduce overall measurement accuracy [137]. SPADs nonetheless excel at lower bit rates, NLOS applications, where their unique combination of sensitivity and photon-counting capability is particularly valuable; however, SPADs were used in Chapter 2 for DUV characterisation at short distances [138].

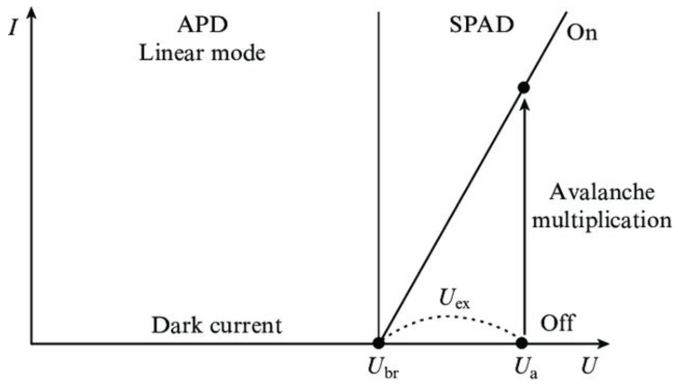

Figure 1-24 Shows the point at which an APD becomes a SPAD (U_{br} breakdown voltage), U_a (an excited state) and U_{ex} is the excess voltage [138].

1.5.3. Photomultiplier Tubes (PMTs)

Photomultiplier tubes (PMTs) are a cornerstone technology in photon detection, operating on the principle of the photoelectric effect. When photons strike the charged metallic photocathode (illustrated in Figure 1-26) they release photoelectrons, a process particularly suited to capturing high-energy photons such as those found in the deep ultraviolet (DUV) spectrum. These photoelectrons are then accelerated by an electric field across a cascade of dynodes, each set at a higher voltage, creating a chain reaction that multiplies the number of electrons and significantly amplifies the original signal. This mechanism allows PMTs to reliably detect even single-photon events, producing measurable photocurrents.

Modern PMT systems incorporate advanced electronic circuitry to enable rapid signal quenching, ensuring that each detected photon generates a distinct electrical pulse. Recent developments by companies like Hamamatsu have introduced integrated electronics capable of digitising the PMT output, which allows for the integration of PMT-based photon counting systems to be used for applications in modern optical communication and sensing systems.

In the context of optical communications, PMTs are highly valued for their remarkable sensitivity under low-light conditions [79,139,140]. However, they are not without limitations: their bandwidth is relatively limited, they are prone to noise, which often necessitates complex filtering to isolate true signals from background interference, and they are based on vacuum tubes, which means they are not as robust to physical damage as a solid-state detector. Despite these challenges, PMTs are especially advantageous in NLOS optical communications, where there is a limited number of photons, and the ability to detect single photons is crucial [86,140,141]. The use of PMT for communications will be explored further in Chapter 5.

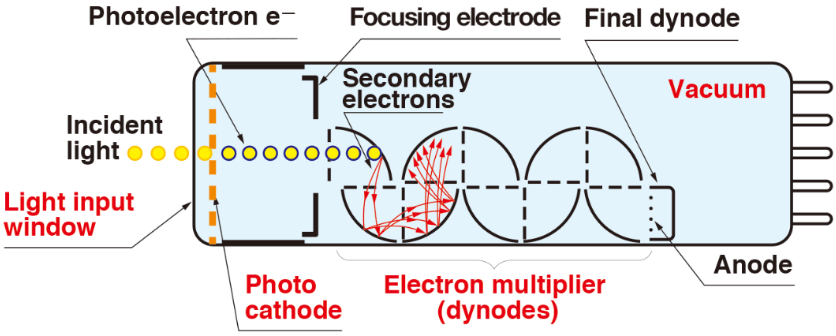

Figure 1-25 A diagram of a photomultiplier tube *[142].*

1. 6 Summary of Chapter

This chapter provided a broad overview of semiconductor junction devices, focusing on LEDs and μLEDs, and detailed how band gaps and doping methods are used to engineer DUV devices. It also briefly reviewed the history of optical communications and described the modulation techniques relevant to this thesis. Finally, the chapter covered the physics and theoretical principles of the photodetectors that will be utilised in the following chapters.

Chapter 2
Size-dependent LED Characterisation

2. 1 Motivation for the Work

This chapter analyses how the size of DUV µLEDs influences their performance. Two DUV µLED arrays with pixel sizes between 20 and 500 µm were investigated. Although µLEDs are defined here as devices smaller than 100 µm, larger mini-LEDs were also examined for comparative purposes. Key device characteristics were assessed for size dependence, including light output and current versus voltage (LIV), relative external quantum efficiency (EQE), electroluminescence spectra, and modulation bandwidth. In addition, arrays emitting at respective peak wavelengths of 285 nm and 275 nm were studied to compare their properties. This research aims to evaluate the performance and trade-offs associated with different device dimensions, with a particular focus on potential applications in communications [102,143]. The work from this chapter informs later work, which is described in Chapter 4.

Considerable research has been conducted on size-dependent phenomena in visible-wavelength LED devices. However, comparable studies in the DUV range have only gained momentum recently due to advancements in wafer material technology. Despite these developments, challenges remain regarding material quality and defect densities, which continue to affect DUV device performance. A central objective of this work is to identify which device size is most suitable for communications applications and to address key issues impeding further progress in device development [144].

Size effects have been extensively studied by researchers working with µLEDs across various disciplines [145–150], especially in the visible spectrum, and now increasingly in the DUV range. Much of the existing literature focuses on fabrication and material considerations. In contrast, this chapter emphasises the implications of size from a communications perspective, concentrating on LIV and modulation bandwidth parameters critical to optical wireless communication systems. An essential consideration in characterising these devices is the Shannon equation, or Shannon-Hartley theorem, which determines the maximum achievable data rate (channel capacity) for a given channel bandwidth and received signal-to-noise ratio (SNR). The theorem is expressed as follows:

$$\boldsymbol{C = B \cdot \log_2(1 + \frac{S}{N})} \quad \textbf{(2.1)}$$

Where *S* = average received signal power in Watts, *N*=average noise power in Watts, *B*=Bandwidth in Hertz, and *C*=Channel capacity in bits per second. From this equation, it is possible to see that the achievable data rates in an optical wireless communications link are proportional to the bandwidth, *B*, and proportional to $\log_2$ of the SNR. So, the key aim of this chapter is to examine how both properties vary with µLED size and, therefore, which device sizes are optimal for a communications system. Firstly, we will cover the devices used, followed by a study of the methodologies used to evaluate the devices' performance, and finally, we will cover the results from the characterisation tests.

2. 2 Size-dependent Devices

2.2.1. Fabrication

µLEDs are fabricated through several carefully controlled steps, beginning with, in our case, a commercial wafer being processed as outlined in Figure 2-1. The initial stage involves acquiring an AlGaN wafer on a commercially available c-plane sapphire substrate, which supports high-quality GaN epitaxial growth via Metalorganic Chemical Vapour Deposition (MOCVD). Sapphire is selected for its transparency, permitting light transmission through the substrate, because it is a cost-effective substrate, and because the lattice constant is a fair match to AlGaN/GaN. The wafer features a bulk layer composed of AlGaN, GaN, or AlInN, serving as a sacrificial layer.

A significant challenge in this process is the lattice mismatch between GaN and the sapphire substrate [151]. AlGaN materials tend to exhibit high dislocation densities [102], particularly in regions where lattice mismatch induces crystallographic strain. Such crystal dislocations [57,152,153]act as non-radiative recombination centres, thereby generating phonons and reducing output power. Therefore, it is crucial to eliminate these defects from active areas to maintain high device quality.

Following the bulk layer, an N-doped GaN layer is deposited, succeeded by the multiple quantum well (MQW) structure discussed in Chapter 1, and this is finally capped with a p-doped layer, as illustrated in Figure 2-1.

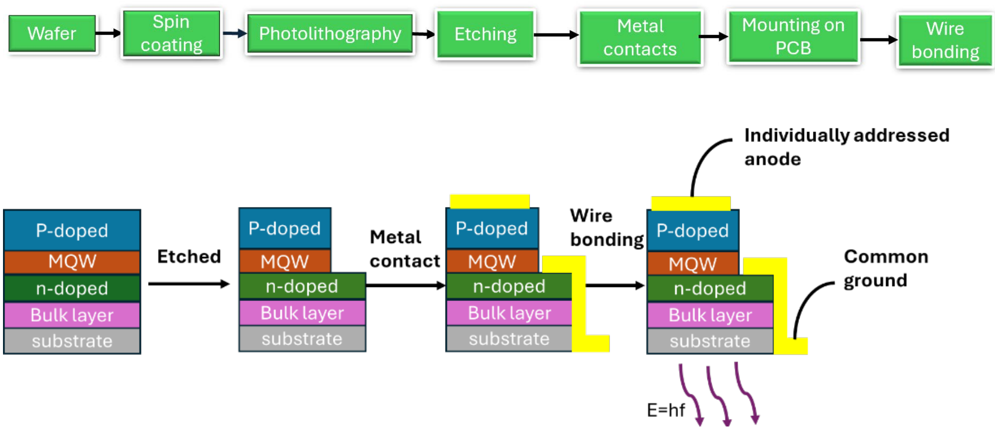

Figure 2-1 Basic fabrication steps of a µLED array.

The next step involves processing the wafer by coating the surface of the epitaxial structure with photoresist (PR). The PR is then patterned through exposure to ultraviolet light using a hard photolithography mask, which delineates the areas protected from etching and those left exposed for further processing. The device is etched down to the N-doped layer, forming a mesa structure. Metal contacts and tracks are added to complete the devices and enhance the electrical characteristics [154].

Thermal annealing is performed to enhance device performance, particularly impacting the quality of the metal contacts, which play a critical role in determining electrical functionality [155–157]. The p-type contact is positioned on top of the P-doped layer, with a buffer layer situated below the n-doped region. The mesa structure extends down to the substrate, where the n-contact metal alloy is deposited onto the n-doped semiconductor and tracks are subsequently added to the n-contacts. An insulating layer is introduced over the electrical tracks, and a metal contact is placed on the p-doped layer at the top of the mesa.

It should be noted that there are issues with the p contacts in GAN devices due to poor current spreading from the devices. This is due to resistance, and this is countered using a Ti/Au gold alloy, which increases conductivity, enabling better current spreading and improving device performance.

These devices subsequently underwent wire bonding, allowing the arrays to be mounted on a printed circuit board (PCB), which facilitates more straightforward operation and integration into various setups. Probing using electrical needle probes is commonly utilised for characterisation, as it minimises external influences on measurements. However, in this instance, the intention was to employ the devices within communication systems, and so the wire bonding was required.

2.2.2. Size-Dependent Micro-LED array design.

As previously noted, arrays with LED diameters ranging from 20 to 500 µm were fabricated following the procedures outlined above. Two distinct arrays were utilised: array 1, spanning 20 to 200 µm and emitting a nominal peak wavelength of 285nm, and array 2, covering 20 to 500 µm, emitting at a nominal peak wavelength of 275nm. It should be noted that particular pixels in both arrays were unintentionally nonfunctional, including the 300-µm device in array 1. An image of array 1, along with a detailed cross-section diagram of its construction, is presented in Figure 2-2 (a) and (b).

(a)

(b)

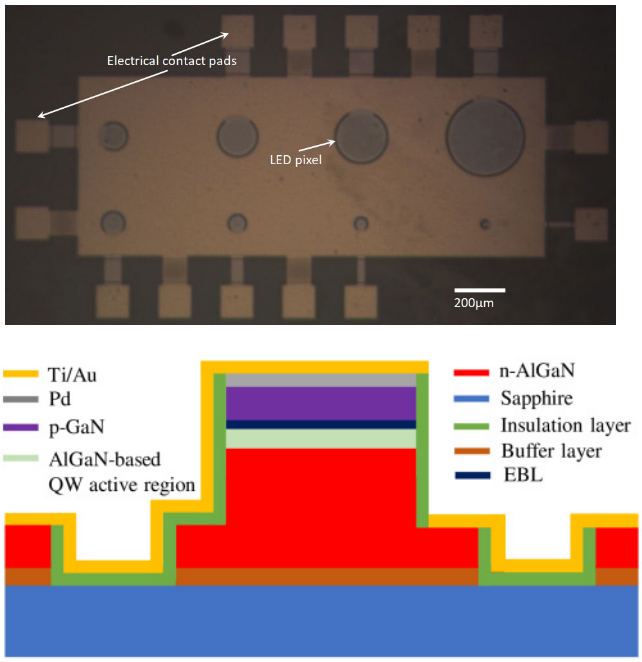

***Figure 2-2 a) plain view optical micrograph image of Array 1, b) a cross-section schematic diagram of a similar device to the one used in this chapter** [102].*

2. 3 Measurements and Experimental Results

This section will discuss the three key characterisation measurements performed: the optical power, the spectral properties and the bandwidth of the devices. Each of these characteristics is important as they can allow for an understanding of the performance and the optimal conditions for communications applications.

2.3.1. Optical output power and current versus voltage (LIV) measurements

The LIV characteristics of the devices were evaluated using an optical power meter and a calibrated power meter head (Thorlabs S120VC), see Figure 2-3. The LED device was positioned directly above the detector, and the measured results were obtained. An XYZ stage was used to accurately align the detector and device. It is important to note that in this setup, light was collected from the front facet of the device, and it is assumed that all of the useful forward-directed light is collected and measured, aligning with the requirements for communications experiments. Although a comprehensive output power measurement would require an integrating sphere, this was not pursued as the focus was on communication-specific performance. However, such measurements could be considered in future work.

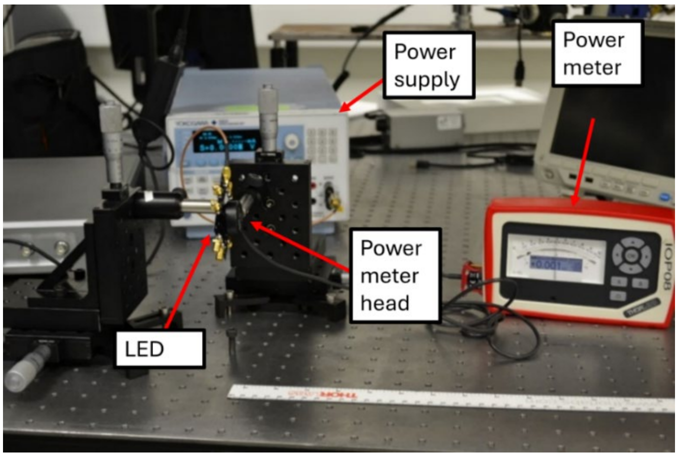

Figure 2-3 Photograph of the setup used for LIV measurement.

The measurements were performed by using a Python™ script to rapidly sweep and measure a range of currents, voltages and output powers, allowing efficient characterisation of the arrays. While the devices demonstrated relative stability during prolonged constant operation, it should be emphasised that maintaining high current values for extended periods may damage the arrays and is not advisable for practical demonstrations. Additionally, it was observed that newly wire-bonded devices required several initial 'burn-in' sweeps to ensure measurement consistency and to mitigate any potential influence from self-annealing effects. Due to the small sizes it was not possible to add an TEC or heatsink.

The optical power was measured using the power meter head in conjunction with a Thorlabs PM100A power meter. Bias current to the LEDs was provided via a Yokogawa GS610 source measure unit (SMU), which also enabled accurate recording of the supplied voltage. The S120VC power meter head is a silicon-based detector whose responsivity depends on wavelength, as illustrated in Figure 2-4. Thus, wavelength selection is essential for sensitivity optimisation. The photodetector produces a photocurrent, which is then converted into an optical power measurement.

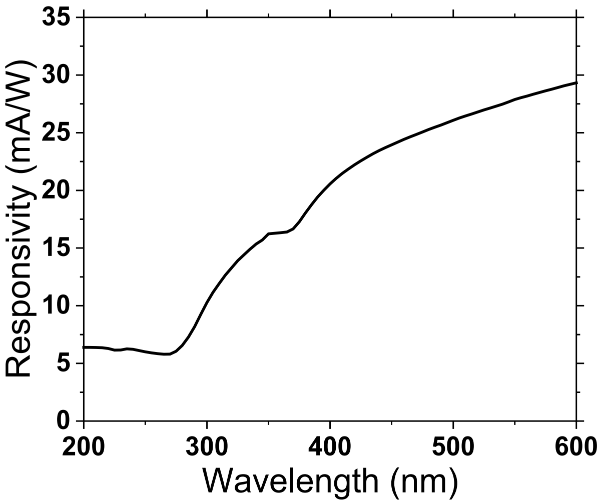

Figure 2-4 Responsivity curve of the Power meter head plotted using Thorlabs data.

The LI measurements revealed a distinct size dependence (Figure 2-5 (a-d)), with smaller devices exhibiting reduced optical output power. This trend is expected due to the reduced active area and relatively increased surface recombination. Additionally, the smaller devices appeared more susceptible to damage and could not sustain high forward currents. Nevertheless, their dimensions allowed them to achieve exceptionally high current densities (as seen in Figure 2-5 (b) and (d)). While the increased surface-to-volume ratio of smaller devices is expected to facilitate improved thermal cooling, our results do not definitively confirm this effect. However, the results indicate that smaller devices have better thermal management and can sustain higher current densities, enabling higher bandwidths, as noted in µLED devices discussed later in the chapter. Further comprehensive studies would be valuable to explore this aspect in greater detail.

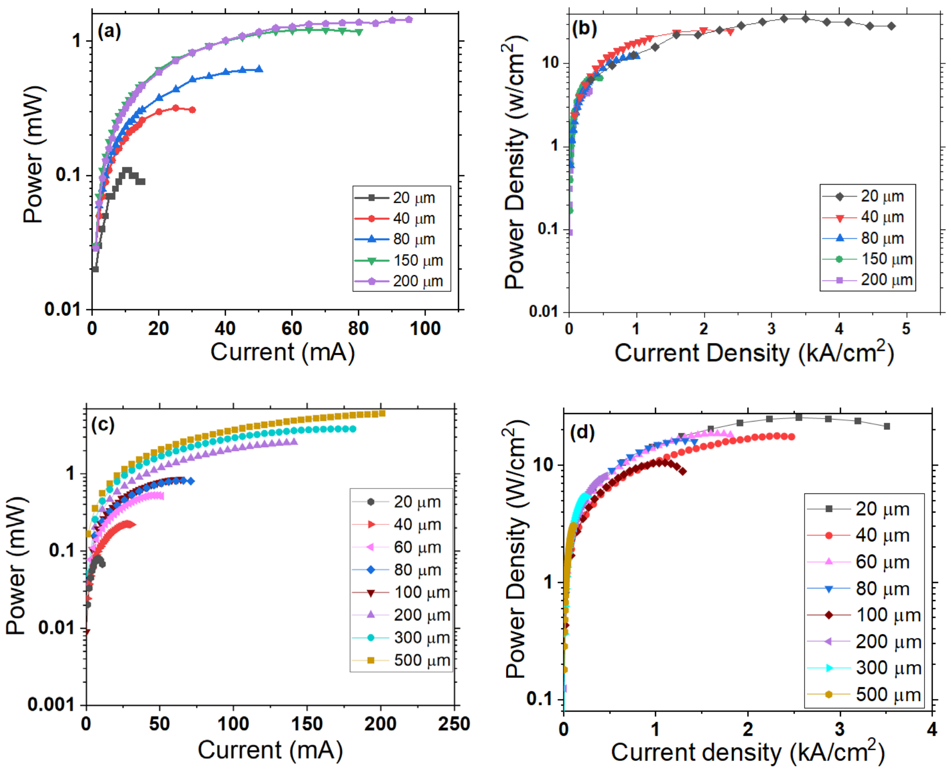

Figure 2-5 LI curves of the different arrays: a) power vs current array 1, b) power density vs current density array 1, c) power vs current array 2, d) power density vs current density array 2.

The power output exhibits a roll-off effect, whereby further increases in the bias current no longer lead to any significant increase in the optical output power, indicating the device is approaching its operational limits. These graphs provide guidance on safe operating currents for the devices when integrated into communication systems. Notably, there is minimal difference in output between the µLEDs, whereas the mini-LEDs (i.e. devices greater than 100µm) show a substantial increase in power due to their larger active areas. However, all the devices do experience "roll over" (i.e. limited increase in optical power with increased current or optical power decrease). This is due to self-heating, carriers escaping QWs due to increases in current density and Auger recombination (see section 1.3.2). Upon reviewing the data, it is evident that the 20 µm devices underperform. This observation was supported by experimental results showing that these devices were prone to degradation. It should be noted, however, when examining current density and power density, the smaller devices can achieve higher power densities [158] as seen in Figure 2-5 b and c.

The LV and IV characteristics were especially significant, as the slope of the curve is a key parameter in communications, influencing the determination of the optimal bias point, as illustrated in the LV curve shown in Figure 2-6. The LED's output power must be a real and positive value, which means that it must be biased and modulated above the μLED's turn-on. When the relationship between the applied voltage and the output optical signal is linear, if the device is modulated in an area where the relationship is no longer linear, the transmitted data signal can become distorted. It should be noted there are slight irregularities in the graphs however this was speculated to be due to measurement artefacts due to measurement step resolutions.

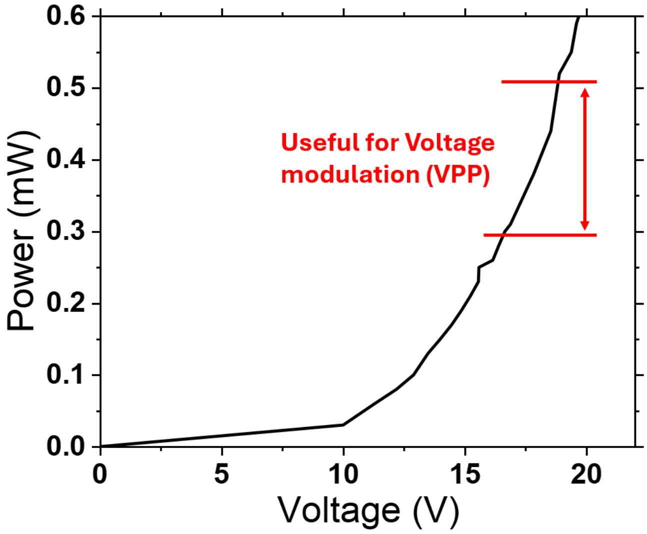

***Figure 2-6 LV graph with ideal modulation region** [166]*

With respect to forward voltage, there is a noticeable size dependence: smaller devices tend to have higher turn-on voltages, see Figure 2-7 (a) and (c), likely due to increased resistance. This issue has historically affected deep ultraviolet (DUV) devices, particularly when developing larger arrays, though advancements over the past decade have led to improvements [13]. Nevertheless, significant challenges persist for DUV μLEDs. Low-voltage performance is critical for optical communications, as the operating voltage modulates the device to produce high and low output states. As noted, this directly influences the emitted power and subsequently impacts the achievable signal-to-noise ratio (SNR). These higher turn-on voltages can prove challenging when used in a "real world" system, with the higher turn-on voltages requiring more specialised drivers to compensate for the system requirements. It should also be noted that these higher turn-on voltages lower the wall plug efficiency of the devices, and in systems which require lower operating powers, this could prove challenging.

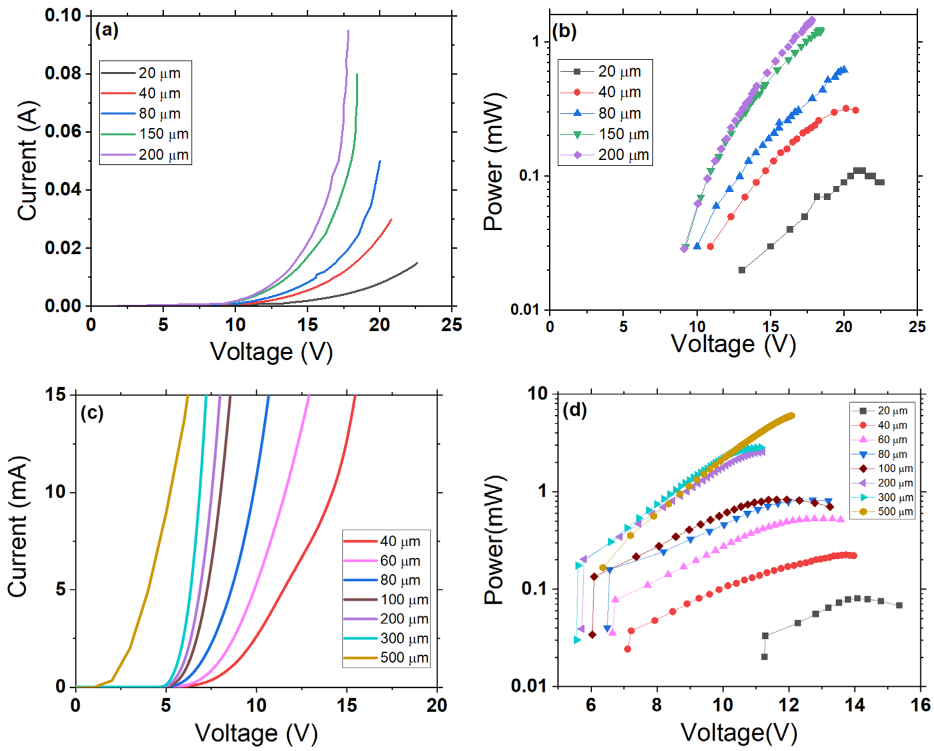

Figure 2-7 a) IV measurements on array 1, b) PV measurement for array 1, c) IV measurement for array 2, d) PV measurement for array 2.

Similar to the current, the voltage and optical power measurements also demonstrate a size dependence (see Figure 2-7 (b) and (d)), with the optical power output increasing rapidly with increased voltage in the larger devices and the smaller devices requiring larger voltages in order to generate a measurable optical power.

Using the data from Figure 2-7 it is possible to show the size dependence by comparing the voltage at approximately 1 mA for array 2, which is shown in the table below. Note that the 500 µm device rapidly turned on at around 2 volts, which could be the result of parasitic leakage and was already registering a current around 2mA (see Table 1) which suggests damage to the device.

Voltage (V) recorded at 1mA		
Size (µm)	Array 1	Array 2
20	13.07	11.26
40	10.9	7.11
80	10	6.49
100	11.4	6.03
200	9.1	5.71
500	N/A	~ 2

Table 1 Turn on voltages at 1mA for both arrays.

Overall, it is clear that there is a size dependence in the forward bias voltage. However, the high turn-on voltage could limit their ability to be used in arrays driven by CMOS drivers [159], which are being developed in the visible region [160–163] and as a result will limit the complexity of DUV communications and its applications. However, from this work, it was possible to identify the ideal current and voltage bias points in order to optimise the system for communications.

2.3.2. External quantum efficiency (EQE) measurement

The efficiency of LEDs is an essential concept for many applications. LEDs in the UV region have had issues with efficiency and usually have a lower efficiency than visible LEDs (see Figure 2-8) [6]. This is a result of defects in the semiconductor materials [164–167]. The relative EQE and wall plug efficiency (WPE) can be calculated using the following equations:

$$EQE = \frac{number\ of\ photons\ produced}{compared\ to\ electons\ injected} = \frac{(\frac{P}{hv})}{(\frac{I}{e})} \tag{2.2}$$

$$\text{WPE}= \frac{optical\ power\ out}{electical\ power\ in} = \frac{P}{IV} \tag{2.3}$$

Where P is the optical power, h is Planck's constant, and v is the photon frequency, I is the current, e is the charge of the electron, and V is the voltage.

The efficiency of the device has always been an issue for DUV devices. As the AlGaN material is not as mature as other forms of GaN materials like InGaN, there are higher levels of dislocations and, as a result, the shorter wavelength UVC/UVB devices typically have an efficiency of <10% when compared to devices in the UVA, which are 10%, as can be seen in Figure 2-8 .

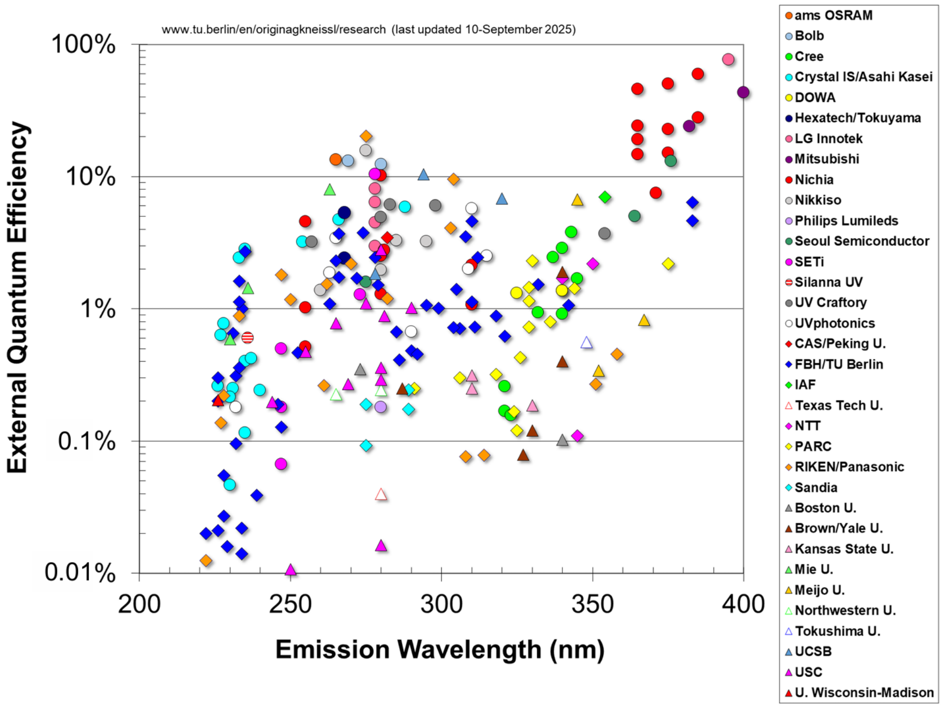

Figure 2-8 Efficiency of UV LEDs as summarised from the literature [168]

In order to determine the EQE of the µLED samples shown here, two methods were used. In the first method, which was used to characterise array 1 with the aim of understanding the current density at which the peak EQE occurs, a SPAD (Thorlabs SPCM20A(/M) photon counting unit) was used. A second method using a power meter was used on array 1 and array 2 in order to determine the relative EQE for various current densities.

The layout of the first method is shown in Figure *2-9*. A Comar band-pass optical filter was placed in front of the SPAD in order to ensure that the counts were only those from the UV source. This SPAD-based method was used due to sensitivity issues with the power meter, which could not detect the low output powers of the µLED, and it was determined that it would be beneficial to measure the low optical output power. The photon count rate was proportional to the light received from the LED. However, it should be noted that due to the fact that the setup is recording only the light being emitted from the front of the device, these measurements should be taken as a relative external efficiency. To measure the true EQE, an integrating sphere would need to be utilised to capture all the light from the source.

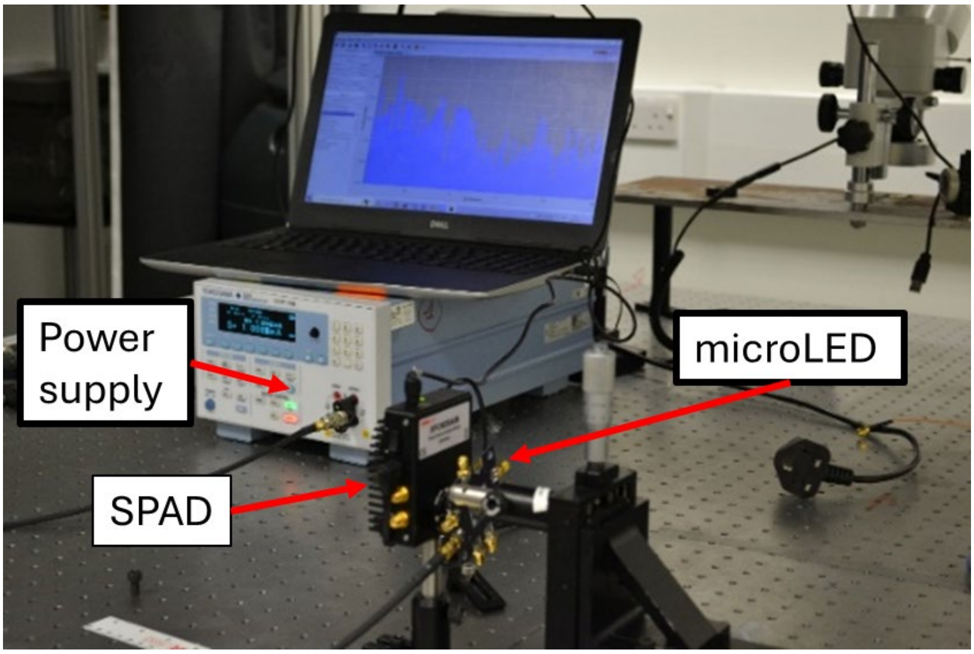

Figure 2-9 An example of a SPAD set up to characterise the devices.

The second method used was to calculate the EQE using a power meter similar to the set shown in the LIV section. Using equations 2.2 and 2.3, it was thus possible to calculate the EQE. This method was used to understand the device's performance as the current increases, and, again, these measurements should be considered relative because we are only measuring power at the front of the device.

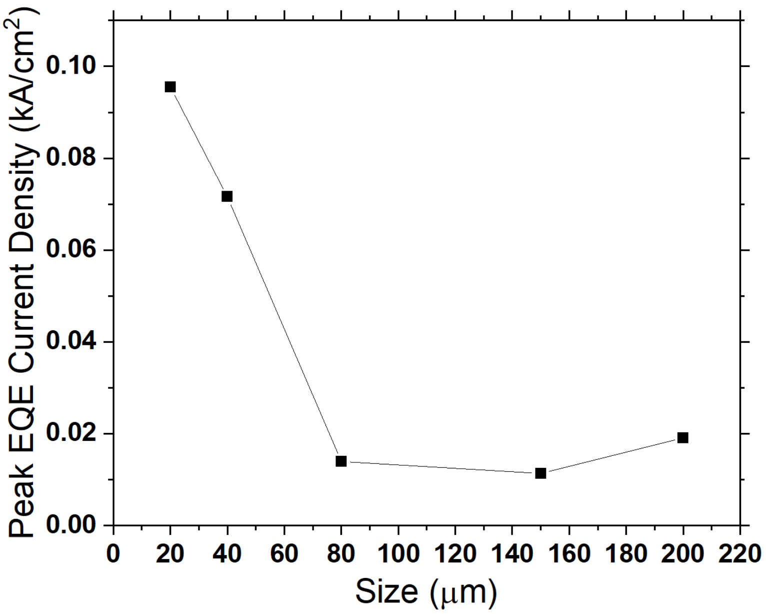

Figure 2-10 The current density at which the peak EQE occurs vs a function of size, measured using method 1 and array 1.

The observed peak EQE, as shown in Figure 2-10, exhibits an apparent size dependence, consistent with findings in other studies. Specifically, smaller devices tend to show peak EQE at higher current densities. This may be due to the carrier diffusion length allowing carriers to reach the damaged etched walls in smaller devices, leading to non-radiative recombination. To investigate this further, method two with the power meter was used. A primary challenge with the SPAD measurements was that the recorded counts were influenced by device alignment. Future experiments should include a diffuser lens to reduce alignment issues. In this study, very low current densities were applied, focusing on performance near the turn-on current (using a 1 mA voltage for simplicity), as this is a critical point at which devices begin operating. It's also noted that as current density increases, efficiency decreases until it reaches a maximum current limit. The next step was comparing the EQE and WPE of the two arrays with the second method, with the results displayed in Figure 2-11.

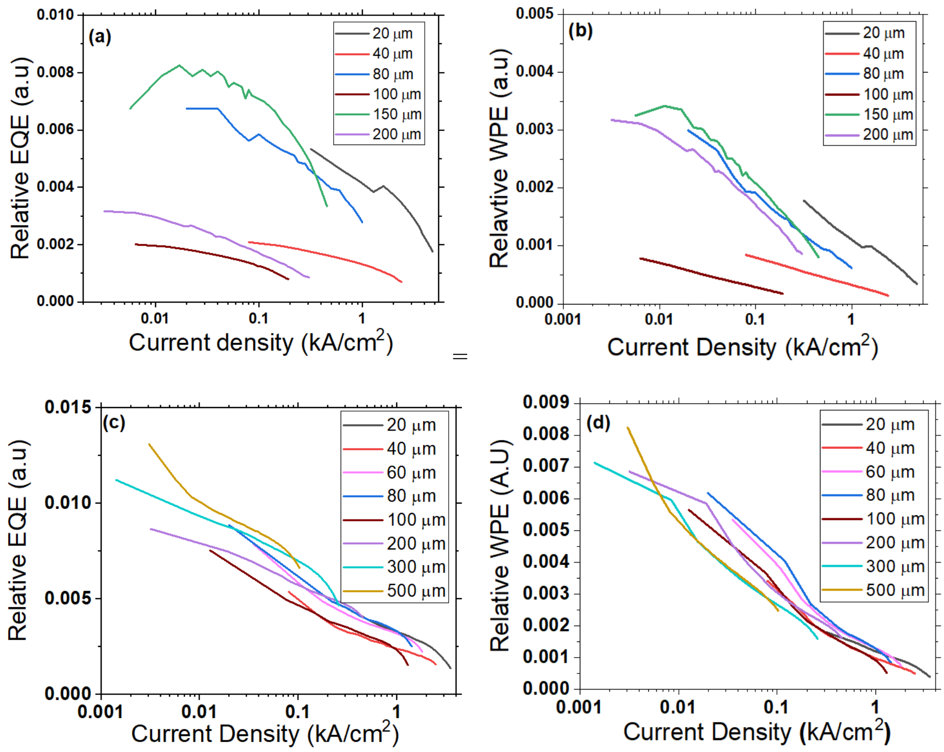

Figure 2-11 ***Efficiencies of array a) External quantum efficiencies array 1, b) relative wall plug efficiency Array 1, c) External quantum efficiencies array 2, d) relative wall plug efficiency Array 2.***

The EQE demonstrated some performance issues in array 1, as seen in Figure 2-11 (a) and (b). It is possible to note that some of the pixels demonstrated lower efficiencies than expected, and these devices also degraded to the point where they were unusable by the end of the measurements. However, Figure 2-11 (c) demonstrates a clear size dependence, with the smaller devices demonstrating lower EQEs, a trend which is also notable in the WPE, which was next to be calculated. These results are just relative values since they were not measured in an integrating sphere. As seen in Figure 2-11 (b) and (d), the larger pixels have a higher WPE due to the reasons mentioned previously, side wall recombination, and the higher turn voltages required for the smaller pixels, resulting in poorer efficiencies (see Figure 2-12). On top of this, compared to similar devices operating in the visible region, DUV devices suffer from poor injection efficiencies [169]. On average, the larger devices performed well at low current densities, with a decrease in efficiency as current densities increased, which was similar to the EQE.

Interestingly, the increased current density does not improve efficiency. This efficiency droop is observed in other types of LEDs, not just DUV devices [170–173]. This work demonstrated that efficiency droops significantly with increasing carrier injection [34,174]. This could be due to heating effects inside the devices; however, the temperature was not measured, and as a result, this is purely speculation. However, as the current increase has been noted to result in increased temperature.

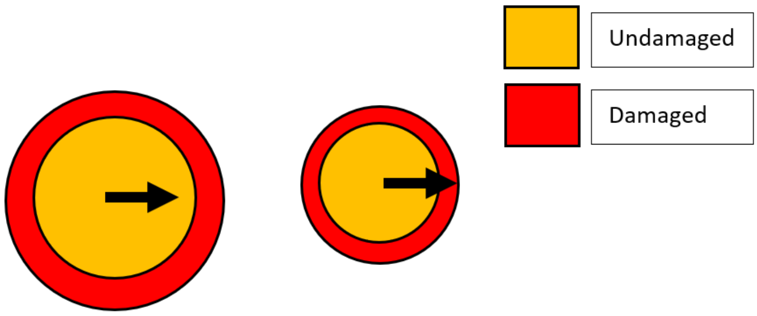

Figure 2-12 Simplified diagram, top-down view of LED, demonstrating size vs damaged side walls for two sizes, demonstrating the effect of size.

2.3.3. Electroluminescence spectra measurements

An Avantes spectrometer (Avantes Avaspec-20482 spectrometer and Ocean Optics QP600-2-SR-BX fibre) was used in the electroluminescence spectra measurements (set up is shown in Figure 2-13). To get an accurate picture of the LED's spectral emission, the optical fibre's absorption spectrum had to be taken into account when calibrating the spectrometer’s measurements. The experimental setup for this work is shown below, with a kinematic mount used to align the LED with the fibre optic cable.

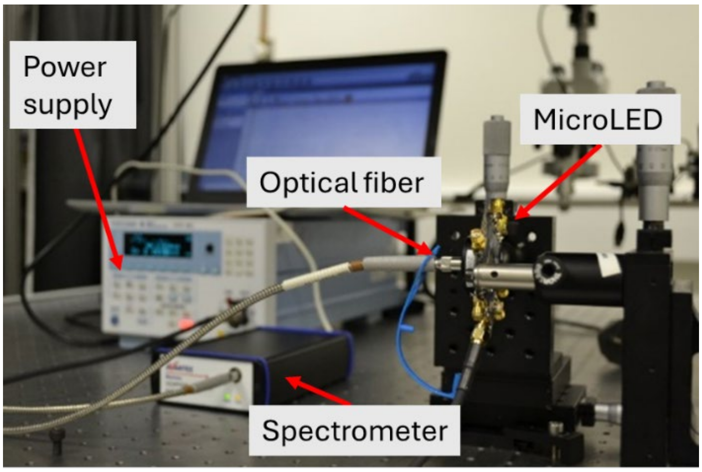

Figure 2-13 Shows the spectra set-up measurement.

Using this instrument, it is also possible to subtract the background and average several measurements to improve the SNR and obtain the best result. Some tests were done on the transmission of the fibre optic cable; however, it had no notable effect on the result, as the emission profiles of the µLEDs were also so narrow that the transmission variation of the fibre at different wavelengths was negligible.

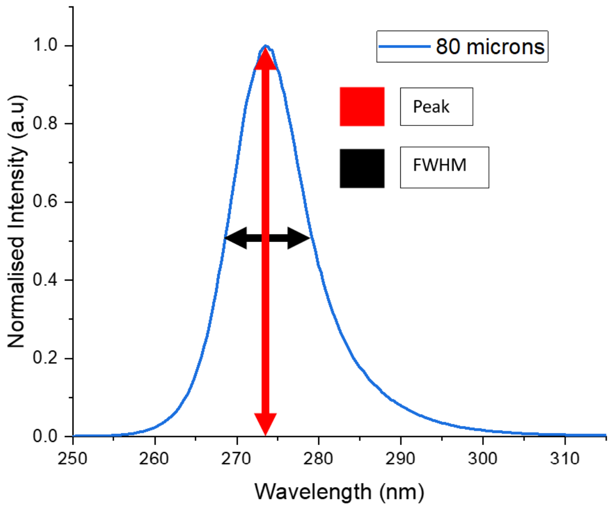

Figure 2-14 Example of spectral peak and FWHM measured for a UV-C LED.

These measurements aim to analyse the spectral FWHM and peak wavelength of the devices, as shown in Figure 2-14. The shifts in peak wavelength and FWHM can be used to identify physical changes in the devices, such as heating, and to characterise the devices to identify the optimal optical filters for future communications work (see Chapter 3).

When examining the full-width half maximum (FWHM), there was some broadening, suggesting that temperature and current density increases are altering certain aspects of the band structure. As can be seen from Figure 2-15 (a-d) all devices appear to show an increase in the FWHM. This may be the result of band filling, which occurs with increased current densities, and as a result, smaller devices are more acutely affected as these devices reach higher current densities when compared to the larger mini-LEDs [175] [176].

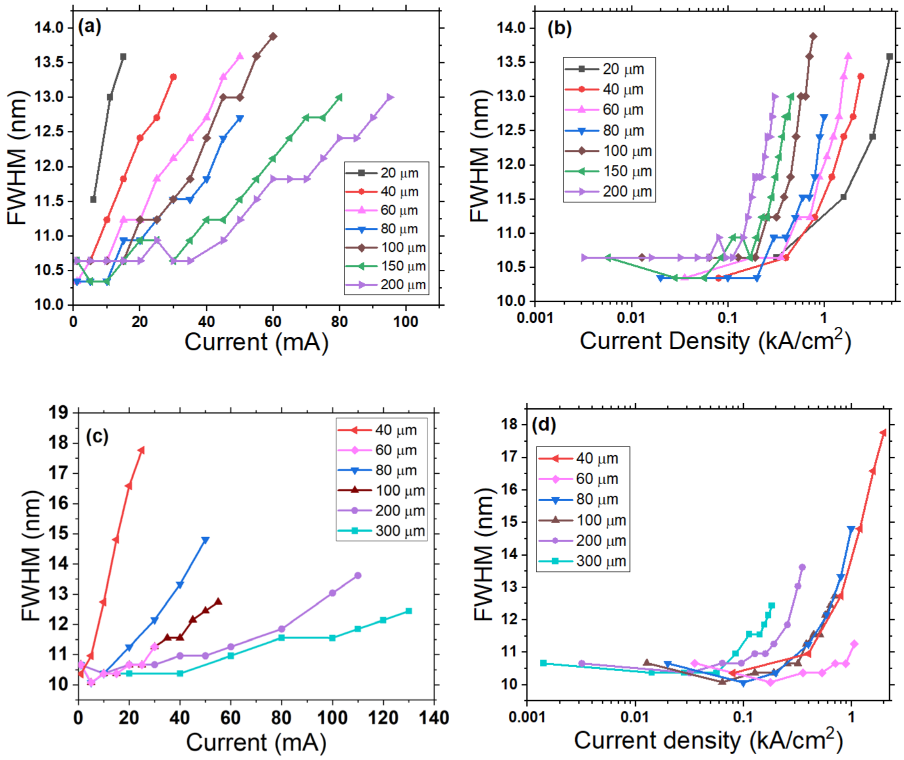

Figure 2-15 The FWHM vs current a) array 1, b) FWHM vs current density for array 1, c) FWHM vs current array 2 and d) FWHM vs current density array 2.

However, the spectral bandwidth of the devices is relatively stable, with the change in FWHM being no more than 7nm even in the worst case (see Figures 2-15 c and d), which permits the selection of relevant filters for communications as discussed in Chapter 4.

When choosing filters, the peak wavelength is also essential, as it enables optimisation with minimal loss of recorded optical power. In measurements conducted by other researchers, it was noted that the peak output wavelength of the LEDs shifted to the red as a function of current [177,178]. This could be due to several issues, such as heating effects on the junction (active region). This can result in changes to the bandgap energy [177,179–184]. This shift was also observed in the devices tested in this thesis, and there was a clear size dependence, as shown in Figure 2-16.

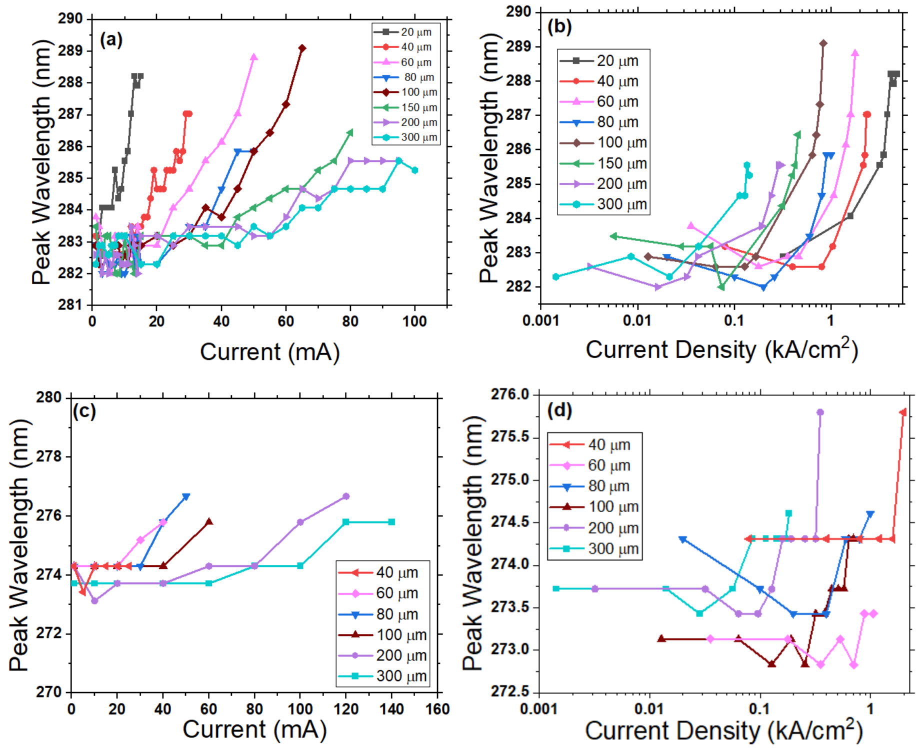

Figure 2-16 The peak emission wavelength vs current. a) array1, b) array2 and peak wavelength vs current density, c) array 1, d) array 2.

The overall results are summarised in Table 2. This demonstrates that there is no clear size dependence in the redshift, and the FWHM of array 2 demonstrates some size dependence, which is not seen in array 1. As a result, it is not possible to give a clear size dependence in the wavelength characteristics. However, as stated previously, this relative stability for all sizes would allow for the use of these devices in a communication system, as the devices are within the FWHM of 10nm, which is used by most commercial filter manufacturers.

	Wavelength redshift (nm)		Increase in FWHM (nm)	
Size (µm)	Array 1	Array 2	Array 1	Array 2
40	3.84	1.49	2.95	6.22
60	5.02	0.3	3.24	6.23
80	2.95	0.3	2.36	5.33
100	5.91	1.18	3.24	4.14
200	2.95	2.06	2.36	3.85
300	2.95	0.89	3.13	2.37

Table 2 Size-dependent spectral changes of array1 and 2

2.3.4. Bandwidth measurements

In this work, the term "bandwidth" (modulation bandwidth) will be used to refer to the -3dB electrical-to-electrical bandwidth of an LED, which is the frequency where the corresponding received electrical power, as measured by a photoreceiver, decreases to 0.5 (-3dB) of its original value. The bandwidth is essential as this limits the data rates that can be achieved (see Shannon-Hartley theorem in section 2.1), and the signal can be distorted if the transmitter does not have the bandwidth to send the data. It is assumed for these µLED devices (based on our group and our collaborators' previous work) that the bandwidth is determined by the average charge carrier lifetime inside the quantum well (QW), which can vary from 10^{-6}-10^{-9} s. However, for other larger commercial devices, one must consider other factors such as parasitic capacitance from the packaging.

It can be noted that the optical -3 dB bandwidth occurs at the same frequency at which the electrical response is reduced by -6 dB. This is because when the LED's optical output power drops by half, the received electrical power drops to ¼ (-6 dB). As the generated photocurrent (I) is proportional to the optical power, but the received electrical power is proportional to I^2.

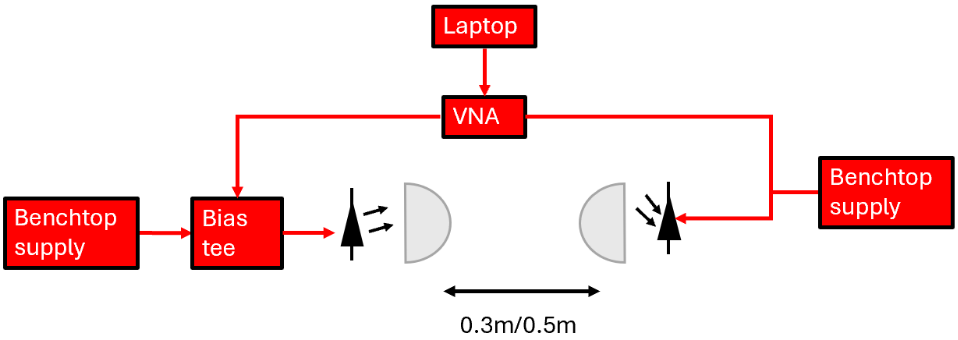

Figure 2-17 Schematic of the setup used to measure the modulation bandwidth.

In our setup (see Figure 2-17), two 2-inch lenses were used to maximise the signal strength collected for a measurement. The LED and detector were mounted on XYZ for optimisation of alignment. The light after the first lens is collimated, producing a spot approximately the same size as the LED in a parallel focus before the detector. The Vector Network Analyser (VNA) generates a chirped sinewave of fixed amplitude and records the corresponding electrical signal from the APD as a function of swept frequency. From this measured frequency response, we can determine the bandwidth.

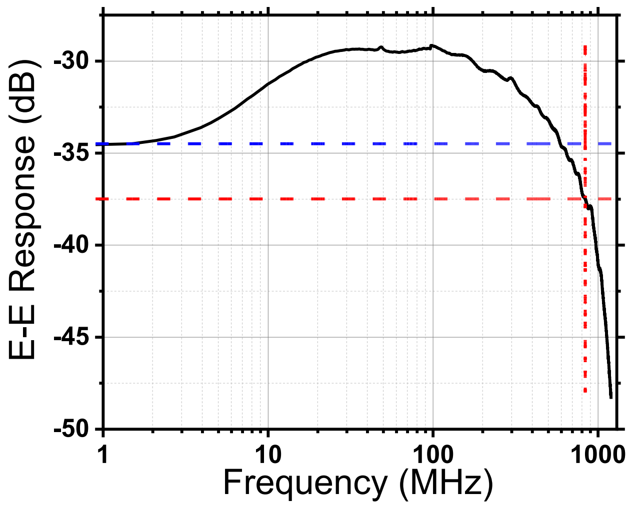

Figure 2-18 electrical -electrical frequency response curve of a DUV LED device (the red line demonstrates -6 dB, and the blue line demonstrates -3 dB)** [185]**.

To determine the -3 dB value, two methodologies were employed. An example of a measured modulation bandwidth is shown in Figure 2-18. The initial approach involved identifying the peak response value and then measuring the -3 dB roll-off from this point, as illustrated in the accompanying diagrams. However, this method may overlook significant portions of the lower-frequency response, which are vital for effective communication. To mitigate this, subsequent bandwidth measurements began at 300 kHz, with the -3 dB point recorded from that point (see Figure 2-18). It is important to note that this modification resulted in higher bandwidth values, owing to a dip in the frequency response at lower frequencies. Nevertheless, the elevated data rates observed subsequently substantiate these results. The bandwidth results obtained by taking the maximum value and subtracting -3 dB are shown in figures 2-19 (a and b), and the results from the second method using lower frequencies are shown in figures 2-19 (c and d).

A comparison of the different samples indicates that subtracting -3 dB from the initial point of the bandwidth measurement yields a higher bandwidth compared to subtracting -3 dB from the maximum response point, which results in a lower bandwidth. Theoretically, this method would yield two -3 dB bandwidths. However, this approach overlooks significant aspects of the frequency response used in communications work, where bits are loaded across the entire frequency curve. A similar dip at the start of the SNR, although less pronounced, is still evident.

What can be seen from Figure 2-19 (c-d) there is a drop in the bandwidth for the smaller devices, which could be due to the current density increases [205–208], resulting in self-heating and corresponding carrier overflow, leading to a reduction in the effective carrier density and an increase in the carrier lifetime [186–189]. However, the bandwidth remains high, above several hundred MHz, and they still have potential applications in communications; these are among the highest bandwidths recorded using a single DUV μLED. It was noted that devices with higher output power exhibit lower bandwidth. This observation warrants further investigation and development.

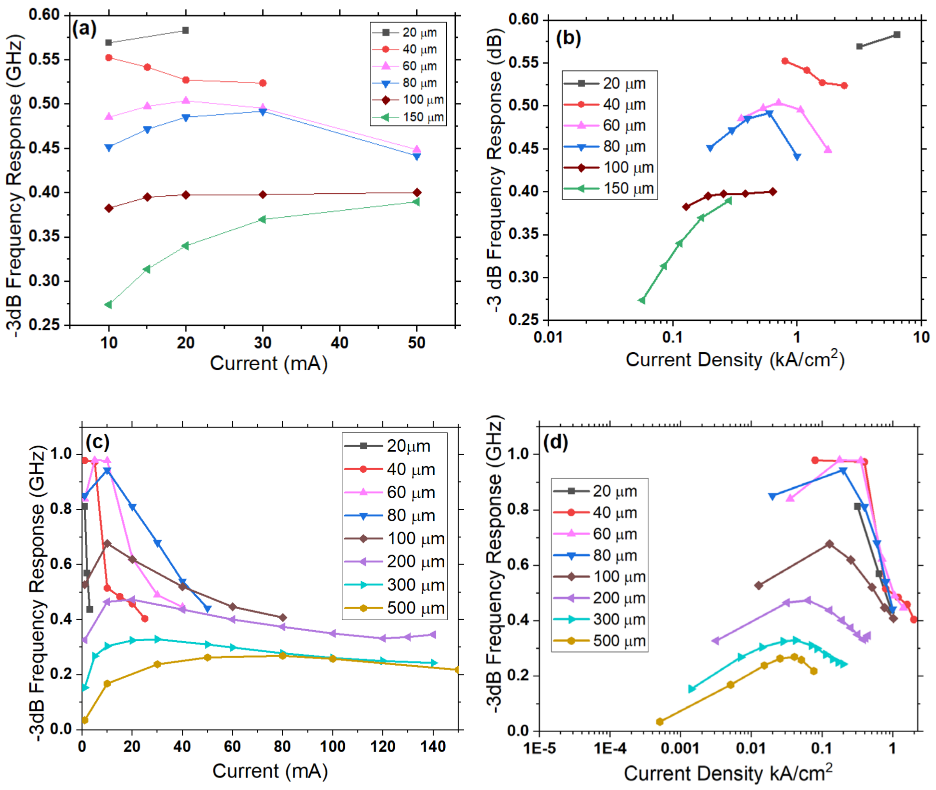

Figure 2-19 a) Bandwidth vs pixel size for various current arrays 1, b) bandwidth vs current density array 1, c) Bandwidth of pixel size vs current array 2 and d) bandwidth vs current density 2.

2. 4 Conclusion

This chapter has demonstrated that device size significantly influences the performance of DUV LED devices. Notably, there is a distinction between µLEDs and mini-LEDs; µLEDs exhibit lower output power and higher turn-on voltages. Device efficiency also declines with reduced dimensions, primarily due to the effects of etched sidewalls [178,190]. Additionally, bandwidth is size-dependent, with smaller devices achieving higher bandwidths, up to 1 GHz. These findings provide valuable insights that enable fabrication teams to address persistent challenges associated with DUV devices. Recent developments have focused on evaluating data communication rates across varying device sizes, paving the way for future advancements. The subsequent chapter will detail the use of UV µLEDs to establish a WDM-based communications setup.

Chapter 3 - Gbps Wavelength Division Multiplexing using ultraviolet micro-LEDs

3. 1 Motivation

Deep ultraviolet (DUV) optical wireless communications have garnered significant attention in recent years owing to the distinctive properties of light within this spectral region, which can be advantageous for optical communications. This includes low natural background noise and scattering properties, which can be used to circumvent physical barriers as mentioned in Chapter 1. Despite these advantages, in most previously reported DUV results that relied on mercury lamps, data rates remain substantially lower, on the order of kbps, than those demonstrated at visible wavelengths, primarily due to the low modulation bandwidths and limited output power of such DUV sources. In comparison, data rates from µLED arrays in the visible spectrum are now surpassing 10 Gbps [191,192]. In recent years, DUV µLEDs have been proposed as a possible solution to the bandwidth limitations that have limited DUV communications. However, thus far, DUV µLED performance has been constrained to a few Gbps and still lags behind their visible counterparts. This is largely attributable to the inherent technical challenges in fabricating LEDs at short UV wavelengths, as discussed in Chapter 2.

Wavelength division multiplexing (WDM) methodologies are widely implemented in optical fibre networks to expand channel capacity. The basic principle is to encode data on multiple wavelength channels in parallel. This approach is also applicable in the visible [193–195], infrared [196] wave bands, which collectively offer a broader spectrum than conventional RF communication systems [197]. The utilisation of more wavelengths in a WDM system has the potential to enhance achievable data rates significantly.

Here we present a WDM demonstration in the ultraviolet which employs three UV µLEDs emitting at peak wavelengths of approximately 285 nm, 317 nm, and 375 nm. By utilising OFDM, data rates of 4.17, 3.02, and 3.13 Gbps were achieved, representing, based on our knowledge, some of the highest recorded values for

DUV µLEDs at these specific wavelengths, with a combined throughput for all three wavelengths exceeding 10 Gbps. This demonstration was performed over a transmission distance of 0.5m.

The organisation of this chapter is as follows: an initial examination of the bespoke µLEDs utilised is followed by a discussion of the custom WDM setup. We then present and discuss an evaluation of the performance of the communication channels and the resulting data rates.

This work is based on a publication in IEEE Photonics Research [185].

3.1.1. UV-A, UV-B and UV-C µLED devices overviews

The AlGaN and AlINGaN µLED arrays employed in this chapter have nominal peak wavelengths of 375nm, 317nm and 285nm, respectively and will henceforth be referred to as the UV-A, UV-B and UV-C µLEDs. Each array was fabricated from commercially available III-nitride LED wafers, grown on 2-inch c-plane sapphire substrates, which represent the standard growth substrate for the µLED devices evaluated in this thesis. Comprehensive descriptions of the wafer structures pertaining to the UV-C and UV-A devices are documented in prior publications [51,198]. In contrast, the UV-B epitaxial material here is less mature, and the wafers were purchased as custom wafers, supplied by Zhixin Semiconductor Co., Ltd. Each wafer features a 2000 nm-thick aluminium nitride (AlN) buffer layer that enhances both structural integrity and lattice matching. This is surmounted by a 1000 nm-thick undoped aluminium gallium nitride (AlGaN) layer, followed by two consecutive n-doped AlGaN: Si layers, each with a thickness of 500 nm and aluminium concentrations of 50% and 55%, respectively, as shown in Figure 3-1.

The active region consists of multiple quantum wells (MQW) structures made from AlGaN with alternating aluminium compositions of 15% and 40%, optimising carrier confinement and optical emission efficiency. A 50 nm-thick electron-blocking layer (EBL) of magnesium-doped AlGaN (AlGaN: Mg) with an aluminium content of 50% is implemented to suppress electron overflow. The device architecture is completed by a 300 nm-thick p-type GaN: Mg layer, facilitating efficient hole injection, and a 10 nm-thick p-contact layer of GaN: Mg to ensure robust electrical conductivity.

The design and fabrication procedures for these µLED arrays closely followed the methods described in Chapter 2 and previous studies [13]. As illustrated in Figure 3-1, each array comprises eight trapezoidal-shaped µLED pixels arranged in a flip-chip configuration, allowing emission through the sapphire substrate to enhance light collection. Each pixel was functionally comparable to a circular pixel with an approximate diameter of 40 µm. The fabricated arrays were subsequently wire-bonded to a printed circuit board for further characterisation, consistent with the approaches detailed in the characterisation chapter.

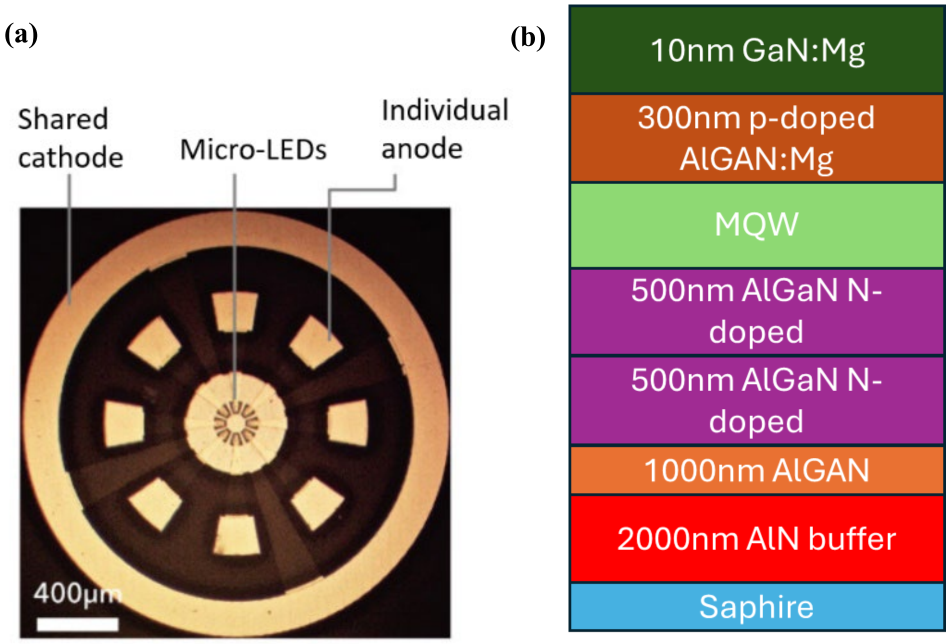

Figure 3-1. Plainview optical micrograph of the µ-LED arrays used in this work, showing the 8 concentric and individually addressable pixels** [185]**, b) a cross-section schematic of the UV-B structure.

3.1.2. Device Characterisation

The initial experiments reported in this chapter aimed to investigate and evaluate the relationships between optical power and bias current (L-I), as well as current and voltage (I-V), using representative pixels from each array. As outlined in Chapter 2, the I-V characteristics were measured with a Yokogawa GS610 Source Measure Unit, while the optical power was assessed using a Thorlabs S120VC power meter head. The findings are presented in Figure 3-2.

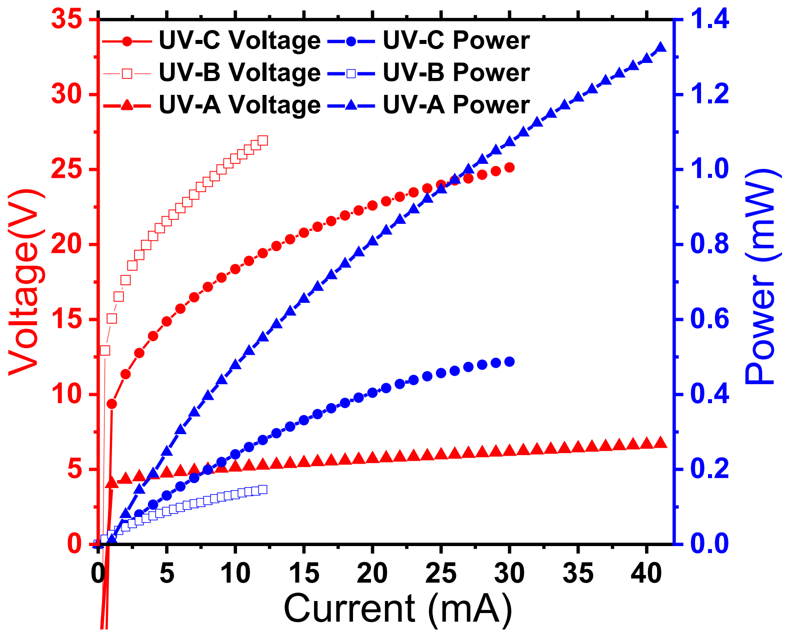

Figure 3-2. L-I-V curves of the devices at UV-A, UV-B, and UV-C wavelengths.

The maximum output powers per pixel are approximately 0.48 mW, 0.14 mW, and 1.32 mW for the UV-C, UV-B, and UV-A devices, respectively. The UV-A device demonstrates superior efficiency, primarily because its underlying material technology is more advanced and exhibits fewer defects compared to the less mature UV-C and UV-B counterparts. Nevertheless, with growing interest in sterilisation applications, it is anticipated that continued research and development will lead to significant improvements in UV-B and UV-C devices over time.

At a current of 10 mA, the forward voltages measured for the UV-C, UV-B, and UV-A devices were 18.4 V, 22.0 V, and 4.4 V, respectively. The elevated turn-on voltages observed in the UV-B and UV-C devices can be attributed to the limited electrical conductivity of AlGaN layers, which hinders efficient carrier injection and complicates the fabrication of low-resistance Ohmic contacts at higher aluminium mole fractions. These challenges are characteristic of DUV materials and devices.

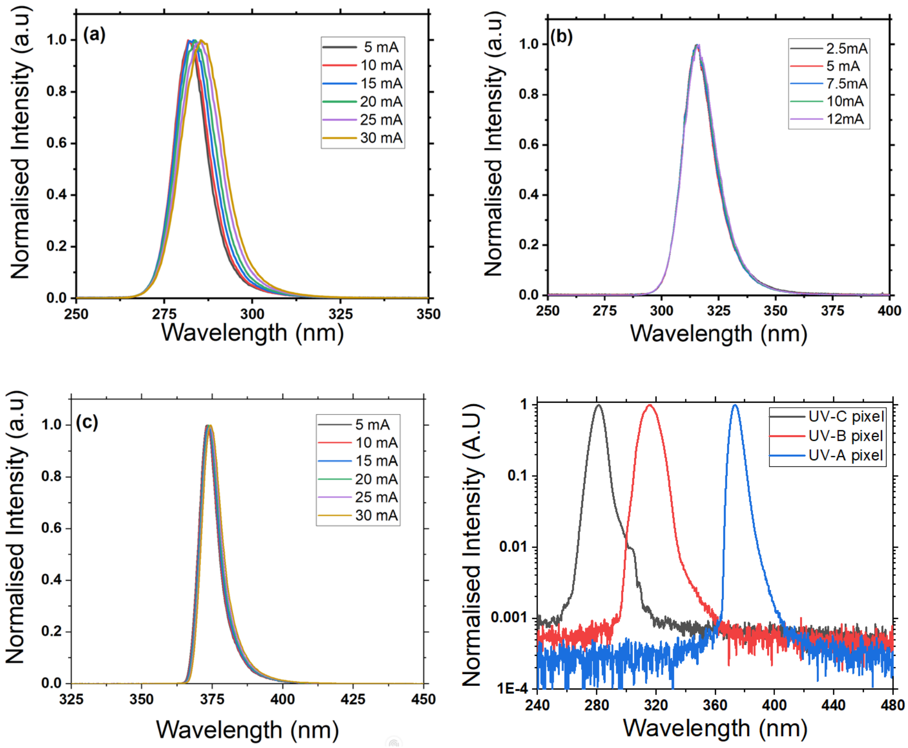

Figure 3-3. a) UV-C device normalised EL spectra vs current, b) UV-B device normalised EL spectra vs current, c) UV-A device normalised EL spectra vs current and d) log scale of the normalised EL spectra off all pixels

The peak operating wavelengths at 10 mA were determined to be 281.7 nm, 316.5 nm, and 373.4 nm for the UV-C, UV-B, and UV-A devices, respectively (see Figure 3.3). As described in Chapter 2, the devices exhibited spectral redshifts attributable to thermal effects, with increased drive current (see Figure 3-3 (a-c)). The UV-C device demonstrated the most pronounced shift in peak wavelength, moving by 3.5 nm (from 281.7 to 285.2 nm) as the current increased from 0 to 30 mA. More minor shifts were observed in the other devices: specifically, redshifts of 1.2 nm and 1.16 nm were recorded for the UV-B and UV-A devices across their respective current ranges. Since WDM systems require that each transmitted channel be spectrally distinguishable, these measured spectra informed the selection of appropriate filters and mirrors to isolate individual channels within the WDM setup. As illustrated in Figure 3-3 (d), some spectral overlap occurred between the DUV devices, potentially leading to crosstalk; this issue will be discussed further in Section 3.3.

The frequency responses of the devices were subsequently characterised following procedures consistent with those outlined in Chapter 2. The measured E-E bandwidths were 960 MHz, 780 MHz, and 140 MHz for the UV-C, UV-B, and UV-A devices, respectively. In comparison to the higher output power UV-A devices, the UV-C and UV-B devices exhibited greater bandwidths. This phenomenon may be attributed to defect-assisted quenching mechanisms in these devices, which could facilitate faster light emission at the expense of a lower EQE and output power, as discussed in Chapter 2. However, further investigation is required to confirm this hypothesis. Notably, to the best of our knowledge, these represent some of the highest bandwidths reported for LEDs/μLEDs in the UV or Visible region [102]. Additionally, the UV-B and UV-C devices displayed frequency response characteristics marked by an initial rise to a broad peak, followed by a gradual roll-off, as seen in Figure 3-4, a behaviour tentatively linked to parasitic impedance originating from wire bonds, packaging, and the μLED structures themselves. The E-E bandwidth versus current for all devices is presented in Figure 3-4.

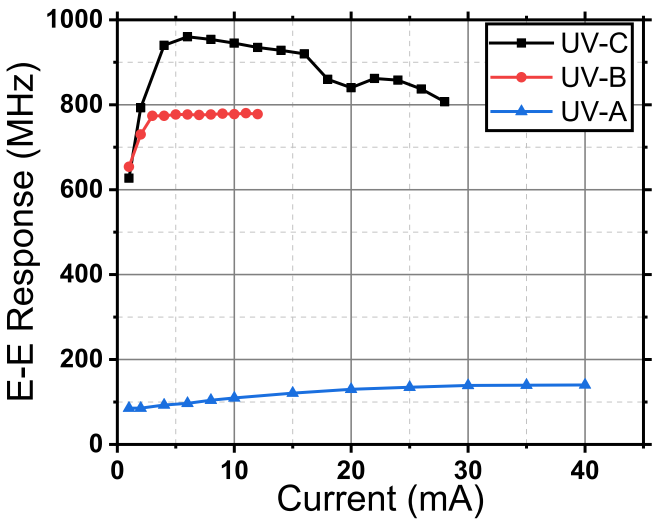

Figure 3-4. Electrical-to-electrical bandwidth response vs current for the respective wavelengths μLED devices.

The UV-B and UV-C devices also demonstrated a decrease in response at higher current levels. The observed saturation and reduction in bandwidth for both UV-B and UV-C devices may be attributed to device heating and thermally induced phenomena, such as carrier overflow. This process reduces carrier density within the quantum wells, resulting in an increased average carrier lifetime and a consequent decrease in bandwidth.

Characterisation Results	UV-C	UV-B	UV-A
Turn on voltage at 1mA (V)	9.37	12.91	3.46
Peak wavelength at 10mA (nm)	281.72	316.5	373.41
Output power at 10mA (mW)	0.24	0.13	0.47
Modulation bandwidth at 10mA (MHz)	945	778	109.5

Table 3 Summary of µLED performance for the devices used in the WDM demonstration.

The key results of this characterisation work are summarised in Table 3 above. Now that the individual devices have been characterised, the following section describes the experimental setup employed in the WDM studies.

3. 2 WDM Experimental Set-up

The WDM optical configuration utilises two long-pass dichroic mirrors, Semrock Di01-R355-25x36 and Alluxa-8113, 300 LP Dichroic, as illustrated in Figure 3-5 (a) below. The dichroic mirrors combine the light from three µLEDs into a single optical path, as shown in Figure 3-5 (a) and (b). All components are integrated within a Thorlabs optomechanical cage system for ease of alignment. The UV-B and UV-A arrays were positioned on manually adjustable XYZ stages with 3D printed mounts to optimise alignment, while the UV-C device was secured directly to the cage structure.

Lenses with a diameter of 2 inches were employed to collect and collimate light from the µLEDs. For the UV-C and UV-B µLEDs, an Edmund Optics 84340 lens (40 mm focal length and NA=0.63) was utilised, while a Thorlabs ACL50832U-A lens (NA=0.76) was used for the UV-A device. The modulated electrical signals were supplied to the optical sources using three bias-tees: Tektronix PSPL5675A, Mini-Circuits ZFBT-4R2G, and Mini-Circuits ZFBT 6GW-FT+. The Tektronix unit was assigned to the actively measured channel, i.e. the channel that was encoded with OFDM data.

(a)

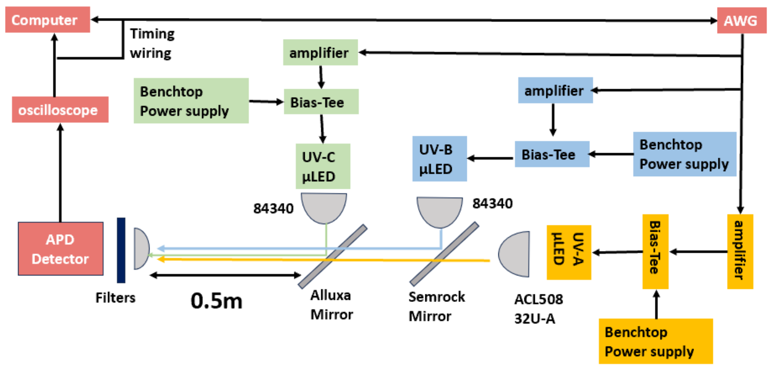

Figure 3-5. Schematic diagram of the optical and electrical setup used for the WDM transmission experiments.

An RF modulation signal was generated by a Keysight M8195A arbitrary waveform generator (AWG), offering a sampling rate of 65 GSamples/s, an analogue bandwidth of 25 GHz, and an 8-bit vertical resolution. In the WDM experiment, each µLED was modulated individually, one at a time, with an OFDM signal, while noise, which served as interference, was generated simultaneously in the other two channels to mimic a real-world system with multiple parallel data streams. In a "real-world" practical WDM system, each optical channel would be incident on a separate detector. However, in this experiment, all three channels were focused onto a single detector APD via bandpass filters mounted on a sliding filter assembly, due to the availability of only one suitable detector.

Three amplifiers, one SFH Communications SFHS126A (frequency range 80 kHz-25 GHz and 29 dB gain) and two Mini-Circuits FL-1000LN+ (frequency range 0.1 MHz-100 MHz and a gain of 2.9 dB), were placed between the AWG and the bias tees to amplify the RF signals to each of the channels and enhance modulation depth. The SFHS126A amplifier, with 29 dB gain, was connected to the µLED that delivered the OFDM signal, which was the channel that was being evaluated for the communications work. This was done as it was a low-noise, high-gain amplifier which produced the best amplified signal. The mini-circuit amplifiers were connected to the channels, thereby generating noise. The receiver was located 0.5

m from the transmitter and thus operated over short distances where scattering effects were negligible [199].

On the receiver side, a 1-inch Thorlabs LA4052 lens (35.1 mm focal length) focused the transmitted light onto an APD (Hamamatsu C5668 8867), selected for its high bandwidth as detailed in Chapter 2. The decision to utilise a single detector was based on both the desire to simplify the setup and limitations regarding the availability of cost-effective, high-speed detectors. However, future systems could use multiple high-bandwidth detectors to allow all channels to run simultaneously and could allow for more channels (i.e. more devices at various wavelengths) to be added.

A Thorlabs CFS1/M sliding filter mount was used to hold three filters (Semrock FF01 280/20-25 bandpass, Envin 308 nm bandpass filter (a custom mirror), and Edmund Optics 34299 350 nm long-pass filter). One of these filters was placed in front of the APD in order to selectively pass light from one of the optical channels. The detector output was captured by a Keysight MXR608A oscilloscope (16 GSamples/s, 6 GHz analogue bandwidth, 10-bit vertical resolution) and recorded for offline processing. This enabled calculation of the SNR, BER, and maximum "error-free" data rates per channel, which will be presented in the following section. Subsequent discussion will address the software and encoding protocols.

3.2.1. Characterisation of the optical set-up

Prior to commencing the communications tests, a thorough characterisation study was conducted to assess the impact of the filters on the experimental setup, to examine the degree of optical crosstalk and the optical power losses due to the optical filtering. It is important to acknowledge that, in general, bandpass filters in the DUV exhibit lower transmission/rejection efficiency than those designed for the visible spectrum. One limitation of this work was the use of only off-the-shelf components; future work incorporating custom-designed parts is expected to enhance overall performance by improving the transmission of the desired wavelengths and rejection of the other channels.

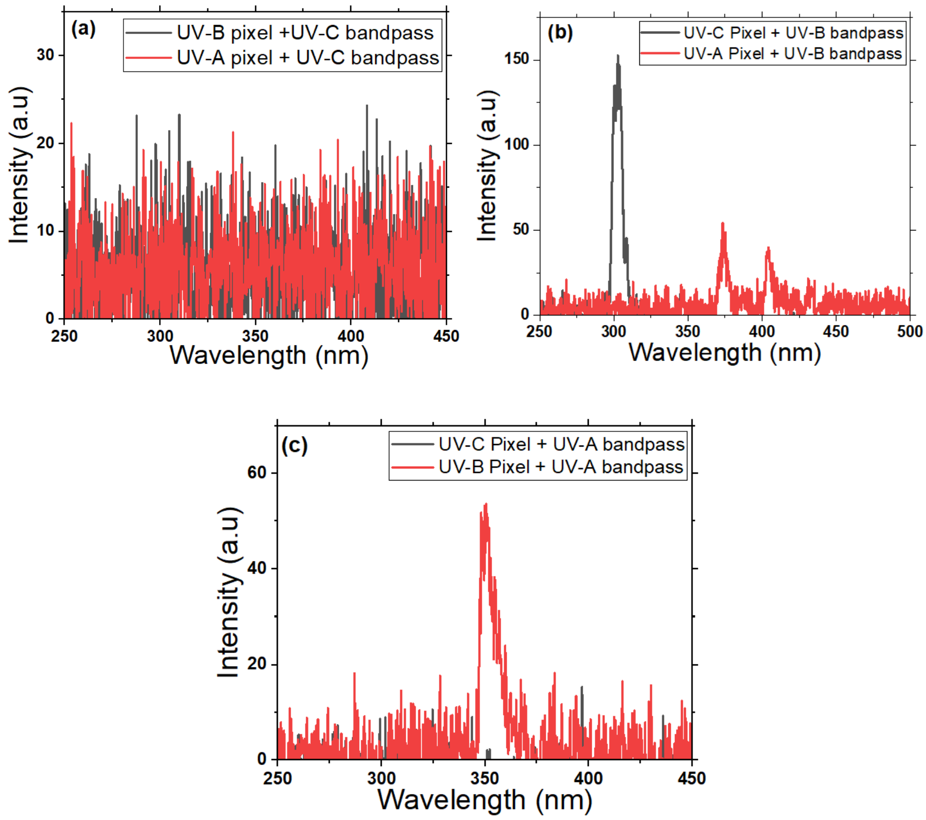

Figure 3-6 Examining the optical crosstalk in the various filters: a) 280nm bandpass filter, b) 315nm bandpass filter, c) 375nm bandpass filter.

The same spectrometer utilised during initial device characterisation was used for subsequent spectral assessments. Measurements involved aligning the spectrometer to maximise signal strength across all three channels and conducting comparative analyses with filters applied. Subsequent steps included characterisation of the spectra with different receiver filters and evaluating their effectiveness at suppressing background light and mitigating crosstalk between channels, as shown in Figure 3-6. However it should be noted that some light is leaking through the filtering system and there is evidence of cross talk which could result in lower BERs than expected.

For the UV-C channel, it was noted that there was no optical crosstalk with the other channels, as shown in Figure 3-6 (a). This could be due to the narrow FWHM of the UV-C bandpass filter and the lack of spectral overlap as seen in Figure 3-3. It was observed that some optical crosstalk occurred, notably between the UVB and UVC channels, due to the broad emission profile of the UVC device. This is evident in Figure 3-6 (b). This outcome was anticipated, as optimising signal collection from the µLEDs necessitated the use of bandpass filters with relatively broad FWHM. Such limitations could be mitigated if narrower optical bandwidth sources or filters were available. From Figure 3-6 (c), the UV-A channel also demonstrated some optical crosstalk with the UV-B channel, which can again be attributed to the broad emission profile of the UV-B device. These findings underscore the need for continued refinement in both filtering strategies and DUV µLED design.

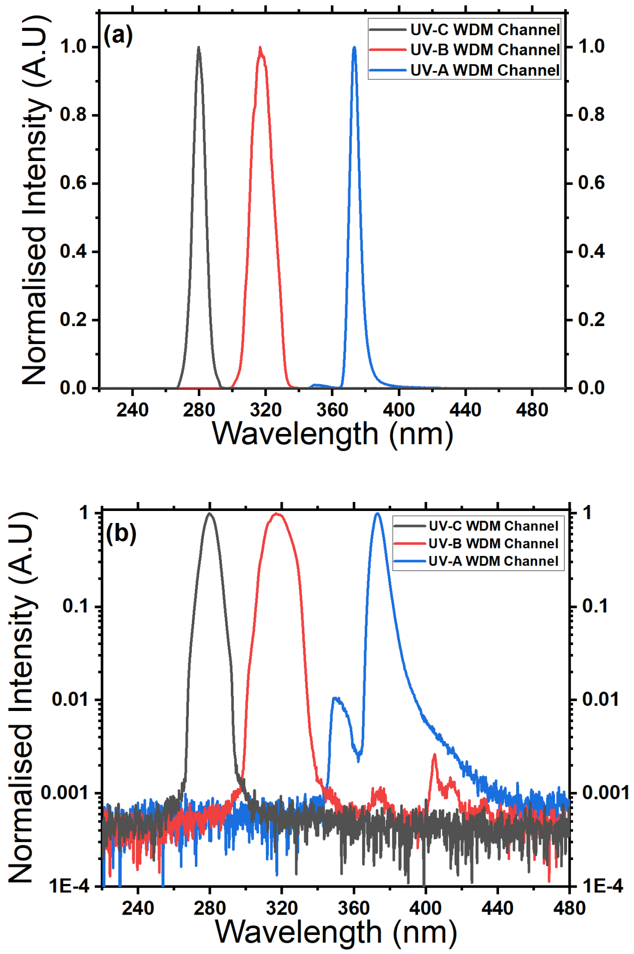

Figure 3-7 Normalised spectra of the WDM system with all LEDs operating at once b) logarithmic scale plot of the same data.

When the graph is presented on a logarithmic scale, it becomes possible to observe lower-intensity wavelength behaviour (see Figure 3-7b). Notably, the UV-A and UVB devices display some optical crosstalk throughout their measurements, which will be further clarified during the analysis of data rates. It was found that the WDM data rates were significantly lower compared to those obtained when only a single LED was active at a time. Interestingly, the 285 nm channel exhibits minimal optical crosstalk, suggesting that reduced signal strength may result from filter quality rather than inherent device characteristics.

A key property of the optical filters used in the setup is their ability to transmit light from the μLED under test while simultaneously rejecting light from the other optical channels. The next test was to examine the optical power that was recorded on each channel with various filters.

The UV-A channel showed less variation between being filtered and unfiltered, as seen in Figure 3-8 (a). This may be attributed to the advanced development of filters designed for the UV-A spectrum, with the filter transmissions closer to 90%. In contrast, the UV-B and UV-C channels demonstrated higher losses when the UV-B and UV-C bandpass filters were applied due to the lower transmissivity of those filters, as illustrated in Figure 3-8 (b) and (c). However, prioritising improved discrimination of each of the three WDM channels at the expense of some signal loss was deemed the most effective solution to maintain the desired system operation.

The UV-A device exhibits higher optical power output but operates with a lower 3 dB bandwidth, as shown in the characterisation section, which, according to the Shannon theorem referenced in Chapter 1, is anticipated to result in a reduced data rate. The analysis shown in Chapter 4 suggests that the bias point for the UV-C device may have been set excessively high. Optimising the bias level both for this device and across the system could have led to enhanced performance. Lowering the bias would permit a comprehensive evaluation of its influence on data rate, especially as the devices approached saturation within their LI and IV characteristics. This saturation likely imposed artificial constraints on data throughput, potentially accounting for some of the observed performance limitations.

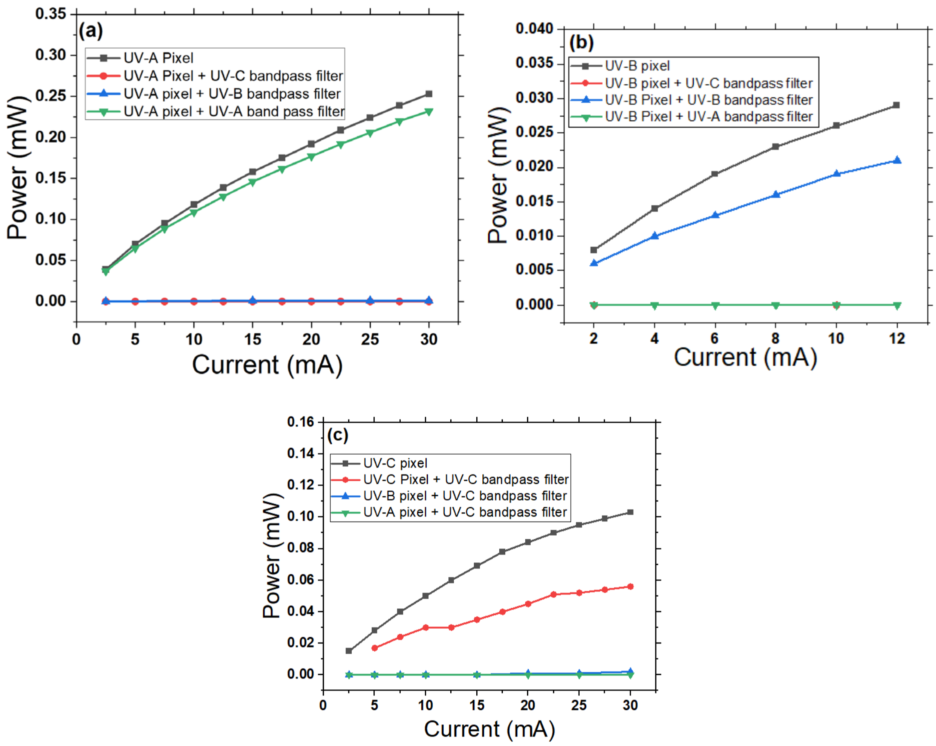

Figure 3-8 Characterisation of the optical power of the optical channel when a bandpass filter is applied to a single pixel: a) UV-A single pixel LED, b) UV-B single pixel LED, c) UV-C single pixel LED.

A calibrated optical power meter was employed to measure the average received powers for each of the channels of the WDM system when all LEDs were simultaneously active, yielding values of 0.25 mW, 0.03 mW, and 0.10 mW for the UV-A, UV-B, and UV-C channels, respectively. These results were consistent with the characterisation measurements, confirming that the UV-A device produced the highest optical power. According to the LIV graph data Figure 3-8, the UV-A device could potentially support an increased bias without adverse effects, possibly enhancing the SNR. However, such adjustments do not guarantee a corresponding improvement in data rate.

3. 3 Communications Results

After completing the optical characterisation of the WDM optical setup, the next stage was to conduct the communications tests. This section will examine the OFDM encoding sequence, include communications tests on a single channel in isolation, and finally demonstrate a complete WDM system.

3.3.1. OFDM encoding.

In the system, OFDM was employed as previously introduced in Chapter 1. This section provides a more comprehensive description of the parameters and equipment required to achieve the reported results [130,194]. MATLAB ® code was used to generate DC-biased optical (DCO)-OFDM data, enabling the assessment and optimisation of communication parameters such as peak-to-peak voltage, OFDM signal clipping, modulation bandwidth, number of subcarriers, cyclic prefix (CP) length, and the target BER. Further details are provided in Table 4 and Figure 3-9. The adaptive bit and energy loading algorithm was implemented to determine the final achieved data rates. Prior to transmitting the OFDM signal, a sinusoidal pilot waveform was applied to establish an appropriate bias point and optimal peak-to-peak voltage, thereby minimising potential nonlinear distortion or saturation that might otherwise impair the performance of the communication channel [200].

Following the initial setup, channel estimation and SNR measurements were performed utilising 4QAM symbols as pilot signals across all subcarriers. Subsequently, a Fast Fourier Transform (FFT) operation was conducted, allowing for comparison of the detected symbols with the original pilots to determine channel gain and SNR for each subcarrier. Adaptive testing was employed during the selection of SNR and channel gain values to optimise the channel link, thereby facilitating the achievement of maximum data rates.

Within the bit loading methodology, it was observed that decreasing SNR resulted in fewer bits being loaded onto each subcarrier. Attempts to increase bit loading under these conditions would have led to elevated BER. It is pertinent to note that all collected data underwent post-processing. Future advancements are required to transition toward a real-time optical communications system. Additionally, precise synchronisation was maintained using a hardwired SMA cable between the oscilloscope and AWG, ensuring accurate data decoding. For increased transmission distances, alternative timing methods would be necessary to maintain decoding accuracy.

Name of variable	Value of parameter
Sampling frequency (MHz)	1600
Sample per symbol	5
Symbol span	64
FFT Size	2048
Maximum constellation	1024
Training length QAM	1504
PAPR (dB)	10.1
Roll of factor	0.1
Cyclic prefix length	15
Cyclic suffix length	5
Lower clipping (σ)	-3.2
Upper clipping (σ)	3.2

Table 4 OFDM parameters used in the WDM system.

The following section will present the results obtained and discuss implications for subsequent research. The adaptive bit and energy loading algorithm played a crucial role by optimising QAM constellation selection and transmission power for each subcarrier, thereby aligning BER outcomes with a predefined threshold and maximising achievable data rates [191,201,202].

The payload OFDM signal was then transmitted, while at the receiver, frequency-domain symbols were equalised using the estimated channel data and subsequently decoded to assess the received binary stream against the original binary stream to determine the BER. A target BER of 3.8×10^{-3} was established, facilitating the employment of Forward Error Correction (FEC) codes to achieve error-free communication with a 7% overhead, as detailed in Chapter 1.

Following alignment, peak-to-peak voltage (VPP) scans were conducted to determine the optimal value and mitigate signal clipping, fully leveraging the dynamic range of the LED an essential consideration as signal strength diminishes. Once the optimal VPP was identified, the selected modulation scheme was applied to the µLED, employing pseudorandom encoding.

Signal clipping thresholds were set at 3.2 times the standard deviation of the time-domain signal, enabling effective mitigation of clipping of the signal and decreasing distortion and optimal use of available dynamic range [129,203]. An FFT size of 2048 was chosen to increase the number of subcarriers, as this balances complexity and resolution. The introduction of suffix and prefix segments established a circular convolution between the signal and response, validating one-tap equalisation and mitigating interference between adjacent OFDM frames. Given the frequency-selective nature of the channel, potentially influenced by low-pass effects from the LED and detector, the lengths of these segments were particularly important.

Data input began as a linear stream before being converted into parallel channels to initiate encoding. A pilot was used to evaluate channel quality prior to bit and power loading. QAM was used to map the signal to the phase and amplitude domains, followed by an inverse fast Fourier transform (IFFT) to convert the signal from the frequency domain to the time domain. The result was reconverted to serial format for transmission. Upon reception, matched filtering removed noise by using the expected signal pulse shape, which was determined during the SNR testing, where a 4 QAM signal was transmitted. and facilitated signal equalisation ahead of reconversion from serial to parallel. Subsequent demodulation converted the data back to a serial format, where timing information enabled direct comparison between the received and transmitted signals, thereby permitting precise determination of the BER.

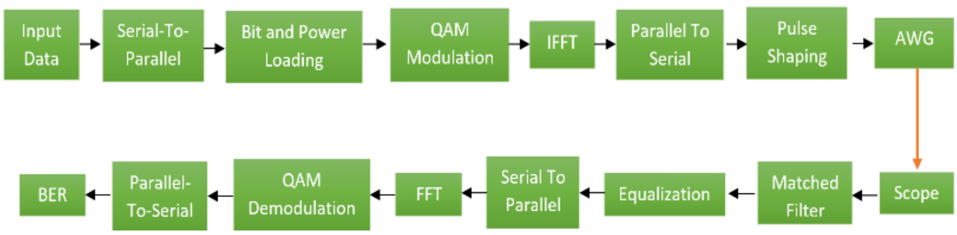

Figure 3-9 Process sequence of the OFDM code*[185],*

3.3.2. Communications results for a single pixel

Following the optical characterisation, it was concluded that it would be of interest to examine the performance of each channel tested in isolation, enabling a direct comparison of data rates obtained with and without a filter placed before the receiver. This methodology supports our detailed characterisation efforts by isolating the effects of both the devices and the filter system. As shown in Figure 3-10, the use of filters led to a measurable decrease in SNR and channel gain for every channel, due to the optical losses introduced by the bandpass filters.

While the channel gain shown in Figure 3-10 (a) and (b) offers some insight as we see the impact of filters, the SNR shown in Figure 3-10 (c) and (d) demonstrates a more direct relationship with both bit allocation and achievable data rates. There is some signal loss when the filters are introduced, mainly in the UVC channel. However, it was determined that this was not a significant issue, and the losses are somewhat limited, with only approximately ~2 dB of signal lost.

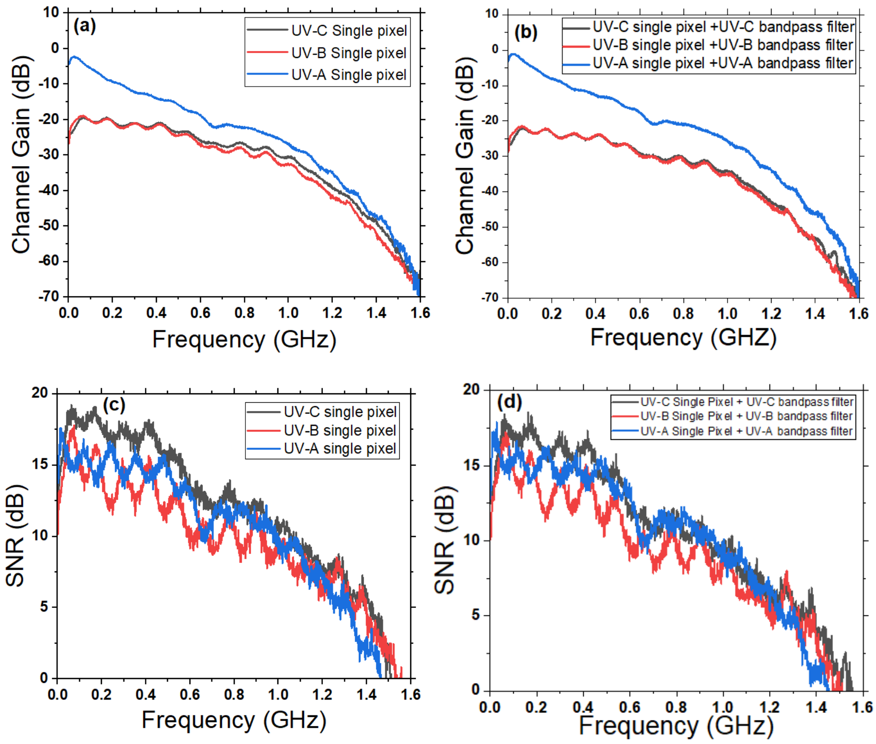

Figure 3-10 A series of tests with a single LED. Channel gain of the devices, a) with and b) without a filter, and a comparison of SNR, c) with and d) without filters.

Based on the data presented above, the filter exerted the most significant negative impact on the UV-C LED, with pronounced differences in both SNR and channel gain. This outcome is unsurprising, considering that filter technology in the DUV is still developing, and there was a minor misalignment between the output of the LEDs and the peak transmission wavelength of the filter, which occurs at 286nm with a maximum transmission of approximately 74%. Nevertheless, implementing the filter system was crucial for the feasibility of the WDM system. The bit loading graphs indicate that at lower frequencies, where the SNR is higher, the system consistently achieves up to 4 bits/Hz for the UV-A and 5 bits in the UV-C (see Figure 3-11 (a) and (c)). At the lower data frequencies for the UV-B channel (as shown in Figure 3-11 (b)), fewer bits can be loaded, with a rapid decline in capacity as frequency increases due to decreasing SNR. Beyond 600MHz, all channels are limited to 2 bits.

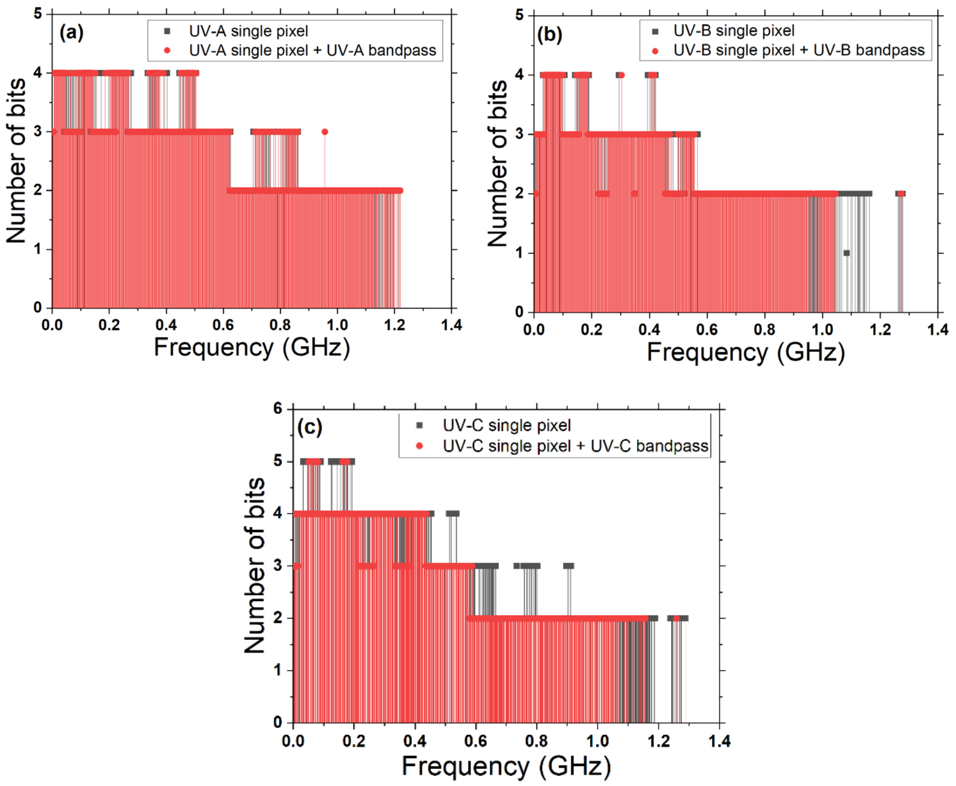

Figure 3-11 A bit loading graph for the single channel: a) UVA single pixel, b) UVB single pixel and c) UVC single pixel.

When the SNR approaches 7dB, system performance deteriorates significantly, ceasing to function past this threshold. Notably, the system remains capable of loading bits at frequencies around 1200MHz. However, due to diminished signal strength, the likelihood of successful bit loading is considerably reduced.

Furthermore, the substantial bandwidth available from each WDM channel allows for the use of numerous parallel OFDM subcarriers, thereby maximising achievable data rates. These results could be enhanced by employing more advanced detectors with higher-bandwidth capabilities.

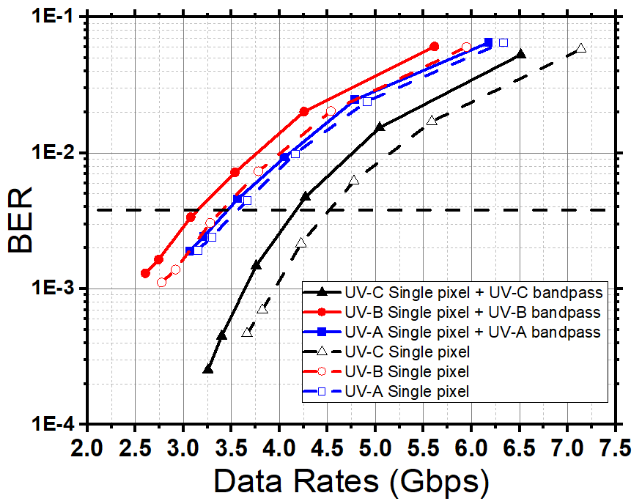

Figure 3-12 Comparison of BER when filters are applied to single pixels.

These findings in Figure 3-12 underscore the significant influence of filter systems on optical performance, particularly in multicarrier transmission systems where advanced equalisation methods facilitate modulation that exceeds the device's 3-dB E-E response, as evidenced both in this investigation and prior studies [130,194]. Using a target BER of $3.8x10^{-3}$, the data rates of each µLED were recorded with and without filters. These are shown in Table 5. Upon completing the single LED tests, the tests were moved to a full WDM test.

Data Rates (Gbps)		
Devices	Single pixel (unfiltered)	Single pixel (filtered)
UVA	3.56	3.46
UVB	3.4	3.15
UVC	4.52	4.17

Table 5. Achieved Data Rates of the single pixel.

3.3.3. WDM Communications Results

Within the complete WDM configuration, where all channels were active, with one transmitting random bit streams and others generating random noise, the SNR of each WDM channel was rigorously characterised. The peak-to-peak modulation voltage supplied by the AWG was consistently 0.25 V, after which the signal was amplified. As expected, the UV-B channel exhibited the lowest SNR due to its lower power output, while optical crosstalk further degraded the SNR of the UV-A channel. The UVC device exhibited the greatest variation after filter application (see Figure 3-12), primarily due to its lower transmission levels. Optical crosstalk in the UV-A and UV-B channels reduced data rates, a problem further exacerbated by the limited optical output power of the UV-B device. Additionally, crosstalk originating from the UV-B channel adversely impacted the SNR of the UV-A device. This limitation may be addressed in future system designs by adopting improved receiver filters. Utilising a threshold of SNR > 5 dB, the measured channel frequencies were 1.30 GHz, 1.10 GHz, and 1.25 GHz for the UVC, UVB, and UVA channels, respectively, as shown in Figure 3-13 (a).

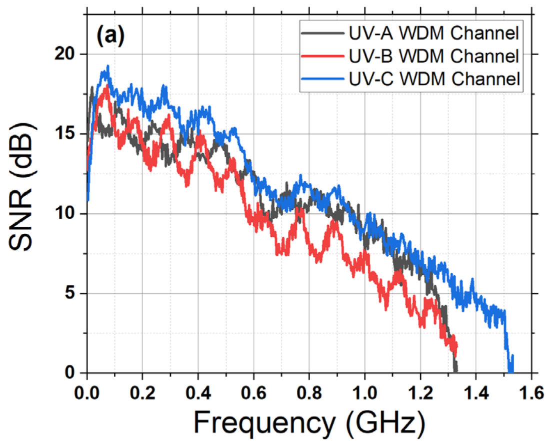

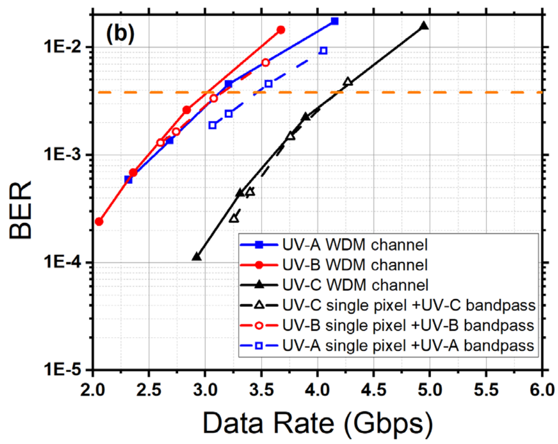

Figure 3-13 a) SNR graph for the WDM system and b) BER of three devices in both single pixel and WDM (the dashed horizontal line corresponds to a BER of 3.8×10^{-3}***).***

The data rates aligned with expectations established by characterisation measurements, with the UV-B device exhibiting the lowest maximum data rate. The UV-B device exhibited the lowest output power among the three evaluated devices. Additionally, a portion of this output power is lost during the combination of emissions for WDM, as achieving complete transmission through the "Alluxa" Mirror (see Figure 3-13 b) is not feasible. Collectively, these factors contribute to the relatively low data rate observed for the UV-B device, despite its higher bandwidth compared to the UVA device.

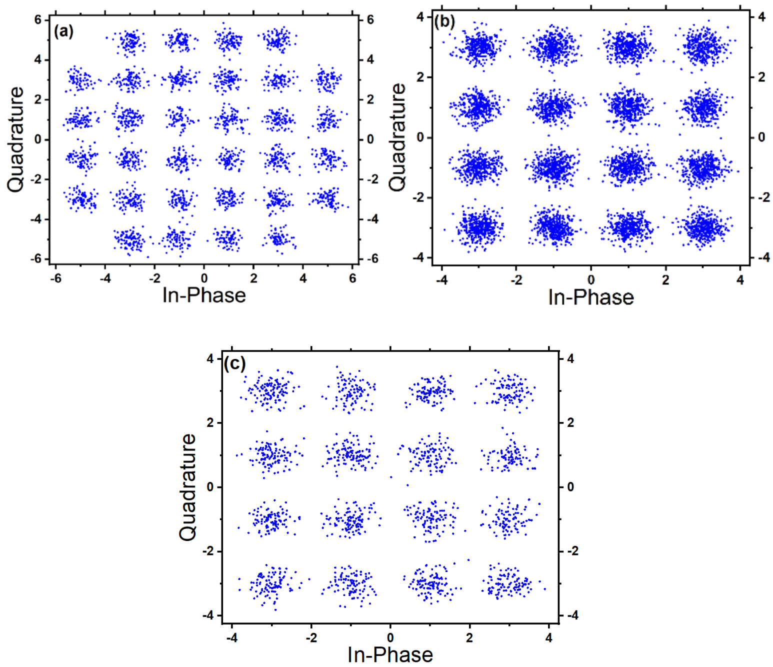

Figure 3-14. Maximum M-QAM constellation sizes achieved a)32 QAM for UV-C, b) 16-QAM for UV-B and c) 16-QAM for UV-A.

Figure 3-14 presents the M-QAM constellation diagrams for each WDM channel. Constellation sizes of 32 for the UV-C channel (Figure 3-14(a)) and 16 for both UV-B and UVA channels were predominantly employed (see figures 3-14 (b) and (c)), yielding bit error rats (BERs) of 1.12×10^{-4}, 2.40×10^{-4}, and 1.36×10^{-4}, respectively. Although QAM graphs provided valuable insights in this analysis, alternative visualisations such as SNR and bit loading graphs may offer additional clarity regarding observed trends. The QAM diagrams effectively illustrated data-point separation, with more tightly clustered points correlating with lower error rates at lower constellation orders. Owing to its superior modulation bandwidth, output power, and SNR, the UV-C channel supported higher-order QAM schemes compared to the other devices. These findings indicate that the UV-C LED is capable of achieving data rates sufficient for larger QAM configurations, though fewer devices reached this performance threshold.

The BER of individual pixels was assessed against values obtained from WDM configurations. Results indicate that the UV-C device yielded consistent performance across both single-channel and WDM scenarios, attributable to the minimal crosstalk present on the UV-C channel. This reduced interference was achieved through efficient filtering of extraneous light from the UV-B and UV-A channels using mirrors and filters. Nevertheless, spectral overlap introduced interference into adjacent channels, particularly impacting the UV-A channel. Discrepancies in the active areas between the power meter sensor (9 mm diameter) and the Avalanche Photodiode (APD) (0.5 mm diameter) suggest that the actual average received power levels were likely lower than initially estimated.

Data rates (Gbps)			
Devices	Single pixel (unfiltered)	Single pixel (filtered)	WDM
UVA	3.56	3.46	3.13
UVB	3.4	3.15	3.02
UVC	4.52	4.17	4.17

Table 6. Achieved Data Rates of the single pixel and full WDM demonstration.

The maximum data rates achieved by the UV-C, UV-B, and UV-A devices were 4.17 Gbps (~3.87 Gbps after deducting a 7% overhead), 3.02 Gbps (~2.80 Gbps), and 3.13 Gbps (~2.91 Gbps), respectively, as presented in Table 6, this details the data rates per channel, with all measurements reflecting a BER of approximately 3.8×10^{-3}. The aggregate WDM data rate obtained was 10.32 Gbps (9.5976 Gbps with 7% overhead).

Both the UV-B and UV-C channels attained data rates surpassing those reported in the literature up to the time of this work. Zhu et al. documented a maximum optical wireless data rate of 2 Gbps for a UV-C µLED [201], while Sun et al. achieved 71 Mbps for a UV-B LED [204]. The data rates observed within this body of work for the UV-A, -B, and -C bands are the highest reported to date (see Figure 3-14). Furthermore, the implementation of WDM with DUV LEDs enabled an aggregate data rate exceeding 10 Gbps for the first time in the DUV spectrum.

3. 4 Conclusion

This chapter presented a three-channel ultraviolet wavelength division multiplexing (UV-WDM) system employing μLEDs that emit at peak wavelengths in the UV-A (375 nm), UV-B (317 nm), and UV-C (285 nm) spectral regions. Utilising an OFDM scheme, the system achieved data rates of 4.17 Gbps, 3.02 Gbps, and 3.13 Gbps from the UV-C, UV-B, and UV-A devices, respectively. These individual channel data rates represent the highest values reported for UV μLEDs to date. Collectively, the channels delivered an aggregate data rate of 10.32 Gbps, thereby demonstrating a UV LED-based optical wireless link with throughput exceeding 10 Gbps.

Notably, the UV-B device exhibited comparatively lower performance than other deep UV devices, highlighting an area for further investigation and optimisation. Future research directions include expanding to additional wavelengths in the deep ultraviolet spectrum, potentially focusing on a dedicated UV-C system for operation in diffuse line-of-sight (LOS) or non-line-of-sight (NLOS) configurations. Such advancements may require modifications to the detector due to the low output powers of the LEDs, which could subsequently affect achievable data rates. Nevertheless, these modifications constitute logical next steps for this research. Additional enhancements can also be explored within the current setup, such as optimising the LED bias point, as will be discussed in subsequent chapters.

The following chapter will examine the feasibility of deploying a UV-C device with a similar architecture for long-range communications, to leverage the inherent high bandwidth of μLEDs to support extended transmission distances.

Chapter 4
DUV Communications up to 100m

This chapter examines the use of trapezoidal-shaped pixel DUV μLED arrays, similar to those used in Chapter 3, for data transmission at various currents and distances up to 116m. This work resulted in one of the highest reported data rates for a single DUV μLED: over 6.5 Gbps at 10 metres, more than 4 Gbps at 60 metres, and 1 Gbps at 100 metres. Moreover, to the best of the authors' knowledge, these results represent the highest data rates achieved at such distances using DUV μLEDs. This work has led to two publications: a submission to the IEEE Photonics Conference and a full paper in Optics Express [144,205] and this chapter expands upon those findings.

4. 1 Introduction

Previous applications of UV-C μLED communications were restricted to short distances of only a few metres (see Figure 4-1). The research presented in this chapter demonstrates Gbps data rates at distances exceeding 100 metres, representing the highest reported data rate at the longest distance to date using μLEDs and LEDs of any wavelength, not just in the UV. This advancement is attributable to improved device quality of the UV-C device material, which has enabled greater optical output power while maintaining high bandwidths essential for long-range optical communication in conjunction with optimisation of all system parameters. Although laser systems achieve longer transmission distances, they tend to be large, expensive, and require cooling with costly thermoelectric cooler (TEC) units. Furthermore, compact laser diodes remain less developed and face reliability challenges, such as low optical powers and current injection issues [206]. This work seeks to bridge the gap between the extended range capabilities of laser systems and the high data rates achieved by μLEDs.

This chapter will analyse the effects of current and peak-to-peak voltage on device performance at various distances. Additionally, it will investigate how transmission distance influences SNR, channel gain, and overall data rate.

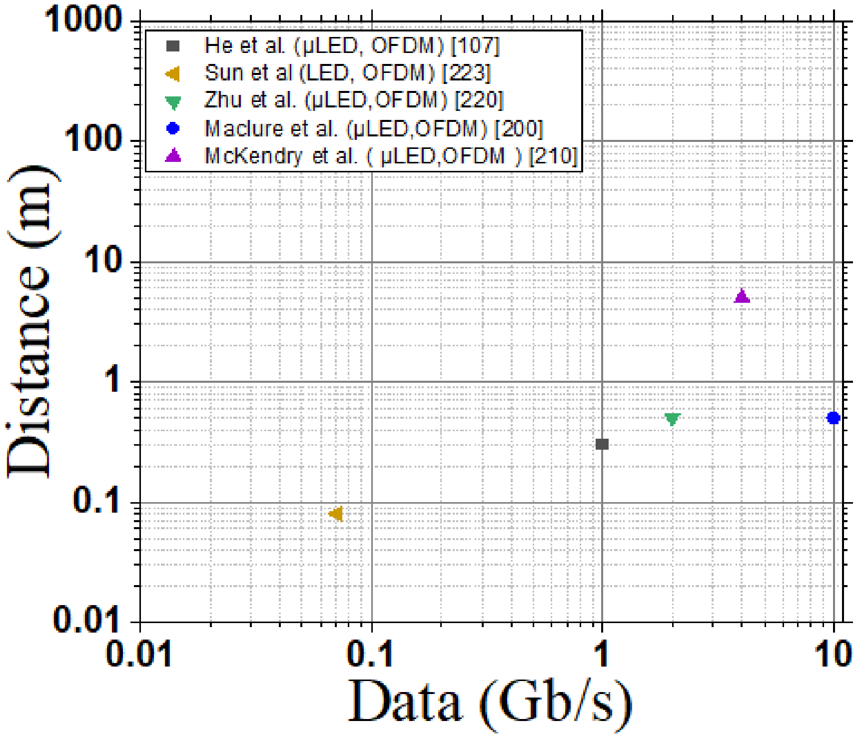

***Figure 4-1 A summary of previous work on data rate vs distance for DUV µLEDs/LED** [205].*

4. 2 Devices and characterisation results

4.2.1. LED Devices

The device utilised in these tests was an eight-segment trapezoidal array, analogous to those described in earlier research and referenced in Chapter 3, Section 3.1.1 [185,207]. It should be noted that the original purpose of this geometry of device was to permit multiple µLED pixel coupling into a polymer optical fibre or waveguide. However, the design proved advantageous for broader optical communication demonstration, not least because there is pixel redundancy in a single packaged chip, and the devices exhibited high modulation bandwidths. A micrograph of the array is shown in Figure 4-2. These devices are recognised for their high bandwidth capabilities, attributable to their elevated current densities, which facilitate rapid carrier recombination. Additionally, this characteristic enhances the EQE, as the carrier diffusion lengths minimise the likelihood of carriers interacting with damaged sidewalls.

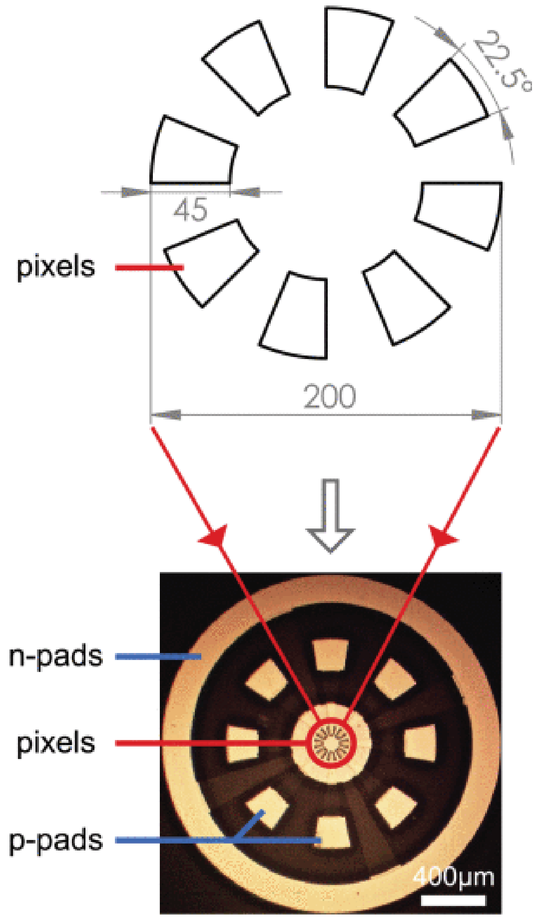

***Figure 4-2. Micrograph of μLED array geometry used in the communications tests. This follows the design in** [51].*

4.2.2. LED Characterisation results

Prior to conducting OFDM measurements on the μLED device, the initial step involved assessing the optical output power, as this parameter directly influences signal strength. The LI measurements indicated a maximum optical output power of approximately 0.4 mW (as seen in Figure 4-3 (a))) While this value is lower than that of visible light devices, it aligns with expectations and performs similarly to the UV-C device shown in Chapter 3. As noted previously, limited optical power can adversely affect both the SNR and data rate, which is described by the Shannon theorem (see section 2.1). The observed turn-on voltage (approximately 7.5V) is markedly higher than that in visible devices but much improved compared to the devices in chapter 2 due to developments in epitaxy, contacting and annealing. The peak optical power is also substantially reduced when compared to visible devices of similar size, consistent with findings presented in chapters 2 and 3. Evaluating the IV characteristics was crucial for determining the appropriate bias point for the OFDM communication systems, with currents in the range of 15–22 mA being particularly relevant (see Figure 4-3).

The device's electroluminescence (EL) spectra exhibit considerable stability as a function of bias current, when measured at room temperature under CW conditions, with only minor redshifts (approximately 2nnm) andslight variations in the FWHM from approximately 11 nm to 13 nm, as seen in Figure 4-3 (c). The μLED device demonstrates a spectral peak at approximately 285 nm. However, the breadth of the FWHM results in coverage extending into both the UVB/UVC regions of the electromagnetic spectrum (UVB range is nominally 280-320 nm and UVC defined as 100nm-280nm). This phenomenon may be attributable to internal heating effects, as fundamentally the spectral line width is determined by carrier distribution in the energy states of the conduction and valence bands. Of course, that distribution is temperature dependent, as evidenced in similar devices [191,208].

Measurements revealed that the device achieves high -3 dB modulation bandwidths, with recorded values exceeding 800 MHz However, signs of thermal roll-off were observed during bandwidth measurements, indicating carrier overflow at larger current densities and that heating effects could compromise pixel integrity and shorten operational lifetime, an important consideration for these μLED devices [209]. Thermal effects may, though, decrease carrier lifetimes, thereby contributing to increased bandwidth. These bandwidth measurements are crucial within this chapter, as the objective of this characterisation work was to evaluate the array under various communication parameters, such as bit loading, and to analyse overall device performance, with bandwidth serving as a central metric. Additionally, it should be noted that the -6 dB optical-electrical bandwidth surpasses that of the detector, which has a stated -3 dB bandwidth of 1 GHz. This represents a challenge in deep ultraviolet optical wireless communications (DUV

OWC), as UV-enhanced detectors often possess lower bandwidths compared to their more mature counterparts used in visible and IR light communications.

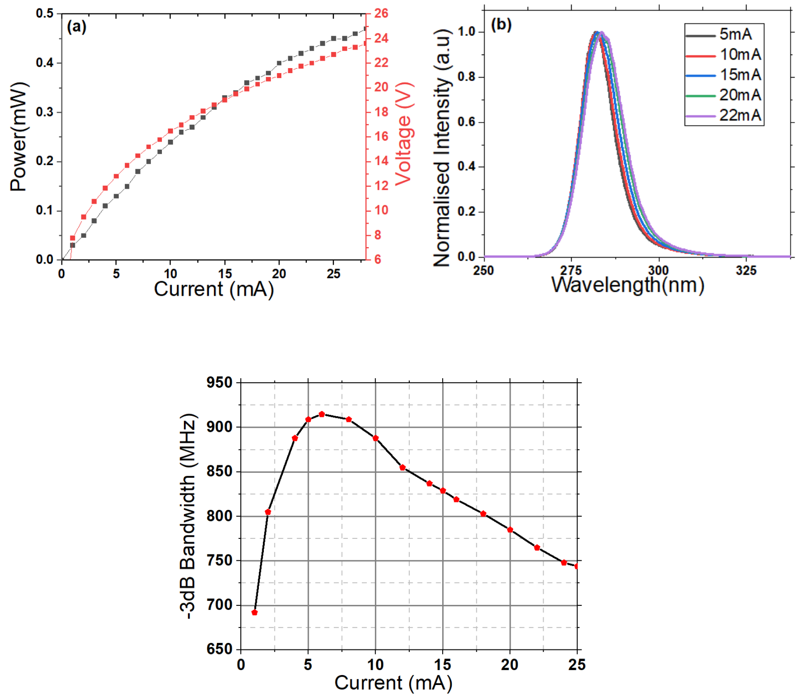

Figure 4-3. Characterisation of the UV-C µLED a) LIV b) normalised spectra and c) -3dB modulation bandwidth.

4. 3 Short-range laboratory tests (<17m)

Due to the spatial constraints of the laboratory setting, the first stage of this work focused on a two-mirror set-up that allowed for the optimisation of a retroreflector-based communication system and facilitated the testing of parameters and evaluation of performance at distances up to 17m. In this section, the system was optimised to achieve the highest data rates achieved by a single DUV µLED at approximately 17m. The following subsections will examine the system that was constructed and the results achieved.

4.3.1. Experimental set-up

The experimental setup utilised in this chapter comprised two 2-inch lenses from Edmund Optics (model 84340, diameter =50mm and NA=0.63), with one lens dedicated to collimating light from the LED array and the other directing the light onto the receiver APD (a diagram of the system is shown in Figure 4-4). A

Yokogawa GS610 power supply provided the necessary voltage and current for the μLED. For data transmission, the modulation signal was generated by an arbitrary waveform generator (AWG, Keysight model M8195A), which was subsequently amplified by an SHF-S126A amplifier. The RF signal and DC supply were combined using a Tektronix bias tee. This configuration closely resembled the arrangement depicted in Chapter 3 for one of the individual channels in the WDM setup. Additionally, two 5.08 cm × 5.08 cm UV-enhanced aluminium mirrors (Thorlabs PFSQ20-03-F01) enabled attainment of the required distances by retroreflecting the transmitted light onto the receiver optics, giving a full path length of up to 17m, constrained by the space available. However, for the 5m results, it should be noted that only one mirror was used.

Signal acquisition was performed using a Keysight MXR608A oscilloscope, facilitating alignment through the use of a pilot sine wave. The same 1 GHz Hamamatsu APD employed in Chapter 3 was utilised on the receiver side. Notably, no optical filters were applied due to the AC-coupled nature of the APD, which allowed effective rejection of low-frequency background noise. Ambient lighting was disabled during system alignment to enhance the visibility of the relatively weak signal at extended distances; this was observed using a viewing card and white printer paper fluorescing under UV illumination. Comparative measurements with and without background lighting revealed a negligible impact on data rate, attributable to the APD's AC coupling, and potentially also the narrow field of view of the optical link.

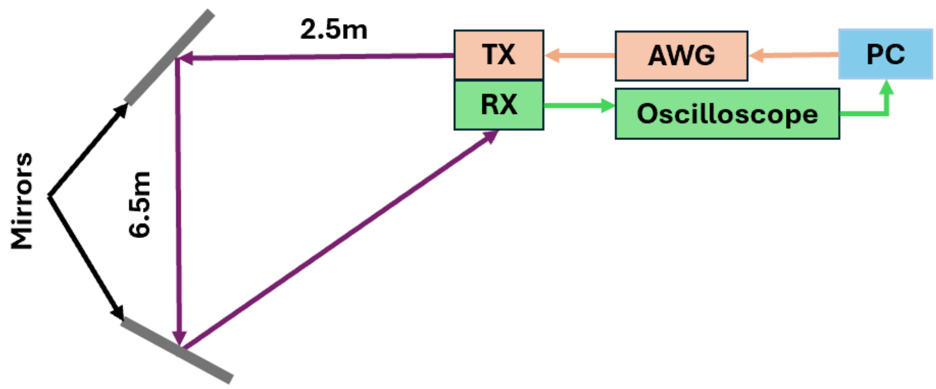

Figure 4-4. Block diagram of a two-mirror setup used for tests up to 17m.

It was determined that the mirrors introduced approximately 10% optical losses within the system, as shown in Figure 4-5 a relatively modest reduction that could potentially be addressed through advancements in UV-enhanced reflective materials. In the two-mirror configuration, total loss reached approximately 19%, underscoring the cumulative effect of multiple reflective surfaces. However, it should be stated that in a real-world single point-to-point system, there would be no need for mirrors, as mirrors were used here to maximise the available path length in the confined laboratory space.

The mirror assembly was mounted on a tripod, facilitating movement along both the X and Y axes, which proved advantageous for accurate alignment. This arrangement permitted close proximity between the detector and receiver, effectively mitigating potential timing discrepancies during decoding and enabling a direct connection between the AWG and oscilloscope. The system utilised KM200S kinematic mounts for mirror alignment, enabling precise angular adjustments that are essential at extended ranges where minor deviations can significantly alter the beam's trajectory.

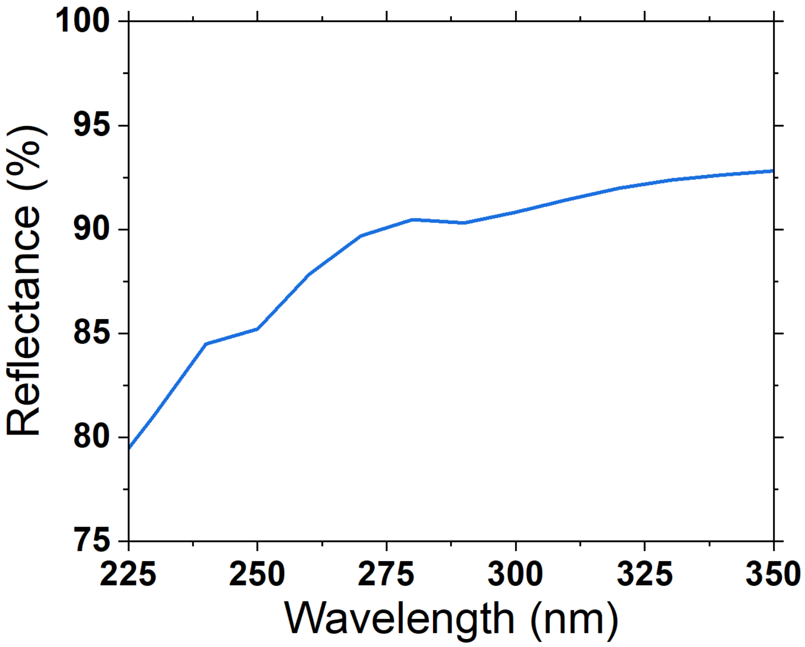

Figure 4-5 The reflective profile of the mirror vs wavelength (Thorlabs PFSQ20-03-F01). This graph was reproduced from the Thorlabs datasheet.

Both the receiver and transmitter were operated via laptops, which controlled the transmitted signals and allowed for adjustable parameters such as VPP. The laptops also interfaced with the oscilloscope to support post-processing activities. This configuration allowed for a short connection to the AWG for synchronisation purposes, thereby avoiding the need for a longer wire or a more advanced communications protocol which included timing.

4.3.2. OFDM Details

In this chapter, OFDM serves as the encoding method (OFDM was discussed in detail in Chapters 1 and 3). This approach is integrated with a bit-loading algorithm to maximise data transmission given the available SNR. Initially, the µLED was biased with a 10-mA current from a DC source, followed by the application of a pilot sine wave to calibrate the system. Upon achieving optimal alignment, the µLED bias was increased to 20 mA. This procedure accords with the setup and OFDM parameters described in Chapter 3. The focus in this chapter is to provide a more detailed examination of the OFDM parameters, such as VPP, which were only briefly discussed previously. Emphasis was placed on analysing these parameters to optimise system performance, while certain key parameters remained constant throughout. The following subsection will describe the two experimental setups utilised in this chapter and evaluate the respective advantages and disadvantages of the hardware implemented.

4.3.3. Short range communications results (<17m)

For this body of work, substantial effort was put into optimising the system, and the following section examines the ideal VPP and bias current for the LED. The ideal VPP was determined through MATLAB code by testing the linear response region of the LED and optimising the pilot sine wave's signal strength, selecting lower current levels where feasible. A lower supplied VPP was necessary, as insufficient current can lead to clipping and limit the device's ability to handle high voltage swings, as discussed in Chapter 3. Maintaining device linearity is also crucial beyond a certain current threshold, optical output power plateaus, so further increasing the voltage swing does not yield notable improvements in SNR.

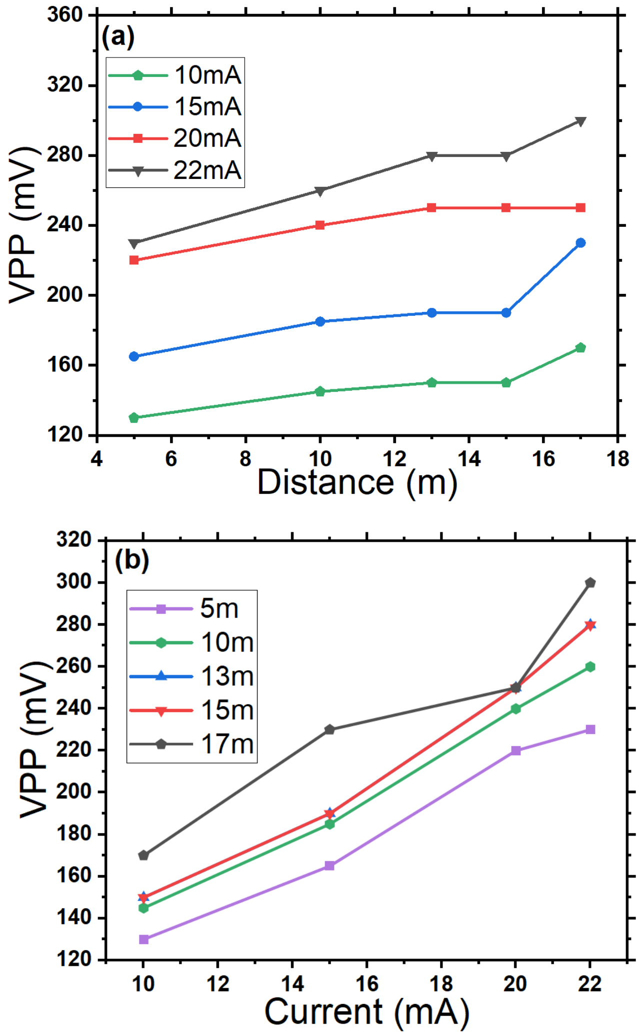

Figure 4-6.The VPP of the set-up generated by the AWG a) The VPP vs distance, and b) VPP vs current *[144].*

Notably, while the optimal VPP increases with higher currents, the incremental improvement in data rate diminishes. In contrast to visible light systems, higher VPPs pose less risk of device damage, since lower operating voltages are typical in the latter, making large voltage swings more challenging to achieve. Although the VPP values referenced herein Figure 4-6 are those provided by the AWG, and they are subsequently amplified by the amplifier as stated in section 4.3.1. The device's capacity for larger voltage sweeps increased with current, as seen in Figure 4-6 (a), Furthermore, the increase in distance also resulted in an increase in the VPP, particularly around 17 meters (see Figure 4-6 (b)). This may be attributed to beam alignment issues or divergence over longer distances, resulting in reduced SNR and necessitating a higher VPP.

While channel gain declines with increased distance, as expected due to the optical beam divergence, supplying greater current can partially counteract this effect; however, after a certain point, further current increases do not enhance data rate performance. Additionally, similar to the devices used in the WDM systems, DUV devices are subject to impedance mismatches, which can cause signal reflections, potentially due to wire bonding or metal contacts, as suggested by the elevated turn-on voltage resulting from resistance. This issue warrants further investigation in future work.

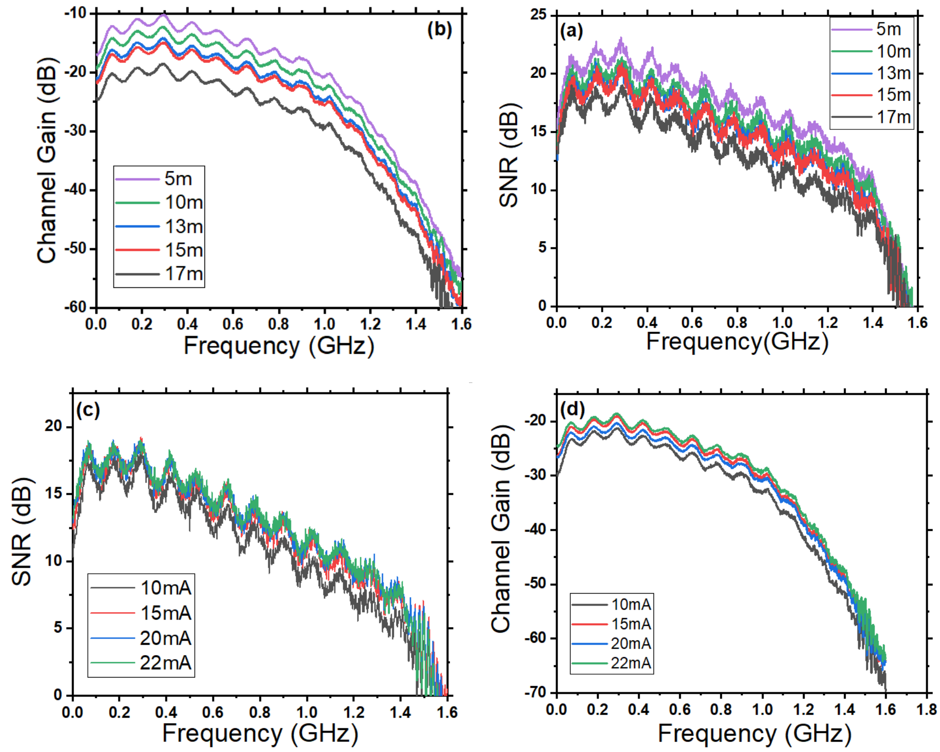

Figure 4-7.a) SNR vs frequency as a function of distance at 22mA and b) the corresponding channel gain vs frequency as a function of distance; c) SNR vs frequency at 17m as a function of current and d) the corresponding channel gain vs frequency at 17m as a function of current

As seen in Figure 4-7 (a), the SNR decreases with distance, a trend consistent with recorded power measurements (see section 4.4), where increased current correlates with higher SNR across the bandwidth. However, the high-frequency component of the 10 mA SNR drops significantly, which could account for the observed reduction in data rates. Ultimately, SNR determines the number of bits that can be assigned to OFDM channels, as explained in Chapter 1 and also in Chapter 3. SNR is notably influenced by changes in distance. However, increasing the current also yields a higher SNR because the device emits more photons. It is essential to recognise that beyond a certain current threshold, further increases provide diminishing improvements in SNR as the device begins to "roll off," causing optical power to plateau and eventually decline as seen in Figure 4-7 (c). The enhancement in SNR with current is consistent across all frequency ranges, not limited to low or high frequencies, and a trend is also reflected in the SNR data. The channel gain (shown in Figure 4-7 (b) and (d)) also decreases with distance however this is more obvious at lower frequencies and the current also has a similar effect on the channel gain as it does with the SNR where increases in current can result in marginal gains from this it is possible to test the number of bits that could be expected per frequency.

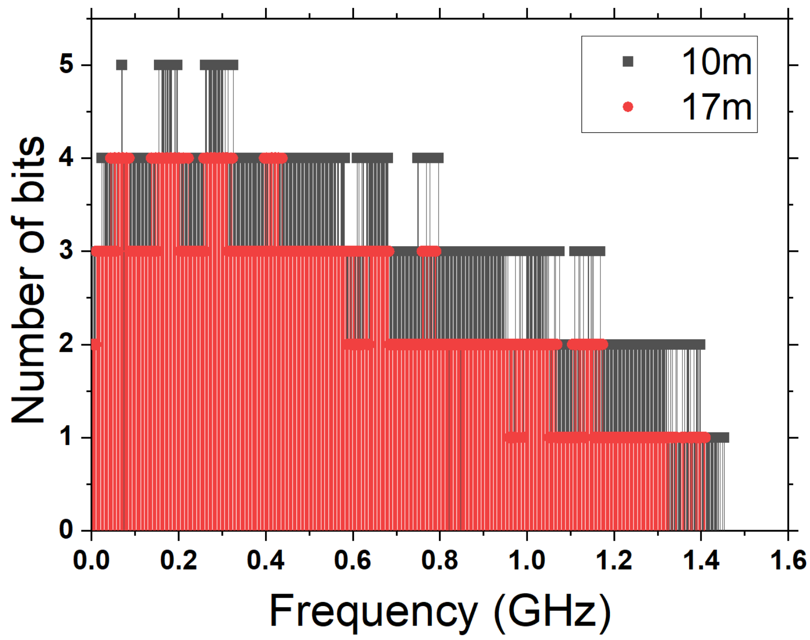

Figure 4-8. The bit loading at 22 mA for 10m and 17m.

As illustrated in Figure 4-8, the number of bits that can be loaded decreases with increasing distance, attributable to the reduction in SNR as the beam diverges. Elevating the current enables an increase in the number of bits loaded, facilitating active bit loading and enabling the system to achieve higher data rates. This adaptive loading mechanism responds to channel quality, as shown in Figure 4-8, where the loaded bit count rises with SNR. Such adaptation supports the achievement of high data rates as described in Chapter 3. Excessive bit loading for a given SNR would lead to a substantial increase in BER, so careful selection of bits per frequency is vital to maintain both high data rates and low BER. This was done using Hughes-Hartog’s algorithm, which is a bit-loading technique used in OFDM systems. It incrementally adds one bit to the subcarrier that requires the least increase in power for an additional bit. This approach maximises the total data rate while staying within the overall power limit [210]. Which was used to optimise the number of bits loaded vs carrier frequency. Notably, the number of bits loaded per carrier drops sharply between the 10m and 17m setups due to the corresponding decrease in SNR.

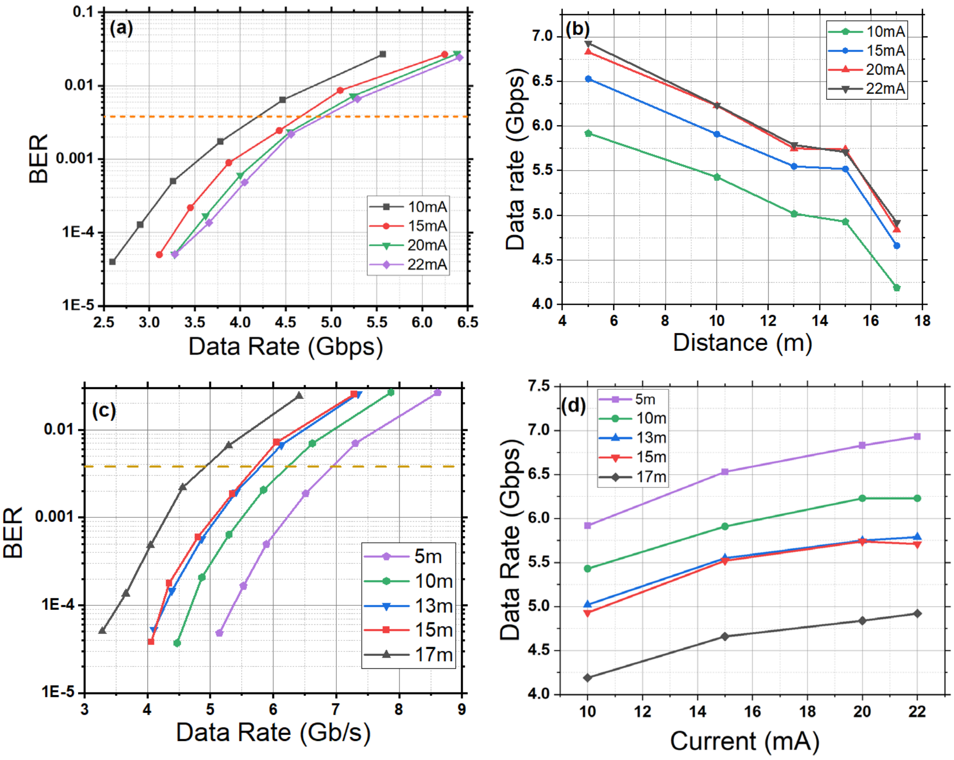

Figure 4-9 a) BER vs data rate at 17m at various currents, b) data rate vs distance at various currents, c) BER vs distance at 22mA, d) Data vs distance at various currents.

The data rate was measured at a BER of 3.8×10^{-3}, consistent with the methodology previously presented in Chapter 3. Although the data rate declines rapidly with increasing distance, raising the current to approximately 20mA, as demonstrated in Figure 4-9 (b), mitigates this decrease by increasing the optical power output of the µLED and thus increasing the SNR. Nonetheless, the benefits of increased current eventually diminish, with the difference between 20mA and 22mA being negligible, which may be attributed to shifts in device linearity with higher currents, as indicated by the LIV characteristics. From this work, it was possible to determine that the system could be further extended to longer distances, which will be discussed in the next section.

4. 4 Long-range system (>100m)

Upon completing the laboratory tests with the two-mirror system, the results demonstrated that the system could be further extended. In order to extend the range, the system was switched to a one-mirror configuration, and the experimental setup was oriented such that the mirror retroreflected the transmitted beam down a corridor to increase the path length, as seen in Figure 4-10. A laser rangefinder was used to measure the distance between the mirrors, transmitter, and receiver. As for the previous two-mirror configuration, the detector and LED were mounted on XYZ translation stages, providing fine alignment capabilities that maintained a suitable SNR over greater distances.

a)

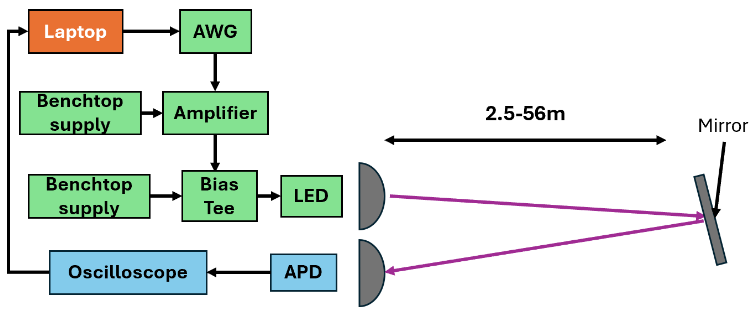

b)

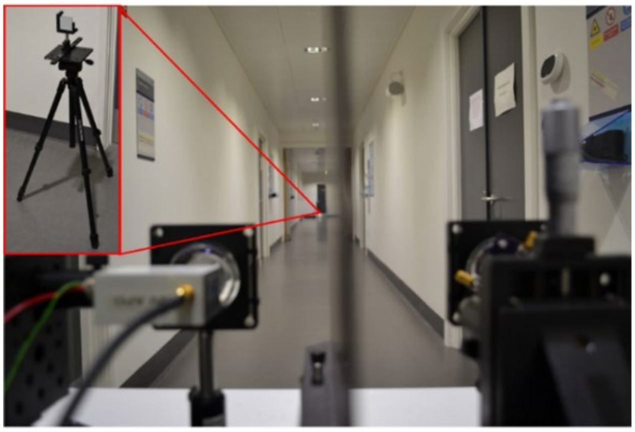

Figure 4-10 a) Diagram of the one mirror system and b) photograph of the one mirror system as set up in the laboratory corridor.

The total length of the corridor was approximately 60m, so using the mirror to retroreflect the transmitted beam increases the optical path length to distances exceeding 100m. The system remained indoors due to its reliance on mains power and to ensure safe measurement conditions, given the potentially hazardous properties of DUV light sources. The following section will examine the performance of this system and the data rates that were achieved.

Maintaining alignment at extended distances proved difficult, as even minor adjustments to the mirror angle could significantly alter the beam direction. Therefore, background lighting had to be minimised during alignment a process that warrants improvement in future work. Having discussed the experimental setups, the following section will address the characteristics of the long-range one-mirror configuration described here.

4.4.1. Long Distance Power measurements

To better understand the system's performance, the first test was to examine the expected received optical power at various distances to ensure the system can operate over longer distances. During these measurements, a single mirror and a tripod were repositioned in 5 m increments from the transmitter, corresponding to 10 m increments due to retroreflection. A Thorlabs power meter and sensor head (Thorlabs S120VC) were used, with the sensor head fitted with a 300 µm pinhole to simulate the active area of the APD, thereby allowing the actual power incident on the APD to be estimated.

As illustrated in Figure 4-11, there is a marked decline in optical power over the initial few metres. However, this decline becomes less significant at greater distances. It is noteworthy that this trend may be influenced by the optical power meter's sensitivity limitations, as power levels approached the detection limits beyond 60 m. The primary cause of power reduction was beam divergence over extended distances, resulting in increasingly divergent light not captured by the receiver lens. The results described above demonstrate that losses associated with the single-mirror system become increasingly significant at greater distances. Upon reviewing the optical power results, it was determined that the optical powers were sufficient to conduct a series of communications tests, and the following section will examine the outcome of these tests.

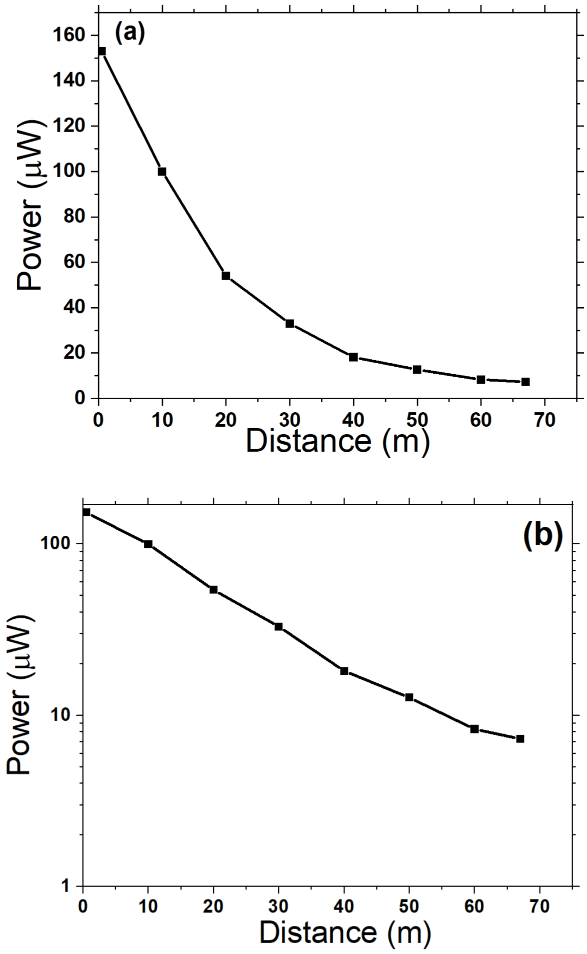

Figure 4-11 a) Power vs distance with pinhole and b) the data plotted on a logarithmic scale.

4.4.2. Long Distance Communication Results

This section presents the optical wireless data transmission results obtained using the one-mirror configuration described earlier. As the transmission distance increases, the number of bits that can be loaded decreases due to reduced SNR stemming from more pronounced beam divergence, lowering the optical power. Notably, active bit loading allows the system to maintain high data rates despite these limitations. Similar to the two-mirror system, the number of bits loaded decreased with distance, as expected, as demonstrated in Figure 4-13. Higher SNR at shorter ranges permits greater bit loading with an average of 5 bits being loaded at lower frequencies for 10m (see Figure 4-12 (a)) with this decreasing to around two bits for 100m.

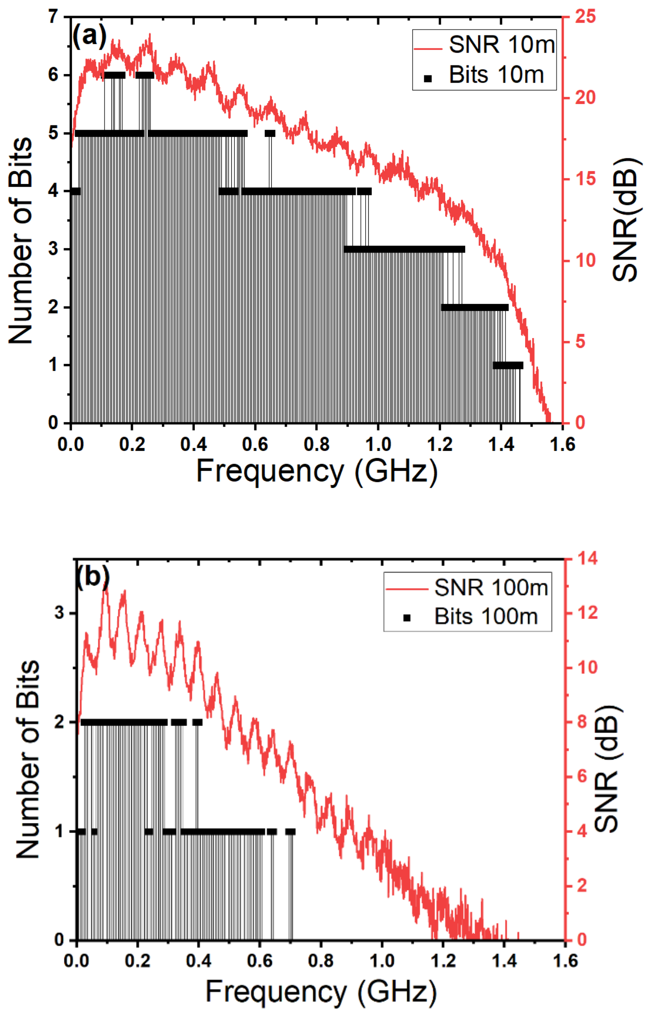

Figure 4-12 a) 10m and b) 100m comparison of SNR to bits loaded.

Figure 4-12 (b) illustrates that bit loading is no longer possible once the SNR falls below 5 dB, highlighting an area suitable for further investigation concerning the limits of the current OFDM bit loading scheme. Additionally, at short ranges, there is a sharp decline in SNR beyond 1300 MHz, which surpasses both the -3 dB detector bandwidth and the μLED's capabilities. Further research is warranted to determine whether this rapid decrease is primarily attributable to the detector or the LED characteristics.

To compensate for SNR reduction with increased range (Figure 4-13 (a)), the peak-to-peak voltage (VPP) was raised, and this necessitated selecting an appropriate bias point. As seen in Figure 4-14 (b), under 10 metres, VPP remains relatively stable near 0.2 V, but approaches over 0.5 V near 100 metres, demonstrating the requirements of VPP variation with distance. However, this would be problematic in a system with fixed voltages; however, adaptability can also be applied to a real-world system.

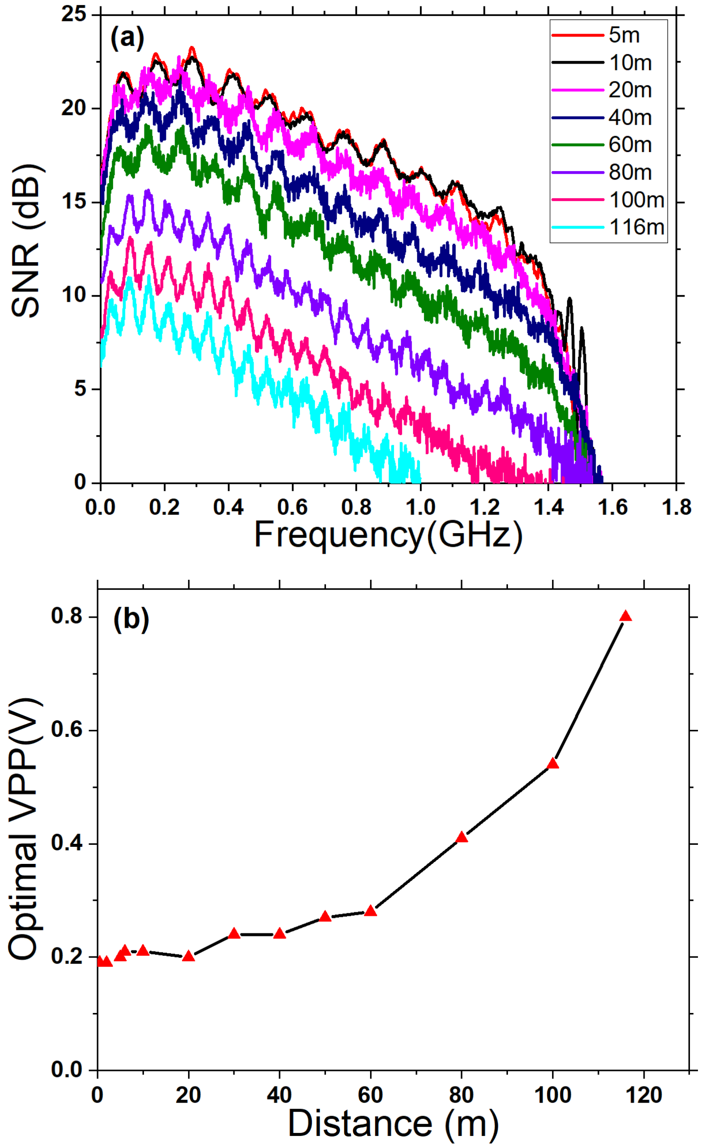

Figure 4-13 (a) SNR vs frequency and b) optimal VPP vs distance.

With increasing distance, SNR diminishes in parallel with channel gain, particularly at higher frequencies. Device nonlinearity and detector noise were also investigated. Beam divergence contributes to SNR reductions, and when compared to scattering, beam divergence is the dominant reason for the reduction. SNR fluctuations, which can be seen Figure 4-13 (a) could be the result of impedance mismatches.

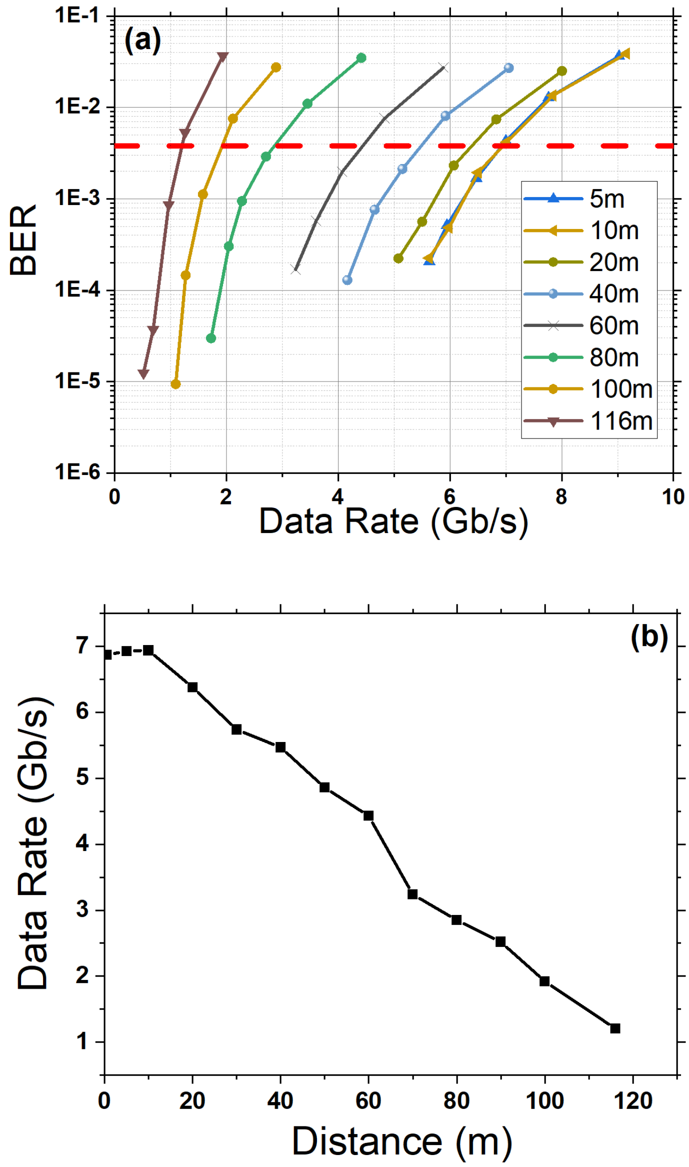

Figure 4-14 a) The BER vs data rate and b) the maximum error-free data rate vs distance.

As previously defined, data rate corresponds to the highest rate with BER below the FEC threshold of 3.8×10^{-3} (Figure 4-14 (a)). At 116 m, comparisons under varying ambient light conditions revealed negligible differences in data rate, demonstrating that the system is robust to ambient lighting due to the detector's AC-coupled preference for modulated signals. Data rates above 6 Gbps were consistently achieved at distances under 10 meters, with a data rate of 1.12 Gbps being achieved at 116m, see Figure 4-14 (b). However, data rates declined with increasing distance due to numerous factors, including alignment shifts, pixel degradation, and changes in the applied VPP. Nonetheless, these experiments achieved some of the highest recorded data rates at any distance using DUV µLEDs. Furthermore, the performance at 100m is a record for any wavelength of µLED. It should be noted that much of this work was past work from our own group (see Figure 4.15 below).

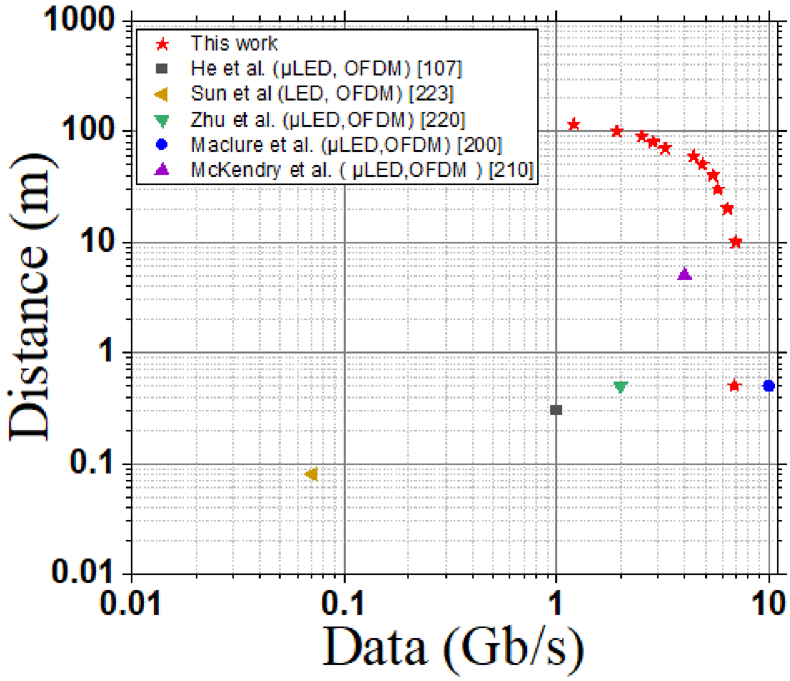

Figure 4-15 A comparison of previous work (correct at the time of publishing this work) *[205].*

4. 5 Conclusions and further development

This chapter has demonstrated that µLEDs are capable of supporting Gbps communication over distances >100m, representing significant progress in the field. Notably, at distances below 10 metres, the highest data rate recorded was achieved using a single DUV µLED. At extended ranges, the system attained record data rates of 1 Gbps at 116 m using a single DUV µLED. The results further indicate that the data transmission rate remains comparatively stable under ambient lighting conditions. To our knowledge, these data rates are the highest reported at nearly every measured distance for single µLED systems and may enable future long-range outdoor applications.

However, in future applications, a number of improvements could be made, such as moving the transmitter and receiver apart, thus allowing for the removal of the mirrors, and changing the system from a low technology readiness level (TRL) demo to a real-world working system. Additionally, automating the mirror alignment processes would further improve operational efficiency by facilitating rapid adjustments and reducing manual intervention, which would assist with pointing and tracking. Refining the timing system has the potential to produce a more robust platform capable of supporting advanced encoding schemes. The next chapter will focus on non-line-of-sight (NLOS) configurations to develop solutions less reliant on precise alignment, thereby increasing practical applicability.

Chapter 5
Non-line-of-sight communications (NLOS)

5. 1 Motivation

One important advantage of DUV technology is that its short-wavelength ultraviolet light is particularly effective for non-line-of-sight (NLOS) communications due to the considerably stronger scattering that takes place compared to visible or infrared wavelengths, enabling the exploitation of both Rayleigh and Mie elastic scattering mechanisms to bypass obstacles that would otherwise obstruct a line-of-sight connection, as discussed in Chapter 1.

This characteristic is especially relevant in practical communication systems, where receivers are frequently not in the direct line of sight of transmitters. Although NLOS propagation typically results in lower received light levels, the minimal background noise in the DUV spectrum enables the detection of extremely weak signals. A schematic of NLOS is shown in Figure 5-1. This chapter presents an initial proof of concept of such a system. It addresses unique challenges encountered during NLOS experimentation challenges absent from previous LOS chapters (i.e., Chapters 3 and 4), including overcoming physical barriers and improving the signal-to-noise ratio.

The primary motivation for this work is to broaden the application of OWC. Previous research discussed in this thesis has focused on finely aligned LOS communications, which are practical in controlled laboratory settings but not always achievable in real-world environments, as outlined in the introduction. The current chapter will present the characterisation of the commercial LEDs and electronics utilised in this work. We developed a NLOS communication system that established a sub-10-metre kbps link. This development should guide future advancements by highlighting both the advantages and challenges inherent in NLOS communications.

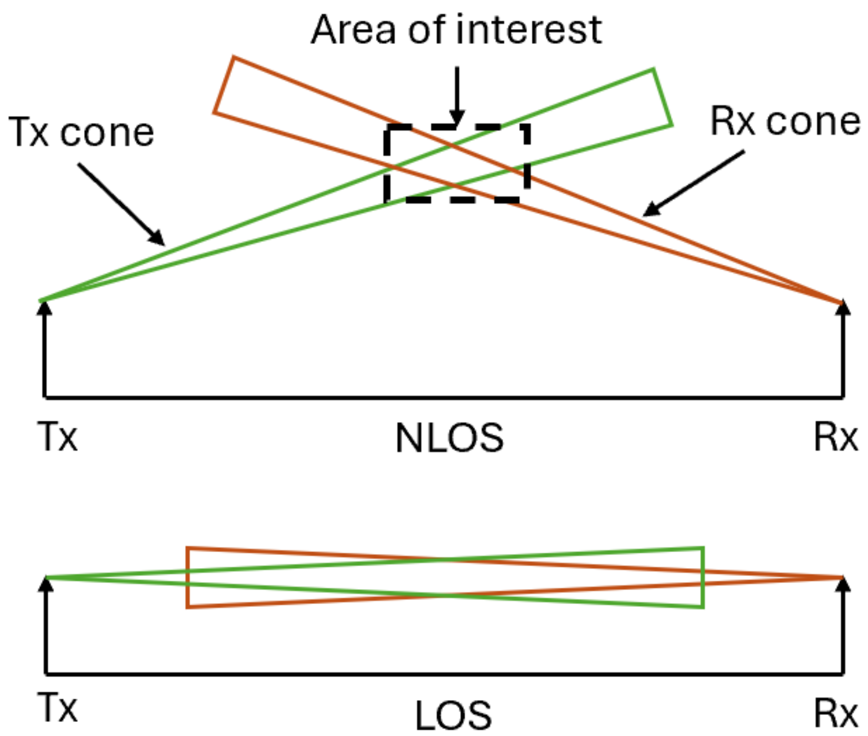

Figure 5-1 Schematic of NLOS vs LOS system configurations.

5.1.1. NLOS research

As previously indicated in the introduction, several scattering mechanisms, particularly Rayleigh and Mie scattering, affect ultraviolet (UV) light as it propagates through air. Rayleigh scattering typically involves particles smaller than the wavelength of light, whereas Mie scattering pertains to larger particles relative to the wavelength (as discussed previously in Chapter 1). These phenomena have numerous applications, including gas sensing and optical scattering measurements. Such mechanisms are particularly relevant in the field of visible underwater communications [211–215], where a key challenge in NLOS studies is the focus on military applications. Another significant issue is that atmospheric scattering models are highly dependent on environmental factors such as dust and humidity, making accurate modelling of these systems challenging.

Several research groups have investigated DUV scattering, noting that its effects become significant at distances on the order of kilometres. However, there is still some scattering at short ranges, as will be demonstrated in this chapter, and as seen in Table 7 [216,217]. Although this chapter will not address NLOS modelling in detail, it should be noted that various approaches, including Monte Carlo simulations, have been explored for NLOS optical communication links. However, describing these methods remains outside the scope of this work. The primary objective is to encode information within the scattered light, an area of growing interest due to advancements in UV LEDs and laser technologies. These technological developments have expanded the feasibility of practical NLOS systems.

Atmospheric Scattering coefficient over km^{-1}					
λ(nm)	$k_s^{Rayleigh}$	k_s^{Mie}	$k_{b=mie+ray}$	$k_{absoption}$	$k_{t=abs+scatt}$
230	0.493	0.623	1.116	2.581	3.697
240	0.406	0.531	0.937	1.731	2.668
250	0.338	0.421	0.759	1.202	1.961
260	0.266	0.284	0.55	0.802	1.352
270	0.241	0.277	0.518	0.621	1.139
280	0.194	0.272	0.466	0.322	0.788
290	0.177	0.266	0.443	0.046	0.489
300	0.145	0.261	0.406	0.039	0.445
310	0.132	0.234	0.366	0.005	0.371

Table 7 Representative atmospheric scattering and coefficients in the DUV absorption (air type not stated)*[218].*

A comparison between DUV LOS and NLOS configurations indicates that devices can achieve significantly higher data rates in LOS setups, primarily due to superior signal-to-noise ratios, which are a critical determinant of system performance. Recent literature includes experimental investigations into DUV NLOS systems, which can be categorised by the type of illumination used: lasers, LEDs, or flashlamps [219–221]. When this research field emerged in the 1960s, flashlamps were commonly utilised, supported by initial modelling studies [222–224]. More recently, there has been notable progress in academic circles, with significant publications appearing over the past year [218,225,226].

From using Table 6 we can see that the total scattering coefficient at 280nm is 0.466 km^{-1}. From the equation $I(\lambda) = I_0(\lambda) \times e^{(-d\times c)}$ where d is the distance and c is the scattering coefficient, it was possible to determine that at 5m, approximately 0.2% of the photons are scattered, resulting in randomness and temporal flux in the system. There is a distribution around the 1 and 0 binary levels, and this can impact the error rate as the photon packet will have expanded (temporally spread). Photons will arrive at different times and appear in time bins where a "0" is expected, which could be read as a "1", resulting in an error. The Poisson statistics of light detection further compound these issues, and as a result, scattering significantly affects the expected photon count, as seen elsewhere in underwater communications.

One persistent challenge in UV NLOS communication is the necessity for higher optical power outputs to compensate for the substantial channel loss. This poses potential health and safety risks, as exposure to shorter wavelength UV radiation can be ionising and hazardous to human health, potentially leading to conditions such as skin cancer [6].

Another significant challenge is that most conventional photoreceivers are not solar-blind and can still detect signals in the visible and sometimes the infrared, as well as the DUV, which can introduce background noise. As a result, the subsequent measurements that were conducted in this chapter had to be performed in a darkened room. There have been steps made towards improving this, with devices specifically designed to block out other regions of the EM spectrum, other than the DUV, such as Ga_3O_2 and AlGaN. However, these devices are still at a low technology readiness level (TRL) and require more development [137].

5.1.2. Device characterisation

The device used in this chapter was a commercial Osram OSLON SU CULDN1.VC (image shown in Figure 5-2). This LED was selected for its high optical output power in the UVC. Notable advancements in commercial devices over recent years have led to increased optical output and extended operational lifetimes, making them an attractive choice for this work, where the system will operate in a setting where high-power optical devices are essential.

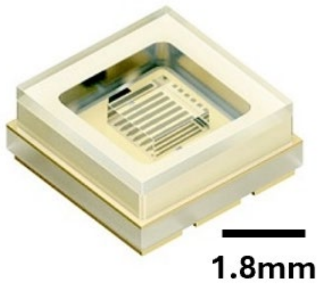

Figure 5-2 Image of LED used in NLOS communications tests (Osram OSLON SU CULDN1.VC.)

The electrical and optical power performance characteristics of the tested LED are illustrated in Figure 5-3. The selected device achieved DC output powers up to 25mW (see Figure 5-3 (a)) and demonstrated stability in peak emission at approximately 275nm (see example of emission spectra in Figure 5-3 (b)) as well as a relatively high -3 dB bandwidth (approximately 100MHz) shown in Figure 5-3 (c). These measurements were taken in our laboratory, with the optical power measured as directed forward output as described previously. Note that the manufacturer's data sheets contain no information on modulation bandwidth. The device has several illuminated strips; this is done to ensure good current spreading and enhance the performance. The device has a turn-on voltage of approximately 5.5V, significantly lower than the custom μLEDs used in the previous chapters, enabling the use of custom driver circuits, which will be discussed later in this chapter. As expected, the bandwidth is significantly lower than that of μLED devices; however, in this work, optical power is prioritised, as the system will operate in a photon-starved regime with single-photon detectors, and lower data rates are expected. The bandwidth is lower than that of μLEDs because their larger areas can result in higher capacitance, and as stated in Chapter 2, for larger-area LEDs, the bandwidth is often defined by a large RC time constant.

The LED device has a small emitter footprint compared to the 2-inch diameter lens used, which facilitates collimation and delivers high optical power into the receiver cone, allowing for optimisation of the system. This improvement enabled higher photon counts to be received and enhanced the SNR for the data communications link under investigation.

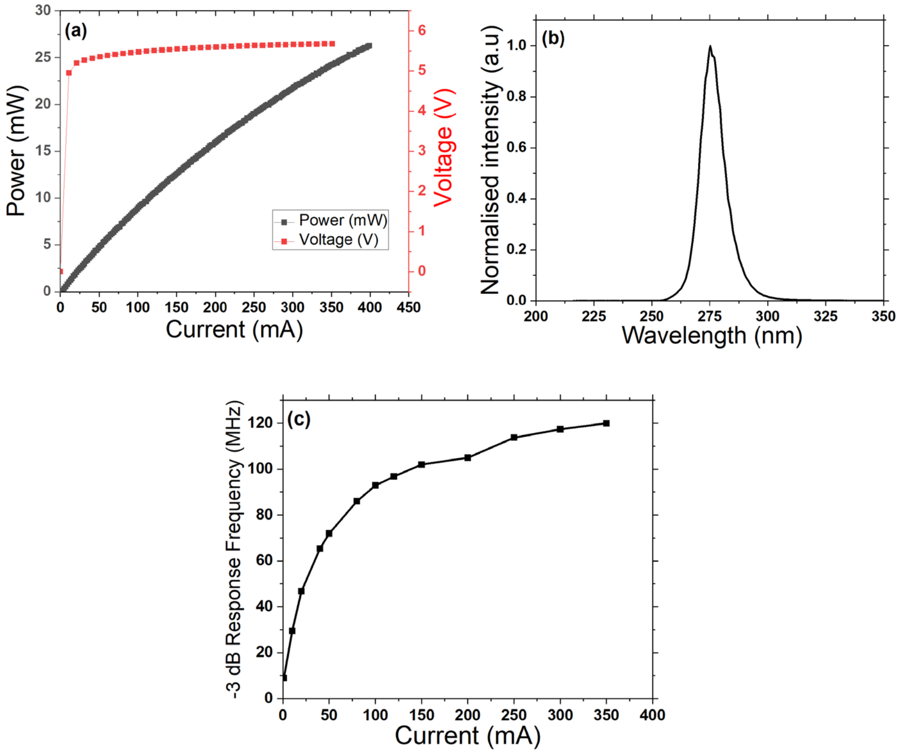

Figure 5-3 Shows the LIV, b) spectra characteristics, and c) bandwidth of the Osram device used here, these are our own data, see text

5. 2 Experimental set-up

In our portable test system, two tripods were used, one for the transmitter and one for the receiver. The optical transmitter system is configured with a two-inch lens (Edmund optics 84340 NA=0.63 and f=21.4mm) mounted directly to the LED PCB, secured within a cage assembly. This approach simplifies the setup compared to previous configurations, maintaining constant XY-axis positioning while allowing Z-axis adjustment for focusing. These adjustments are facilitated by repositioning the tripod, which permits precise targeting and manipulation of the transmission cone's size and shape along the Z-axis, without affecting the cone shape on the X or Y axes. A block diagram of the setup is shown in Figure 5-4(a).

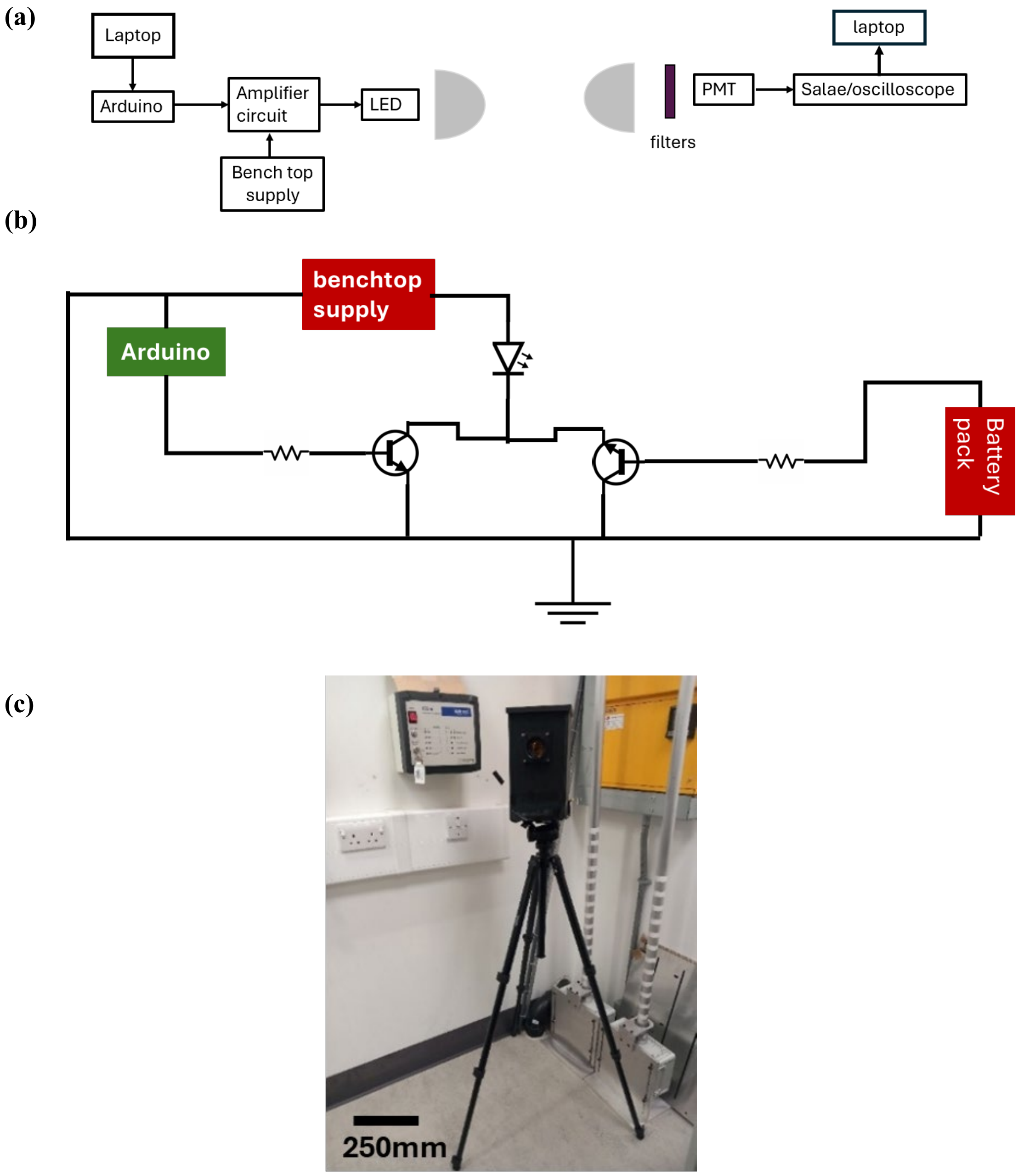

Figure 5-4 a) block diagram of the system, b) diagram of the transmitter circuitry and c) image of the tripod receiver system.

An Arduino Uno was chosen because it could be rapidly configured to transmit a square wave and a PRBS (pseudo-random bit stream). The system was designed so that when a “1” was transmitted, the LED was off, and when a 0 " was transmitted, the LED was on. An amplification circuit was implemented to increase the current delivered to the LED, addressing the Arduino Uno microcontroller’s inability to supply sufficient current at its standard 5 V output (a diagram is shown in Figure

5-4 (b)). A further essential aspect involved ensuring the LED was deactivated during low signal intervals, while maintaining a bias just below the activation threshold to facilitate rapid response when the signal increased.

Additionally, collimating the emission of the LED was critical to maintaining consistent beam divergence across varying distances. The DC input was supplied by a Yokogawa Source Measure Unit (SMU), which allowed measurement of current draw corresponding to the system voltage requirements, typically around 7–8 V, with currents ranging from 100 mA to 125 mA, producing an optical power of approximately 11 mW.

The receiver system employed a Hamamatsu H12386-101 photon counting PMT, chosen for its exceptional sensitivity, a feature previously discussed in Chapter 1. The device used has a sensitive area which detects the photon, and the signal is amplified, and a quenching circuit results in digital output voltage pulses (0 to 3.3 V) with a width of 10 ns, with each pulse corresponding to a single photon detection. The PMT has an active area diameter of 8 mm, a dark count rate of 50 s^{-1}. To focus incoming light onto the detector, an Edmund Optics 67218 (diameter 2 inches, f=75mm and NA=0.33) lens was mounted at the receiver. The output signal from the PMT was then recorded using a Saleae logic analyser, which enabled effective reading and analysis of the LED signals (a photograph of the enclosed receiver is shown in Figure 5-4 (c)).

Conventional avalanche photodiodes (APDs) used in earlier studies were found to be inadequate for this application due to their limited sensitivity, underscoring the importance of detectors capable of single-photon detection. However, while PMTs offer this level of sensitivity, they also present certain limitations, such as restricted bandwidth and an inherent dead time between pulses. These characteristics can result in inconsistent photon counts during periods of high signal intensity, making accurate SNR measurements more challenging. However, due to the high channel loss expected when operating a link in an NLOS configuration, it was not expected that the received signal would be sufficient to saturate the PMT.

Additionally, PMTs are highly sensitive to background light, which makes effective optical filtering essential, especially in environments with significant ambient illumination. To mitigate background noise, the entire receiver system was enclosed within a custom 3D-printed housing (see Figure 5-4), supplemented by a metal shield surrounding the detector. Despite these precautions, achieving complete light-tightness proved difficult due to the PMT's extreme sensitivity. Additionally, several filters were used concurrently to minimise background light reaching the PMT (FF01-280/20-25 280/20 nm BrightLine® single-band bandpass filter, Thorlabs FGUV5M-FGUV5 - Ø25 mm UG5 Coloured Glass Bandpass Filter, 240 - 395 nm, and Newport 10BPF10-280 280 nm bandpass). However, these filters also reduce the received signal strength, as they often have lower transmission than their visible counterparts. Another issue is that while the filters have a high optical density (OD) in the UVB, UVA and the visible spectrum, they are less effective at blocking light at longer wavelengths, especially in the red region of the visible spectrum and the infrared, which can introduce noise in the system, primarily when operating outside.

A compact USB-powered Saleae Logic 8 Pro logic analyser (digital sampling rate of 500 MS/s and analogue sampling rate of 50 MS/s) enabled testing across a broader range of locations. A fixed-voltage threshold of 1.65 V was applied to convert the PMT analogue pulsed signal into digital signals. These were subsequently recorded and processed offline using MATLAB, as will be discussed later in the chapter. Now that the system has been discussed, subsequent sections will present the testing of its performance across several NLOS configurations.

5. 3 Signal strength tests.

After completing the characterisation of the LED, the next step was to test the channel performance, and expected photon counts in a test range. It was chosen to conduct the work in a disused building on campus, which enabled longer-range tests than would be possible within a small laboratory. In the initial work, signal-strength tests were conducted across a number of parameters, including angle and distance. Subsequently, a MATLAB code employing a scanning window was used to analyse the data. The code traversed the signal, counting the number of photons within predefined time windows, enabling the determination of the total received photon count per bit period.

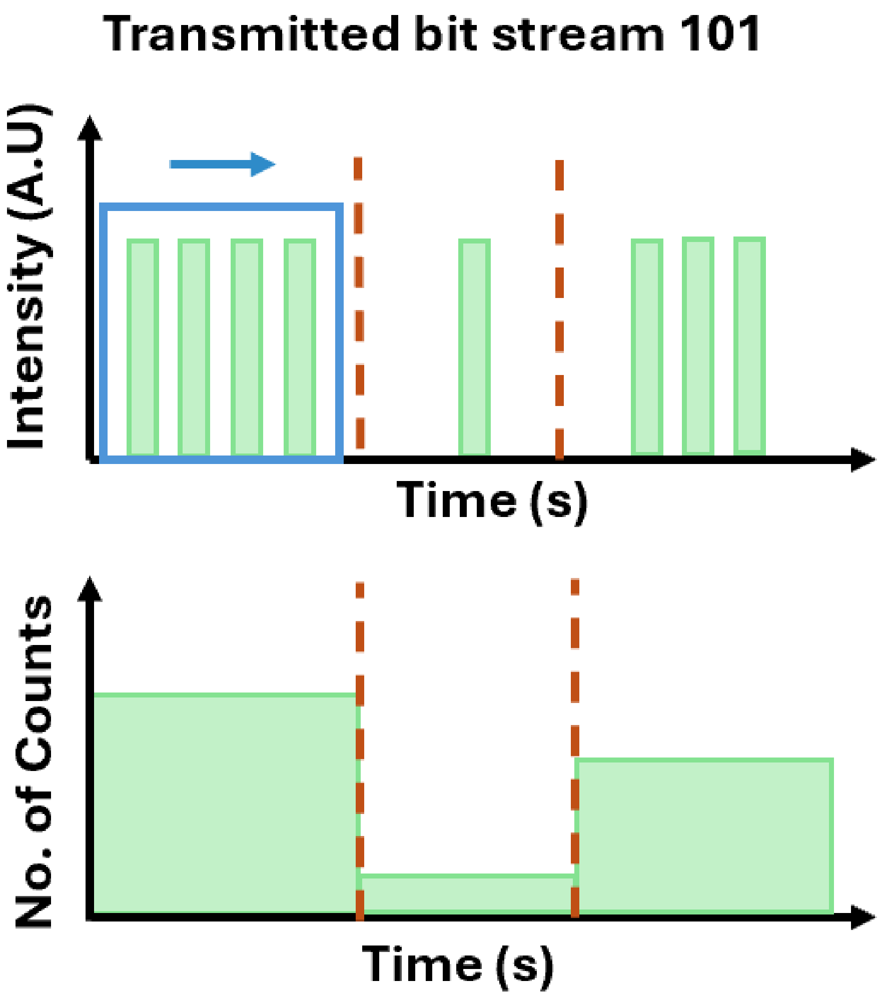

Figure 5-5 ***Diagram of the photon counting method used in the characterisation tests.***

5.3.1. Signal strength mapping vs angle.

A typical configuration seen in theoretical NLOS studies is based on a Rx (detector system FOV) and Tx (LED emission) being varied by angle, and modelling the signal (see the diagram and photograph of the setup shown in Figure 5-6) conducted at extended distances to examine parameters such as the separation from the transmitted beam and the elevation angle of both transmitter and receiver. The initial objective was to replicate previous measurements to assess the system's capability to scatter signals around an object. These experiments were performed in an open setting. The environment was specifically selected to reduce reflections from surrounding surfaces.

(a)

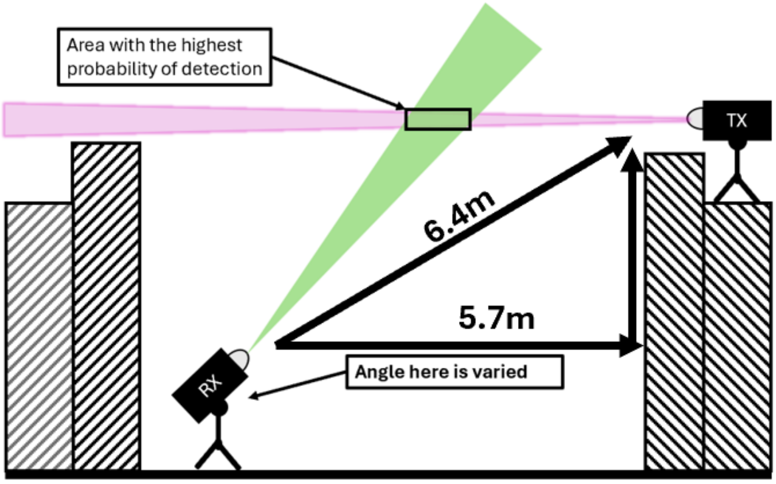

(b)

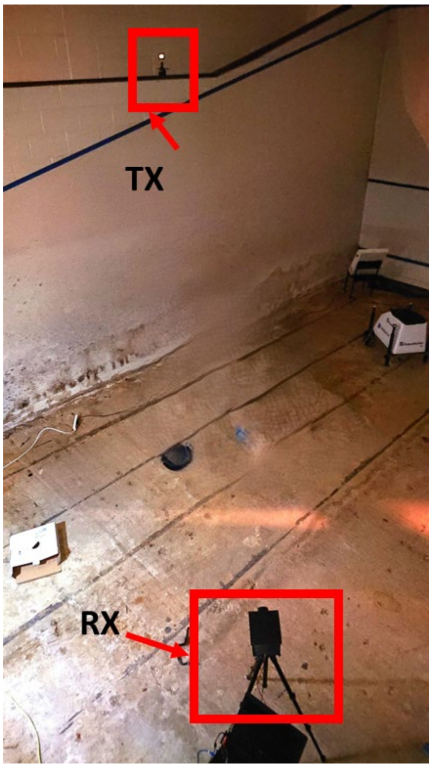

Figure 5-6schematic of how we tested the signal strength as a function of angle, and b) a photograph in the test area.

The system was tested in both pulsed mode and CW mode, which allowed for the testing of photon count rates and analysis for potential communications links, as illustrated in Figure 5-7. Optical transmitted powers of 11.8 mW, a drive current of 0.2 A, a duty cycle of 50%, pulse widths of 50ns, receiver FOV =105 mrad and transmitter angle of approximately 37.5 mrad, were used in this particular setup, as this was the maximum output of the driver system. The first test was to evaluate the CW performance of the system, and the results are shown in *Figure 5-7* (a) below:

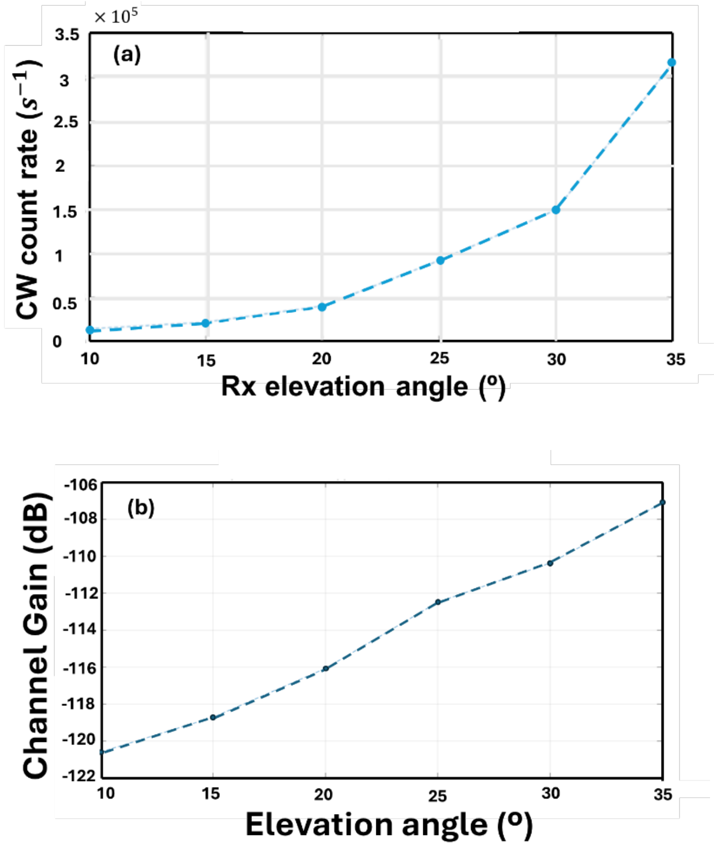

Figure 5-7 a) Summary of CW counts vs angle and b) estimated channel gain vs angle.

It is evident from the CW results (see Figure 5-7 (a)) that there is an increase in the number of counts per second as the angle increases, and this could be attributed to ballistic and scattered photons being detected directly from the transmitter. However, detecting LOS or diffuse NLOS signals is not the target of this demonstration, and as a result, it was decided not to use this configuration for the communications work; however, it should be noted that this could be a future avenue of work, analysing reduced-pointing and tracking line-of-sight communication systems. It is important to note that, because the PMT lacked AC coupling, the LED had to remain off when not transmitting data or representing a "0" bit. The next step, using the results from the CW tests, it was possible to determine the channel gain of the system using the equation below:

$$Channel\ Gain = 10\log_{10}\left(\frac{Received\ photons/second}{Transmitted\ photons/second}\right) \tag{5.1}$$

The results of this equation are shown in Figure 5-7 (b). The channel gain demonstrates that as the angle increases, the signal strength increases as expected due to ballistic photons inflating the photon counts. It should be noted that the measurements started at 10 degrees, as 5 degrees or less resulted in the system pointing parallel to the floor.

After testing the CW performance, the next stage was to test the pulsed performance of the system. In Figure 5-8 (a) it can be seen that at 10 degrees elevation angle, the number of photons per pulse is approximately 50, and as the angle increases to 35 degrees, it increases to 1500 received photons per pulse Figure 5-8 (b). The increasing signal with angle is as expected, as with the Rx pointing at the Tx, the probability for detecting ballistic photons increases.

(a)

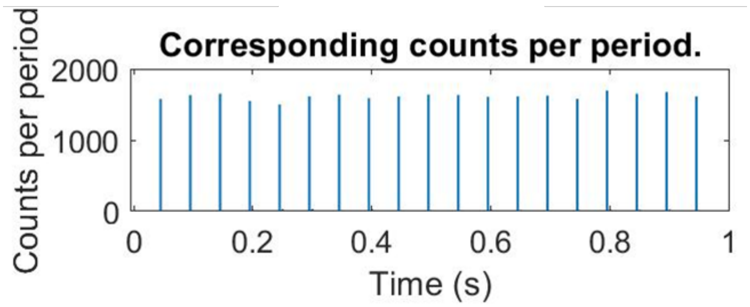

(b)

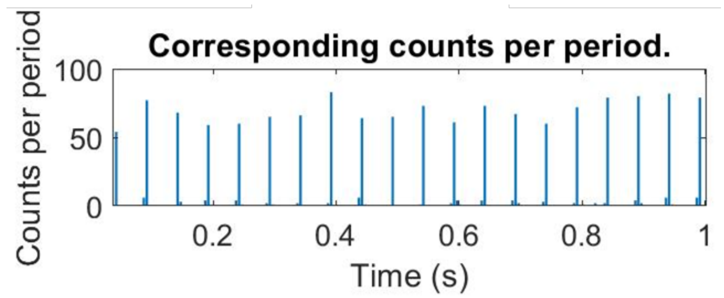

Figure 5-8 Pulse performance counts per period vs time at a) 10 degrees and b) 35 degrees.

Clear transmitted pulses were observable, although some noise and signal strength inconsistencies (stemming from variable scattering and the Poissonian statistics of light, where photons that were transmitted and detected are not easily predictable, and there is inherent randomness, which is obvious at lower photon counts) were present, resulting in photon packets with varying intensities. As a result of ballistic photons increasing the count rates, it was decided to test a second configuration, which would include shielding in order to prevent this issue.

5.3.2. Signal strength test vs distance.

The second test centred around a study of the system as a function of distance, with the transmitter located at the entrance of an enclosed space where the transmitter and receiver were perpendicular to one another (see Figure 5-9). Thick, absorbing glass panes, marked as black diagonal blocks in the diagram, were used to enclose the area and conceal the transmitter, thereby mitigating the risk of stray ballistic photons affecting the results, which, as described above, was a considerable problem in the previous setup.

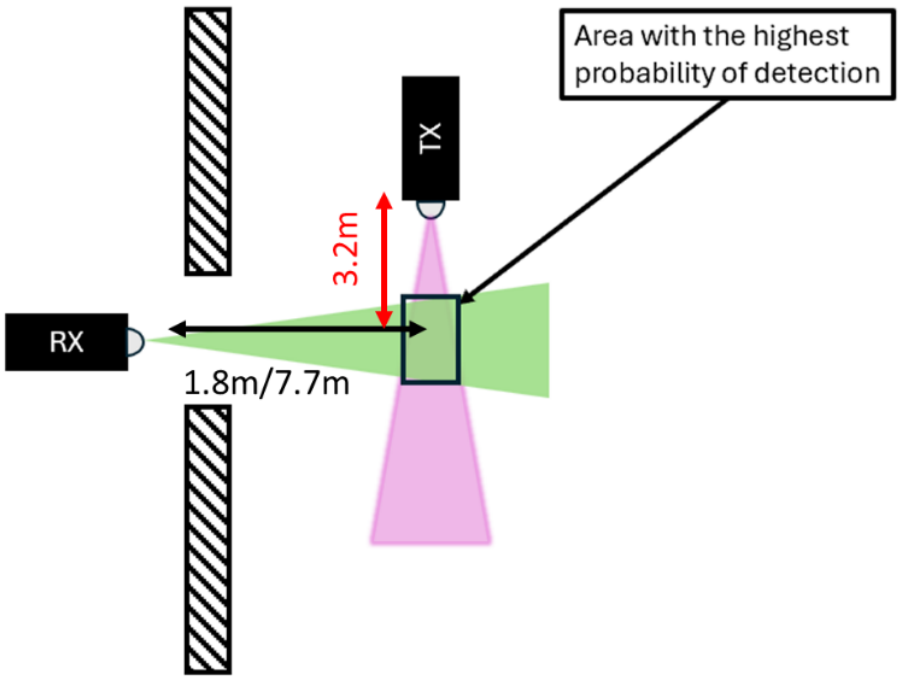

Figure 5-9 Top-down schematic view of NLOS experimental set-up for communications tests (the system height was 1m).

As in the angle tests shown in the previous section, CW and pulsed measurements were taken to evaluate photon counts at various distances and determine their suitability for communication. The photon counts shown in Figure 5-10 (a) were notably lower than those of the angled system discussed previously. However, this could be due to fewer ballistic photons being detected, which interfered with the results.

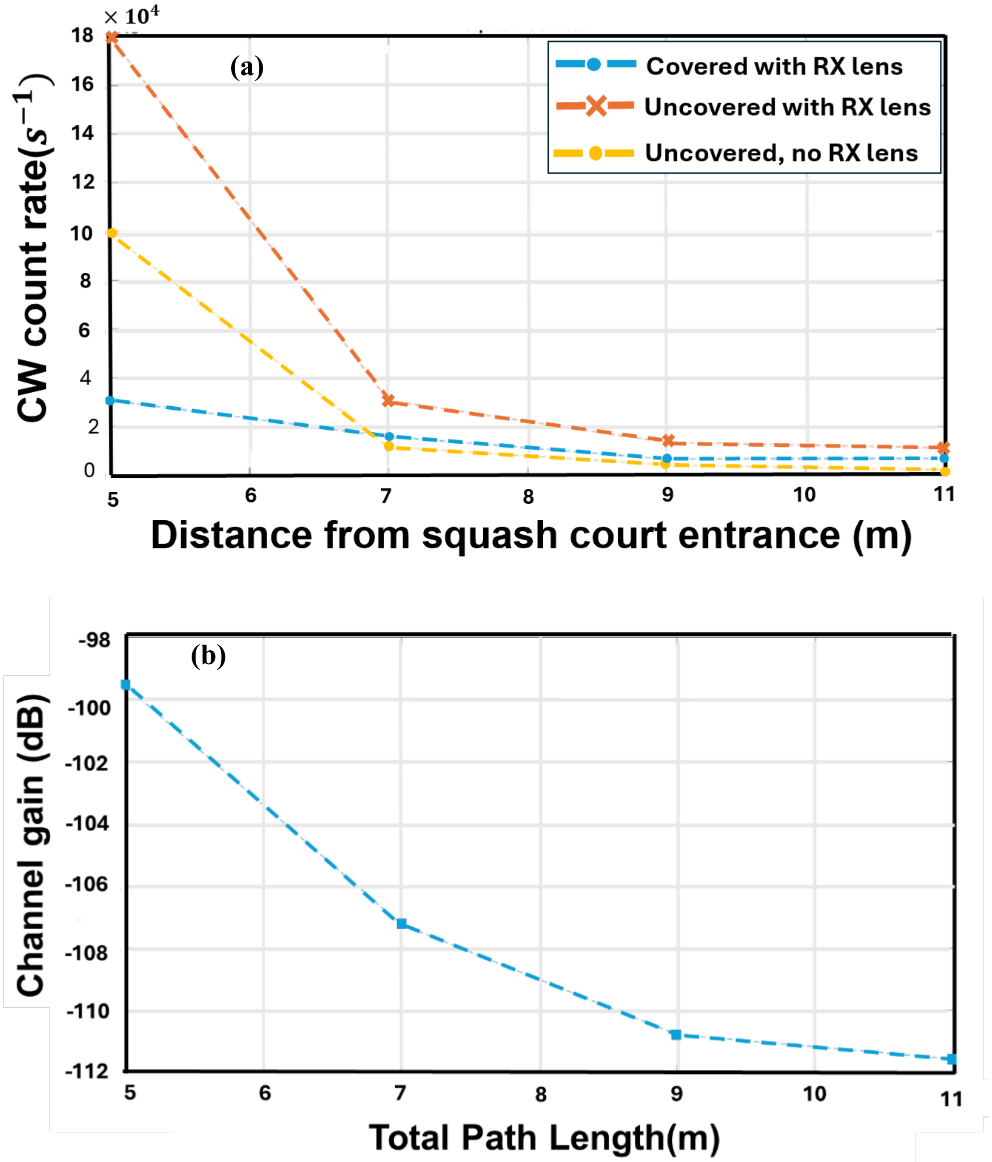

Figure 5-10 CW photon counts vs distances and b) total path length vs channel gain for the configuration shown in Figure 5-9

Maintaining a dark environment was essential to minimise noise with background counts being recorded as 50 $counts\ s^{-1}$. To ensure that only light emitted by the Tx unit was directed along the main NLOS path, the LED and optics were covered up, preventing stray light from escaping and being detected by the PMT via multipath reflections or other mechanisms (see Figure 5-10 (a)). Future work should prioritise developing methods to filter out ambient or reflected light completely, and creating a more robust enclosure for the transmitter is a possible route. Moreover, during this test and the previous test, the commercial LEDs introduced additional challenges due to their patterned outputs, leading to inconsistent intensities and greater divergence compared to the µLEDs discussed in earlier chapters. Signal quality was most influenced by the overlap of emission cones the wider the cone, the stronger the signal in theory, but an expanded field of view also led to increased noise, potentially compromising the communication channel. Further, the channel gain was also calculated and is shown in Figure 5-10 (b). The channel gain was notably affected by distance from the entrance of the enclosed area, corresponding to a decrease in the received photon counts.

Similar to the angled system, the next stage was to test the pulse performance to evaluate the possibility of using the system for communications tests.

(a)

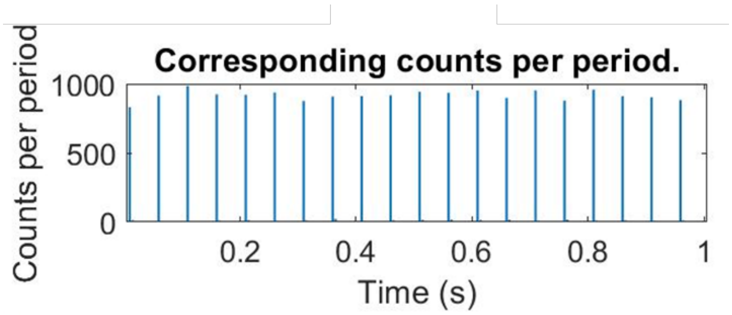

(b)

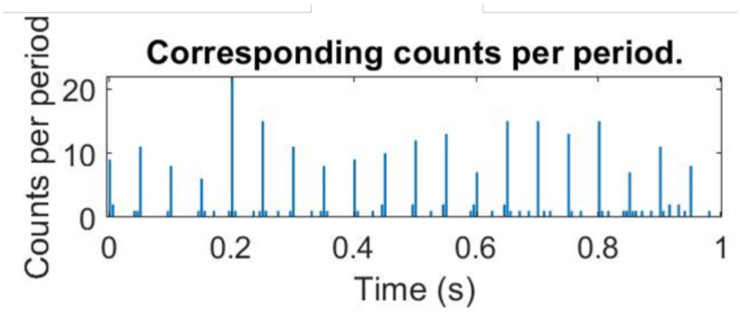

Figure 5-11 The pulse performance of the system at a) 5m and b) 11m.

The pulsed results shown above in Figure 5-11 corresponded with the CW results, and as distance increases, the number of photons per pulse decreases from approximately 750 counts per period to approximately 15 counts per period. It can be seen from Figure 5-11 (b) that, at 11m, fluctuations in photon counts at longer distances become more apparent when photon counts are low, due to the inherent randomness in the system. This can be ascribed to the increasing divergence of the Tx beam, and this results in a corresponding drop in the number of scattered photons that are present in the volume of the overlap between the Tx and Rx.

Similar to the CW tests, the number of photons decreases with distance. It was assumed, as stated in section 5.1, that approximately 0.2% of photons were scattered and using an average power of 11mW and a pulse width of 50ms, it was possible to calculate the ideal theoretical number of photons that were scattered:

$$Energy\ per\ pulse = P_{avg} \cdot t = 11 \times 10^{-3} \cdot 50 \times 10^{-3} = 5.5 \times 10^{-4} J \quad (5.2)$$

The next stage is to calculate the photon energy (using peak wavelength 275nm as λ)

$$Photon\ energy = \frac{hc}{\lambda} = \frac{6.626\times10^{-34}\cdot 2.998\times10^{8}}{275\times10^{-7}} = 7.22 \times 10^{-19} J \quad (5.3)$$

$$Photons\ per\ pulse = \frac{Energy\ per\ pulse}{Photon\ energy} = \frac{5.5\times10^{-4}}{7.22\times10^{-19}} = 7.6 \times 10^{14} \quad (5.4)$$

$$number\ of\ scatter\ photons = 2\% \cdot 7.6 \times 10^{14} = 1.5 \times 10^{12} \quad (5.5)$$

With approximately 1.5$\times 10^{12}$ photons being scattered, it may be expected that the counts seen in *Figure 5-13* would be higher; however, it should be stated that most of the scattering is forward scattered, i.e. most of those photons are not scattered in the direction of the receiver, and with a perpendicular system, the number of counts would be lower.

However, based on all the previous tests, it was decided that the 5m distance with this configuration would be the ideal system for testing an active communications link, as there is a significant number of scattered photons, and results suggest that the signal drops rapidly after 5m, and it would not be possible to create a communications system that could achieve any significant data rates.

5. 4 DUV NLOS Communications tests

After completing the signal tests, it was decided that the communications test should be conducted using the perpendicular configuration shown in Figure 5-12. This configuration was chosen because it can be considered an actual NLOS setup: only limited direct photons were detected, and most were scattered, as observed in the configuration of the experimental system. Based on the signal strength tests, it was decided to test the system at a path length of 5m.

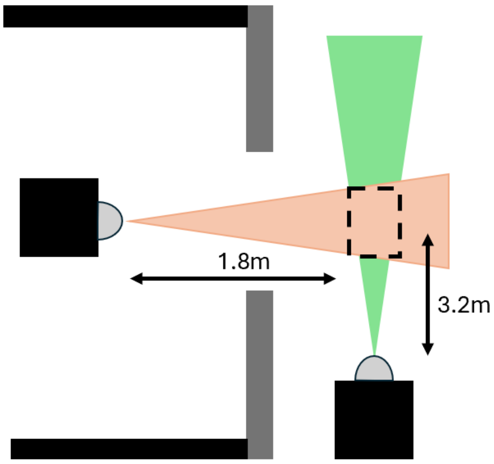

Figure 5-12 Schematic diagram of communication test configuration (5 m path length). The dashed box shows the overlap of the FOV and the transmission profile of the LED.

The channel conditions did not support the implementation of advanced modulation schemes, such as OFDM, as previously discussed in this thesis, due to the very low SNR. Therefore, an On-Off Keying (OOK) system was implemented due to the limited bandwidth of the detector, and this was discussed in Chapter 1. An Arduino Uno microcontroller board was utilised to allow for the setting of data rates and encoding of pseudo-random bit sequences. Once the signal was received, it was processed, and a threshold was used to determine if the signal was a "0" or a "1" (see an example given in Figure 5-13).

On-off keying is not considered ideal for communication systems, as it remains vulnerable to background interference. A major challenge encountered during testing was insufficient optical power, especially when compared to previous studies documented in the thesis. Significant losses occurred throughout the system, and the collimation allowed excessive beam divergence, making it difficult to capture even a small portion of the transmitted signal, as the receiver cones did not cover the entire transmitter cones. Consequently, further development should prioritise addressing power constraints as advanced encoding methods offer little benefit without adequate signal strength. Therefore, basic encoding approaches, such as on-off keying, are essential during the initial phases of research due to the low signal strength.

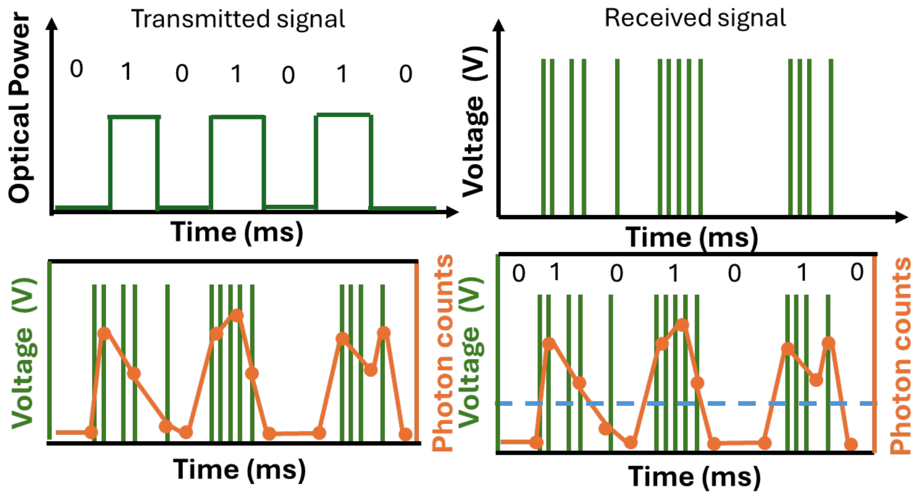

Figure 5-13 An example of On-Off Keying (where the blue dashed line is the threshold).

Due to the reliance on detecting weak signals in scattered light, non-line-of-sight (NLOS) experiments pose significant challenges for optical communications, and this results in NLOS systems relying on single-photon detectors. These initial experiments were conducted to understand the performance of the photomultiplier tube (PMT), as decoding is complicated by the fact that it does not generate a simple analogue signal but a series of digital pulses. Consequently, the signal must be sampled and converted into a quasi-analogue form using the number of photons, as seen in Figure 5-13. Thresholding is then applied: if the signal exceeds a predetermined threshold, a bit is recorded. The resulting bitstream is subsequently compared to the transmitted bits to determine the bit error rate (BER). Communication tests were conducted using the configuration stated above at 5m, as this demonstrated the strongest signal strength. The blue signal in Figure 5-14 (a) represents normalised digitised data subsequently converted to photon counts for 10kbps, enabling the calculation of photon counts per second. This normalisation permitted direct comparison between consecutive signals and the received signal, as shown in Figure 5-14 (b).

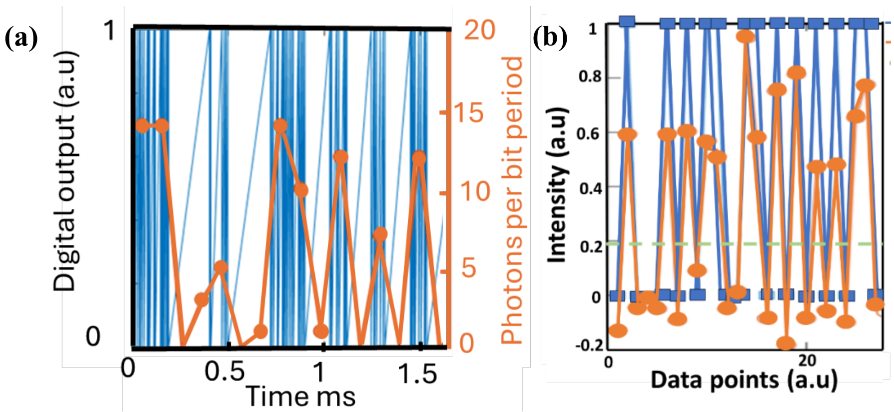

Figure 5-14 a) An example of photon pulses (blue lines) and photon counts per packet using a moving window average (10kb/s). b) transmitted signal vs recovered signal (10kb/s) (green line dashed line)

A thresholding process was then applied to the received signal, allowing the code to differentiate between high and low states for data decoding. Specifically, a bit was designated as "1" if the signal exceeded a defined voltage. This approach proved effective for low data rates with extended pulse widths and higher photon counts, facilitating rapid signal decoding. The result of this thresholding optimisation vs BER is shown in Figure 5-15. This shape of the graph was expected; if the threshold were set too low, noise would start to interfere, resulting in misidentification of ones and zeros. And if the threshold was set too high, there would also be misidentification of bits as the signal received is not always uniform, and fewer photons can arrive at a one than expected, and this lowers the photons per bin, which affects the normalisation process and results in lower intensities, and as a result, some ones may be mis recorded as 0 if the threshold is too high.

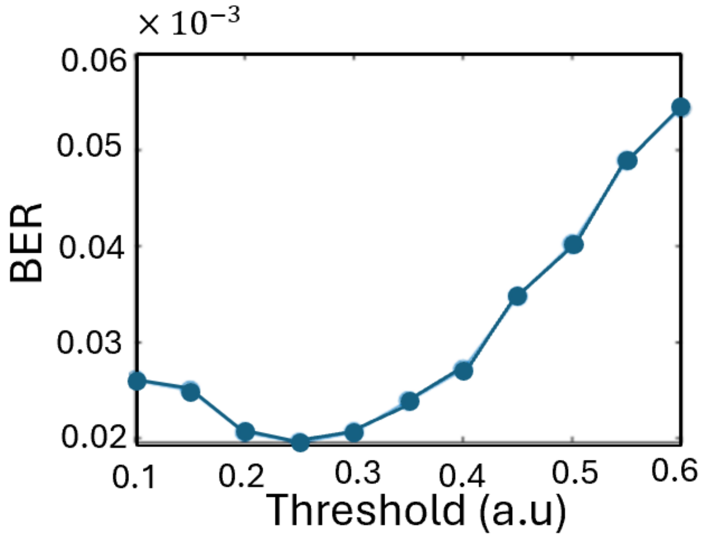

Figure 5-15 An example of BER vs threshold level as described in the text.

Comparisons between received and transmitted data enabled the determination of both the error rate and the actual channel data rate. As shown in Figure 5-16, error rates increase significantly at higher data rates compared to lower rates. This aligns with expectations given the reduced photon counts per pulse due to the decreasing pulse widths and, as a result, the randomness of the scattering impacts on the number of photons arriving, which can be seen in the pulse characterisation in the previous section, diminishing channel resilience and increasing susceptibility to noise and limitations in decoding methods. Notably, BERs for 5 kbps (200 µs) and 6.7 kbps (150 µs) are zero, as seen in Table 7.

Achieving a data rate of approximately 10 kbps demonstrated that it was possible to create a UV-C NLOS link using the setup shown in this chapter, providing an initial foundation for exploring non-line-of-sight (NLOS) communication systems. The inherent challenges of this configuration originate from its dependence on external factors, such as atmospheric scattering influenced by air quality and humidity. These environmental variables, being outside the scope of control, introduce additional complexities to the system.

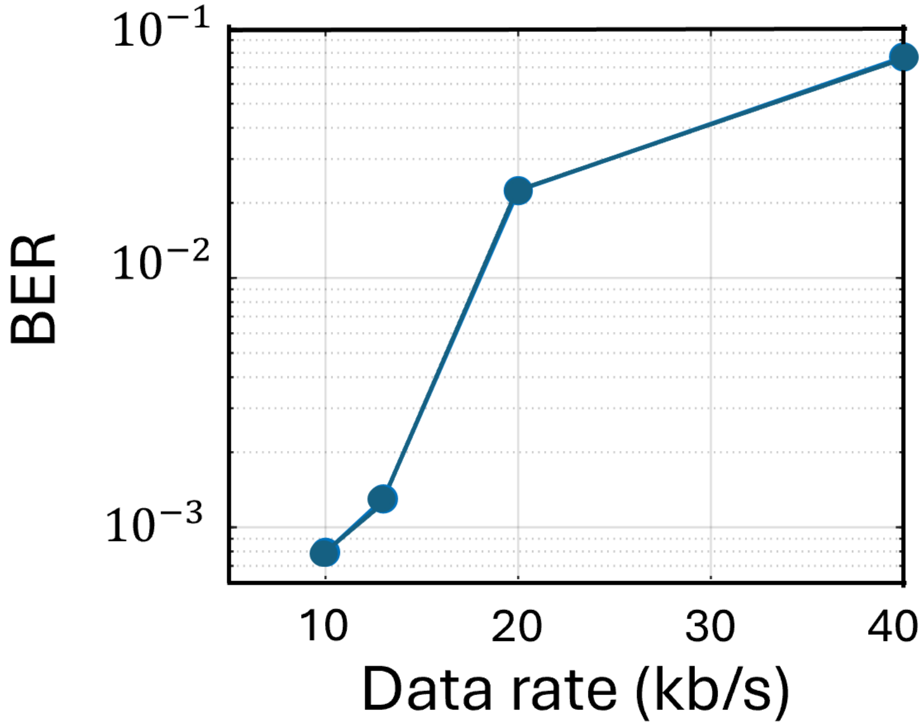

Figure 5-16 BER and data rate at 5m.

Future work would benefit from conducting experiments in a controlled environment, where parameters such as humidity, turbulence, temperature gradients, and fog could be systematically varied. Such efforts would contribute to the development of a more robust model for further research and system optimisation. It should be noted that in Table 8, a BER was stated as 0 for data rates less than 10 kbps, i.e. as an error rate of less than $7.94E^{-4}$. This is due to the system used to compare the transmitted signals and states that, in the future, a longer data length is needed to obtain a more accurate BER value. However, below 10m, it should be noted that the system is essentially below the FEC threshold, and the communication could be classed as error-free.

Data rate vs BER at 5m						
Data rate (kbps)	5	6.7	10	13	20	40
BER	0	0	7.94E-04	0.0013	0.0224	0.077

Table 8: Summary of data rate vs BER at 5m.

5. 5 Conclusions and future development

This chapter demonstrated a DUV NLOS link achieving data rates above 10 kbps at 5m. A crucial insight is that further development of DUV LED technology is needed to increase optical output power, a significant challenge relative to legacy flashlamp systems, even though current device bandwidths are already adequate for such applications. Optical collection also posed difficulties; future tests may benefit from employing a higher NA lens to enhance performance. While these results are valuable for academic research, their practical application could remain limited unless larger lenses can be accommodated, as might be feasible in vehicle-based implementations. The use of lens tubes helped reduce noise and simplify the setup, but may have constrained collection angles, an aspect that also warrants further investigation.

Environmental factors presented another limitation for communication via scattering, affecting system reliability under varying conditions, such as high humidity. To improve robustness, future designs could incorporate reflections from solid surfaces to offset channel instability. Operating in a dark room was necessary to minimise noise, highlighting the need for more noise-resistant communication channels suitable for outdoor use. The advancement of DUV communication technology is impeded by the limited sensitivity of current detectors and the inadequacy of UV filters, which are mainly designed for microscopy and perform poorly in strong background light. Some filters allow both infrared and ultraviolet emissions, increasing noise, while some coloured glass UV filters tend to fluoresce under sunlight, further degrading signal quality. Retrospectively, filter mounting could have been enhanced by angling the filters to reduce interference and optimising them for the LED’s spectral profile. These technical challenges underscore the need for continued research to improve the reliability and performance of DUV communication systems, particularly in NLOS configurations.

Additionally, progress in UV source development driven by demand in disinfection applications could benefit DUV NLOS communications, although these devices currently offer lower bandwidth than their μLED and mini-LED counterparts, and μLEDs still lack sufficient optical power. Incorporating an automated tripod system could provide a more stable platform for UV communications development, broadening its practical applications by allowing the operator to have more granular control over pitch and tilt to optimise signal strength. Future work will benefit from improved understanding of scattering mechanisms under various environmental conditions, including outdoor weather variations. Focusing on a diffuse line-of-sight could substantially increase data rates, and characterising the wavelength dependence within the NLOS channel would provide valuable insights into variations in signal strength.

Overall, the results of this work provide a solid foundation for refining NLOS experimental setups and advancing research.

Chapter 6 Conclusion

6. 1 Summary of the work

This work identified key behaviours of DUV µLEDs, including size-dependent output power and modulation bandwidth. We also explored DUV µLEDs' potential in optical communications. Chapter 3 demonstrated a 10 Gbps wavelength division multiplexing setup, and in Chapter 4, we demonstrated that it was possible to achieve UV-C data transmission at 1 Gbps over 100 meters. In Chapter 5, additional experiments showed an LED-based NLOS communication at kbps rates. The following subsections summarise the main results from each chapter.

6.1.1. The size-dependent characterisation

The study demonstrated that UV-C LED device size in the range 20-500 µm significantly influences both power output and efficiency, with larger devices emitting more power and achieving higher overall efficiency. Additionally, this work characterised electrical behaviour, including turn-on voltage, revealing a size dependence in which smaller devices exhibited higher turn-on voltages. Notably, advancements in fabrication over recent years have resulted in reduced turn-on voltages for the latest generation of small µLED devices. Building upon the findings presented in this thesis, these improvements enabled the first integration of a UVC µLED array with Complementary Metal-Oxide-Semiconductor (CMOS) electronics [86], a very significant enabling step for more sophisticated µLED architectures.

Despite these advances, smaller devices still displayed higher turn-on voltages than optimum compared to their more mature visible-spectrum counterparts, indicating an area requiring further investigation. However, ultimately the turn-on voltage is limited by the bandgap, so even for fully optimised epitaxy and contacting, a UV device will have a higher turn-on than a visible one. The results also indicated that deep ultraviolet (DUV) devices, akin to visible light devices, exhibited external quantum efficiency (EQE) that varied with device size; however, DUV devices consistently showed lower EQE values than visible devices, warranting additional research.

Furthermore, the data revealed that smaller devices achieved higher modulation bandwidths than larger mini-LEDs, attributable to reduced capacitance and higher current densities and the influence of surface recombination on carrier lifetime. Specifically, the 20 µm device achieved the highest bandwidth and surpassed its visible equivalents in this parameter, the highest -3 dB modulation bandwidth we optimised in these studies being ~1 GHz. These outcomes underscore the potential of deep UV devices for optical communications, particularly in enabling higher data transmission rates.

6.1.2. Optical Wireless Communications

The WDM work demonstrated that multiple UV LED wavelengths can be utilised in communication systems to increase overall data rates. A data rate of 10 Gbps was achieved, which is among the highest reported so far in the UV range. This result indicates the potential for further studies using multiple wavelengths in different setups. The configuration also enabled examination of AlInGaN device structures commonly used in UV LED research. One observation was that UVB devices exhibited lower performance than other devices, while UVA devices showed the highest optical output power, suggesting that improvements are needed for UVB materials. Additionally, the UVA device produced notable optical power but had a lower bandwidth than the UVC device, suggesting a relationship between bandwidth and optical power that warrants detailed investigation in the AlGaN LED structure.

In the long-distance experiment, a 1 Gbps data rate was achieved over 100 meters, demonstrating the use of UVC µLEDs for medium-range communications links. According to available information, we believe this to be the first optical wireless link exceeding 100 metres using a UV µLED and indeed µLED. The study also examined the impact of device-bias conditions on performance, an area that has not been explored in detail previously. The work emphasised optimisation, yielding higher data rates over longer distances than previously observed in the DUV range. The two-mirror setup also indicated that system alignment is feasible at distances of tens of meters, with minimal loss at shorter ranges, suggesting scalability based on application requirements.

The NLOS experiments showed it is possible to establish non-line-of-sight optical communications links exceeding 10 kbps using commercial UV-CLEDs. Measurements confirmed the ability to transmit pulses and receive signals around obstacles. These findings indicate that DUV can facilitate communication when direct line-of-sight between the transmitter and receiver is unavailable, which may support the future development of optical wireless communication systems.

Our headline, results compared with some benchmark data rates for other UV-C devices are shown below in Figure 6-1. Please note that a number of earlier results are also from our group.

6. 2 Future work and development

This final subsection outlines potential future work, both building on examples from this thesis and exploring new areas. Future research should prioritise long-range LOS and NLOS DUV communications above 100m and potentially beyond 1km, requiring improved beam steering and tracking systems. Other important directions include developing multiple-input multiple-output (MIMO) NLOS setups, building on work done in the visible and UV, integrating UV communications with platforms like CubeSats or terrestrial systems and combining DUV with other wavelengths, such as infrared [97,99,227–230]. Due to health and safety concerns, consumer applications for DUV sources need careful consideration, but there is progress in moving to shorter wavelengths (<250nm), where the hazard function decreases [231]. This is because such wavelengths are predominantly absorbed in the dead layer of the skin. Figure 2-8 indicates some of this progress. However, military use cases such as QKD satellite and secure communications networks are more probable. This thesis also indicates that μLEDs can be effectively used as a source in these developments.

6.2.1. Size-dependent behaviour

Previous research within the group has initiated studies on size-dependent communications, with recent efforts shifting towards examining current density. While the primary objective of this PhD was to enhance understanding of devices for communication purposes, internal quantum efficiencies were not investigated; this presents a potential direction for future research. Additionally, exploring advanced packaging and integration techniques to analyse other aspects of device performance, such as addressing impedance-mismatch issues, remains an area for further investigation by subsequent researchers, as our work focused primarily on applications. It is noteworthy that later devices in this thesis exhibited unusual device geometries compared to the circular devices used in earlier size-dependent experiments. Consequently, it would be valuable to investigate how device shape and active area of device parameters influence size dependence and overall performance [232]. Additionally, focusing on large arrays of devices could assist in a number of applications, both in communications and in areas like photolithography [159].

6.2.2. Optical Wireless Communications

From a scientific perspective, the WDM system offers significant potential for further development. Future work may include creating a second WDM setup, increasing the number of channels by utilising additional wavelengths, and incorporating a dichroic mirror system at the receiver to automatically separate channels, eliminating the need for manual filter selection. This advancement would support autonomous operation and facilitate integration into other systems. Subsequent steps could involve extending the operational distance of the setup to several hundred metres, with the eventual goal of reaching one km. Initial efforts might focus on achieving a 100-metre point-to-point test after removing the mirror system and with additional focus on more real-world challenges [233]. Should DUV lens technology improve, smaller lenses could be employed in more compact designs, enhancing suitability for commercial applications.

NLOS systems require substantial improvement across multiple aspects. Further research could explore performance in outdoor or artificially lit indoor environments, as well as practical applications such as beam steering and tracking. Another research direction involves developing a modelling system; however, time limitations precluded this in the current study. With additional resources, further expansion in this area could be possible.

The DUV LED field continues to grow due to attention from professionals in sanitation and infectious disease control, leading to new generations of devices with enhanced communication capabilities. Secure communications are another area of interest, though commercial applications may remain constrained by ongoing health and safety considerations.

6. 3 Overall summary

In summary, UV-C μLEDs for optical communications is a rapidly growing field, as evidenced by the increasing number of publications. If current trends persist, further advancements are expected, with both military and commercial applications driving progress in DUV communications and μLEDs, respectively. The future of DUV technology may be concentrated in military uses, in space or in areas with low human population density. At the same time, other wavelengths, such as infrared, may remain dominant for commercial communications. Prospects for DUV devices appear favourable as new applications emerge. For μLEDs, their role in communications is likely to involve device arrays and integration into outdoor settings and other optical systems.

References

1. L. Łukasiak and A. Jakubowski, "History of Semiconductors," JTIT **39**(1), 3–9 (2010).
2. D. Zhu and C. J. Humphreys, "Solid-State Lighting Based on Light Emitting Diode Technology," in *Optics in Our Time*, M. D. Al-Amri, M. M. El-Gomati, and M. Suhail Zubairy, eds. (Springer International Publishing, 2016), pp. 87–118.
3. M. A. Shampo, R. A. Kyle, and D. P. Steensma, "William Shockley and the Transistor," Mayo Clin. Proc. **87**(6), e43 (2012).
4. T. Jenkins, "Physics Education A brief history of. .. semiconductors," Phys. Educ. **5**(40), 430–439 (2005).
5. N. Zheludev, "The life and times of the LED - A 100-year history," Nat. Photonics **1**(4), 189–192 (2007).
6. T. Bhattarai, A. Ebong, and M. Y. A. Raja, "A Review of Light-Emitting Diodes and Ultraviolet Light-Emitting Diodes and Their Applications," Photonics **11**(6), (2024).
7. K. Song, M. Mohseni, and F. Taghipour, "Mechanisms investigation on bacterial inactivation through combinations of UV wavelengths," Water Res. **163**, 114875 (2019).
8. H. Singh, S. K. Bhardwaj, M. Khatri, K.-H. Kim, and N. Bhardwaj, "UVC radiation for food safety: An emerging technology for the microbial disinfection of food products," Chemical Engineering Journal **417**(1385–8947), 128084 (2020).
9. I. R. M. Barnard, E. Eadie, and K. Wood, "Further evidence that far-UVC for disinfection is unlikely to cause erythema or pre-mutagenic DNA lesions in skin," Photodermatol. Photoimmunol. Photomed. **6**(36), 476–477 (2020).
10. D. K. Kim and D. H. Kang, "Investigation of a new UVC LEDs array continuous type water disinfection system for inactivating Escherichia coli O157:H7 according to flow rate and electrical energy efficiency analysis," Food Control **119**(July 2020), 107470 (2021).
11. L. Shen, T. M. Griffith, P. O. Nyangaresi, Y. Qin, X. Pang, G. Chen, M. Li, Y. Lu, and B. Zhang, "Efficacy of UVC-LED in water disinfection on Bacillus species with consideration of antibiotic resistance issue," J. Hazard. Mater. **386**(October 2019), 121968 (2020).
12. C. Weisbuch, "Review—On The Search for Efficient Solid State Light Emitters: Past, Present, Future," ECS Journal of Solid State Science and Technology **9**(1), 016022 (2020).

13. H. Amano, R. Collazo, C. De Santi, S. Einfeldt, M. Funato, J. Glaab, S. Hagedorn, A. Hirano, H. Hirayama, R. Ishii, Y. Kashima, Y. Kawakami, R. Kirste, M. Kneissl, R. Martin, F. Mehnke, M. Meneghini, A. Ougazzaden, P. J. Parbrook, S. Rajan, P. Reddy, F. Römer, J. Ruschel, B. Sarkar, F. Scholz, L. J. Schowalter, P. Shields, Z. Sitar, L. Sulmoni, T. Wang, T. Wernicke, M. Weyers, B. Witzigmann, Y. R. Wu, T. Wunderer, and Y. Zhang, "The 2020 UV emitter roadmap," J. Phys. D Appl. Phys. **53**(50), (2020).

14. S. Morab, M. M. Sundaram, and A. Pivrikas, "Review on Charge Carrier Transport in Inorganic and Organic Semiconductors," Coatings **13**(9), (2023).

15. H. Jiang, "Nitride microLEDs and beyond - a decade progress review," Optics InfoBase Conference Papers **21**(May), 475–484 (2012).

16. H. Yu, Q. Chen, Z. Ren, M. Tian, S. Long, J. Dai, C. Chen, and H. Sun, "Enhanced Performance of an AlGaN-Based Deep-Ultraviolet LED Having Graded Quantum Well Structure," IEEE Photonics J. **11**(4), (2019).

17. L. X. Zhao, S. C. Zhu, C. H. Wu, C. Yang, Z. G. Yu, H. Yang, and L. Liu, "GaN-based LEDs for light communication," Sci. China Phys. Mech. Astron. **59**(10), (2016).

18. Y. Huang, Y. Li, and D. Xiang, "A Review of Recent Research Advances on AlGaN-Based Deep Ultraviolet Light-Emitting Diodes," IEEE Access **12**, 131188–131204 (2024).

19. Y. Nagasawa and A. Hirano, "A review of AlGaN-based deep-ultraviolet light-emitting diodes on sapphire," Applied Sciences (Switzerland) **8**(8), (2018).

20. S. Xiao, H. Yu, M. H. Memon, H. Jia, Y. Luo, R. Wang, and H. Sun, "In-Depth Investigation of Deep Ultraviolet MicroLED Geometry for Enhanced Performance," IEEE Electron Device Letters **44**(9), 1520–1523 (2023).

21. F. Kwong, L. Low, S. Oh, and Z. Hass, "Gallium Nitride: An Overview of Structural Defects," in *Optoelectronics - Materials and Techniques*, Padmanabhan Predeep, ed. (IntechOpen, 2011).

22. Steven P . DenBaars, "Introduction to Nitride Semiconductor Blue Lasers and Light Emitting Diodes," in *Introduction to Nitride Semiconductor Blue Lasers and Light Emitting Diodes*, S. Nakamura and S. F. Chichibu, eds. (CRC Press, 2000), pp. 1–25.

23. H. J. Shih, I. Lo, Y. C. Wang, C. Da Tsai, Y. C. Lin, Y. Y. Lu, and H. C. Huang, "Growth and Characterization of GaN/InxGa1−xN/InyAl1−yN Quantum Wells by Plasma-Assisted Molecular Beam Epitaxy," Crystals (Basel). **12**(3), (2022).

24. F. Schubert, *Light-Emitting Diodes*, 2nd Editio (Cambridge University Press, 2006).

25. X. Zhang, J. X. Shen, and C. G. Van de Walle, "First-Principles Simulation of Carrier Recombination Mechanisms in Halide Perovskites," Adv. Energy Mater. **10**(13), (2020).

26. Z. Chen, S. Yan, and C. Danesh, "MicroLED technologies and applications: Characteristics, fabrication, progress, and challenges," J. Phys. D Appl. Phys. **54**(12), (2021).

27. F. Nippert, M. Tollabi Mazraehno, M. J. Davies, M. P. Hoffmann, H. J. Lugauer, T. Kure, M. Kneissl, A. Hoffmann, and M. R. Wagner, "Auger recombination in AlGaN quantum wells for UV light-emitting diodes," Appl. Phys. Lett. **113**(7), (2018).

28. K. Ban, J. I. Yamamoto, K. Takeda, K. Ide, M. Iwaya, T. Takeuchi, S. Kamiyama, I. Akasaki, and H. Amano, "Internal quantum efficiency of whole-composition-range AlGaN multiquantum wells," Applied Physics Express **4**(5), 1–4 (2011).

29. D. A. B. Miller, D. S. Chemla, T. C. Damen, A. C. Gossard, W. Wiegmann, T. H. Wood, and C. A. Burrus, "Band-edge electroabsorption in quantum well structures: The quantum-confined stark effect," Phys. Rev. Lett. **53**(22), 2173–2176 (1984).

30. M. Hajdel, M. Chlipała, M. Siekacz, H. Turski, P. Wolny, K. Nowakowski-Szkudlarek, A. Feduniewicz-żmuda, C. Skierbiszewski, and G. Muziol, "Dependence of ingan quantum well thickness on the nature of optical transitions in leds," Materials **15**(1), (2022).

31. J. Yun, J. I. Shim, and H. Hirayama, "Analysis of efficiency droop in 280-nm AlGaN multiple-quantum-well light-emitting diodes based on carrier rate equation," Applied Physics Express **8**(2), 022104 (2015).

32. A. Pandey et al, "High-efficiency AlGaN / GaN / AlGaN tunnel junction ultraviolet light-emitting diodes," Photon. Res. **8**(3), 331–337 (2020).

33. S. Gamal, T. Ismail, and I. E. Talkhan, "Improving FWHM and extraction efficiency of RGB OLEDs with MQW structure," in *ICEEM 2021 - 2nd IEEE International Conference on Electronic Engineering* (Institute of Electrical and Electronics Engineers Inc., 2021), pp. 1–4.

34. J. Lang, F. Xu, J. Wang, L. Zhang, X. Fang, Z. Zhang, X. Guo, C. Ji, C. Ji, F. Tan, Y. Wu, X. Yang, X. Kang, Z. Qin, N. Tang, X. Wang, W. Ge, and B. Shen, "Progress in Performance of AlGaN-Based Ultraviolet Light Emitting Diodes," Adv. Electron. Mater. **11**(1), 2300840 (2024).

35. H. Hirayama, Y. Tsukada, T. Maeda, and N. Kamata, "Marked enhancement in the efficiency of deep-ultraviolet AlGaN light-emitting diodes by using a multiquantum-barrier electron blocking layer," Applied Physics Express **3**(3), (2010).

36. S. Chichibu, A. Abare, M. Mack, M. Minsky, T. Deguchi, D. Cohen, P. Kozodoy, S. Fleischer, S. Keller, J. Speck, J. Bowers, E. Hu, U. Mishra, L. Coldren, S. DenBaars, K. Wada, T. Sota, and S. Nakamura, "Optical properties of InGaN quantum wells," Materials Science and Engineering: B **59**(1), 298–306 (1999).

37. M. S. Shur and R. Gaska, "Deep-ultraviolet light-emitting diodes," IEEE Trans. Electron Devices **57**(1), 12–25 (2010).

38. J. Zhang, X. Hu, A. Lunev, J. Deng, Y. Bilenko, T. M. Katona, M. S. Shur, R. Gaska, and M. A. Khan, "AlGaN deep-ultraviolet light-emitting diodes,"

Japanese Journal of Applied Physics, Part 1: Regular Papers and Short Notes and Review Papers **44**(10), 7250–7253 (2005).

39. Z. Yuan, Y. Li, X. Lu, Z. Wang, P. Qiu, X. Cui, P. Tian, Q. Wang, and G. Zhang, "Investigation of Modulation Bandwidth of InGaN Green Micro-LEDs by Varying Quantum Barrier Thickness," IEEE Trans. Electron Devices **69**(8), 4298–4305 (2022).

40. T. Y. Lee, L. Y. Chen, Y. Y. Lo, S. S. Swayamprabha, A. Kumar, Y. M. Huang, S. C. Chen, H. W. Zan, F. C. Chen, R. H. Horng, and H. C. Kuo, "Technology and Applications of Micro-LEDs: Their Characteristics, Fabrication, Advancement, and Challenges," ACS Photonics **9**(9), 2905–2930 (2022).

41. K. Ding, V. Avrutin, N. Izyumskaya, Ü. Özgür, and H. Morkoç, "Micro-LEDs, a manufacturability perspective," Applied Sciences (Switzerland) **9**(6), (2019).

42. A. Paranjpe, J. Montgomery, S. M. Lee, and C. Morath, " 45-2: Invited Paper: Micro-LED Displays: Key Manufacturing Challenges and Solutions ," SID Symposium Digest of Technical Papers **49**(1), 597–600 (2018).

43. X. Li, L. Wu, Z. Liu, B. Hussain, W. C. Chong, K. M. Lau, and C. P. Yue, "Design and characterization of active matrix LED microdisplays with embedded visible light communication transmitter," Journal of Lightwave Technology **34**(14), 3449–3457 (2016).

44. H. Haas, C. Chen, and D. O. Brien, "Progress in Quantum Electronics A guide to wireless networking by light," Prog. Quantum Electron. **55**(June), 88–111 (2017).

45. N. Bani Hassan, F. Dehkhoda, E. Xie, J. Herrnsdorf, M. J. Strain, R. Henderson, and M. D. Dawson, "Ultrahigh frame rate digital light projector using chip-scale LED-on-CMOS technology," Photonics Res. **10**(10), 2434 (2022).

46. "https://news.samsung.com/us/samsung-the-wall-microled-146-inch-tv-ces2018/," https://news.samsung.com/us/samsung-the-wall-microled-146-inch-tv-ces2018/.

47. T. Lu, X. Lin, W. Guo, C. C. Tu, S. Liu, C. J. Lin, Z. Chen, H. C. Kuo, and T. Wu, "High-speed visible light communication based on micro-LED: A technology with wide applications in next generation communication," Opto-Electronic Science **1**(12), (2022).

48. J. J. D. McKendry, R. P. Green, A. E. Kelly, Z. Gong, B. Guilhabert, D. Massoubre, E. Gu, and M. D. Dawson, "High-speed visible light communications using individual pixels in a micro light-emitting diode array," IEEE Photonics Technology Letters **22**(18), 1346–1348 (2010).

49. H.-Y. Lan, I.-C. Tseng, Y.-H. Lin, G.-R. Lin, D.-W. Huang, and C.-H. Wu, "High-speed integrated micro-LED array for visible light communication," Opt. Lett. **45**(8), 2203 (2020).

50. Y. Liao, X. Shan, Z. Rao, G. Wang, R. Lin, X. Cui, K. Xu, and P. Tian, "Size-Dependent Characteristics of High-Bandwidth Photodetector Based on GaN

Micro-LEDs and LEDs for High-Speed Visible Light Communication," Journal of Lightwave Technology **42**(17), 5902–5909 (2024).

51. R. X. G. Ferreira, E. Xie, J. J. D. McKendry, S. Rajbhandari, H. Chun, G. Faulkner, S. Watson, D. C. O. Brien, and M. D. Dawson, "High Bandwidth GaN-Based Micro-LEDs for Multi-Gb / s Visible Light Communications," IEEE Photonics Technology Letters **28**(19), 2023–2026 (2016).

52. X. Sun, M. Kong, O. Alkhazragi, C. Shen, E. N. Ooi, X. Zhang, U. Buttner, T. K. Ng, and B. S. Ooi, "Non-line-of-sight methodology for high-speed wireless optical communication in highly turbid water," Opt. Commun. **461**(January), 125264 (2020).

53. S. Rajbhandari, H. Chun, G. Faulkner, K. Cameron, A. V. N. Jalajakumari, R. Henderson, D. Tsonev, M. Ijaz, Z. Chen, H. Haas, E. Xie, J. J. D. McKendry, J. Herrnsdorf, E. Gu, M. D. Dawson, and D. O'Brien, "High-Speed Integrated Visible Light Communication System: Device Constraints and Design Considerations," IEEE Journal on Selected Areas in Communications **33**(9), 1750–1757 (2015).

54. T. Kishi, H. Tanaka, Y. Umeda, and O. Takyu, "A high-speed LED driver that sweeps out the remaining carriers for visible light communications," Journal of Lightwave Technology **32**(2), 239–249 (2014).

55. E. Xie, C. Chen, C. Ouyang, J. Hill, J. J. D McKendry, Y. Zhang, E. Gu, J. Herrnsdorf, H. Haas, M. D. Dawson, E. Gu Enyuan Xie, and J. Her-rnsdorf, "GaN-Based Series Hybrid LED Array: A Dual-Function Light Source With Illumination and High-Speed Visible Light Communication Capabilities," JOURNAL OF LIGHTWAVE TECHNOLOGY **42**(1), (2024).

56. R. Floyd, M. Gaevski, K. Hussain, A. Mamun, M. V. S. Chandrashekhar, G. Simin, and A. Khan, "Enhanced light extraction efficiency of micropixel geometry AlGaN DUV light-emitting diodes," Applied Physics Express **14**, (2021).

57. N. Trivellin, D. Monti, F. Piva, M. Buffolo, C. De Santi, E. Zanoni, G. Meneghesso, and M. Meneghini, "Degradation processes of 280 nm high power DUV LEDs : impact on parasitic luminescence," Jpn. J. Appl. Phys. **58**, SCCC19 (2019).

58. M. E. Rudinsky and S. Y. Karpov, "Radiative and Auger Recombination Constants and Internal Quantum Efficiency of (0001) AlGaN Deep-UV Light-Emitting Diode Structures," Physica Status Solidi (A) Applications and Materials Science **1900878**(0001), 1–6 (2019).

59. M. Kneissl, T. Y. Seong, J. Han, and H. Amano, "The emergence and prospects of deep-ultraviolet light-emitting diode technologies," Nat. Photonics **13**(4), 233–244 (2019).

60. P. Tian, X. Shan, S. Zhu, E. Xie, J. J. D. McKendry, E. Gu, and M. D. Dawson, "AlGaN Ultraviolet Micro-LEDs," IEEE J. Quantum Electron. **58**(4), (2022).

61. E. Margariti, G. Quinn, D. Jevtics, B. Guilhabert, M. D. Dawson, and M. J. Strain, "Continuous roller transfer-printing and automated metrology of

>75,000 micro-LED pixels in a single shot," Opt. Mater. Express **13**(8), 2236 (2023).

62. Z. Wang, S. Zhu, X. Shan, Z. Yuan, Z. Qian, X. Lu, Y. Fu, K. Tu, H. Guan, X. Cui, and P. Tian, "Red, green and blue InGaN micro-LEDs for display application: temperature and current density effects," Opt. Express **30**(20), 36403 (2022).

63. M. Z. Chowdhury, M. Shahjalal, M. K. Hasan, and Y. M. Jang, "The role of optical wireless communication technologies in 5G/6G and IoT solutions: Prospects, directions, and challenges," Applied Sciences (Switzerland) **9**(20), (2019).

64. G. Bucci, F. Ciancetta, E. Fiorucci, A. Fioravanti, A. Prudenzi, and S. Mari, "An IoT condition monitoring system for resilience based on spectral analysis of vibration," in *2020 IEEE International Workshop on Metrology for Industry 4.0 and IoT, MetroInd 4.0 and IoT 2020 - Proceedings* (Institute of Electrical and Electronics Engineers Inc., 2020), pp. 38–43.

65. S. Rajbhandari, J. J. D. McKendry, J. Herrnsdorf, H. Chun, G. Faulkner, H. Haas, I. M. Watson, D. O'Brien, and M. D. Dawson, "A review of gallium nitride LEDs for multi-gigabit-per-second visible light data communications," Semicond. Sci. Technol. **32**(2), (2017).

66. H. Haas, "LiFi is a paradigm-shifting 5G technology," Reviews in Physics **3**(October 2017), 26–31 (2018).

67. G. B. Nair and S. J. Dhoble, "Digital communications and display devices," in *The Fundamentals and Applications of Light-Emitting Diodes* (Woodhead Publishing, 2021), pp. 177–200.

68. M. Attaran, "The impact of 5G on the evolution of intelligent automation and industry digitization," J. Ambient Intell. Humaniz. Comput. **14**(5), 5977–5993 (2023).

69. A. Krishnamoorthy, H. Safi, O. Younus, H. Kazemi, I. N. O. Osahon, M. Liu, Y. Liu, S. Babadi, R. Ahmad, A. Ihsan, B. Majlesein, Y. Huang, J. Herrnsdorf, S. Rajbhandari, J. J. D. McKendry, I. Tavakkolnia, H. Caglayan, H. Helmers, G. Turnbull, I. D. W. Samuel, M. D. Dawson, R. Schober, and H. Haas, "Optical Wireless Communications: Enabling the Next-Generation Network of Networks," IEEE Vehicular Technology Magazine **20**(2), 20–39 (2025).

70. H. Kaushal and G. Kaddoum, "Optical Communication in Space: Challenges and Mitigation Techniques," IEEE Communications Surveys and Tutorials **19**(1), 57–96 (2017).

71. C. Weisbuch, "Review—On The Search for Efficient Solid State Light Emitters: Past, Present, Future," ECS Journal of Solid State Science and Technology **9**(1), 016022 (2020).

72. M. R. Krames, O. B. Shchekin, R. Mueller-Mach, G. O. Mueller, L. Zhou, G. Harbers, and M. G. Craford, "Status and future of high-power light-emitting diodes for solid-state lighting," IEEE/OSA Journal of Display Technology **3**(2), 160–175 (2007).

73. J. Huang, G. Wang, H. Xu, F. Xu, T. Zhi, W. Chen, Y. Sang, D. Zhang, J. Yu, H. He, K. Xu, P. Tian, T. Tao, B. Liu, and R. Zhang, "GaN-Based Freestanding Micro-LEDs With GHz Bandwidth and Low Efficiency Droop for Visible Light Communication," IEEE Trans. Electron Devices (2024).

74. H. Haas, "LiFi is a paradigm-shifting 5G technology," Reviews in Physics **3**(October 2017), 26–31 (2018).

75. V. Kumar, D. Patel, and U. D. Dalal, "A 100Mbps Visible Light Communication System using Optical Wireless Channel for Indoor Application Based on Composite White Light Generated using RGB LEDs," Procedia - Procedia Computer Science **93**(September), 655–661 (2016).

76. X. Zhou, P. Tian, C. Sher, J. Wu, H. Liu, R. Liu, and H. Kuo, "Progress in Quantum Electronics Growth , transfer printing and colour conversion techniques towards full-colour micro-LED display," Prog. Quantum Electron. **71**(April), 100263 (2020).

77. R. Yuan and J. Ma, "Review of ultraviolet non-line-of-sight communication," China Communications **13**(6), 63–75 (2016).

78. R. J. Drost and B. M. Sadler, "Survey of ultraviolet non-line-of-sight communications," Semicond. Sci. Technol. **29**(8), (2014).

79. Z. Xu and B. M. Sadler, "Ultraviolet Communications: Potential and State-of-the-Art," Topics in Optical Communications **46**(5), 67–73 (2008).

80. H. Zhang, H. Yin, H. Jia, J. Yang, and S. Chang, "Study of effects of obstacle on non-line-of-sight ultraviolet communication links," Opt. Express **19**(22), 21216 (2011).

81. N. Kalikulov, R. C. Kizilirmak, and M. Uysal, "Unmanned-aerial-vehicle-assisted cooperative communications for visible light communications-based vehicular networks," Optical Engineering **58**(08), 1 (2019).

82. M. Uysal, *Optical Wireless Communications* (2016).

83. Z. Ghassemlooy, W. O. Popoola, and S. Rajbhandari, *Optical Wireless Communications -System and Channel Modelling with MATLAB*, 1st Editio (CRC Press, 2013).

84. R. Yuan, S. Wang, G. Liu, and M. Peng, "Non-Line-of-Sight Ultraviolet Positioning Using Linearly-Arrayed Photon-Counting Receivers," IEEE Journal on Selected Areas in Communications **42**(9), 2535–2549 (2024).

85. M. Wang, T. Cao, S. Chen, C. Pan, and J. Song, "A 1 km Line-of-Sight Ultraviolet Communication System with a Data Rate of 26.6kbps," in *Proceedings of the 2023 International Conference on Electrical Engineering and Photonics, EExPolytech 2023* (Institute of Electrical and Electronics Engineers Inc., 2023), pp. 394–397.

86. Z. Xu, G. Chen, F. Abou-Galala, and M. Leonardi, "Experimental performance evaluation of non-line-of-sight ultraviolet communication systems," in *Free-Space Laser Communications VII* (SPIE, 2007), **6709**, p. 67090Y.

87. H. Yin, S. Chang, H. Jia, J. Yang, and J. Yang, "Non-line-of-sight multiscatter propagation model," Journal of the Optical Society of America A **26**(11), 2466 (2009).

88. B. Castellani, E. Morini, M. Filipponi, A. Nicolini, M. Palombo, F. Cotana, and F. Rossi, "Comparative analysis of monitoring devices for particulate content in exhaust gases," Sustainability (Switzerland) **6**(7), 4287–4307 (2014).

89. L. Elterman, "Rayleigh and Extinction Coefficients to 50 km for the Region 027 μ to 055 μ," Appl. Opt. **3**(10), 1139 (1964).

90. C. Mätzler, "MATLAB Functions for Mie Scattering and Absorption," IAP Res Rep **2002–08**(July 2002), 1139–1151 (2002).

91. H. Du, "Mie-scattering calculation," Appl. Opt. **43**(9), 1951–1956 (2004).

92. C. Tomasi, V. Vitale, B. Petkov, A. Lupi, and A. Cacciari, "Improved algorithm for calculations of Rayleigh-scattering optical depth in standard atmospheres," Appl. Opt. **44**(16), 3320–3341 (2005).

93. Lord Rayleigh, "XXXIV. On the transmission of light through an atmosphere containing small particles in suspension, and on the origin of the blue of the sky," The London, Edinburgh, and Dublin Philosophical Magazine and Journal of Science **47**(287), 375–384 (1899).

94. J. Vitásek, J. Látal, S. Hejduk, J. Bocheza, P. Koudelka, J. Šiškapa, P. Siska, and V. Vašinek, "Atmospheric turbulences in Free Space Optics channel," 2011 34th International Conference on Telecommunications and Signal Processing, TSP 2011 - Proceedings (August), 104–107 (2011).

95. D. De Leonardis, S. Mori, S. Di Bartolo, and F.-S. Marzano, "Atmospheric scattering and turbulence modeling for ultraviolet wavelength applications," Bulletin of Atmospheric Science and Technology **1**(2), 205–229 (2020).

96. S. Arya and Y. H. Chung, "Spectrum sensing for free space optical communications in strong atmospheric turbulence channel," Opt. Commun. **445**(April), 24–28 (2019).

97. D. Chen, G. Huang, G. Liu, and Y. Lei, "Performance of adaptive subcarrier modulated MIMO wireless optical communications in Malaga turbulence," Opt. Commun. **435**(August 2018), 265–270 (2019).

98. N. Chandrasekaran, S. Member, J. H. Shapiro, and L. Fellow, "Through Atmospheric Turbulence – Part I : Channel Model and Propagation Statistics," **32**(6), 1075–1087 (2014).

99. M. H. Ardakani, A. R. Heidarpour, and M. Uysal, "Performance analysis of MIMO NLOS UV communications over atmospheric turbulence channels," 2016 IEEE Wireless Communications and Networking Conference Workshops, WCNCW 2016 (Owc), 1–5 (2016).

100. C. Xu, H. Zhang, and J. Cheng, "Effects of haze particles and fog droplets on NLOS ultraviolet communication channels," Opt. Express **23**(18), 23259 (2015).

101. "Solar irradiance spectrum above atmosphere and at surface," By Robert A. Rohde - This image has been extracted from another file, CC BY-SA 3.0, https://commons.wikimedia.org/w/index.php?curid=24648395 (n.d.).

102. X. He, E. Xie, M. S. Islim, A. A. Purwita, J. J. D. McKendry, E. Gu, H. Haas, and M. D. Dawson, "1 Gbps free-space deep-ultraviolet communications based on III-nitride micro-LEDs emitting at 262 nm," Photonics Res. **7**(7), B41 (2019).

103. P. Tian, X. Shan, S. Zhu, E. Xie, J. J. D. McKendry, E. Gu, and M. D. Dawson, "AlGaN Ultraviolet Micro-LEDs," IEEE J. Quantum Electron. **58**(4), (2022).

104. Harvey G.L, "A survey of ultraviolet communication systems," Naval Research Laboratory Technical Report, Washington D.C. (1964).

105. H. Kurosawa, S. Tsuzuki, M. Taniguchi, and S. I. Inoue, "Solar-Blind Optical Wireless Communications Over 80 Meters Using a 265-nm High-Power Single-Chip DUV-LED Over 500 mW in Sunlight," IEEE Photonics J. **15**(3), (2023).

106. Y. Kang, J. Zhao, J. Wu, L. Zhang, J. Zhao, Y. Zhang, Y. Zhao, and X. Wang, "Superior Deep-Ultraviolet Source Pumped by an Electron Beam for NLOS Communication," IEEE Trans. Electron Devices **67**(8), 3391–3394 (2020).

107. J. Tang, Y. Ding, T. Lin, L. Sun, Y. Pan, C. Gong, and Z. Xu, "Ultraviolet communication with a large scattering angle via artificial agglomerate fog," Opt. Express **31**(14), 23149 (2023).

108. L. Guo, Y. Guo, J. Wang, and T. Wei, "Ultraviolet communication technique and its application," Journal of Semiconductors **42**(8), (2021).

109. X. Li, X. Xue, C. Zhou, J. Ma, and P. Su, "A Review of UV Communications for UAVs," IEEE Open Journal of the Communications Society **5**, 6495–6534 (2024).

110. M. V. Tarasenkov, E. S. Poznakharev, and A. V. Fedosov, "Non-Line-of-Sight Atmospheric Optical Communication in the Visible Wavelength Range between UAV and the Ground Surface," Atmosphere (Basel). **15**(1), (2024).

111. J. Ma, G. Lu, L. Tan, S. Yu, Y. Fu, F. Li, and M. Carlo, "Satellite platform vibration influence on acquisition system for intersatellite optical communications," Opt. Laser Technol. **138**(December 2020), 106874 (2021).

112. T. Inazu, S. Fukahori, C. Pernot, M. H. Kim, T. Fujita, Y. Nagasawa, A. Hirano, M. Ippommatsu, M. Iwaya, T. Takeuchi, S. Kamiyama, M. Yamaguchi, Y. Honda, H. Amano, and I. Akasaki, "Improvement of light extraction efficiency for AlGaN-based deep ultraviolet light-emitting diodes," Jpn. J. Appl. Phys. **50**(12), (2011).

113. P. U. Alves, J. Hill, E. Xie, E. G. Durmusoglu, M. Sharma, H. V. Demir, J. J. D. McKendry, M. D. Dawson, and N. Laurand, "Deep UV LED-pumped Quantum Well Supraparticles for Visible Light Communication," in *2024 IEEE Photonics Conference, IPC 2024 - Proceedings* (Institute of Electrical and Electronics Engineers Inc., 2024).

114. H. Elgala, R. Mesleh, H. Haas, and B. Pricope, "OFDM Visible Light Wireless Communication Based on White LEDs," in *2007 IEEE 65th Vehicular Technology Conference - VTC2007-Spring* (IEEE, 2007), pp. 2185–2189.

115. Z. Lu, P. Tian, H. Chen, I. Baranowski, H. Fu, X. Huang, J. Montes, Y. Fan, H. Wang, X. Liu, R. Liu, and Y. Zhao, "Active tracking system for visible light communication using a GaN-based micro-LED and NRZ-OOK," Opt. Express **25**(15), 17971 (2017).

116. S. Dimitrov and H. Haas, "Digital modulation schemes," in *Principles of LED Light Communications* (Cambridge University Press, 2015), pp. 72–94.

117. S. Hranilovic, *Wireless Optical Communication Systems*, 1st Editio (Springer, 2005).

118. P. A. Hoeher, "Modulation Schemes for Optical Wireless Communications," in *Visible Light Communications* (Hanser, 2019), pp. 65–132.

119. H. Haas and M. Sufyan Islim, "Modulation Techniques for Li-Fi," ZTE Communications **14**(S0), 32–36 (2016).

120. A. Assimi, N. Zarka, and A. Khalil, *Adaptive Modulation and Coding Simulations for Mobile Communication Networks* (2016).

121. Z. Geng, X. Tang, and Y. Dong, "Layered Optical OFDM Schemes for IM/DD OWC Systems," in *IEEE Wireless Communications and Networking Conference, WCNC* (Institute of Electrical and Electronics Engineers Inc., 2024).

122. X. Han, W. Wang, P. Li, G. Li, W. Nie, Z. Xie, S. Jia, C. Chang, P. Liao, and X. Xie, "Demonstration of anti-diffracting optical pin-like beam enabled 5Gbit/s OFDM underwater wireless optical communication system," Opt. Commun. **579**, (2025).

123. Z. Yu, R. J. Baxley, and G. T. Zhou, "Peak-to-average power ratio and illumination-to-communication efficiency considerations in visible light OFDM systems," ICASSP, IEEE International Conference on Acoustics, Speech and Signal Processing - Proceedings (July), 5397–5401 (2013).

124. "https://helpfiles.keysight.com/csg/89600B/Webhelp/Subsystems/wlan-ofdm/content/ofdm_basicprinciplesoverview.htm," .

125. S. Dimitrov and H. Haas, "Information rate of OFDM-based optical wireless communication systems with nonlinear distortion," Journal of Lightwave Technology **31**(6), 918–929 (2013).

126. M. Li, Y. Rui, and Z. Bu, "Fourier Transform Based Transmission Systems for Broadband Wireless Communications," in *Fourier Transforms - New Analytical Approaches and FTIR Strategies* (InTech, 2011).

127. S. Dimitrov and H. Haas, "Optical wireless communication," in *Principles of LED Light Communications* (Cambridge University Press, 2015), pp. 12–56.

128. J. M. Kahn and J. R. Barry, "Wireless Infrared Communications," Proceedings of the IEEE **85**(2), 265–298 (1997).

129. D. Tsonev, S. Sinanovic, and H. Haas, "Complete modeling of nonlinear distortion in OFDM-based optical wireless communication," Journal of Lightwave Technology **31**(18), 3064–3076 (2013).

130. D. Tsonev, H. Chun, S. Rajbhandari, J. J. D. McKendry, S. Videv, E. Gu, M. Haji, S. Watson, A. E. Kelly, G. Faulkner, M. D. Dawson, H. Haas, and D. O. Brien, "A 3-Gb / s Single-LED OFDM-Based Wireless VLC Link Using a Gallium Nitride μ LED," IEEE Photonics Technology Letters **26**(7), 637–640 (2014).

131. W. Yao, Y. Shi, L. He, and S. Pamarti, "Worst-case estimation for data-dependent timing jitter and amplitude noise in high-speed differential link," in *IEEE Transactions on Very Large Scale Integration (VLSI) Systems* (2012), **20**(1), pp. 89–97.

132. D. Tse and P. Viswanath, "Capacity of wireless channels," in *Fundamentals of Wireless Communication* (Cambridge University Press, 2012), pp. 166–227.

133. "https://support.huawei.com/enterprise/en/doc/EDOC1100460590/725a8832/overview-of-fec," .

134. K. A. Lozovoy, R. M. H. Douhan, V. V. Dirko, H. Deeb, K. I. Khomyakova, O. I. Kukenov, A. S. Sokolov, N. Y. Akimenko, and A. P. Kokhanenko, "Silicon-Based Avalanche Photodiodes: Advancements and Applications in Medical Imaging," Nanomaterials **13**(23), (2023).

135. O. Skorka and D. Joseph, "CMOS digital pixel sensors: technology and applications," in *Nanosensors, Biosensors, and Info-Tech Sensors and Systems 2014* (SPIE, 2014), **9060**, p. 90600G.

136. F. Nolet, S. Parent, N. Roy, M. O. Mercier, S. A. Charlebois, R. Fontaine, and J. F. Pratte, "Quenching circuit and spad integrated in cmos 65 nm with 7.8 ps fwhm single photon timing resolution," Instruments **2**(4), (2018).

137. X. Wang, L. Mao, F. Qin, X. Lu, C. Huang, X. Yang, G. Zhu, Z. Shi, Q. Cui, and C. Xu, "Solar-Blind Ultraviolet Photodetectors Based on Porous β-Ga2O3 Nanorods for Deep-Ultraviolet Communications," ACS Appl. Nano Mater. **8**(8), 4199–4205 (2025).

138. A. A. Koziy, A. V. Losev, V. V. Zavodilenko, Yu. V. Kurochkin, and A. A. Gorbatsevich, "Modern methods of detecting single photons and their application in quantum communications," Quantum Elec. (Woodbury). **51**(8), 655–669 (2021).

139. X. Liu, H. Lu, Y. Zhu, J. Ma, R. Hao, D. Chen, and J. Wang, "Experimental study on the transmission performance of an ultraviolet and visible light communication system under an artificial fog channel," Opt. Express **32**(17), 30622 (2024).

140. F. Li, Y. Zuo, Z. Du, X. Song, and J. Wu, "High Data Transfer Rate Spatial Division Multiplexing for Short Range Non-Line-of-Sight Ultraviolet Optical Transmission," IEEE Photonics J. **13**(3), 1–19 (2021).

141. F. Liu, J. Farmer, G. Faulkner, J. J. D. McKendry, E. Xie, Q. Zheng, Z. Wang, J. Wang, J. Hill, J. Herrnsdorf, M. D. Dawson, and D. O'Brien, "Ultralow Photon Flux OWC Links Using UV-C Single-Photon Detection," Laser Photon. Rev. **19**(13), 2401804 (2025).

142. "https://www.hamamatsu.com/us/en/product/optical-sensors/pmt/about_pmts.html," .

143. J. Hill, C. Chen, E. Xie, J. J. D. McKendry, J. Herrnsdorf, E. Gu, H. Haas, and M. D. Dawson, "Effects of LED Device Size on UV-C Short-Range LoS Optical Wireless Communication," IEEE Photonics J. **15**(6), (2023).

144. D. M. Maclure et al., "Gb/s Optical Wireless Communications up to 17 meters using a UV-C Micro-Light-Emitting Diode," in *2022 IEEE Photonics Conference (IPC)* (IEEE, 2022), pp. 1–2.

145. Z. Qian, D. Li, F. Hu, P. Qiu, C. Ma, C. Shen, S. Zhang, N. Chi, X. Cui, and P. Tian, "Size-Dependent UV-C Communication Performance of AlGaN Micro-LEDs and LEDs," Journal of Lightwave Technology **40**(22), 7289–7296 (2022).

146. F. Olivier, S. Tirano, L. Dupré, B. Aventurier, C. Largeron, and F. Templier, "Influence of size-reduction on the performances of GaN-based micro-LEDs for display application," J. Lumin. **191**, 112–116 (2017).

147. M. Asad, Q. Li, M. Sachdev, and W. S. Wong, "Size-dependent optoelectrical properties of 365 nm ultraviolet light-emitting diodes," Nanotechnology **30**(50), (2019).

148. P. Li, H. Zhang, H. Li, M. Iza, Y. Yao, M. S. Wong, N. Palmquist, J. S. Speck, S. Nakamura, and S. P. DenBaars, "Size-independent low voltage of InGaN micro-light-emitting diodes with epitaxial tunnel junctions using selective area growth by metalorganic chemical vapor deposition," Opt. Express **28**(13), 18707 (2020).

149. J. M. Smith, R. Ley, M. S. Wong, Y. H. Baek, J. H. Kang, C. H. Kim, M. J. Gordon, S. Nakamura, J. S. Speck, and S. P. DenBaars, "Comparison of size-dependent characteristics of blue and green InGaN microLEDs down to 1 μm in diameter," Appl. Phys. Lett. **116**(7), 71102 (2020).

150. S. S. Konoplev, K. A. Bulashevich, and S. Y. Karpov, "From Large-Size to Micro-LEDs: Scaling Trends Revealed by Modeling," Physica Status Solidi (A) Applications and Materials Science **215**(10), 1–6 (2018).

151. P. Dong, J. Yan, J. Wang, Y. Zhang, C. Geng, T. Wei, P. Cong, Y. Zhang, J. Zeng, Y. Tian, L. Sun, Q. Yan, J. Li, S. Fan, and Z. Qin, "282-nm AlGaN-based deep ultraviolet light-emitting diodes with improved performance on nano-patterned sapphire substrates," Appl. Phys. Lett. **102**(24), 2–6 (2013).

152. B. C. Letson, J. W. Conklin, P. Wass, S. Barke, G. Mueller, M. A. J. Rasel, A. Haque, S. J. Pearton, and F. Ren, "Review—Reliability and Degradation Mechanisms of Deep UV AlGaN LEDs," ECS Journal of Solid State Science and Technology **12**(6), 066002 (2023).

153. Y. Gu, Z. Zhang, X. Shan, Y. Ruan, D. Shen, S. Zhang, X. Cui, and P. Tian, "Research on degradation characteristics of 253 nm AlGaN-based micro-LEDs for charge management application," Opt. Express **33**(7), 15327 (2025).

154. Q. Chen, Y. Wei, J. Gao, G. Gao, H. Liu, M. Lou, S. Qi, J. Ye, and W. Guo, "Performance enhancement in AlGaN deep ultraviolet light-emitting diodes with step doping n-AlGaN contact layer," Opt. Express **33**(3), 5040 (2025).

155. A. Knauer, T. Kolbe, S. Hagedorn, J. Hoepfner, M. Guttmann, H. K. Cho, J. Rass, J. Ruschel, S. Einfeldt, M. Kneissl, and M. Weyers, "Strain induced power enhancement of far-UVC LEDs on high temperature annealed AlN templates," Appl. Phys. Lett. **122**(1), (2023).

156. K. Nagamatsu, X. Liu, K. Uesugi, and H. Miyake, "Improved emission intensity of uvc-leds from using strain relaxation layer on sputter-annealed aln," Jpn. J. Appl. Phys. **58**(SC), (2019).

157. R. Kamei, T. Kamiya, H. Amano, N. Sawaki, H. Kobayashi, H. Saka, M. Irie, Y. Honda, and H. Iwata, "Annealing effect on threading dislocations in a GaN grown on Si substrate," J. Cryst. Growth **468**(January), 835–838 (2017).

158. S. Wang, Z. Liu, C. Zhang, G. Xu, C. Ge, Z. Zeng, X. Zhang, and P. Tian, "Variation of carrier lifetime with optical excitation power density in micro-LEDs," Opt. Express **32**(18), 31939 (2024).

159. J. J. D. Mckendry, E. Xie, J. Hill, H. Zimi, J. Herrnsdorf, E. Gu, R. K. Henderson, and M. D. Dawson, "Deep Ultraviolet CMOS-Controlled Micro Light-Emitting Diode Array," IEEE Photonics J. **15**(6), 1–6 (2023).

160. A. L. D. G. Griffiths, M. O. S. U. I. Slim, J. O. H. Errnsdorf, J. O. J. D. M. C. K. Endry, R. O. H. Enderson, H. A. H. Aas, and E. G. U. Rdan, "CMOS-integrated GaN LED array for discrete power level stepping in visible light communications," **25**(8), 47–48 (2017).

161. J. J. D. McKendry, D. Massoubre, S. Zhang, B. R. Rae, R. P. Green, E. Gu, R. K. Henderson, A. E. Kelly, and M. D. Dawson, "Visible-light communications using a CMOS-controlled micro-light-emitting- diode array," Journal of Lightwave Technology **30**(1), 61–67 (2012).

162. J. J. D. McKendry, B. R. Rae, Z. Gong, K. R. Muir, B. Guilhabert, D. Massoubre, E. Gu, D. Renshaw, M. D. Dawson, and R. K. Henderson, "Individually addressable AlInGaN micro-LED arrays with CMOS control and subnanosecond output pulses," IEEE Photonics Technology Letters **21**(12), 811–813 (2009).

163. A. D. Griffiths, "Novel optical communications and imaging enabled by CMOS interfaced LED technology," (May), (2018).

164. G. Naresh-Kumar, B. Hourahine, A. Vilalta-Clemente, P. Ruterana, P. Gamarra, C. Lacam, M. Tordjman, M. A. Di Forte-Poisson, P. J. Parbrook, A. P. Day, G. England, and C. Trager-Cowan, "Imaging and identifying defects in nitride semiconductor thin films using a scanning electron microscope," Physica Status Solidi (A) Applications and Materials Science **209**(3), 424–426 (2012).

165. R. Bertram, I. Han, F. Y. Meng, S. Mahajan, E. Lindow, H. McFelea, C. Werkhoven, and C. Arena, "Direct observation of formation of threading dislocations from stacking faults in GaN layer grown on (0001) sapphire," Scr. Mater. **64**(1), 93–96 (2010).

166. V. I. Orlov, T. Kim, P. S. Vergeles, A. Y. Polyakov, E. B. Yakimov, and I.-H. Lee, "Recombination and optical properties of dislocations gliding at room temperature in GaN under applied stress," J. Alloys Compd. **776**, 181–186 (2018).

167. I. Yonenaga, Y. Ohno, T. Yao, and K. Edagawa, "Optical and electrical properties of dislocations in plastically deformed GaN," J. Cryst. Growth **403**, 72–76 (2014).

168. M. Kneissl, "UV LED Efficiency Sept-2025," https://www.tu.berlin/en/originagkneissl/research.

169. A. P. Andey, "High-efficiency AlGaN / GaN / AlGaN tunnel junction ultraviolet light-emitting diodes," **8**(3), (2020).

170. J. Cho, E. F. Schubert, and J. K. Kim, "Efficiency droop in light-emitting diodes: Challenges and counter measures," Laser Photon. Rev. **7**(3), 408–421 (2013).

171. G. Verzellesi, D. Saguatti, M. Meneghini, F. Bertazzi, M. Goano, G. Meneghesso, and E. Zanoni, "Efficiency droop in InGaN/GaN blue light-emitting diodes: Physical mechanisms and remedies," J. Appl. Phys. **114**(7), (2013).

172. P. Tian, J. J. D. McKendry, Z. Gong, B. Guilhabert, I. M. Watson, E. Gu, Z. Chen, G. Zhang, and M. D. Dawson, "Size-dependent efficiency and efficiency droop of blue InGaN micro-light emitting diodes," Appl. Phys. Lett. **101**(23), (2012).

173. Z. Wu, K. Ren, X. Zhang, Y. An, L. Yin, X. Lu, A. Guo, and J. Zhang, "Physical mechanisms on the size-effect in GaN-based Micro-LEDs," Micro and Nanostructures **177**, (2023).

174. A. You, M. A. Y. Be, and I. In, "Efficiency droop in 245 – 247 nm AlGaN light-emitting diodes with continuous wave 2 mW output power," **061102**(February 2010), 245–248 (2017).

175. C. Tian, S. xu Guo, J. qiu Liang, Z. zhu Liang, and F. li Gao, "Effects of unit size on current density and illuminance of micro-LED-array," Optoelectron. Lett. **13**(2), 84–89 (2017).

176. Z. Gong, S. Jin, Y. Chen, J. McKendry, D. Massoubre, I. M. Watson, E. Gu, and M. D. Dawson, "Size-dependent light output, spectral shift, and self-heating of 400 nm InGaN light-emitting diodes," J. Appl. Phys. **107**(1), (2010).

177. Y. Liao, D. Li, Q. Guo, Y. Liu, H. Wang, W. Hu, and Z. L. Wang, "Temperature-dependent study on AlGaN-based deep ultraviolet light-emitting diode for the origin of high ideality factor," AIP Adv. **11**(10), 1ENG (2021).

178. Z. Gong, S. Jin, Y. Chen, J. J. D. McKendry, D. Massoubre, I. M. Watson, E. Gu, and M. D. Dawson, "Size-dependent light output, spectral shift, and self-heating of 400 nm InGaN light-emitting diodes," J. Appl. Phys. **107**(1), (2010).

179. Z. Peng, W. Guo, T. Wu, Z. Guo, Y. Lu, Y. Zheng, Y. Lin, and Z. Chen, "Temperature-Dependent Carrier Recombination and Efficiency Droop of AlGaN Deep Ultraviolet Light-Emitting Diodes," IEEE Photonics J. **12**(1), 1–8 (2020).

180. Z. Zhang, M. Kushimoto, T. Sakai, N. Sugiyama, L. J. Schowalter, C. Sasaoka, and H. Amano, "A 271.8 nm deep-ultraviolet laser diode for room temperature operation," Applied Physics Express **12**(12), 8–12 (2019).

181. D. S. Meyaard, Q. Shan, J. Cho, E. Fred Schubert, S. H. Han, M. H. Kim, C. Sone, S. Jae Oh, and J. Kyu Kim, "Temperature dependent efficiency droop in GaInN light-emitting diodes with different current densities," Appl. Phys. Lett. **100**(8), 1–4 (2012).

182. E. Kioupakis, Q. Yan, D. Steiauf, and C. G. Van De Walle, "Temperature and carrier-density dependence of Auger and radiative recombination in nitride optoelectronic devices," New J. Phys. **15**, (2013).

183. D. S. Meyaard, J. Cho, E. Fred Schubert, S. H. Han, M. H. Kim, and C. Sone, "Analysis of the temperature dependence of the forward voltage characteristics of GaInN light-emitting diodes," Appl. Phys. Lett. **103**(12), 1–4 (2013).

184. Z. G. Ju, S. T. Tan, Z. H. Zhang, Y. Ji, Z. Kyaw, Y. Dikme, X. W. Sun, and H. V. Demir, "On the origin of the redshift in the emission wavelength of InGaN/GaN blue light emitting diodes grown with a higher temperature interlayer," Appl. Phys. Lett. **100**(12), 10–14 (2012).

185. D. M. Maclure, J. J. D. McKendry, M. S. Islim, E. Xie, C. Chen, X. Sun, X. Liang, X. Huang, H. Abumarshoud, J. Herrnsdorf, E. Gu, H. Haas, and M. D. Dawson, "10 Gbps wavelength division multiplexing using UV-A, UV-B, and UV-C micro-LEDs," Photonics Res. **10**(2), 516 (2022).

186. R. P. Green, J. J. D. McKendry, D. Massoubre, E. Gu, M. D. Dawson, and A. E. Kelly, "Modulation bandwidth studies of recombination processes in blue and green InGaN quantum well micro-light-emitting diodes," Appl. Phys. Lett. **102**(9), 1–5 (2013).

187. Y. Huang, Z. Guo, H. Huang, and H. Sun, "Influence of Current Density and Capacitance on the Bandwidth of VLC LED," IEEE Photonics Technology Letters **30**(9), 773–776 (2018).

188. D. Li, S. Liu, Z. Qian, Q. Liu, K. Zhou, D. Liu, S. Sheng, B. Sheng, F. Liu, Z. Chen, P. Wang, T. Wang, X. Rong, R. Tao, J. Kang, F. Chen, J. Kang, Y. Yuan, Q. Wang, M. Sun, W. Ge, B. Shen, P. Tian, and X. Wang, "Deep-Ultraviolet Micro-LEDs Exhibiting High Output Power and High Modulation Bandwidth Simultaneously," Advanced Materials **34**(19), 1–10 (2022).

189. D. Zhai, K. Tian, C. Chu, Y. Zhang, Q. Zheng, Q. Li, and Z. Zhang, "Impact of carrier injection and recombination on the −3 dB bandwidth for GaN-based VCSELs," Opt. Lett. **50**(11), 3720 (2025).

190. M. S. Wong, D. Hwang, A. I. Alhassan, C. Lee, R. Ley, S. Nakamura, and S. P. DenBaars, "High efficiency of III-nitride micro-light-emitting diodes by sidewall passivation using atomic layer deposition," Opt. Express **26**(16), 21324 (2018).

191. M. S. Islim, R. X. Ferreira, X. He, E. Xie, S. Videv, S. Viola, S. Watson, N. Bamiedakis, R. V. Penty, I. H. White, A. E. Kelly, E. Gu, H. Haas, and M. D. Dawson, "Towards 10 Gb/s orthogonal frequency division multiplexing-based visible light communication using a GaN violet micro-LED," Photonics Res. **5**(2), A35 (2017).

192. J. J. D. McKendry, C. Chen, D. MacLure, J. Hill, E. Xie, I. Tavakkolnia, J. Herrnsdorf, H. Haas, and M. D. Dawson, "Beyond 10 Gigabit/s Visible Light Communication Using Micro-Light-Emitting Diodes and Orthogonal Frequency Division Multiplexing," in *IET Conference Proceedings* (Institution of Engineering and Technology, 2023), **2023**(34), pp. 1760–1763.

193. H. Chun, S. Rajbhandari, G. Faulkner, D. Tsonev, E. Xie, J. J. D. McKendry, E. Gu, M. D. Dawson, D. C. O'Brien, and H. Haas, "LED based wavelength division multiplexed 10 Gb/s visible light communications," Journal of Lightwave Technology **34**(13), 3047–3052 (2016).

194. X. Liu, Z. Wei, M. Li, L. Wang, Z. Liu, C. Yu, L. Wang, Y. Luo, and H. Y. Fu, "Experimental investigation of 16.6 Gbps SDM-WDM visible light communication based on a neural network receiver and tricolor mini-LEDs," Opt. Lett. **46**(12), 2888 (2021).

195. R. Poboril, J. Latal, P. Koudelka, J. Vitasek, P. Siska, J. Skapa, and V. Vasinek, "A concept of ahybrid WDM/TDM topologyusing the fabry-perot laser in the optiwave simulation environment," Advances in Electrical and Electronic Engineering **9**(4), 167–178 (2011).

196. K. Zou, K. Pang, H. Song, J. Fan, Z. Zhao, H. Song, R. Zhang, H. Zhou, A. Minoofar, C. Liu, X. Su, N. Hu, A. McClung, M. Torfeh, A. Arbabi, M. Tur, and A. E. Willner, "High-capacity free-space optical communications using wavelength- and mode-division-multiplexing in the mid-infrared region," Nat. Commun. **13**(1), (2022).

197. H. Ishio, J. Minowa, and K. Nosu, "Review and Status of Wavelength-Division-Multiplexing Technology and Its Application (Invited Overview)," Journal of Lightwave Technology **2**(4), 448–463 (1984).

198. B. Guilhabert, D. Massoubre, E. Richardson, J. J. D. McKendry, G. Valentine, R. K. Henderson, I. M. Watson, E. Gu, and M. D. Dawson, "Sub-micron lithography using InGaN micro-LEDs: Mask-free fabrication of LED arrays," IEEE Photonics Technology Letters **24**(24), 2221–2224 (2012).

199. E. Xie, M. Stonehouse, R. Ferreira, J. J. D. McKendry, J. Herrnsdorf, X. He, S. Rajbhandari, H. Chun, A. V. N. Jalajakumari, O. Almer, G. Faulkner, I. M. Watson, E. Gu, R. Henderson, D. O'Brien, and M. D. Dawson, "Design,

Fabrication, and Application of GaN-Based Micro-LED Arrays with Individual Addressing by N-Electrodes," IEEE Photonics J. **9**(6), (2017).

200. J. Li, R. Yuan, S. Wang, C. Yang, and M. Peng, "Hybrid Grouped Transmission and Probabilistic Shaping for Mitigating High-SNR Nonlinearities in UV DCO-OFDM Communication System," in *2025 13th International Conference on Intelligent Computing and Wireless Optical Communications (ICWOC)* (IEEE, 2025), pp. 246–251.

201. S. Zhu, P. Qiu, Z. Qian, X. Shan, Z. Wang, K. Jiang, X. Sun, X. Cui, G. Zhang, D. Li, and P. Tian, "2 Gbps free-space ultraviolet-C communication based on a high-bandwidth micro-LED achieved with pre-equalization," Opt. Lett. **46**(9), 2147 (2021).

202. J. J. D. McKendry, E. Xie, M. S. Islim, X. Sun, D. MacLure, E. Gu, H. Haas, and M. D. Dawson, "4 Gbps wireless optical communications up to 5 m using a UV-C micro-light-emitting diode array," 2021 IEEE Photonics Conference, IPC 2021 - Proceedings **1**, 2022–2023 (2021).

203. J. F. C. Carreira, E. Xie, R. Bian, J. Herrnsdorf, H. Haas, E. Gu, M. J. Strain, and M. D. Dawson, "Gigabit per second visible light communication based on AlGaInP red micro-LED micro-transfer printed onto diamond and glass," Opt. Express **28**(8), 12149 (2020).

204. X. Sun, Z. Zhang, A. Chaaban, T. K. Ng, C. Shen, R. Chen, J. Yan, H. Sun, X. Li, J. Wang, J. Li, M.-S. Alouini, and B. S. Ooi, "71-Mbit/s ultraviolet-B LED communication link based on 8-QAM-OFDM modulation," Opt. Express **25**(19), 23267 (2017).

205. D. M. Maclure, C. Chen, J. J. D. McKendry, E. Xie, J. Hill, J. Herrnsdorf, E. Gu, H. Haas, and M. D. Dawson, "Hundred-meter Gb/s deep ultraviolet wireless communications using AlGaN micro-LEDs," Opt. Express **30**(26), 46811 (2022).

206. Z. Zhang, M. Kushimoto, A. Yoshikawa, K. Aoto, L. J. Schowalter, C. Sasaoka, and H. Amano, "Continuous-wave lasing of AlGaN-based ultraviolet laser diode at 274.8 nm by current injection," Applied Physics Express **15**(4), (2022).

207. G. Cossu, A. M. Khalid, P. Choudhury, R. Corsini, and E. Ciaramella, "3.4 Gbit / s visible optical wireless transmission based on RGB LED," **20**(26), 501–506 (2012).

208. D. M. Maclure, J. J. D. Mckendry, J. Herrnsdorf, X. He, E. Xie, E. Gu, and M. D. Dawson, "Size-Dependent Characterization of Deep UV Micro-Light- Emitting Diodes," in *2020 IEEE Photonics Conference (IPC)* (IEEE, 2020), (1), pp. 1–2.

209. M. Shatalov, A. Chitnis, P. Yadav, M. F. Hasan, J. Khan, V. Adivarahan, H. P. Maruska, W. H. Sun, and M. A. Khan, "Thermal analysis of flip-chip packaged 280 nm nitride-based deep ultraviolet light-emitting diodes," Appl. Phys. Lett. **86**(20), 1–3 (2005).

210. J. H. I. de Souza and T. Abrão, "Hybrid Hughes-Hartogs power allocation algorithms for OFDMA systems," IET Signal Processing **12**(9), 1185–1192 (2018).

211. Z. Chen, Z. Chen, L. Liu, B. Deng, Y. Li, X. Tang, and H. Y. Fu, "UV LED-Based NLOS Underwater Optical Communication System," IEEE Photonics Technology Letters (2025).

212. V. V. Belov, I. Juwiler, N. Blaunstein, M. V. Tarasenkov, and E. S. Poznakharev, "Nlos communication: Theory and experiments in the atmosphere and underwater," Atmosphere (Basel). **11**(10), (2020).

213. J. Zhang, L. Kou, Y. Yang, F. He, and Z. Duan, "Monte-Carlo-based optical wireless underwater channel modeling with oceanic turbulence," Opt. Commun. **475**(April), 126214 (2020).

214. G. Arvanitakis, R. Bian, J. J. D. Mckendry, and C. Chen, "Gb / s Underwater Wireless Optical Communications Using Series-Connected GaN Micro-LED Arrays," IEEE Photonics J. **12**(April), 1–10 (2020).

215. P. Yue, X. R. Wang, D. L. Xu, and S. Xu, "Non-line-of-sight scattering channel modeling of MIMO links for underwater wireless optical communication," Opt. Commun. **578**, (2025).

216. R. J. Drost, T. J. Moore, and B. M. Sadler, "Ultraviolet scattering propagation modeling: analysis of path loss versus range," Journal of the Optical Society of America A **30**(11), 2259 (2013).

217. X. Sun, G. M. Bonner, J. J. D. Mckendry, and M. D. Dawson, "A study on the optical power requirement of kilometer-range solar-blind NLOS communication links," in *2021 IEEE Photonics Conference (IPC)* (IEEE, 2021), pp. 1–2.

218. Z. Xu, H. Ding, and B. M. Sadler, "A path loss model for non-line-of-sight ultraviolet multiple scattering channels," EURASIP J. Wirel. Commun. Netw. **2010**, (2010).

219. L. Zhang, Z. Sun, T. Bai, P. Li, and Y. Qin, "1Mbps NLOS solar-blind ultraviolet communication system based on UV-LED array," in (SPIE-Intl Soc Optical Eng, 2018), p. 37.

220. M. V. Tarasenkov, V. V. Belov, and E. S. Poznakharev, "Estimation of optimal wavelengths for atmospheric non-line-of-sight optical communication in the UV range of the spectrum in daytime and at night for baseline distances from 50 m to 50 km," Journal of the Optical Society of America A **39**(2), 177 (2022).

221. Y. Zhang, C. Gong, and Z. Xu, "Bi-directional ultra-violet communication with self-interference," Opt. Express **30**(21), 38534 (2022).

222. L. Elterman, "Atmospheric Attenuation Model, 1964, in the Ultraviolet, Visible, and Infra red Regions for Altitudes to 50 km," Environmental Reasearch Papers (46), 1–42 (1964).

223. E. M. Patterson and J. B. Gillespie, "Simplified ultraviolet and visible wavelength atmospheric propagation model," Appl. Opt. **28**(3), 425 (1989).

224. J. J. Puschell and R. Bayse, "High data rate ultraviolet communication systems for the tactical battlefield," Conference Proceedings on Tactical Communications **1**, 253–267 (1990).

225. G. Chen, Z. Xu, H. Ding, and B. Sadler, "Path loss modeling and performance trade-off study for short-range non-line-of-sight ultraviolet communications," Opt. Express **17**(5), 3929 (2009).

226. G. Wang, K. Wang, C. Gong, Di. Zou, Z. Jiang, and Z. Xu, "A 1Mbps Real-Time NLOS UV Scattering Communication System with Receiver Diversity over 1km," IEEE Photonics J. **10**(2), (2018).

227. S. Dimitrov and H. Haas, "MIMO transmission," in *Principles of LED Light Communications* (Cambridge University Press, 2015), pp. 130–150.

228. F. Li, Y. Zuo, A. Li, Z. Du, and J. Wu, "Spatially correlated MIMO for exploiting the capacity of NLOS ultraviolet turbulent channels," Opt. Express **27**(21), 30639 (2019).

229. M. Huang, S. Zhou, and J. Wang, "Analysis of Tomlinson-Harashima precoding in multiuser MIMO systems with imperfect channel state information," IEEE Trans. Veh. Technol. **57**(5), 2856–2867 (2008).

230. H. Ge, X. Zhou, Y. Chen, J. Zhang, W. Ni, X. Wang, and L. Zheng, "Shot-noise-limited photon-counting precoding scheme for MIMO ultraviolet communication in atmospheric turbulence," Opt. Express **31**(1), 426 (2023).

231. J. J. McKendry, H. Zimi, Y. Shao, S. Rajbhandari, S. Member, J. Herrnsdorf, and M. D. Dawson, "Eye and skin-safe 150 Mbps Optical Wireless Communications over 1 m using UVC LEDs," IEEE Photonics Technology Letters **37**(24), 1451–1454 (2025).

232. Y. Dong, Y. Wu, C. Chu, K. Tian, H. Liu, X. Wei, J. Yan, Y. Zhang, and Z.-H. Zhang, "The effect of mesa length-width aspect ratio on the thermal performance of deep ultraviolet flip-chip micro-light-emitting diodes," Phys. Scr. **100**(9), 095114 (2025).

233. T. Cao, P. Wang, T. Wu, mingyang wang, H. Zhang, K. Wang, and J. Song, "Performance analysis of non-line-of-sight ultraviolet communications under periodic pulse jamming attack through turbulent channels," Opt. Express **33**(17), 35146–35163 (2025).

Appendix A

A.1. post graduate course and development.

Spider work

RD901 23/20

RD902 10/10

RD903 10/10

RD904 10/10

RD905 13/10

All essays have been submitted and all reports submitted and signed off.

A.2. Presentations and conferences.

A.2.1 Regional conferences and published abstracts.

1. Quantic student poster presentation (1st author)
2. 1st international SPAD conference poster presentation (1st author)
3. UKNC 2022- talk 1st author.
4. IWN 2022 talk 1st author

A.2.2. Regional conferences and published abstracts.

1. **IPC 2020 – talk 1st author**. D. M. Maclure et al., *"Size-Dependent Characterization of Deep UV Micro-Light-Emitting Diodes,"* 2020 IEEE Photonics Conference (IPC), Vancouver, BC, Canada, 2020, pp. 1-2, doi: 10.1109/IPC47351.2020.9252420.

2. **IPC 2021- talk 5th author -** J. J. D. McKendry et al., *"4 Gbps wireless optical communications up to 5 m using a UV-C micro-light-emitting diode array,"* 2021 IEEE Photonics Conference (IPC), Vancouver, BC, Canada, 2021, pp. 1-2, doi: 10.1109/IPC48725.2021.9593005.

3. **IPC 2022- talk 1st author-** D. M. Maclure et al., *"Gb/s Optical Wireless Communications up to 17 meters using a UV-C Micro-Light-Emitting Diode,"* 2022 IEEE Photonics Conference (IPC), Vancouver, BC, Canada, 2022, pp. 1-2, doi: 10.1109/IPC53466.2022.9975654.

4. **IPC 2023 – talk 2nd author-** H. Zimi *et al*., *"Gigabit Per Second UV-C LEDs for Communications," 2023 IEEE Photonics Conference (IPC)*, Orlando, FL, USA, 2023, pp. 1-2, doi: 10.1109/IPC57732.2023.10360631.

5. **ECOC 2023- 3rd author-** J. J. D. McKendry *et al*., *"Beyond 10 Gigabit/s visible light communication using micro-light-emitting diodes and orthogonal frequency division multiplexing," 49th European Conference on Optical Communications (ECOC 2023)*, Hybrid Conference, Glasgow, UK, 2023, pp. 1760-1763, doi: 10.1049/icp.2024.1809.

A.3. Presentations and conferences.

1. **Submitted and accepted 1st author-** Daniel M. Maclure, et al. *"10 Gbps wavelength division multiplexing using UV-A, UV-B, and UV-C micro-LEDs,"* Photon. Res. 10, 516-523 (2022)

2. **Submitted and accepted 1st author-** Daniel M. Maclure et. Al. *"Hundred-meter Gb/s deep ultraviolet wireless communications using AlGaN micro-LEDs,"* Opt. Express 30, 46811-46821 (2022)

PHOTONICS Research

10 Gbps wavelength division multiplexing using UV-A, UV-B, and UV-C micro-LEDs

Daniel M. Maclure,[1,5] Jonathan J. D. McKendry,[1] Mohamed Sufyan Islim,[2] Enyuan Xie,[1] Cheng Chen,[2] Xiaobin Sun,[3] Xudong Liang,[4] Xiaohui Huang,[4] Hanaa Abumarshoud,[2] Johannes Herrnsdorf,[1] Erdan Gu,[1,6] Harald Haas,[2] and Martin D. Dawson[1]

[1]Institute of Photonics, Department of Physics, SUPA, University of Strathclyde, Glasgow G1 1RD, UK
[2]LiFi Research and Development Centre, Department of Electronic & Electrical Engineering, University of Strathclyde, Technology & Innovation Centre, Glasgow G1 1RD, UK
[3]Fraunhofer Center of Applied Photonics, Technology & Innovation Centre, Glasgow G1 1RD, UK
[4]Zhixin Semiconductor (Hangzhou) Co., Ltd., Hangzhou 311200, China
[5]e-mail: daniel.maclure@strath.ac.uk
[6]e-mail: erdan.gu@strath.ac.uk

Received 25 October 2021; revised 8 December 2021; accepted 8 December 2021; posted 13 December 2021 (Doc. ID 445984); published 1 February 2022

Deep ultraviolet (DUV) optical wireless communications have seen increased interest in recent years due to the unique properties of light in this spectral region. However, the reported DUV data rates remain significantly lower than comparable demonstrations at visible wavelengths due to lower modulation bandwidths and/or output power of the sources. Here, we present a wavelength division multiplexing demonstration using three UV micro-light-emitting diodes emitting at nominal peak wavelengths of 285, 317, and 375 nm, respectively, each with an emitting area of approximately 1369 μm^2 (equivalent to circular device pixels of diameter ∼40 μm). Using orthogonal frequency division multiplexing, data rates of 4.17, 3.02, and 3.13 Gbps were achieved from the 285, 317, and 375 nm devices, respectively, for a combined data rate of 10.32 Gbps transmitted over a distance of 0.5 m.

https://doi.org/10.1364/PRJ.445984

1. INTRODUCTION

Optical wireless communication (OWC) has seen much attention as a possible solution to the predicted "data crunch" facing radio frequency (RF) communications [1,2]. The visible and ultraviolet regions of the electromagnetic spectrum are license-free and largely unexploited thus far and, as a result, offer additional frequency bandwidth to complement RF communications.

Ultraviolet (UV) communication is an important emerging area of OWC, as it can be used in a wide range of applications such as secure communications and non-line of sight (NLOS) communications. A significant benefit of operating at deep UV (DUV) wavelengths, i.e., in the UV-B (280–315 nm) or UV-C (100–280 nm) spectral bands, is that sunlight at these wavelengths is absorbed by the upper atmosphere, resulting in an essentially noiseless environment for terrestrial DUV communication [3]. Furthermore, it also benefits secure intersatellite communications, as the space-based ultraviolet signal is obscured from ground observers. UV light is also strongly scattered by air, allowing for NLOS wireless optical communication over/around physical obstacles such as buildings. This is due to the fact that the strength of Rayleigh scattering is inversely proportional to λ^4, where λ is the wavelength of light, and thus short-wavelength UV is much more strongly scattered by air than visible wavelengths. This property can help support NLOS wireless optical communication through the atmosphere, relaxing the constraints on transceiver pointing and tracking, and allowing physical obstacles such as buildings that might block LOS links to be overcome.

UV sources have seen significant improvements recently. Previously, mercury lamps with kHz optical modulation bandwidths were the primary sources available, meaning it was impossible to achieve high data rates. These sources are also bulky and fragile, and contain toxic materials. DUV lasers have also attracted interest due to their high bandwidth and high power [4]. However, their highly directional emission and eye safety requirements [5,6] and challenges in fabricating laser diodes emitting at wavelengths below 315 nm hamper their wide-scale adoption in real-world applications [7]. On the other hand, with improving semiconductor material quality, output power, and efficiency, UV light-emitting diodes (LEDs) are becoming the source of choice for various applications, including sterilization and UV optical communications.

In this work, we use micrometer scale (<100 μm) LEDs (μLEDs) as optical transmitters. Such μLEDs have witnessed a surge of interest with recent developments such as high-resolution displays [8] and visible light applications [9,10]. The main benefit of μLEDs for optical communications, when compared with conventional large area LEDs, is their high bandwidth. Due to their small size, μLED capacitance is small; hence, their bandwidth is limited by the carrier lifetimes rather than a large RC time constant as in conventional LEDs [11]. This allows for faster modulation, with bandwidths in excess of 650 MHz being reported [12], compared with around 10 MHz for a conventional LED. Data rates achieved from single visible-emitting μLEDs have approached 10 Gbps [12]; however, corresponding rates from UV μLEDs have thus far been limited to around 2 Gbps [13], primarily due to the comparatively low output powers at these wavelengths.

This paper demonstrates wavelength division multiplexing (WDM) using three UV μLEDs with peak emission at 285, 317, and 375 nm, respectively. WDM allows optical data to be encoded separately in different wavelength bands and transmitted in parallel to increase throughput. Using orthogonal frequency division multiplexing (OFDM) and quadrature amplitude modulation (QAM) encoding, data rates of 4.17, 3.02, and 3.13 Gbps from the 285, 317, and 375 nm μLEDs, respectively, were demonstrated, giving a total aggregate data rate of 10.32 Gbps transmitted over 0.5 m. This, to the best of our knowledge, is the highest data rate yet reported using UV LEDs and for the first time that WDM has been used for OWC across the UV spectrum.

2. μLED DEVICES

In this work, three μLED arrays with peak emission wavelengths within the UV-C (285 nm), UV-B (317 nm), and UV-A (375 nm) regions of the spectrum were fabricated from commercial-grade III-nitride LED wafers grown on 2 in. *c*-plane sapphire substrates. Details of the wafer structures for the UV-C and UV-A devices can be found in our previous work [14–16].

The UV-B wafer was custom fabricated for this work by Zhixin Semiconductor Co., Ltd. on a 2 in. sapphire substrate. The wafer contained a 2000 nm thick AlN buffer, a 1000 nm thick undoped AlGaN layer, and two 500 nm n-doped layers of AlGaN:Si with Al concentrations of 50% and 55%, respectively. The active region contained a multiple quantum well (MQW) region and consisted of AlGaN with Al concentration of 15%/40%, a 50 nm thick electron blocking layer (EBL) of AlGaN:Mg with Al composition of 50%, and, finally, a 300 nm p-doped region of GaN:Mg and a 10 nm thick GaN:Mg p-contact region.

The design and fabrication process of these μLED arrays were similar to those reported in our previous work [17]. As shown in Fig. 1, each array consists of eight trapezoidal-shaped μLED pixels in a flip-chip configuration, with each pixel having an emission area of 1369 μm^2, an area equivalent to a circular disk-shaped pixel of ~40 μm diameter. The trapezoidal-shaped pixels were first reported in Ref. [17], where it was speculated that the shape increased the surface-to-active-area ratio, thus enabling a more efficient thermal dissipation. The fabricated arrays were then wire-bonded to a printed circuit board for further characterization.

The light output power versus current (*L-I*) and current versus voltage (*I-V*) relationships were measured from representative pixels from each device. The *I-V* characteristics were measured using a Yokogawa GS610 source measure unit, and the *L-I* characteristics were measured by placing the pixels in close proximity to a calibrated Thorlabs S120VC power meter head. The results are shown in Fig. 2.

The maximum output powers per pixel are approximately 0.48, 0.14, and 1.32 mW for the UV-C, UV-B, and UV-A devices, respectively. The most efficient device was the UV-A, which was expected, as this material technology is the most mature, and issues such as defects are minimized. The relatively low output power of the UV-B device may be attributed to the relative lack of development of material at these wavelengths, as there is currently no high-volume application for LEDs emitting in this range [18].

The forward voltages at 10 mA were 18.4, 22.0, and 4.4 V for the UV-C, UV-B, and UV-A devices, respectively. The

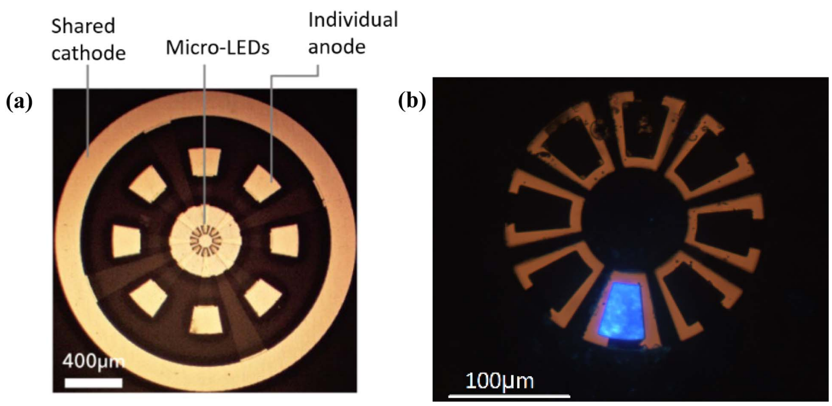

Fig. 1. (a) Top-down micrograph image representation of a micro-LED array, showing the eight concentric and individually addressable pixels. (b) UV-C pixel in operation.

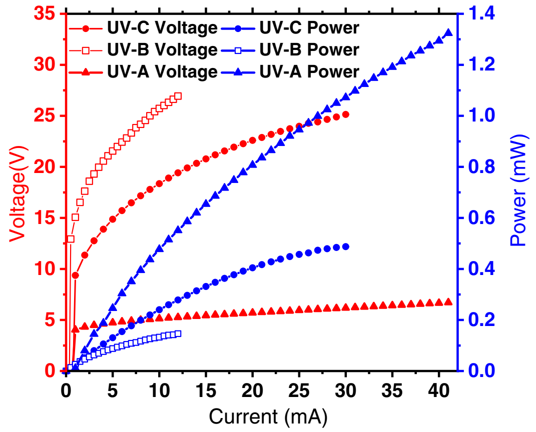

Fig. 2. *L-I-V* curves of the devices at UV-A, UV-B, and UV-C wavelengths.

higher turn-on voltages for the UV-B and UV-C devices can be attributed to the poor electrical conductivity of AlGaN layers, resulting in inferior carrier injection [18] and difficulties in creating low-resistance Ohmic contacts at higher Al mole fractions. These are prevalent issues in DUV material, and devices with higher turn-on voltages also being reported in the literature [5,19].

The EL spectra of the devices as a function of current were measured using a spectrometer and fiber optic (Avantes Avaspec-20482 spectrometer and Ocean Optics QP600-2-SR-BX fiber) (see Fig. 3). The peak wavelengths for each device were measured to be 281.7, 316.5, and 373.4 nm, respectively, when operating at 10 mA.

The spectra of the devices demonstrated different redshifts with the increasing current. This suggests heating effects were a more prominent issue in the UV-C device, which demonstrated a shift in the peak wavelength of 3.5 nm (from 281.7 to 285.2 nm) with increasing current from 0 to 30 mA. The shift is not as prominent in the other devices, with shifts of 1.2 nm being recorded for the UV-B over a current range of 0–12 mA and 1.16 nm being recorded in the UV-A devices, over the same range of current as the UV-C device. The measured spectra helped inform what filters and mirrors would be used in the WDM setup, which will be discussed in Section 3. It was noted that there was spectral overlap between

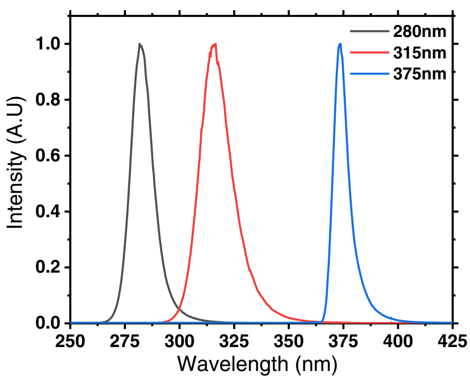

Fig. 3. EL spectra of the three devices at 10 mA.

the UV-C and UV-B devices, which could result in a degree of crosstalk between these WDM channels.

Finally, the frequency responses of the devices were measured using an avalanche photodiode (APD, Hamamatsu C5668 8867) with a bandwidth range of 100 kHz to 1 GHz, following a similar procedure, as outlined in our previous work [16]. Values for each device's −3 dB electrical-to-electrical (E-E) bandwidths were obtained from the recorded frequency responses as a function of current.

Conventionally, when plotted on a logarithmic frequency scale, the frequency response of an LED should appear flat at low frequencies before gradually rolling off above a certain cut-off frequency. The −3 dB bandwidths can then simply be obtained by finding the frequency at which the response of the LED is −3 dB lower than the flat low-frequency part of the response curve. However, the UV-B and UV-C devices exhibited frequency response behaviors, which showed the response initially rising to a broad peak, before gradually rolling over, as shown in Fig. 4. This complicates the process of estimating the devices' bandwidths. We tentatively attribute this behavior to the effect of parasitic impedance from wire bonds and packaging and the μLEDs themselves.

Our approach was to arbitrarily set the response at 1 MHz as the low-frequency reference and define the μLED bandwidth as the frequency at which the response declined to −3 dB below this point. This is illustrated in Fig. 4. This allowed the general behavior of μLED bandwidth versus current to be estimated, though it makes a like-for-like comparison of μLED bandwidths reported elsewhere challenging. The resulting E-E bandwidth as a function of current for all devices is shown in Fig. 5.

The corresponding E-E bandwidths were found to be 960, 780, and 140 MHz, respectively. It is worth noting that the APD bandwidth (1 GHz) is close to that of the UV-B and -C μLEDs and, as a consequence, may have affected the estimated bandwidths. The further development of high-bandwidth UV/DUV sensitive APDs is urgently needed to facilitate the full measurement of μLED devices such as those reported here. Compared with their UV-A counterparts, the high modulation bandwidths and lower output power of the UV-B and -C devices

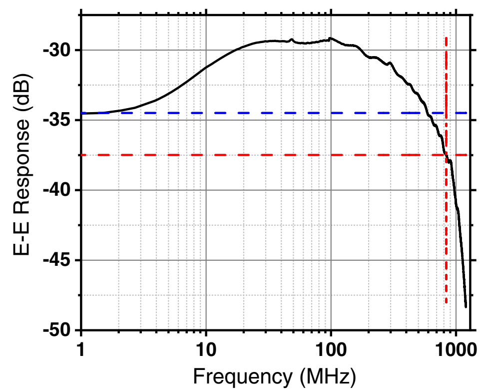

Fig. 4. Frequency response of the UV-C μLED measured at 20 mA (black). The response at 1 MHz (indicated by the blue horizontal dotted line) is used as the low-frequency reference point to estimate the E-E −3 dB bandwidth (indicated by the red crosshair).

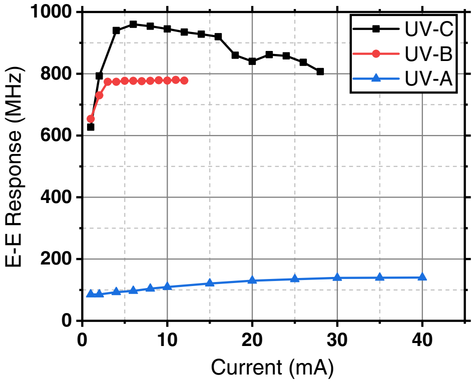

Fig. 5. Electrical-to-electrical bandwidth response versus current for the respective wavelengths.

may be attributed to higher defect densities and thus increased nonradiative recombination at shorter wavelengths. This would lead to lower output power and higher bandwidth via a reduced carrier recombination lifetime. We speculate that the saturation and decrease of the bandwidth as seen in the UV-B and UV-C, respectively, may be attributed to device heating and thermally mediated effects such as carrier overflow reducing the carrier density in the quantum wells, thus increasing the average carrier lifetime and reducing the bandwidth [20].

3. WDM EXPERIMENTAL SETUP

The WDM optical setup consists of the three UV μLED arrays and two long-pass dichroic mirrors with cut-on wavelengths of 355 nm (Semrock Di01-R355-25 × 36) and 300 nm (Alluxa-8113, 300 LP Dichroic). The transmission spectra of these mirrors are shown in Fig. 6, along with the respective device spectra at 10 mA. The mirrors were used to combine the light from the three μLEDs into a common optical path, as seen in Fig. 7. These components were connected in an optomechanical cage system with the arrays mounted on manually adjustable stages to facilitate optimized alignment. The relatively small variation in the μLED emission spectra as a function of current was not found to cause any significant problems in discriminating between channels.

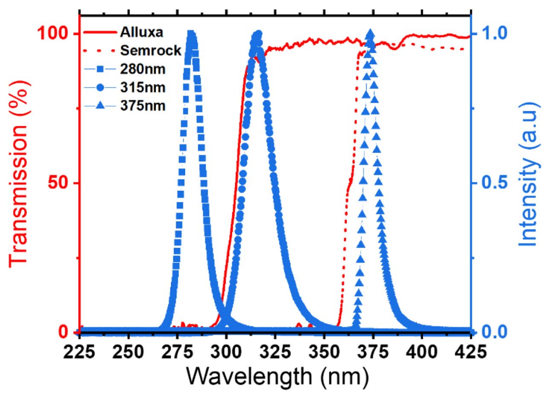

Fig. 6. Spectra (red curves) of the dichroic mirrors used in the setup, and the spectra (blue data points) of the devices with each device operated at 10 mA.

The emission from each μLED array was focused using a separate 2 in. diameter lens [Edmund Eptics 84340, focal length 40 mm for the UV-C and UV-B μLEDs, Thorlabs ACL50832U-A lens (NA = 0.76) for UV-A]. Three bias-TEEs (Tektronix PSPL5675A, a Mini-Circuits ZFBT-4R2G, and Mini-Circuits ZFBT 6GW-FT+) supplied the RF modulation signals and DC power to the pixels. A Keysight M8195A arbitrary waveform generator (AWG), with a peak-to-peak voltage of 250 mV, sampling rate of 65 GSamples/s, analogue bandwidth of 25 GHz, and vertical resolution of 8 bits, was used to provide the modulation signals. Figure 7 shows a schematic of the experimental arrangement.

A MATLAB code was used to generate the DC-biased optical (DCO)-OFDM data similar to our previous work [16,21,22]. This code allowed for the evaluation and control of the setup's performance, such as the peak-to-peak voltage, OFDM signal clipping, modulation bandwidth, number of subcarriers, cyclic prefix (CP) length, and the target bit error rate (BER) for adaptive bit and energy loading algorithm, which determined the final data rates achieved. Before transmitting the OFDM signal, a sinusoidal waveform was used to find an appropriate bias point with suitable peak-to-peak voltage and avoid any severe nonlinear distortion or saturation. After analyzing the performance, the following parameters were used: CP length of 20, normalized clipping level set to 3.2 of the signal standard deviation, corresponding PAPR of 10.1 dB, an FFT size of 2048, and a training length of 1504 QAM OFDM frames.

Next, a channel and signal-to-noise ratio (SNR) estimation procedure is executed, where 4QAM symbols are supplied to all subcarriers as the pilot signals. After an FFT (fast Fourier transform) operation, the detected symbols were compared with the original pilot symbols to estimate the channel gain and SNR for each subcarrier. The SNR information enables the use of an adaptive bit and energy loading algorithm [12], which selects the most suitable QAM constellation and transmission power for each subcarrier so that the eventual achieved BER will converge to a predefined threshold, thus maximizing the achievable data rate.

Next, the payload OFDM signal is transmitted. The QAM constellation and power control on each subcarrier are defined based on the adaptive bit and energy loading result. On the receiver side, the detected frequency-domain symbols are equalized using the estimated channel. Finally, the equalized symbols are decoded and compared with the original binary bits for BER calculation. The BER target used here is 3.8×10^{-3}, as this value allows the use of forwarding error correction codes to provide virtually error-free communication with a 7% overhead.

In the WDM experiment, one μLED at a time was modulated with an OFDM signal, while the code simultaneously generated interfering signals in the other two μLED channels in order to simulate a real-world system with multiple parallel data streams. Furthermore, three amplifiers (one SFHS126A and two Minicircuits FL-1000LN+ amplifiers) were connected between the AWG and the bias TEE to amplify the RF signal

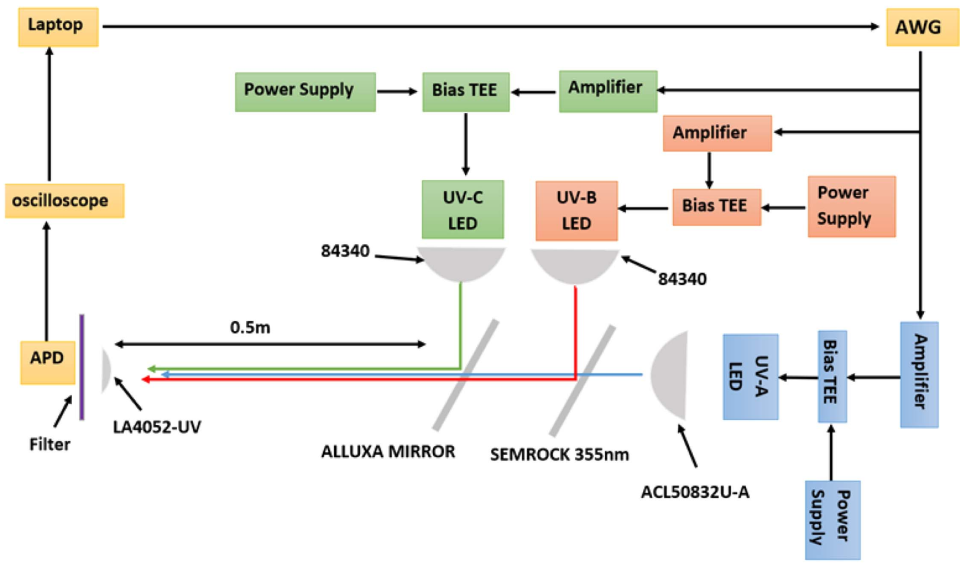

Fig. 7. Schematic diagram of the optical and electrical setup used for the WDM transmission experiments.

and increase the signal modulation depth. The SFHS126A amplifier, with a gain of 29 dB, was connected to the μLED sending the desired OFDM signal. The receiver was situated 0.5 m from the transmitter. According to Ref. [23], the absorption and scattering coefficients at these wavelengths are on the order of 0.1–0.3 km^{-1}, meaning that, at this transmission distance, the absorption and scattering effects can be considered negligible. In particular, this means that there is effectively no difference in scattering of the three selected WDM wavelengths over distances well beyond the tens of meters range. A single 1 in. lens (Thorlabs LA4052, focal length 35.1 mm) was used to focus the received signals onto the receiver. A sliding filter mount (Thorlabs CFS1/M) was used to mount three filters (Semrock FF01 280/20-25, Envin 308 nm bandpass filter, and Edmund Optics 34299 350 nm long-pass filter) and select the channel of interest. Finally, an APD with 1 GHz bandwidth (Hamamatsu C5668 8867) was used as the detector. Only one detector is used in this configuration compared with the multiple detector methods commonly used in this field [24]. This choice was made to simplify the setup. This detector was connected to an oscilloscope (Keysight MXR608A: sampling rate, 16 GSamples/s; analogue bandwidth, 6 GHz; vertical resolution, 10 bits) and a laptop to capture received waveforms for offline processing. From this, it was possible to determine the SNR, bit error rate (BER), and the maximum "error-free" data rates per channel, which will be discussed in the next section.

4. EXPERIMENTAL RESULTS

Before carrying out the main WDM experiment, the effect of the optical setup on the performance of the individual devices was examined. The performance of individual channels was evaluated where only one channel was operating at a time, and the performance was compared with and without a filter in front of the receiver. When filters were applied, a decrease in the SNR of each channel was observed due to optical losses from the filters. The decrease in SNR translated to an increase in the BER and thus a decrease of the maximum data rate.

The BER versus data rate for each channel with and without the corresponding receiver filter is shown in Fig. 8(a). The maximum data rates for the UV-A device were 3.46 and 3.56 Gbps with and without the filter, respectively. The UV-B maximum data rate decreased from 3.4 Gbps without the filter to 3.15 Gbps with the filter; for the UV-C, the corresponding decrease was from 4.52 to 4.17 Gbps. We note that, in multicarrier transmission systems such as what is used here, advanced equalization techniques permit modulation well beyond the 3 dB E-E response of the device, as shown here and demonstrated in other studies [25]. For the full WDM configuration, with all channels active and modulated with one channel transmitting a random bit stream and the other channels generating random noise, the SNR of each of the WDM channels was characterized. The peak-to-peak modulation voltage supplied by the AWG in all cases was 0.25 V. This was amplified, and the corresponding bias current for each μLED is shown in Table 1. As shown in Fig. 8(b), the SNR of the UV-B device is lower than that of the other devices. This was expected, as the power output of this device was notably less than that of the other devices. Furthermore, the SNR of the UV-A channel is degraded by optical crosstalk from the UV-B device. This could be mitigated in the future with improved receiver filters. Figure 8(b) shows that approximately 1.30, 1.10, and 1.25 GHz channel bandwidth was accomplished with an SNR > 5 dB for the UV-C, -B, and -A channels, respectively. The large bandwidth available from each WDM channel allows a substantial number of parallel OFDM subcarriers to be used and maximize the achievable data rates.

M-QAM constellation diagrams from each WDM channel are shown in Fig. 9. As shown, the largest constellation sizes used were 32, 16, and 16 for the UV-C, -B, and -A channels, respectively, with corresponding BERs of 1.12×10^{-4}, 2.40×10^{-4}, and 1.36×10^{-4}. A larger constellation could be

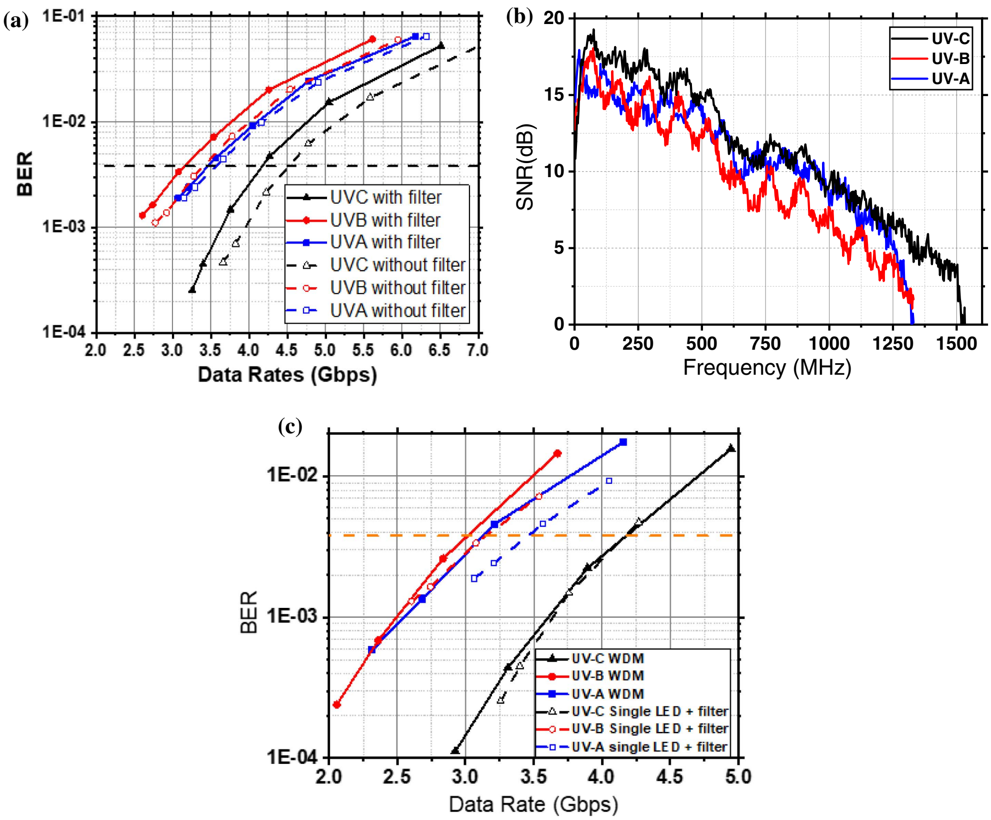

Fig. 8. (a) Comparison of BER when filters are applied to single pixels. (b) SNR of the devices in the WDM setup. (c) BER of three devices in the WDM setup. The dashed horizontal line in (a) and (c) corresponds to a BER of 3.8×10^{-3}.

Table 1. OFDM Parameters and Achieved Data Rates

Device	Operating Current (mA)	Maximum Data Rate (Gbps)
UV-A	30	3.13
UV-B	12	3.02
UV-C	30	4.17
Total		10.32

used on the UV-C channel due to it having higher modulation bandwidth than the UV-A channel and higher output power and SNR than the UV-B device.

The maximum data rates recorded were 4.17, 3.02, and 3.13 Gbps for the UV-C, -B, and -A devices, respectively, as can be seen in Fig. 8(c). The data rates per channel are also given in Table 1, at a BER of approximately 3.8×10^{-3}. The total aggregate WDM data rate achieved was 10.32 Gbps.

The performance of the devices behaved as expected based on the characterization measurements, with the UV-B showing the lowest maximum data rate. As shown in Fig. 2, the UV-B device emits the lowest output power among the three devices shown here. A small fraction of this output power is also lost when combining the three devices' emission together for WDM, due to the less than 100% transmission of the "Alluxa" mirror, as shown in Fig. 6. It also has lower bandwidth than the UV-C device. These factors all contribute to the comparatively low data rate achieved by the UV-B device, even though this device had a higher bandwidth than the UV-A device.

When comparing the BER of the single pixels operating individually with the WDM values, the UV-C device produces similar results in both the WDM and the single device configuration. This can be attributed to the fact that the UV-C experienced the least crosstalk, as the filters and mirrors removed the unwanted light from the UV-B and -A devices. Conversely, the UV-B and UV-A channels show a marked improvement when only one pixel is on. This is due to the spectral overlap resulting in interference from adjacent channels affecting them, which is especially clear in the UV-A channel. The average received powers were estimated using a calibrated optical power meter to be 0.25, 0.03, and 0.10 mW for the UV-A, -B, and -C, respectively. However, due to the difference in active area between the power meter sensor and APD (9 and 0.5 mm diameter, respectively), the actual average received powers are likely to be significantly lower than this.

To the best of our knowledge, the highest optical wireless data rate reported for a single DUV μLED was 2 Gbps obtained by Zhu *et al.* [13] for a UV-C μLED. In the UV-B, Sun *et al.* demonstrated 71 Mbps using an LED [26]. As shown in Table 1, our UV-B and UV-C channels significantly exceed these, and the maximum data rates shown here are, to the best of our knowledge, the highest reported in each of the UV-A, -B, and -C bands. Furthermore, this first demonstration of applying WDM to DUV LEDs allowed the aggregate data rate to

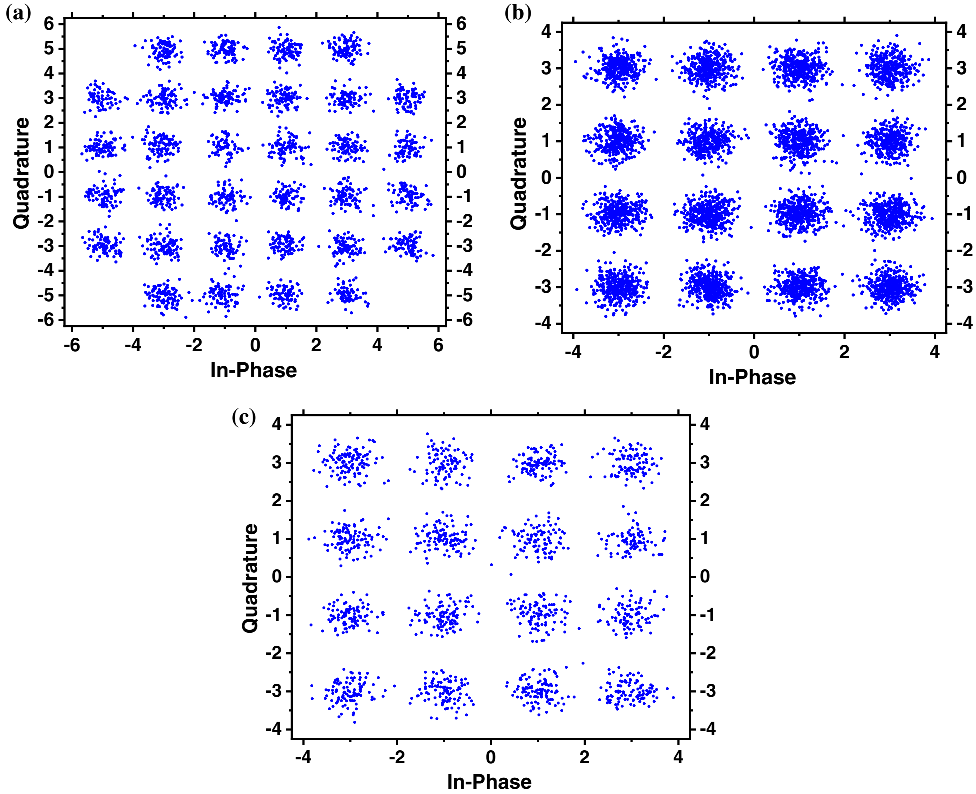

Fig. 9. Maximum *M*-QAM constellation sizes achieved: (a) 32 QAM for UV-C, (b) 16-QAM for UV-B, and (c) 16-QAM for UV-A.

exceed the benchmark of 10 Gbps for the first time using LEDs emitting in the DUV.

5. CONCLUSION

This work has demonstrated a three-channel UV-WDM setup using μLEDs with peak emission in the UV-A (375 nm), UV-B (317 nm), and UV-C (285 nm) regions of the ultraviolet spectrum. Using OFDM and QAM modulation schemes and forward error correction, we achieved data rates of 4.17, 3.02, and 3.13 Gbps from the UV-C, UV-B, and UV-A devices, respectively. The data rates from each individual channel, taken in isolation, represent, to our best knowledge, the highest rates yet reported for a UV μLED and, added together, result in a combined data rate of 10.32 Gbps, demonstrating an LED-based UV optical wireless link exceeding 10 Gbps.

Funding. Engineering and Physical Sciences Research Council (EP/M01326X/1, EP/S001751/1, EP/T00097X/1).

Acknowledgment. We acknowledge Zhixin Semiconductor Co., Ltd. for the LED wafer material. We acknowledge Fraunhofer UK Research Ltd. for DM's PhD studentship funding. All authors declare there are no competing financial interests involved in this work.

Disclosures. The authors declare no conflicts of interest.

Data Availability. The data are available at [27].

REFERENCES

1. H. Haas, "LiFi is a paradigm-shifting 5G technology," Rev. Phys. **3**, 26–31 (2017).
2. D. O'Brien, S. Rajbhandari, and H. Chun, "Transmitter and receiver technologies for optical wireless," Philos. Trans. R. Soc. A **378**, 20190182 (2020).
3. R. J. Drost and B. M. Sadler, "Survey of ultraviolet non-line-of-sight communications," Semicond. Sci. Technol. **29**, 084006 (2014).
4. G. Chen, Z. Xu, and B. M. Sadler, "Experimental demonstration of ultraviolet pulse broadening in short-range non-line-of-sight communication channels," Opt. Express **18**, 10500–10509 (2010).
5. A. Vavoulas, H. G. Sandalidis, N. D. Chatzidiamantis, Z. Xu, and G. K. Karagiannidis, "A survey on ultraviolet C-band (UV-C) communications," Commun. Surveys Tuts. **21**, 2111–2133 (2019).
6. Z. Xu and B. M. Sadler, "Ultraviolet communications: potential and state-of-the-art," IEEE Commun. Mag. **46**, 67–73 (2008).
7. Z. Zhang, M. Kushimoto, T. Sakai, N. Sugiyama, L. Schowalter, C. Sasaoka, and H. Amano, "A 271.8 nm deep-ultraviolet laser diode for room temperature operation," Appl. Phys. Express **12**, 8–12 (2019).
8. H. S. Wasisto, J. D. Prades, J. Gülink, and A. Waag, "Beyond solid-state lighting: miniaturization, hybrid integration, and applications of GaN nano-and micro-LEDs," Appl. Phys. Rev. **6**, 041315 (2019).
9. G.-R. Lin, H.-C. Kuo, C.-H. Cheng, Y.-C. Wu, Y.-M. Huang, F.-J. Liou, and Y.-C. Lee, "Ultrafast 2×2 green micro-LED array for optical wireless communication beyond 5 Gbit/s," Photon. Res. **9**, 2077–2087 (2021).
10. D. Peng, K. Zhang, and Z. Liu, "Design and fabrication of fine-pitch pixelated-addressed micro-LED arrays on printed circuit board for display and communication applications," IEEE J. Electron Devices Soc. **5**, 90–94 (2017).
11. R. P. Green, J. J. D. McKendry, D. Massoubre, E. Gu, M. D. Dawson, and A. E. Kelly, "Modulation bandwidth studies of recombination processes in blue and green InGaN quantum well micro-light-emitting diodes," Appl. Phys. Lett. **102**, 091103 (2013).

12. M. S. Islim, R. X. Ferreira, X. He, E. Xie, S. Videv, S. Viola, S. Watson, N. Bamiedakis, R. V. Penty, I. H. White, A. E. Kelly, E. Gu, H. Haas, and M. D. Dawson, "Towards 10 Gb/s orthogonal frequency division multiplexing-based visible light communication using a GaN violet micro-LED," Photon. Res. **5**, A35–A43 (2017).
13. S. Zhu, P. Qiu, Z. Qian, X. Shan, Z. Wang, K. Jiang, X. Sun, X. Cui, G. Zhang, D. Li, and P. Tian, "2 Gbps free-space ultraviolet-C communication based on a high-bandwidth micro-LED achieved with pre-equalization," Opt. Lett. **46**, 2147–2150 (2021).
14. C. Jeon, H. W. Choi, E. Gu, M. D. Dawson, and S. Member, "High-density matrix-addressable AlInGaN-based 368-nm microarray light-emitting diodes," IEEE Photon. Technol. Lett. **16**, 2421–2423 (2004).
15. B. Guilhabert, D. Massoubre, E. Richardson, J. J. D. McKendry, G. Valentine, R. K. Henderson, I. M. Watson, E. Gu, and M. D. Dawson, "Sub-micron lithography using InGaN micro-LEDs: mask-free fabrication of LED arrays," IEEE Photon. Technol. Lett. **24**, 2221–2224 (2012).
16. X. He, E. Xie, M. S. Islim, A. A. Purwita, J. J. D. McKendry, E. Gu, H. Haas, and M. D. Dawson, "1 Gbps free-space deep-ultraviolet communications based on III-nitride micro-LEDs emitting at 262 nm," Photon. Res. **7**, B41–B47 (2019).
17. R. X. G. Ferreira, E. Xie, J. J. D. McKendry, S. Rajbhandari, H. Chun, G. Faulkner, S. Watson, A. E. Kelly, and E. Gu, "High bandwidth GaN-based micro-LEDs for multi-Gb/s visible light communications," IEEE Photon. Technol. Lett. **28**, 2023–2026 (2016).
18. H. Amano, R. Collazo, C. D. Santi, S. Einfeldt, M. Funato, J. Glaab, S. Hagedorn, A. Hirano, H. Hirayama, R. Ishii, Y. Kashima, R. Kirste, M. Kneissl, R. W. Martin, F. Mehnke, M. Meneghini, A. Ougazzaden, P. Parbrook, S. Rajan, and P. Reddy, "The 2020 UV emitter roadmap," J. Phys. D **53**, 503001 (2020).
19. M. Kneissl, T. Y. Seong, J. Han, and H. Amano, "The emergence and prospects of deep-ultraviolet light-emitting diode technologies," Nat. Photonics **13**, 233–244 (2019).
20. S. W. H. Chen, Y.-M. Huang, Y.-H. Chang, Y. Lin, F.-J. Liou, Y.-C. Hsu, J. Song, J. Choi, C.-W. Chow, C.-C. Lin, R.-H. Horng, Z. Chen, J. Han, T. Wu, and H.-C. Kuo, "High-bandwidth green semipolar (20-21) InGaN/GaN micro light-emitting diodes for visible light communication," ACS Photon. **7**, 2228–2235 (2020).
21. D. Tsonev, H. Chun, S. Rajbhandari, J. J. D. McKendry, S. Videv, E. Gu, and M. Haji, "A 3-Gb/s single-LED OFDM-based wireless VLC link using a gallium nitride μLED," IEEE Photon. Technol. Lett. **26**, 637–640 (2014).
22. J. F. C. Carreira, E. Xie, R. Bian, J. Herrnsdorf, H. Haas, E. Gu, M. J. Strain, and M. D. Dawson, "Gigabit per second visible light communication based on AlGaInP red micro-LED micro-transfer printed onto diamond and glass," Opt. Express **28**, 12149–12156 (2020).
23. H. Ding, G. Chen, A. K. Majumdar, B. M. Sadler, and Z. Xu, "Modeling of non-line-of-sight ultraviolet scattering channels for communication," IEEE J. Sel. Areas Commun. **27**, 1535–1544 (2009).
24. X. Liu, Z. Wei, M. Li, L. Wang, Z. Liu, C. Yu, L. Wang, Y. Luo, and H. Y. Fu, "Experimental investigation of 16.6 Gbps SDM-WDM visible light communication based on a neural network receiver and tricolor mini-LEDs," Opt. Lett. **46**, 2888–2891 (2021).
25. G. Cossu, A. M. Khalid, P. Choudhury, R. Corsini, and E. Ciaramella, "3.4 Gbit/s visible optical wireless transmission based on RGB LED," Optics Express **20**, B501–B506 (2012).
26. X. Sun, Z. Zhang, A. Chaaban, T. K. Ng, C. Shen, R. Chen, J. Yan, H. Sun, X. Li, J. Wang, J. Li, M.-S. Alouini, and B. S. Ooi, "71-Mbit/s ultraviolet-B LED communication link based on 8-QAM-OFDM modulation," Opt. Express **25**, 23267–23274 (2017).
27. https://doi.org/10.15129/1899e15a-2d46-4e80-9d3f-93f3b66abeb7.

Research Article | Vol. 30, No. 26 / 19 Dec 2022 / Optics Express 46811

Optics EXPRESS

Hundred-meter Gb/s deep ultraviolet wireless communications using AlGaN micro-LEDs

DANIEL M. MACLURE,[1,3,*] CHENG CHEN,[2,3,4] JONATHAN J. D. MCKENDRY,[1,3] ENYUAN XIE,[1] JORDAN HILL,[1] JOHANNES HERRNSDORF,[1] ERDAN GU,[1] HARALD HAAS,[2] AND MARTIN D. DAWSON[1]

[1] *Institute of Photonics, Department of Physics, SUPA, University of Strathclyde, Glasgow G1 1RD, UK*
[2] *LiFi Research and Development Centre, Department of Electronic & Electrical Engineering, The University of Strathclyde, Glasgow G1 1RD, UK*
[3] *These authors contributed equally to this work.*
[4] *c.chen@strath.ac.uk*
[*] *daniel.maclure@strath.ac.uk*

Abstract: We demonstrate the use of deep ultraviolet (DUV) micro-light-emitting diodes (LEDs) for long-distance line-of-sight optical wireless communications. With a single 285 nm-emitting micro-LED, we have respectively achieved data rates greater than 6.5 Gb/s at a distance of 10 m and 4 Gb/s at 60 m. Moreover, we obtained >1 Gb/s data rates at a distance of 116 m. To our knowledge, these results are the highest data rates at such distances thus far reported using DUV micro-LEDs and the first demonstration of Gb/s communication at >100 m using any micro-LED-based transmitter.

1. Introduction

Radio frequency (RF) communications technology is, on its own, unlikely to meet the ever-growing demand for wireless data transmission [1]. There is thus a move towards alternative communication systems such as optical wireless communications (OWC) [2] to complement the existing RF infrastructure. These new OWC systems utilize an additional license-free region of the EM spectrum and can also benefit communications applications in sectors such as defense [3] and financial services. In recent years, the extension of OWC to the deep ultraviolet (DUV, 200-315 nm) has seen increased interest as the atmosphere attenuates and scatters DUV more strongly than at longer wavelengths [4,5]. As the upper atmosphere absorbs nearly all of the DUV region of the electromagnetic spectrum, it is a good candidate for secure inter-satellite communications as the signal is hidden from ground observers [6]. Moreover, this allows DUV terrestrial communications links to operate in a near noise-free environment [7]. Furthermore, due to the strong Rayleigh and Mie scattering of DUV by the atmosphere, it is possible to use DUV in a non-line-of-sight (NLOS) configuration [8,9]. Diffuse LOS and NLOS OWC could help overcome obstacles blocking the communication channel and relax constraints on pointing and tracking between transmitters and receivers [7]. Initial work in the DUV focused on low bandwidth mercury flash lamps, however, in recent years, high-quality UV lasers and light-emitting diodes (LEDs) have been developed, which provide new opportunities in DUV communications.

Micro-LEDs (μLEDs) are LED devices with active region a few microns to several 10's of microns in size. These devices are under intensive development for numerous applications [10], such as micro-displays [11] and small size, weight, and power (low SWaP) optical communications

#475049 https://doi.org/10.1364/OE.475049
Journal © 2022 Received 7 Sep 2022; revised 24 Oct 2022; accepted 10 Nov 2022; published 8 Dec 2022

Corrected 24 April 2023

Optics EXPRESS

[12]. There are several benefits to using µLEDs in OWC, such as their reduced capacitance [13,14]. As a result, the carrier lifetime of the devices substantially defines the bandwidth, allowing for modulation bandwidths of many hundreds of MHz to above a GHz, compared to around 10 MHz for a conventional LED format [15]. This higher bandwidth is advantageous in communications, resulting in high data rates due to the resulting increased channel capacity [16]. In previous work, most µLED or LED OWC demonstrations were limited to distances of a few meters [6,17,18], with the research largely being focused on high data rate 'benchtop' systems using a variety of modulation techniques. Here, by optimizing a wide range of device and systems parameters, we demonstrate Gb/s data rates at >100 m transmission distances using a single DUV µLED pixel with a peak emission wavelength of approximately 285 nm. Furthermore, we demonstrate the ability to transmit these high data rates with relatively low power (on the order of µWatts), and we demonstrate the ability of µLED communication systems to operate in ambient light (see Section 4). We also examine the effect of peak-to-peak voltage (VPP) and bit loading on the data rate. Finally, at all distances recorded we achieved Gb/s data rates and these results are, to our knowledge, the highest data rates at the longest distances reported using a single DUV µLED pixel.

2. Devices and characterization

2.1. µLED device design and fabrication

The device used in this work is an 8-segment concentric array of individually addressable trapezoidal-shaped µLEDs, each with an approximate active area of 1369 μm^2 (equivalent area to a circular pixel of diameter ~40 µm). The benefits and features of this pixel geometry were presented in previous publications [6,17,19]. Similarly, the device structure chosen was the same as described in [17], which had been previously shown empirically to be a pixel size and design that provided a good compromise between output power and modulation bandwidth. The devices are made from AlGaN-based LED epistructures grown on a c-plane sapphire substrate, the substrate being optically polished afterwards. The pixels were mesa etched, with individually addressable anodes and a shared cathode, and with an insulating layer surrounding the mesa. The pixels are configured to operate in a flip-chip configuration with the light emitted through the transparent sapphire substrate. The pixel has a six-period quantum well (QW) active region of AlGaN, the n-type layer comprises of 2µm-thick AlGaN, and the p-type layer consists of 310nm-thick p-doped GaN. Further details of the epi-structure are provided in our previous work [6].

2.2. µLED characterization

To measure the device's light output and current versus voltage (L-I-V) characteristics, the individual µLED pixels and an optical power meter were aligned in close proximity. We collected the light from the front of the device, i.e., from the sapphire substrate side, which is the format used in the communications setup described below. The optical power was measured using a calibrated optical power meter (Thorlabs PM100A) and sensor (S120VC), and the current and voltage were recorded using a Yokogawa GS610 Source-Measure Unit. The spectra were measured using a spectrometer (Aventes Avaspec-2048) and collection fiber-optic (Ocean Optics© QP600-2-SR-BX fiber). The modulation bandwidth was measured using an avalanche photodiode (APD, Hamamatsu C5668 8867 with a -3 dB bandwidth of 1 GHz), two 2" lenses (Edmund Optics 84340) set around 19 cm apart, and a network analyzer (PicoVNA 106, 300kHz-6 GHz bandwidth) to record the frequency response. The bandwidth was estimated by measuring the frequency corresponding to a -3 dB decrease from the 1 MHz point, as detailed in [17]. The L-I characteristic (Fig. 1(a)) of a representative µLED pixel demonstrates a through-sapphire directed output power of around 0.4 mW at a current of 20 mA. The turn-on voltage (Fig. 1(a)), around 7.8 V (at

1 mA current), is improved from our previous work but still shows effects of the poor electrical conductivity of AlGaN layers, an issue widely reported for DUV LEDs [20]. The L-I-V curve is used to help determine the optimum bias point of the µLED for the communications system demonstration (which uses direct current optical orthogonal frequency-division multiplexing, DCO-OFDM), as described in Section 3.

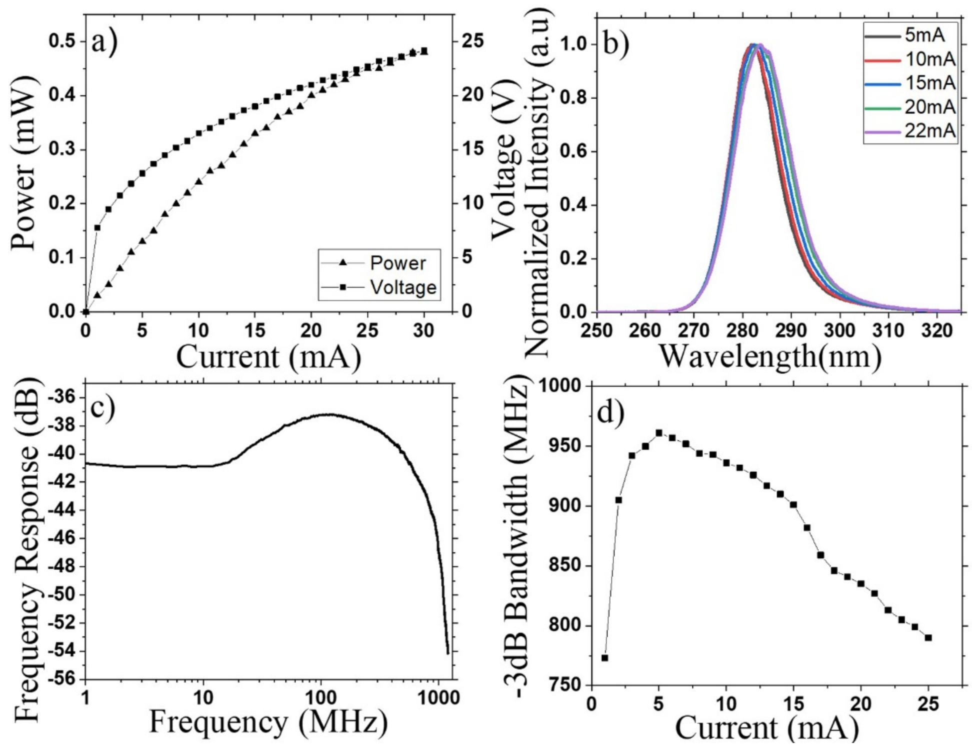

Fig. 1. Pertinent characteristics of the µLED pixels, (a) LIV characteristics, (b) normalized spectra for a range of drive currents. (c) Representative frequency response curve measured at 20 mA and (d) modulation bandwidth.

The µLED electroluminescence (EL) spectra versus current are shown in Fig. 1(b) for a representative single pixel. The µLED device has a peak emission wavelength of around 285 nm at 20 mA. The EL full width half maximum (FWHM) is approximately 10 nm, and as a result, the spectra cover part of both the UVB (280-315 nm) and UVC (100-280 nm) regions of the spectrum. The spectra of the µLEDs are relatively stable with current, with slight redshifts and small changes in the FWHM of the device, influenced by numerous factors such as band filling, field screening and thermal effects as observed in similar devices [21]. The small-signal frequency response measured at a bias of 20 mA is shown in Fig. 1(c). This is the same bias as used to obtain the data transmission results as will be shown in Section 4. As in previous work [17] we observe a slight kink in the 1-100 MHz region of the frequency response, which we are currently investigating. We assume the bandwidth response at 100 m is similar to that at short distances. From this the -3 dB electrical-electrical (E-E) modulation bandwidth of the devices was recorded, with a maximum of around 960 MHz being achieved (see Fig. 1(d)). However, we observed that the bandwidth gradually decreases to approximately 800 MHz as the current is increased to 20 mA. We tentatively attribute this to the effects of increased current density dependent carrier overflow from the MQWs resulting in increased carrier lifetimes [20]. This is still under investigation, however it has been noted in our other DUV devices and at higher

Optics EXPRESS

current densities in our UVA devices. The bandwidth measurements are crucial in OWC for optimizing pilot signals and bit loading, as will be discussed in Section 3.

3. DCO-OFDM setup

3.1. Experimental setup of the DCO-OFDM data link

A UV-enhanced APD (Hamamatsu C56688867) with a bandwidth of 1 GHz, and a nominal responsivity of 7 A/W at 280 nm, was used as a receiver, and an oscilloscope (Keysight MXR608A sampling rate, 16 GSamples/s; analog bandwidth, 6 GHz) captured the received signal for analysis. A laptop was used to generate the digital transmitted signal, analyze the received signal and set the parameters such as the peak-to-peak voltage (VPP). To facilitate the long-distance measurements, the µLED transmitter (Tx) and the receiver (Rx) were placed side-by-side, facing in parallel with a metal sheet placed between them to prevent interference (Fig. 2 shows the view down the optical channel with the metal sheet edge-on in the center). A 5.08 cm × 5.08 cm UV-enhanced aluminum mirror (PFSQ20-03-F01) with an average reflectance of approximately 90% was used to reflect the optical signal from the Tx back to the Rx, and this double-pass configuration allowed the total path length to be increased up to 116 m. This mirror was mounted on a Thorlabs Kinematic mount (KM200S) which enabled fine alignment of the mirror. Kinematic mounts were used on the Tx, Rx, and mirror to assist with the alignment of all the optical components where the lenses remained stationary, and the LED and detector were moved ±5 mm to carefully optimize the received signal strength at each distance.

Fig. 2. Photographic view of the optical channel, with the micro-LED transmitter on the right and the APD receiver on the left. Inset is a close-up view of the mirror used to retro-reflect the optical signal to increase the path length.

The optical setup used in this work included two 2” diameter fused silica lenses (Edmund Optics 84340 with a numerical aperture of 0.63 and transmittance of 90% at 280 nm) one to collimate the light from the µLED array and the other to focus the returned light onto the receiver. To power the µLEDs, a Yokogawa GS610 power supply was used. For the data transmission, an arbitrary waveform generator (AWG) converts the digital signal to an analog voltage signal (Keysight M8195A, sampling rate 65 GSamples/s; analog bandwidth, 25 GHz;), and the signal from the AWG was amplified (amplifier SHF-S126A), and finally, the RF signal and DC supply were combined using a bias tee (Tektronix PSPL5675A). We use DCO-OFDM for intensity modulation / direct detection (IM/DD) in this work as it allows the use of higher order modulation such as M-QAM (quadrature amplitude modulation), where M denotes the number of constellation points.

Optics EXPRESS

Moreover, the underlying DCO-OFDM technique can effectively be implemented with digital signal processors (DSPs) [22]. Furthermore, DCO-OFDM, in conjunction with optimum bit and power loading, achieves very high data rates compared to other modulation techniques [23]. The parameters used are shown in Table 1 and were selected with particular care based on empirical optimization guided by theoretical considerations. The implementation steps are shown in Fig. 3. We used DCO-OFDM and applied bit and power loading per subcarrier to maximize the overall data rate given the achieved signal-to-noise ratio (SNR) per subcarrier. This approach enables us to modulate the channel beyond the -3 dB bandwidth of the system. Once the optical alignment was optimized, the bias of the μLED was increased to 20 mA, a bias current that provided an optimal trade-off between increased μLED output power and bandwidth (c.f. Fig. 1), operating in a relatively linear region of the μLED output power versus voltage response. Moreover, we aimed to select a current value that would not damage the device in the long term. The background lighting was turned off in order to aid alignment.

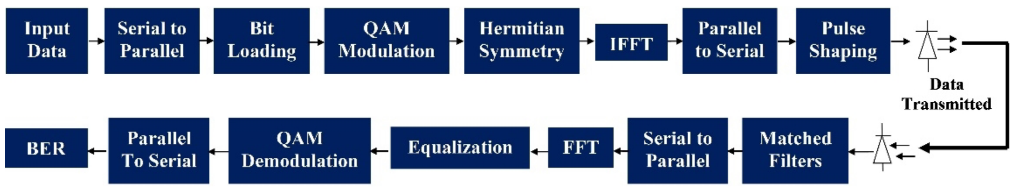

Fig. 3. Block diagram of the DCO-OFDM transmission system.

Table 1. OFDM parameters used in this work.

Name of Variable	Value of Parameter
Sampling frequency (MHz)	16000
Sample per symbol	5
Symbol span	64
Roll off factor	0.1
FFT Size	2048
Cyclic prefix length	15
Cyclic suffix length	5
Lower clipping	-3.2σ
Upper clipping	3.2σ

The VPP was then scanned to pick out the optimum peak-to-peak voltage VPP to use in the experiment to minimize signal clipping and allow us to use the full dynamic range of the μLED. As the transmission distance was increased, the received SNR decreased, primarily due to beam divergence. As a result, the VPP was optimized at each measured distance. Once the VPP was selected, the modulation scheme was applied to a pseudorandom bit stream. The DCO-OFDM time-domain signal clipping level was chosen to be 3.2 times the standard deviation (σ) of the unclipped signal [24] and this enabled us to achieve the highest data rate from the available dynamic range [25]. A fast Fourier transform (FFT) size of 2048 was used to enable 1023 information-carrying subcarriers. This setting leads to a smaller cyclic prefix to FFT size ratio, which means that the redundant cyclic prefix symbols are transmitted less frequently. The larger FFT size results in increased peak-to-average-power-ratio (PAPR). However, In the experiments, we found that a clipping level of 3.2 achieves a good trade-off between PAPR and nonlinear distortion. The suffix and prefix were used to create a circular convolution between the signal and response so that one-tap equalization is valid and prevents interference between the adjacent

Optics EXPRESS

OFDM frames. The suffix and prefix lengths are essential to this work as the channel is frequency selective with low pass effects possibly coming from the LED and detector. Single tap frequency domain equalization was used.

In the first stage of implementation (Fig. 3), a pilot wave was used to assess channel quality, and after this, the bit and power loading was carried out. The data input was initially in a serial form and was changed to parallel channels. M-QAM then converts the signal to phase and amplitude. After this, an inverse fast Fourier transform (IFFT) was applied to convert the signal from the frequency domain to the time domain. This result is then converted back to serial for transmission. On the receiver side, a matched filter was used before equalization and data decoding. From this, we compared the received signal vs. the signal transmitted and determined the bit error ratio (BER). We considered forward error correction (FEC) coding with a 7% overhead. Furthermore, we assume a BER threshold of 3.8×10^{-3} for error-free data reception after FEC [24]. When selecting the SNR and Channel gain, multiple adaptive tests were run. Furthermore, we also examined the non-linear (NL) distortion of the µLED and the receiver noise when examining the SNR.

4. Communication results

4.1. Received power vs. distance

The received optical power focused on the detector is crucial as it determines the SNR and consequently the data rate. The first step in the DCO-OFDM measurement was therefore to examine the power being received by the detector (see Fig. 4).

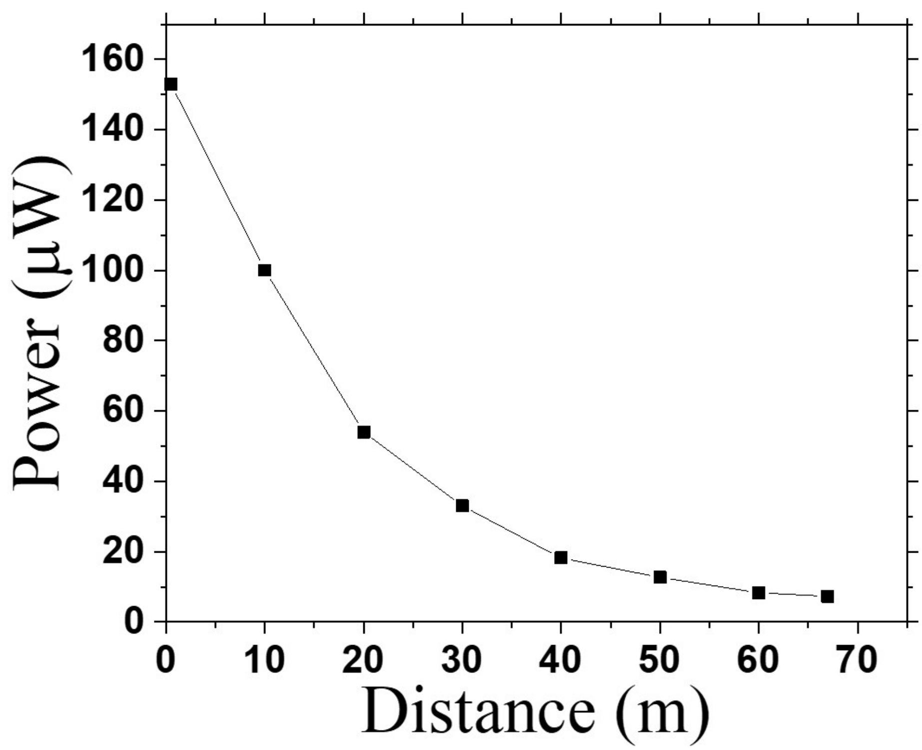

Fig. 4. The received optical power vs. distance, measured with a 300 µm pinhole.

The power was measured using the same power meter used in the L-I measurements, to which a 300 µm pinhole (Thorlabs P300K) was added. This was done in order to reduce the active area of the power meter to the same size as that of the APD. It can be seen in Fig. 4 that the power remains relatively high below 12 m, and only beyond this distance does the intensity of the central spot noticeably decrease, attributed to a combination of beam divergence and the criticality of alignment. After 60 m, we were close to the sensitivity limit of the power meter, so it was not possible to accurately measure the power at greater distances. However, based on the trend data, we assume that the power is on the order of 100s of nanowatts at 116 m. The power measurements were used as a guide to the distances at which we could usefully transmit data.

4.2. Optical communication results

Before transmitting and recording any data, the setup was aligned at each measured distance using a reference sine wave to achieve the optimal SNR (see Fig. 5(a)). The µLED was biased with 20 mA, this current being selected as described above, and VPP value of the AWG output was adjusted. In Fig. 5(a) we observe that a low-pass characteristic of the achieved SNR against frequency can be observed. Due to the wide modulation bandwidth of the designed device, the rate of decrease of SNR with frequency is lower compared to commercial broad area LEDs. Moreover, we observe that as the distance increases, the SNR decreases as the signal becomes weaker, primarily due to beam divergence. At these 10's of meter distances, DUV absorption and scattering are not considered to have a significant impact. It is interesting to note that the SNR remains relevantly constant under 10 m (see Fig. 5(a)). To test whether the alignment of the mirror was causing this, we removed the mirror for the 0.5 m set up and used a simple back-to-back bench top set up for reference. However, we saw no improvement in the SNR, which suggests that the data rate may be capped. It is difficult to specify what power would produce a particular data rate, as increases in power do not predictably increase the data rate due to issues such as the nonlinearity of the device, spot size on the detector and noise from the transmitter side, which can cap the SNR and the data rate. However, as the distance increases, the data rate drops rapidly between 10 m – 40 m, although this stabilizes between 40 m – 60 m.

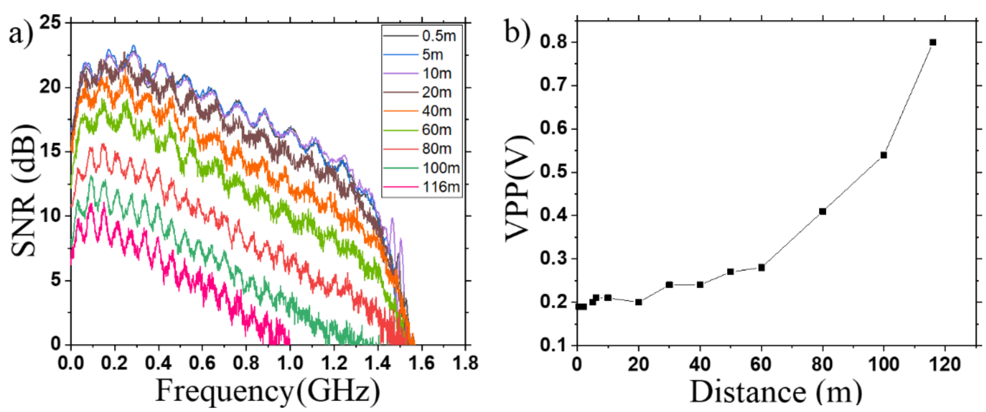

Fig. 5. (a) SNR vs. frequency at different distances and (b) optimal VPP vs. distance.

The selection of VPP leads to a trade-off between signal strength and NL signal distortion [26]. When applying a greater VPP to the µLED, the optical signal has a higher modulation depth so that the signal strength is boosted. However, the µLED device has a nonlinear behaviour as shown in Fig. 1(a). A greater VPP also means using a greater dynamic range which leads to severer nonlinear distortion. When the link distance is short (under 10 m), the path loss is small, and the SNR is limited by NL distortion. Therefore, a smaller optimal VPP has been found to overcome dominant NL distortion. When the link distance is very large (100 m), the significant optics- and alignment-dependent path loss makes the SNR limited by receiver noise. Therefore, the optimal VPP at these distances is higher. In Fig. 5(b) the optimal VPP supplied by the AWG remains relatively constant around a value of 0.2 V with only minor changes under 20 m. However, as the distance approaches 100 m, the VPP increases rapidly to around 0.5 V. The amplifier has a typical gain of 29 dB and from Fig. 1(a), this gain could put us in a non-linear regime for the device. Furthermore, the ripple features seen in the SNR, as shown in Fig. 5(a), could be a result of impedance mismatch effects between the µLED and drive electronics.

The bit loading algorithm is based on the Hughes-Hartogs algorithm [27]. In that approach, using a given amount of transmission energy, it is possible to load as many bits as possible onto the subcarriers and maintain a targeted BER. As a result, this algorithm can maximize the achievable data rate and adapt to various channel conditions. Figure 6(a) and Fig. 6(b) respectively demonstrate the number of bits loaded at the lowest BER data points at 10 m and 100 m. As Fig. 6(a) shows, 4 or 5 bits could be loaded at shorter distances as the SNR is relatively high. However, as Fig. 6(b) shows, at approximately 100 m, this dropped to 1 or 2 bits due to the decrease in the SNR. Figure 6(a) and Fig. 6(b) show that no bit is loaded to subcarriers at SNR lower than approximately 2 dB. Due to the low pass characteristics of the device, fewer bits can be loaded on the high frequency subcarriers. In Fig. 7, we discuss the data rates achieved using this method.

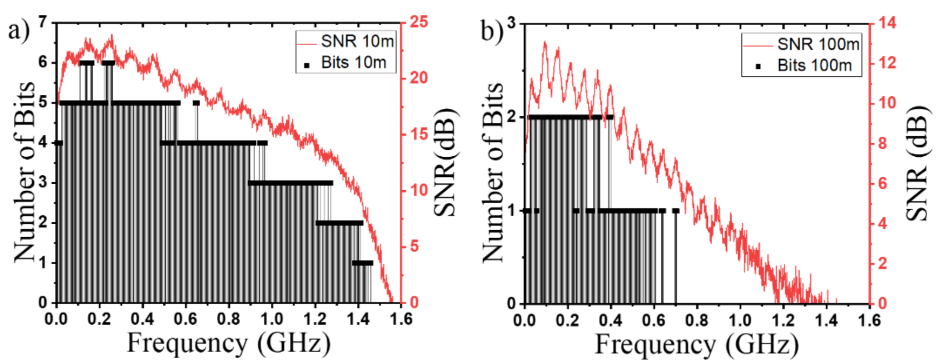

Fig. 6. SNR and bits loaded vs frequency at distances of (a) 10 m and (b) 100 m.

We examined the data rate below a BER of approximately 3.8×10^{-3}, which allows for the application of forward error correction (FEC) (represented by the horizontal dashed line in Fig. 7(a)). Under 10 m, the data rate was relatively constant at greater than 6 Gb/s (see Fig. 7(b)) with approximately 6.94 Gb/s achieved (6.45 Gb/s with 7% overhead applied) at 10 m. As the distance increases, the data rate decreases approximately linearly as shown in Fig. 7(b), although it is important to note that the VPP was optimized at each distance to attempt to compensate for signal loss due to beam divergence. The maximum link distance of 116 m was limited by the available laboratory corridor space. At this distance, a data rate of approximately 1.20 Gb/s (1.12 Gb/s with 7% overhead applied) was obtained. To the best of our knowledge, this represents the first demonstration of a data rate >1 Gb/s at >100 m using a single DUV µLED, and the longest distance at which 1 Gb/s has been achieved using a µLED of any wavelength. After completing the measurements in a darkened corridor, we repeated the 116 m measurement in ambient light. This had little effect on the data rate, with a data rate of 1.19 Gb/s (1.11Gb/s with 7% correction) at 116 m being recorded. The light shielding of the components and their tight and carefully controlled optical alignment may be a factor here. This shows promise for practical free-space communications applications of these devices in such as arena, warehouse, and factory environments.

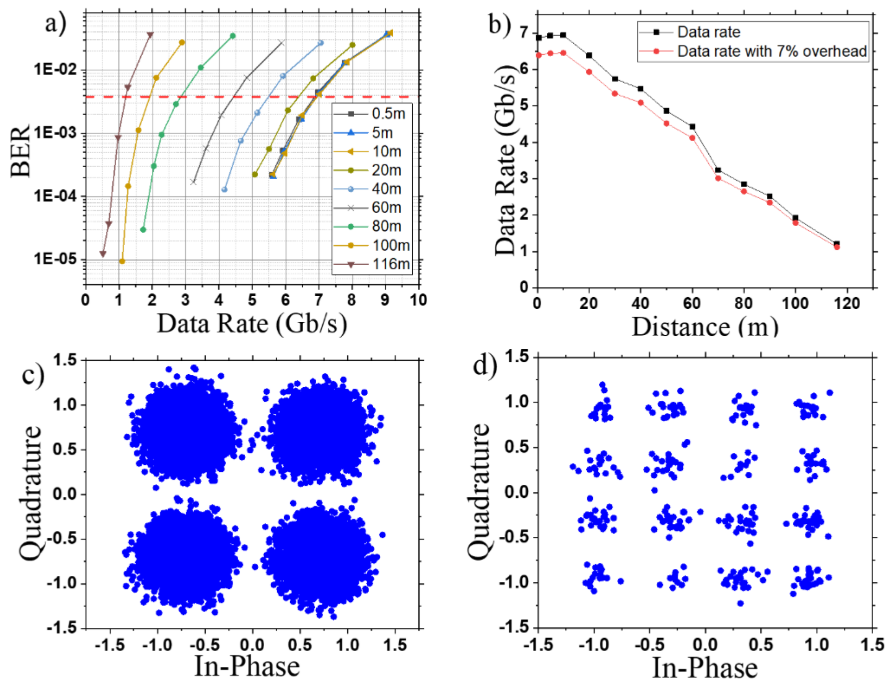

Fig. 7. (a) BER vs. data rate (dashed line represents a BER of 3.8×10^{-3}). (b) Data rate vs. distance. (c) 4-QAM constellation at 70 m. (d) 16-QAM constellation at 70 m.

A detailed study of all the link parameters such as transmitter area, beam divergence angle etc. is beyond the scope of the technology demonstrator shown here. However, long transmission distances were achieved here through careful consideration of the optics used, to ensure sufficient

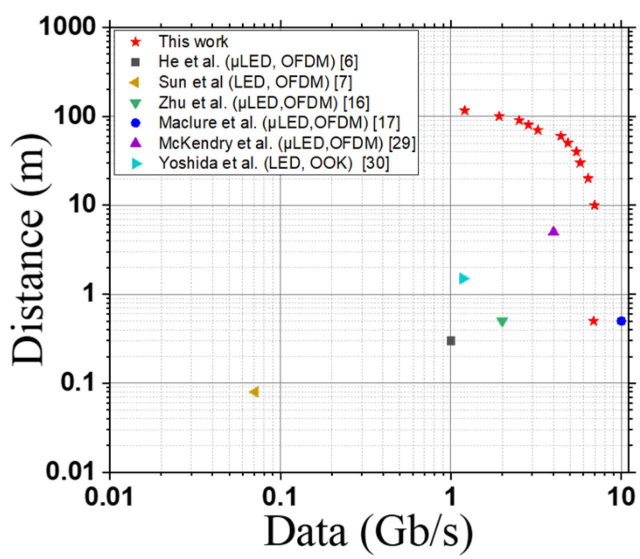

Fig. 8. Comparison of the results obtained here to selected previous work in the literature.

received optical power, guided by modelling of the long-distance link using commercial ray-tracing software (Zemax OpticStudio). A detailed study on the optimisation of device parameters and modulation schemes for optical wireless communication may be found in work by H. Chun et al. [28]. When compared with results from the literature in Fig. 8 [6,7,16,17,29,30], it is evident that this work has demonstrated the possibility of using µLED-based DUV communications for > 100 m high data rate applications. We have achieved similar Gb/s data rates but at much greater distances: in some cases, × 10 greater. Several important developments have been implemented to facilitate this. We have improved the fabrication, contacting and operation of the µLED devices, increasing the available (through-sapphire-directed) single-µLED optical output power by a factor of approximately 2.5× from 200 µW [6] to 500 µW. We have also introduced higher numerical aperture optics (using 2-inch lenses here, compared to 1-inch previously).

Furthermore, we have taken particular care over the optical alignment and parameter optimization (including VPP) for the DCO-OFDM protocol, and we have used a receiver with higher bandwidth (1 GHz vs 400 MHz) which has helped in the detection of DUV data rates up to approximately 6.94 Gb/s. We note that the transmission distances demonstrated here were limited by the available laboratory corridor space and not by the intrinsic performance of the system. Even longer transmission distances should thus be achievable, although at increasing distances the effects of atmospheric absorption and scattering will increasingly affect the optical channel. This high data rate line-of-sight (LOS) work, as well as being applicable in its own right, is informing possible NLOS performance improvements for applications such as secure military communications [3].

5. Conclusion

By careful and detailed optimization of the devices, optical system and communications parameters, we have demonstrated that DUV µLEDs can be used for Gb/s free-space communications at distances of over 100 m in a manner not obviously affected by ambient light. Overall, our results show new optical communication capabilities for DUV µLEDs. Such performance at this distance is a benchmark for OWC application of µLEDs in such practical situations as office environments, lecture theaters, arenas, and warehouses. Furthermore, it gives indications of the potential use of such µLEDs in space-based applications and provides characterization data and design parameters to inform the implementation of high-performance non-line-of-sight communications systems.

Funding. Fraunhofer UK Research Ltd.; Engineering and Physical Sciences Research Council (EP/T00097X/1).

Acknowledgment. We acknowledge Zhixin Semiconductor Co., Ltd. for the LED wafer material. All authors declare there are no competing financial interests involved in this work.

Disclosures. The authors declare no conflicts of interest.

Data availability. The data are available in Ref. [31].

References

1. H. Haas, "LiFi is a paradigm-shifting 5 G technology," Rev. Phys. **3**, 26–31 (2018).
2. I. K. Son and S. Mao, "A survey of free space optical networks," Digit. Commun. Netw **3**(2), 67–77 (2017).
3. D. Moriarty and B. Hombs, "System design of tactical communications with solar blind ultraviolet non line-of-sight systems," *Military Communications Conference* 1–7 (IEEE, 2009).
4. A. Vavoulas, H. G. Sandalidis, N. D. Chatzidiamantis, Z. Xu, and G. K. Karagiannidis, "A Survey on Ultraviolet C-Band (UV-C) Communications," IEEE Commun. Surv. Tutorials **21**(3), 2111–2133 (2019).
5. T. Y. Aung, S. Arya, and Y. H. Chung, "Performance dependence of non-line-of-sight ultraviolet communications on atmospheric parameters of the ultraviolet channel," Opt. Commun. **443**, 7–11 (2019).
6. X. He, E. Xie, M. S. Islim, A. A. Purwita, J. J. D. McKendry, E. Gu, H. Haas, and M. D. Dawson, "1 Gbps free-space deep-ultraviolet communications based on III-nitride micro-LEDs emitting at 262 nm," Photonics Res. **7**(7), B41 (2019).
7. X. Sun, Z. Zhang, A. Chaaban, T. K. Ng, C. Shen, R. Chen, J. Yan, H. Sun, X. Li, J. Wang, J. Li, M.-S. Alouini, and B. S. Ooi, "71-Mbit/s ultraviolet-B LED communication link based on 8-QAM-OFDM modulation," Opt. Express **25**(19), 23267 (2017).

Optics EXPRESS

8. V. V. Belov, I. Juwiler, N. Blaunstein, M. V. Tarasenkov, and E. S. Poznakharev, "NLOS communication: Theory and experiments in the atmosphere and underwater," Atmosphere **11**(10), 1122 (2020).
9. D. Han, Y. Liu, K. Zhang, P. Luo, and M. Zhang, "Theoretical and experimental research on diversity reception technology in NLOS UV communication system," Opt. Express **20**(14), 15833 (2012).
10. J. Y. Lin and H. X. Jiang, "Development of microLED," Appl. Phys. Lett. **116**(10), 100502–8 (2020).
11. J. F. C. Carreira, E. Xie, R. Bian, J. Herrnsdorf, H. Haas, E. Gu, M. J. Strain, and M. D. Dawson, "Gigabit per second visible light communication based on AlGaInP red micro-LED micro-transfer printed onto diamond and glass," Opt. Express **28**(8), 12149 (2020).
12. A. D. Griffiths, J. Herrnsdorf, M. J. Strain, and M. D. Dawson, "Scalable visible light communications with a micro-LED array projector and high-speed smartphone camera," Opt. Express **27**(11), 15585 (2019).
13. J. J. D. McKendry, R. P. Green, A. E. Kelly, Z. Gong, B. Guilhabert, D. Massoubre, E. Gu, and M. D. Dawson, "High-speed visible light communications using individual pixels in a micro light-emitting diode array," IEEE Photonics Technol. Lett. **22**(18), 1346–1348 (2010).
14. G.-R. Lin, H.-C. Kuo, C.-H. Cheng, Y.-C. Wu, Y.-M. Huang, F.-J. Liou, and Y.-C. Lee, "Ultrafast 2×2 green micro-LED array for optical wireless communication beyond 5 Gbit/s," Photonics Res. **9**(10), 2077 (2021).
15. Y. Huang, Z. Guo, H. Huang, and H. Sun, "Influence of Current Density and Capacitance on the Bandwidth of VLC LED," IEEE Photonics Technol. Lett. **30**(9), 773–776 (2018).
16. S. Zhu, P. Qiu, Z. Qian, X. Shan, Z. Wang, K. Jiang, X. Sun, X. Cui, G. Zhang, D. Li, and P. Tian, "2 Gbps free-space ultraviolet-C communication based on a high-bandwidth micro-LED achieved with pre-equalization," Opt. Lett. **46**(9), 2147 (2021).
17. D. M. Maclure, J. J. D. McKendry, M. S. Islim, E. Xie, C. Chen, X. Sun, X. Liang, X. Huang, H. Abumarshoud, J. Herrnsdorf, E. Gu, H. Haas, and M. D. Dawson, "10 Gbps wavelength division multiplexing using UV-A, UV-B, and UV-C micro-LEDs," Photonics Res. **10**(2), 516 (2022).
18. G. Arvanitakis, R. Bian, J. J. D. Mckendry, and C. Chen, "Gb / s Underwater Wireless Optical Communications Using Series-Connected GaN Micro-LED Arrays," IEEE Photonics J. **12**(2), 1–10 (2020).
19. R. X. G. Ferreira, E. Xie, J. J. D. McKendry, S. Rajbhandari, H. Chun, G. Faulkner, S. Watson, D. C. O. Brien, and M. D. Dawson, "High Bandwidth GaN-Based Micro-LEDs for Multi-Gb / s Visible Light Communications," IEEE Photonics Technol. Lett. **28**(19), 2023–2026 (2016).
20. W. Sun, M. Shatalov, J. Deng, X. Hu, J. Yang, A. Lunev, Y. Bilenko, M. Shur, and R. Gaska, "Efficiency droop in 245-247 nm AlGaN light-emitting diodes with continuous wave 2 mW output power," Appl. Phys. Lett. **96**(6), 061102–248 (2010).
21. D. M. Maclure, J. J. D. Mckendry, J. Herrnsdorf, X. He, E. Xie, E. Gu, and M. D. Dawson, "Size-Dependent Characterization of Deep UV Micro-Light- Emitting Diodes," *Proceedings of IEEE Conference IPC (1)*, 2020–2021 (2020).
22. D. Tsonev, S. Sinanovic, and H. Haas, "Complete modeling of nonlinear distortion in OFDM-based optical wireless communication," J. Lightwave Technol. **31**(18), 3064–3076 (2013).
23. D. Tsonev, S. Videv, and H. Haas, "Unlocking Spectral Efficiency in Intensity Modulation and Direct Detection Systems," IEEE J. Select. Areas Commun. **33**(9), 1758–1770 (2015).
24. M. S. Islim, R. X. Ferreira, X. He, E. Xie, S. Videv, S. Viola, S. Watson, N. Bamiedakis, R. V. Penty, I. H. White, A. E. Kelly, E. Gu, H. Haas, and M. D. Dawson, "Towards 10 Gb/s orthogonal frequency division multiplexing-based visible light communication using a GaN violet micro-LED," Photonics Res. **5**(2), A35 (2017).
25. D. Tsonev, H. Chun, S. Rajbhandari, J. J. D. McKendry, S. Videv, E. Gu, M. Haji, S. Watson, A. E. Kelly, G. Faulkner, M. D. Dawson, H. Haas, and D. O'Brien, "A 3-Gb/s single-LED OFDM-based wireless VLC link using a gallium nitride μ LED," IEEE Photonics Technol. Lett. **26**(7), 637–640 (2014).
26. S. Dimitrov and H. Haas, "Information rate of OFDM-based optical wireless communication systems with nonlinear distortion," J. Lightwave Technol. **31**(6), 918–929 (2013).
27. D. Hughes-Hartogs, "Ensemble modem structure for imperfect transmission media," (July 7, 1987), U.S. Patent 4679227; 4731816, March 1988; 4833706, May 1989.
28. H. Chun, S. Rajbhandari, G. Faulkner, E. Xie, J. J. D. Mckendry, E. Gu, M. D. Dawson, and D. O'Brien, "Optimum Device and Modulation Scheme Selection for Optical Wireless Communications," J. Lightwave Technol. **39**(8), 2281–2287 (2021).
29. J. J. D. McKendry, E. Xie, M. S. Islim, X. Sun, D. MacLure, E. Gu, H. Haas, and M. D. Dawson, "4 Gbps wireless optical communications up to 5 m using a UV-C micro-light-emitting diode array," *Photonics Conference Proceedings* **1**, 2022–2023 (IEEE, 2021).
30. Y. Yoshida, K. Kojima, M. Shiraiwa, Y. Awaji, A. Kanno, N. Yamamoto, S. F. Chichibu, A. Hirano, and M. Ippommatsu, "An Outdoor Evaluation of 1-Gbps Optical Wireless Communication using AlGaN-based LED in 280-nm Band," *Conference on Lasers and Electro-Optics Proceedings* (OSA, 2019), paper SM2G.1.
31. D. Maclure, C. Chen, J. McKendry, E. Xie, J. Hill, J. Herrnsdorf, E. Gu, H. Haas, and M. Dawson, Data for: "116 m Gb/s Deep Ultraviolet Wireless Communications using AlGaN Micro-LEDs", University of Strathclyde (2022), https://doi.org/10.15129/ea008020-bd2f-466a-bd53-ec31f74901eb